UNIVERSITE DE NICE-SOPHIA ANTIPOLIS – UFR Sciences
Ecole Doctorale des Sciences Fondamentales et Aplliquées

ALBERT-LUDWIGS-UNIVERSITÄT FREIBURG

DISSERTATION

Submitted for the degree of doctor of sciences

In Physics

by

Amel ZAATRI

Study of the dynamics of the subsurface layers of the sun using local helioseismology

Thesis directed by Grec GERARD & Von der Luehe OSKAR

To be defended on 17/12/2009
Jury:

John W. LEIBACHER	Referee
Thierry ROUDIER	Referee
Markus ROTH	Examinator
Patrick BOUMIER	Examinator
Janine PROVOST	Defense Guest
Thierry CORBARD	Co-advisor
Gerard GREC	Advisor
Oskar Von der Luehe	Advisor

Contents

List of Figures

Introduction

We can only see a short distance ahead, but we can see plenty there that needs to be done

A. M. Turing

Shems, Soleil, Sun, Sonne, are words that I am using to reach the human perception when referring to the diurnal star of our world. Beautifully, the majestic letter S is ubiquitous in all these words whatever their etymological origin is. S also reigns the words Surface, Sub-Surface, Structure, Sound and harmoniously lead us to the word 'Seismology of the Sun' which is the Science that Seeks to unveil the Secrets of the interior of the Sun by Struggling with the information hold by the Sound waves observed at its Surface.

Undoubtedly, since the discovery of acoustic waves at the solar surface, their exploration has provided us with the most precious details of the dynamics and structure of the solar interior. Since acoustic waves are sensitive to physical properties of the plasma in which they propagate, Seismology of the Sun, or simply helioseismology, acts as a real 'microscope' to check the reliability of the physical processes included in solar models obtained from the stellar evolution theory. This is performed by comparing seismic quantities such as sound speed or density inferred from the inversion of the observed acoustic oscillation frequencies, estimated by what is know as 'global helioseismology', to those corresponding to the standard solar model. Perhaps, the greatest example in this context is the chemical elements diffusion which were neglected in standard solar models but has been confirmed from these comparisons to be of great importance in the material transport inside the Sun. Diffusive solar models reached an amazing accuracy of less than 2.10^{-3} between the seismic and the model sound speed. However, this incredible concordance between the theoretical and the observed Sun broke down recently when the solar heavy element abundances have been found to be lower than previously assumed to build solar models. The new model reveals now a discrepancy up to $1.5.10^{-2}$ between the seismic and theoretical sound speed.

Helioseismology is not only able to tell us about the solar internal structure but also about the dynamics of the Sun which is dominated by the differential rotation that breaks the degeneracy of oscillation modes by splitting them into multiplets. By inverting the observed splittings, rotation in radius and latitude has been unveiled in an unexpected picture where the convection zone of the Sun rotates differentially in latitude and radius whereas rotation becomes uniform in the radiative zone. The transition between the convective and radiative zones is a shear layer called the tachocline. However, no information about the north-south asymmetry of the flows can be inferred from global helioseismology. Moreover, flows also exist along solar meridians but are not resolved from the multiplets because of their very weak amplitude compared to the angular velocity. Nonetheless, their measurement in the Sun is as important as the rotation, notably, because of the role they play in solar dynamo models for clocking the overall solar activity cycle. In order to have access to this missing information in global helioseismology studies, acoustic waves are studied locally rather than in the whole Sun. This is known as local helioseismology. It gathers several techniques that have been successfully used in order to study large scale flow fields in a 3D view of the sub-surface layers, and at smaller scales, the structure and underlying flows below active regions. This thesis is a contribution to the study of the internal dynamics and structure of the Sun through a new analysis of its widely explored oscillation frequencies. This work has been motivated by the availability of continuous observational acoustic oscillation data spanning the whole declining phase of solar cycle 23 from the ground-based Global Oscillation Network Group (GONG) providing us with the opportunity to study long term variations of the flow fields as a function of latitude, longitude, depth and the changing magnetic activity level, that help us lifting some hints on the solar cycle mechanism. Ring diagram analysis which is one of the current successfully used helioseismology techniques is applied to GONG Dopplergrams to measure sub-surface horizontal flow fields. However, care has been taken on using this technique by systematically studying how the data processing parameters can influence the results. Also, I will discuss the origin of some artifacts that can alter our inference of the solar velocity fields.

In part I of this manuscript, I will try to give a concise answer to the two questions that are my main motivations on holding this work; 'why do we need to measure flow fields inside the Sun?' and 'How can we measure them?'. To answer the first question, I will devote the chapter 1 to an overview of the solar dynamo theory and emphasize the importance of having accurate measurements of flow fields inside the Sun along lines of latitudes (rotation) and lines of longitudes (meridional circulation) which are crucial inputs of the flux transport solar dynamo models of the solar activity cycle. The second question is answered via a concise state of the art of rotation and meridional circulation measurements which, inside the Sun, have entirely been deduced from helioseismology. Notably, I will discuss the radial gradient of angular velocity which might reveal another shear at high latitudes close to the surface, but is still hardly resolved from current helioseismic measurements. Helioseismology is the principal tool to assess flow fields inside the Sun hence it is important to understand both its theoretical and observational basements. Hence, chapter 2 will be an overview on helioseismology starting with its theoretical foundations to establish the nature and properties of solar oscillations as well as the effect of a flow field on the frequencies of solar modes. Then, a short summary on the actual observational facilities from space and ground-based network is given. Finally, two investigation methods of helioseismic data; global and local helioseismology, are discussed.

In part II, I have considered two particular problems that are both inspired from the same question of 'How the standard solar model parameters affect solar oscillation properties?' even though their purposes are quite different. Chapter 3 is devoted to the use of helioseismic constraints to check the reliability of solar models that I have computed from a stellar evolution code (Code dÉvolution Stellaire Adaptatif et Modulaire; CESAM). Several mixtures of heavy element abundances have been used, notably those recently determined with lower abundances of C, N and O than their old determinations. I will present my contribution on this issue and show that the change in solar heavy element abundances is affecting the modeling of the whole solar interior including the core when taking into account helioseismic constraints given by the observed small separations of low degree modes. Because most of the work presented in this thesis is about the measurement of large scale velocity fields inside the Sun rather than the structure, I will present in chapter 4 my outcomes on the effect of the change in solar model parameters on the sensitivity functions (or kernels) that are relating solar oscillation frequency perturbations to the underlying velocity fields. The study of these kernels is of a great importance, since they are the main ingredient of the inverse problem that consist of infering flow fields from the observed perturbations of the acoustic power spectra. I will limit this study to high degree modes that are the only set of solar oscillations that can be used for local helioseismology.

In part III, I will discuss in chapter 5 the ring diagram analysis which is one of the local helioseismology techniques that can be used to infer rotation and meridional circulation below the surface. This technique seeks distortions in the 3D solar oscillation power spectra of localized regions of the Sun that are directly related to the underlying flows. It assumes that acoustic waves are locally plane waves which in return require the use of small spatial sizes. Consequently, the observed modes will be restricted to those having shorter wavelengths than the spatial size which have high degrees, roughly from 100 to 1000. These modes limit the probed internal layers to immediate sub-photospheric layers (down to about 16 Mm, i.e. $\tilde{2}$% of the solar radius). To infer subsurface flows from sequences of solar images at different latitudes and longitudes, I analyzed GONG Dopplergrams using the ring diagram pipeline, that I either modified or upgraded in several aspects. Notably, I used the sensitivity functions discussed in chapter 4 to study the effect of solar model ingredients in sub-surface velocity field measurements. I will devote chapter 6 to the study of the effect of the geometric mapping used to define a proper spatial sampling of each region of interest on the solar surface. Indeed, a bad mapping can lead to distorted power spectra and biased measurements. By using several types of mappings, I tried to deduce the one that leads to the weakest artifacts in the measurements.

In part IV, I will give in chapter 7 my results on the study of long term variations of sub-photospheric horizontal flow fields derived from ring diagram analysis of continuous GONG Dopplergrams with 1 min cadence and spanning the period July 2001 until June 2008 which covers 93 Carrington rotations. Velocities are given for a set of latitudes and longitudes at depths going from the first Mm below the surface down to about 16 Mm. I have then assembled velocity fields into synoptic maps that give a general view of the flows as a function of latitude and Carrington longitude at different depths for each Carrington rotation. Meridional and zonal (residual of the rotation) flows are assembled from these maps and averaged in Carrington longitudes for each latitude and depth to perform a study on their north-south asymmetries. Such averaging reveals a strong one year periodicity in the temporal variation of the meridional flow at high latitudes that we have been able to correct after identifying it as an artifact linked to the yearly B_0-angle variation. Other eventual sources of artifacts are also discussed. Moreover, northern and southern horizontal flow fields inferred at different magnetic activity levels are discussed. In the context of the search for relationships between solar activity and the horizontal sub-surface flows, a study on the comparison between sub-photospheric layers rotation and that derived from tracing small bright coronal structures has been accomplished. Finally, I will present in chapter 8, my study on the long term variation of the sub-photospheric radial gradient of angular velocity and try to extend the ring diagram analysis to latitudes up to 60° in an attempt to confirm the sign reversal of the gradient previously hinted around this latitude from global heliosseismology.

Part I

Dynamics of the Sun and Helioseismology

Chapter 1

Dynamo and Dynamics

The solar dynamo is like a jigsaw, where each
individual piece of physics must be understood
before the pieces are assembled in a global model.
S. M. Tobias

Abstract

The solar magnetic cycle is driven by large scale motions of the plasma that advect the primary magnetic flux and contribute to the generation of strong magnetic fields. The Sun is then believed to act as a huge dynamo maintaining its magnetic field from differential rotation and meridional circulation.

1.1 Milestones of the solar dynamics

The detection and explanation of the dynamics of the Sun have been a tremendous problem in science since early times. Thanks to continuous observations of the solar surface since the advent of the telescope in the 17th century, especially systematic observations of sunspots have established the first milestones of the dynamics of the sun. First, Schwabe (1838) discovered the solar cycle after noticing a cyclic change of the sunspot number over years and concluded a period of about 10 years. This period has been reviewed to be 11.111 ± 0.038 years by Wolf (1852) who assembled sunspot observations from several years and recovered solar cycles down to 1761 from which he started counting the solar cycle number[1]. Second, Carrington (1858) discovered two main features of the solar dynamics. He noticed that the higher the latitude of the sunspots the slower is their zonal displacement, this is known as 'differential rotation'. Carrington also realized that the latitudes where sunspots are seen decrease from the maximum to the minimum of a solar cycle. At the minimum, sunspots are confined in an equatorial belt of about 20° north and south, whereas during the maximum this activity belt is enlarged to 40° north and south. This feature is clearly seen through the butterfly diagram represented first by Maunder (1904) shown in figure 1.1.

These findings and the discovery of the magnetic origin of sunspots by Hale (1908) from the detection of the Zeeman effect in the sunspot spectrum helped on establishing the basic thoughts on the origin and the development of solar activity. This was completed by many observations such as the tilt angle between the leading sunspot and the following ones in a sunspot group (Joy's Law), cycle polarity reversals, the poleward migration of the diffuse magnetic field at the surface and the north-south magnetic asymmetry.

All these observations led to a tremendous work on modeling the magneto-hydrodynamical properties of the polarized solar plasma (MHD models) in order to reproduce the solar activity mechanism. Nowadays it is still the major unresolved problem in solar physics. The generally accepted concept is that the sun

---

[1] Wolf's identification of solar cycles is based on the sunspot number $R = K(t + 10g)$ where t is the number of individual sunspots, g is the number of group spots and K is a correcting coefficient related to the used observational tools. This number, called Wolf Number or sunspot number, is still used today to quantify the solar activity.

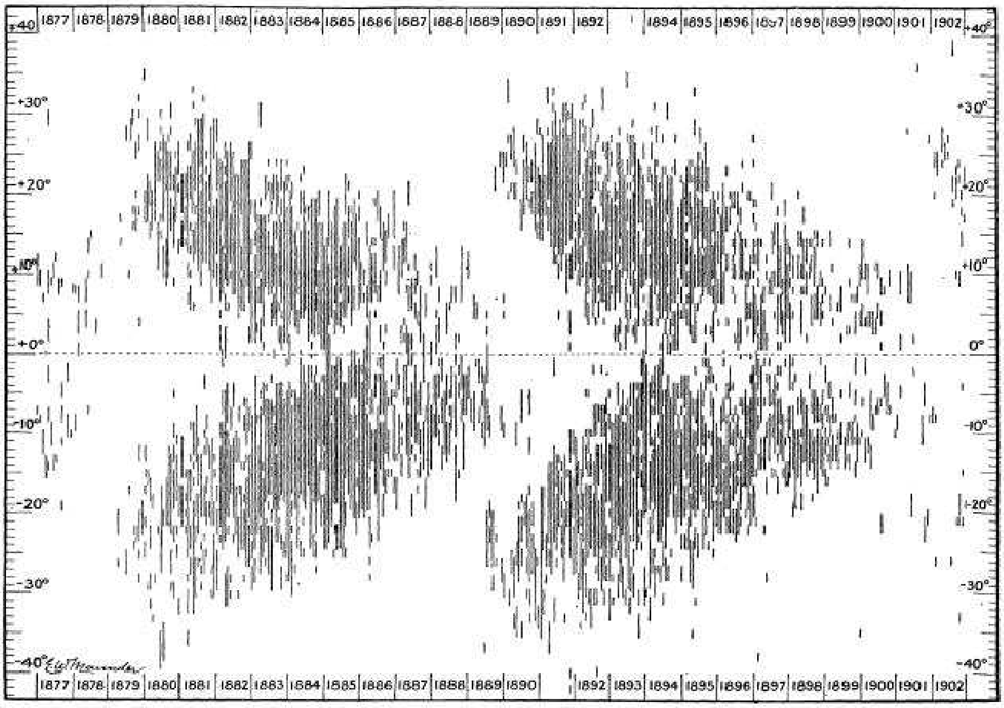

FIG. 8.—DISTRIBUTION OF SPOT-CENTRES IN LATITUDE, ROTATION BY ROTATION, 1877-1902.

Figure 1.1: First butterfly diagram constructed by Maunder in 1904 showing the distribution of sunspots in latitude from year 1877 to year 1902.

is a huge dynamo operating in the convection zone by large scale motions of the conducting fluids to generate the magnetic field.

Even though several dynamo models have been proposed so far, in the following I will only describe the widely and successfully used mean field dynamo models and assess the importance of measuring subsurface flows at the latest. A very extensive literature is now available on this topic (e.g Charbonneau, 2005, 2009; Nandy, 2009; Stix, 2002; Weiss and Thompson, 2009)

1.2 Basics on solar dynamo modeling

The essential problem for creating a solar dynamo model is based on finding the solution to the magnetohydrodynamical induction equation, generated from

Maxwell's equations, that gives temporal evolution of the magnetic field $\mathbf{B}$ (1.1), where the divergence-free condition $\nabla.\mathbf{B} = 0$ is always maintained:

$$\frac{\delta \mathbf{B}}{\delta t} = \nabla \times (\mathbf{u} \times \mathbf{B} - \eta \nabla \times \mathbf{B}), \tag{1.1}$$

where η is the magnetic diffusivity. The term holding it in the equation 1.1 (second term of the right hand side (RHS)) represents the resistive dissipation of the current systems supporting the magnetic field and thus is a cooling source term for B. The first term of the RHS represents the inductive action of the flow field $\mathbf{u}$, and thus is the source term for B. Basically, resolving the solar dynamo problem consists on finding a flow field $\mathbf{u}$ capable to preserve B against the ohmic dissipation. In addition, the solar dynamo model needs to reproduce the many observed solar cycle characteristics such as butterfly diagram and polarity reversal.

One way to simplify this problem is to separate the magnetic field and the flow field into a mean axisymmetric component and a fluctuating component that gathers all the non-axisymmetric contributions such as $\mathbf{B} = \bar{\mathbf{B}} + \grave{\mathbf{b}}$ and $\mathbf{u} = \bar{\mathbf{u}} + \grave{\mathbf{u}}$. Two equations corresponding to the two components are then deduced from the induction equation. However, the two components are coupled by the term $\grave{\mathbf{u}} \times \grave{\mathbf{b}}$ which is usually approximated as an expansion of $\bar{\mathbf{B}}$ such as $\grave{\mathbf{u}} \times \grave{\mathbf{b}} = \alpha \bar{\mathbf{B}} + \beta(\nabla \times \bar{\mathbf{B}})$[1] where α and β are parameters of the turbulence of the fluid. The mean field induction equation which governs what is known as ”the mean field solar dynamo theory” is then given by

$$\frac{\delta \bar{\mathbf{B}}}{\delta t} = \nabla \times (\bar{\mathbf{u}} \times \bar{\mathbf{B}} + \alpha \bar{\mathbf{B}} - \eta_t \nabla \times \bar{\mathbf{B}}), \tag{1.2}$$

where $\eta_t = \eta + \beta$ is now the total diffusivity of the fluid.
Moreover, the mean magnetic field can be written in spherical coordinates (r, θ, ϕ) as a sum of a toroidal component B_ϕ (longitudinal or azimuthal) and a poloidal component $\mathbf{B_p} = \nabla \times A\mathbf{e}_\phi$ (contained in the meridional plane, i.e. has a radial

---

[1] this equation is given under the approximation of a homogeneous, weakly isotropic turbulence otherwise α and β are pseudo tensors defined from a turbulence model.

and a meridional component) such as $\bar{\mathbf{B}} = B_\phi \mathbf{e}_\phi + \mathbf{B_p}$. The flow field can also be decomposed in the same way $\bar{\mathbf{u}} = u_\phi \mathbf{e}_\phi + \mathbf{u_p}$ where $u_\phi = r \sin\theta\Omega(r,\theta)$; Ω is the angular velocity and $\mathbf{u_p}$=$u_r\mathbf{e_r}$+$u_\theta\mathbf{e}_\theta$ is the meridional circulation. By taking into account these two decompositions in addition to the constraint $\nabla.\bar{\mathbf{B}} = 0$, one can obtain separate equations of the temporal evolution of the two magnetic field components from equation 1.2.

$$\frac{\delta A}{\delta t} = \eta_t(\nabla^2 - \frac{1}{r^2 \sin^2\theta})A - \frac{\mathbf{u_p}}{r\sin\theta}.\nabla(r\sin\theta A) + \alpha\bar{B} \tag{1.3}$$

$$\begin{aligned} \frac{\delta B_\phi}{\delta t} &= -\frac{1}{r}[\frac{\delta}{\delta r}(r u_r B_\phi) + \frac{\delta}{\delta\theta}(u_\theta B_\phi)] \\ +rsin\theta(\mathbf{B_p}.\nabla)\Omega - \mathbf{e}_\phi.[\nabla\eta_t \times \nabla \times B_\phi \mathbf{e}_\phi] &+ \eta_t(\nabla^2 - \frac{1}{r^2\sin^2\theta})B_\phi \end{aligned} \tag{1.4}$$

The source term $[r\sin\theta(\mathbf{B_p}.\nabla)\Omega]$ in the equation of the temporal evolution of B_ϕ 1.4 corresponds to **the production of the toroidal field (B_ϕ) from the stretching of the poloidal field B_p by the differential rotation gradient (the Ω-effect)**. The source term $[\alpha\bar{B}]$ in the equation of the temporal evolution of B_p 1.3 reveals the regeneration of the poloidal field from the twisting of the toroidal field by turbulence (the α-effect, introduced first by Parker (1955)). On the other hand, terms including meridional circulation u_p are advection terms i.e **meridional circulation transports magnetic field but does not creat it nor destroy it**. The rotation gradient, the meridional circulation and the α coefficient are input ingredients to the model, hence it is necessary to correctly infer their profiles in depth and latitude either from simulations or from observation. This model is known as the "flux-transport $\alpha\Omega$ mean field dynamo model" (Choudhuri *et al.*, 1995), its global scenario is illustrated in figure 1.2 and can be summarized as follows :

1. Differential rotation creates the toroidal magnetic field by stretching a pre-existing poloidal field at the base of the convection zone where the tachocline (a strong rotation shear layer) is located.

2. The toroidal field rises to the solar surface by magnetic buoyancy and erupts out through the surface creating sunspots.

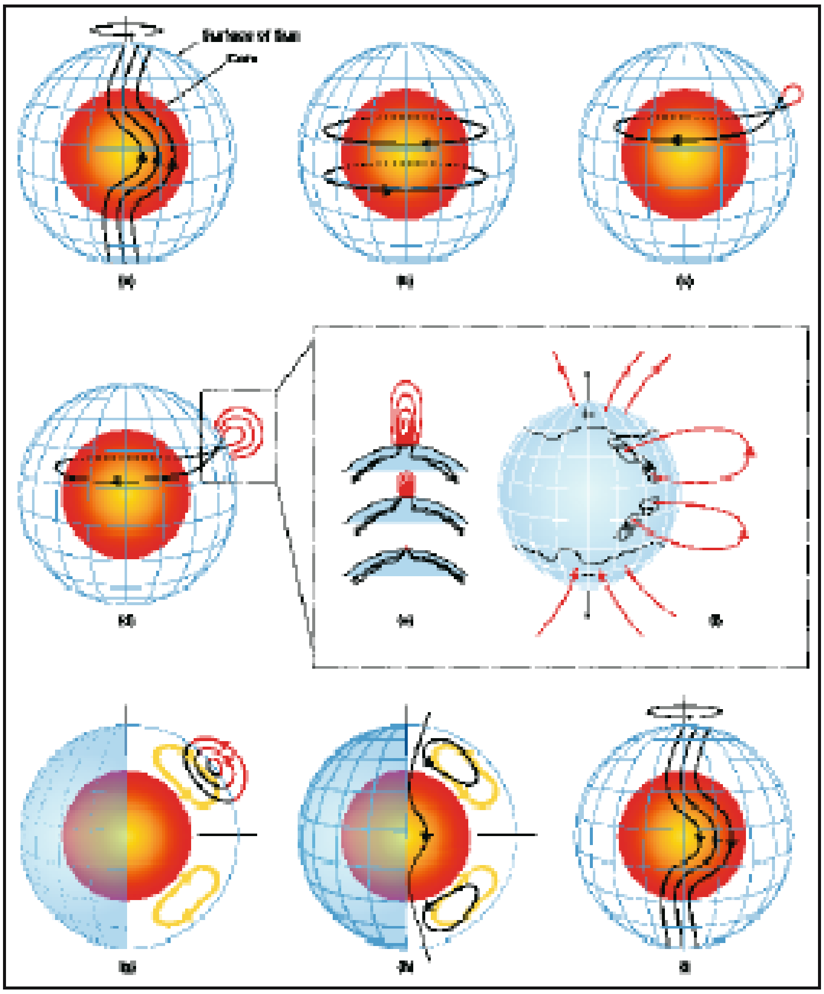

Figure 1. Schematic of solar flux-transport dynamo processes. Red inner sphere represents the Sun's radiative core and blue mesh the solar surface. In between is the solar convection zone where dynamo resides. **(a)** Shearing of poloidal field by the Sun's differential rotation near convection zone bottom. The Sun rotates faster at the equator than the pole. **(b)** Toroidal field produced due to this shearing by differential rotation. **(c)** When toroidal field is strong enough, buoyant loops rise to the surface, twisting as they rise due to rotational influence. Sunspots (two black dots) are formed from these loops. **(d, e, f)** Additional flux emerges (**d, e**) and spreads (**f**) in latitude and longitude from decaying spots (as described in Fig. 5 of Babcock 1961). **(g)** Meridional flow (yellow circulation with arrows) carries surface magnetic flux poleward, causing polar fields to reverse. **(h)** Some of this flux is then transported downward to the bottom and towards the equator. These poloidal fields have sign opposite to those at the beginning of the sequence, in frame (a). **(i)** This reversed poloidal flux is then sheared again near the bottom by the differential rotation to produce the new toroidal field opposite in sign to that shown in (b).

Figure 1.2: source: Dikpati and Gilman (2009).

3. The non-axisymmetric mechanism "$\alpha-$effect" (turbulence) regenerates the poloidal field from the toroidal field at near surface layers.
4. Meridional circulation transports back the poloidal field to the base of the convection zone where the amplification and storage of the toroidal field take place. Thereby, the cycle is maintained.

Nowadays, this scenario is one of the most plausible dynamo models as it allows to reproduce most of the observed solar cycle characteristics such as the butterfly diagram, the tilt of the bipolar sunspot pairs and the period of the solar cycle (Dikpati and Gilman, 2009). However, opinions differ as to the location and origin of the $\alpha-$effect, which makes mainly the most important difference between the current solar dynamo models. Also, the location of the generation and amplification of the toroidal field is still questionable and near surface dynamos have been suggested (Brandenburg, 2005; Dikpati *et al.*, 2002) regarding the recent helioseismology observations of a near surface radial shear (Corbard and Thompson, 2002).

1.3 Large scale flow measurements

As shown from the previous section, Meridional circulation and Rotation are crucial ingredients of the solar dynamo theory. The advent of heliosesimology, which consists on the exploration of information about the dynamics and the structure of the Sun that is carried by the acoustic solar oscillation, unabled us to measure these large scale flows inside the Sun. In this section, I will summarize the state-of-the-art of our current knowledge on the measurement of solar rotation (see Howe, 2009) and meridional circulation.

1.3.1 Solar differential rotation

Surface rotation

Before helioseismology techniques were available, only solar surface rotation has been accessible by observation with several techniques (Beck, 1999). In addi-

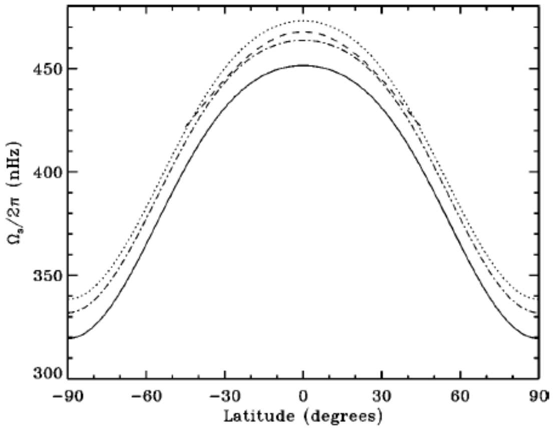

Figure 2 Near-surface solar-rotation rates as determined from surface spectroscopic Doppler-velocity measurements (*solid line*), tracking magnetic features (*dashed line* from tracking sunspots, *dot-dashed line* from magnetogram correlation tracking), and tracking Doppler features resulting from large-scale (supergranular) convective flow patterns (*dotted line*); the curves correspond to fits of the form given in Equation 1, with coefficients adapted from Beck (2000). A rotation rate of 320 nHz corresponds to a period of 36 days, and a rate of 460 nHz corresponds to a period of 25 days.

Figure 1.3: Source: Thompson *et al.* (2003)

tion to the oldest method of sunspot tracking, different magnetic tracers such as faculae, plages and supergranulation, have been used to estimate the solar rotation rate (Bumba and Klvana, 1994). Magnetic features are usually rotating at different speeds and faster than the solar photosphere as revealed from Doppler measurements of the photosphere as shown in figure 1.3 (e.g. Foukal, 1976). This is widely admitted to be due to the fact that the active regions are anchored inside the sun at different inner layers rotating faster than the surface. Also, most of the magnetic tracers are confined in the activity belt (up to 45° north and south at the beginning of the cycle and few degrees around the equator at the end of the cycle) which limits the latitudinal extension of rotation measurements. Solar rotation at the surface has been known to be differential in latitude since early sunspot observations and the first empirical differential rotation law was formulated by Carrington such as $\Omega(\mathrm{nHz}) = 456.53 - 64.97 \sin^{7/4}\theta$, where θ is the latitude. The equatorial rotation in this formula (i.e. 456.53 nHz or

14.2 deg/day or a sidereal rotation period of 25.38 days[1]) is still used in heliographic coordinates to define the longitude -called Carrington longitude- of solar magnetic features in time. Carrington's formula was revised several times due to better observations of sunspots but also due to spectroscopic measurements of Doppler shifts of solar spectral lines, that allow rotation measurements to much higher latitudes, as well as from other measurements. Currently, the rotation law is widely accepted to be given as function of the sin of the latitude θ such as

$$\Omega(\mathrm{nHz}) = \mathrm{a}_0 - \mathrm{a}_1 \sin^2\theta - \mathrm{a}_2 \sin^4\theta \tag{1.5}$$

a coefficients are called 'tracking rates', a_0 is the equatorial rotation rate and a_1 and a_2 are the differential rotation rates. Their values strongly depend on the used tracer or method, they are higher for magnetic feature tracers than for the quiet Sun. Tracking rates measured by Snodgrass (1984) are the most commonly used photospheric tracking rates and are given such as $a_0 = 451.43$ nHz, $a_1 = 54.77$ nHz, $a_2 = 80.17$ nHz.

Internal rotation

In the last two decades, helioseismology enabled us to measure solar rotation, by investigating the solar acoustic waves, not only at the surface but also in the interior (Thompson *et al.*, 1996). The main idea is that the rotation causes splittings on the acoustic oscillation frequencies from which the properties of the rotation can be inferred. More explicitly, in a sphericaly symmetric Sun, all the acoustic eigenmodes with same radial order (n) and angular order (ℓ) would have the same eigenfrequency ω_{nl} (see chapter 2), but because the sun is rotating, each mode is splitted into $2\ell+1$ components identified by an additional number called the azimuthal number $m = -\ell, -\ell+1, ...\ell$. This splitting of the frequencies is the main observational quantity for helioseismic measurements of the solar internal

---

[1] The Carrington rotation period also fixes the Carrington rotation number since Carrington started to count it on November 9, 1853. For instance, November 10, 2009 corresponds to the beginning of Carrington rotation 2090.

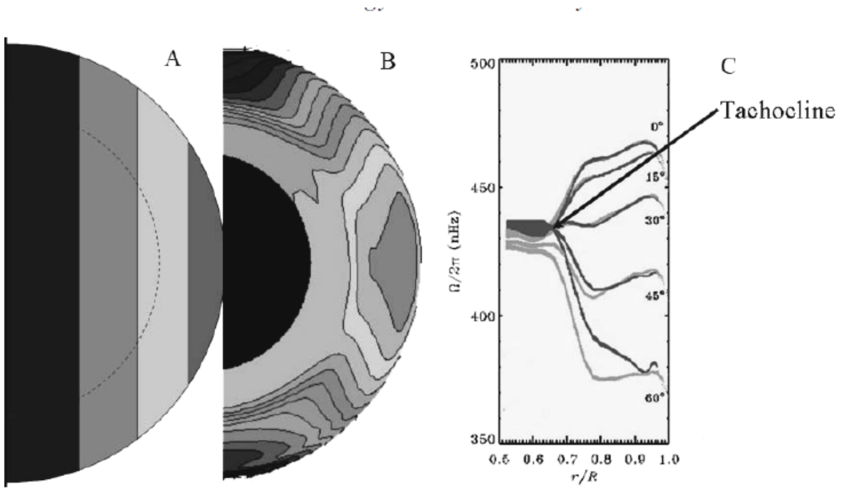

Figure 2. Panel (A): The isorotation contours assumed by pre-1988 dynamo theories. Panel (B): The isorotation contours revealed by helioseismology. Panel (C): Depth profiles of the rotational velocity at five latitudes. Dark grey lines are from MDI data, light grey lines are obtained from GONG data. The width of the lines shows the uncertainty in the measurements. The tachocline is indicated, where differential rotation in the convection zone transitions to solid-body rotation in the radiative envelope.

Figure 1.4: Internal rotation profile before and after helioseismology. Source: Hill (2008).

rotation. In the case of rigid rotation, it is given by:

$$\omega_{nl0} - \omega_{nlm} = mC_{nl}\Omega, \tag{1.6}$$

Ω is the rotation rate and C_{nl} is a constant depending on the considered solar model and the properties of the eigenmode. First reliable splittings have been resolved by Duvall and Harvey (1984) and inverted by Duvall *et al.* (1984) who gave the first estimation of the rotation inside the sun. This helioseismic analysis is commonly called 'global helioseismology' as the used acoustic modes are propagating through the whole sun. Afterwards, better inversion methods have been developed either as a function of radius only in the equatorial plane or as a function of radius and latitude through 2D inversions (see Corbard (1998) for more details on the inversion of helioseismic data to infer solar rotation). Furthermore, the launch of SOlar Heliospheric Observatory (SOHO) in 1995 allowed to get unprecedented observed frequency splittings from the Michelson Doppler Imager (SOHO/MDI) data with a precision down to 1nHz (Schou *et al.* (1998)).

One of the most important helioseismic results was the radial and latitudinal profile of the differential rotation rate where the convective zone rotates differentially and the radiative zone as a solid body - rotation of about 345nHz - . This tremendous change of the rotation regime happens after crossing a shear layer, less than 0.1 solar radius thick, called the tachocline (Spiegel and Zahn, 1992). This result was unexpected and hence revolutionized the contemporary dynamo models. In fact, before the advent of helioseismology, the used internal rotation profile was that obtained from numerical simulations of rotating convection in spherical shells (e.g. Gilman and Miller, 1986) that suggested that rotation velocity should be nearly constant on cylinders of constant angular momentum aligned with the rotation axis and decreasing inward with decreasing the distance to the rotation axis. Figure 1.4 illustrates the profile of the internal solar rotation given from simulations[1] (A) and that revealed from helioseismology (B). Panel C of the same figure displays latitudinal and radial profile of the rotation as revealed from helioseismic analysis of the most commonly used data sets provided by MDI and the ground-based Global Oscillation Network Group network (GONG). In this figure, the tachocline is shown in addition to a near-surface shear layer that I will discuss in the next section. Thompson *et al.* (2003) give a complete overview of observational and theoretical insights on the solar internal rotation .

Subsurface rotation

The difference between the spectral Doppler shift and tracer measurements of the rotation gave first hints of a negative gradient of the rotation below the surface (rotation increasing with depth). First helioseismic attempts to measure the rotation just below the surface were made by Rhodes *et al.* (1990) who claimed the detection of a negative subsurface gradient from the inversion of intermediate degrees of p-modes ($3 < \ell < 170$). However, splitting uncertainties of the mid-80's did not allow to confirm this result until GONG and MDI data became available. Thompson *et al.* (1996) confirmed the detection of a distinctive near-surface shear at low to mid-latitudes using global mode inversion of frequency splittings from

---

[1] Nowadays, supercomputing facilities allowing to include more complex ingredients in the simulation of rotating convective fluids are bringing the results more and more close to the helioseismic profile of the internal rotation (e.g. Brun and Toomre, 2002).

GONG. Kosovichev *et al.* (1997) and Schou *et al.* (1998) used multiplet frequency splittings from MDI and confirmed the detection of a significant rotational shear in a thin layer below the surface. Basu and Antia (2001) investigated the near-surface shear in both GONG and MDI data and found that the shear layer persists in all latitudes when using frequency splittings from GONG but vanishes at high latitudes (sign reversal of the gradient) when using MDI data. The appearance of sign reversal at high latitudes in MDI data has been related to the 'jet' like features observed in this data (Schou *et al.*, 1998).

Corbard and Thompson (2002) restricted their inversion to the use of surface-gravity waves (f-mode) frequency splittings from MDI with modes up to $\ell = 300$ in order to focus on the near-surface rotation only (up to 15Mm) and investigated the latitudinal variation of the rotational gradient up to 75°. They found that the radial gradient has a constant value of -400 nHz/$\mathrm{R_{sun}}$ from the equator up to 30° (i.e. the rotation rate increases linearly with depth). Above 30° the gradient starts to decrease until reaching a very small value at around 50°. And by filtering only high degree modes ($\ell > 250$) they found a sign reversal of the rotational gradient which might then be localized in the outer most 5 Mm. Corbard *et al.* (2008) repeated the same study with higher degree modes (ℓ up to 1000) obtained by Reiter (2007) from a ridge fitting technique. From this data set, they have been able to recover their previous results by using only modes up to $\ell = 300$. However, using all modes up to $\ell = 1000$, i.e. when the shallowest layers are included, the linear behavior of the rotation breaks down. Nonetheless, it is hard to tell how reliable the determination of high degree mode splittings from the ridge fitting techniques is since the amplitudes of these modes are weak and the signal to noise ratio of the solar acoustic oscillation spectrum increases dramatically in this part. This issue bring us to the importance of using local helioseismology techniques to measure underlying flows and their gradients.

Indeed, local helioseismology which consists on the exploration of short lived waves in localized areas, and hence limited to shallow layers, is suitable to measure radial gradient in the near-surface. Several helioseismology techniques such as ring diagram analysis, time-distance, and Fourier-Hankel decomposition have been developed since the end 80's and are nicely summarized in Duvall (1998) with an extensive literature to the early works related to each technique. Local

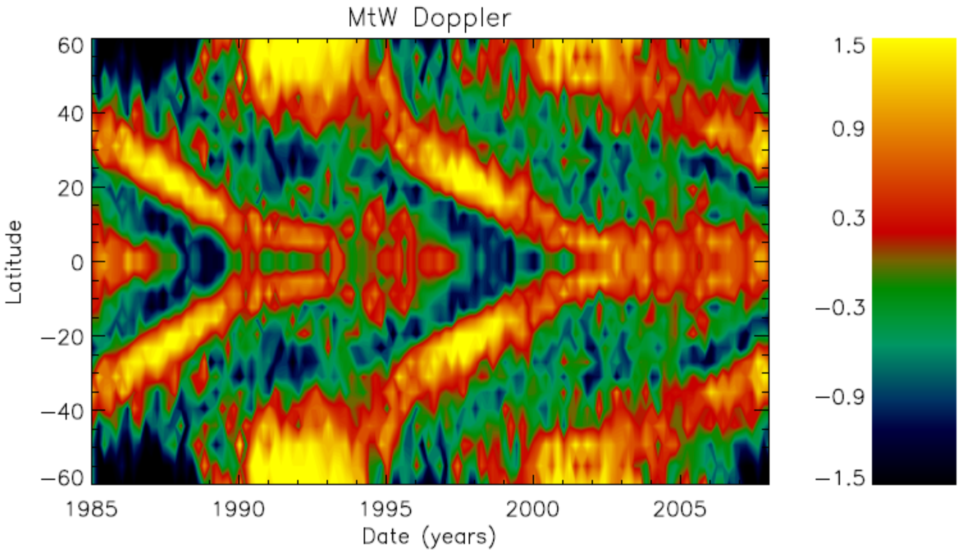

Figure 1.5: Torsional oscillations obtained from Mont Wilson data since 1986. Source Howe (2009).

heliosiesmology of MDI and GONG images has allowed important achievements in the exploration of the solar flow fields. For instance, Komm *et al.* (2004) analyzed zonal flows inferred from the ring diagram local helioseismology analysis (see chapter 3) and found that the radial gradient of the zonal flow (rotation residual) is mainly negative except within 2 Mm below the surface at latitudes poleward of about 20°. Also the authors found good correlation between the magnetic field and the radial gradient. More results are discussed in chapter 7.

Torsional oscillations

Solar rotation also displays a well structured temporal variation seen when subtracting the mean differential rotation from the daily rotation, first detected by Howard and Labonte (1980). This pattern named 'Torsional oscillation' corresponds to equatorward migrating branches of faster and slower than average zonal flows of a few m/s symmetric about the equator (see figure 1.5). Interestingly, the torsional oscillation pattern is well correlated with the solar cycle where it appears at the beginning of the solar cycle at the pole and reaches the equator at the end of the cycle. More precisely, the torsional oscillation pattern begins at the pole little time before the first sunspots of the new solar cycle start to appear. This has been assumed to be due to the formation of a strong toroidal field in the high-latitude tachocline before the beginning of the sunspot cycle (Chakraborty *et al.* (2009)). Global helioseismology has been able to confirm that the torsional oscillation pattern is not a near-surface phenomenon but rather penetrates deep into the convection zone. Howe *et al.* (2000) used combined rotational splittings from GONG and MDI and reported a radial extension of the torsional oscillation pattern down to about 60Mm (about 8% of the solar radius). Moreover, Vorontsov *et al.* (2002) analyzed 6 years of MDI data and found that the torsional oscillation persist in the entire solar convection zone. The torsional oscillation pattern resolved for the year 2008 has been one of the key explanations of the current extended solar minimum (end cycle 23 – beginning of cycle 24). Indeed, (Howe *et al.* (2009)) reported that the flow band corresponding to the new cycle has been moving more slowly toward the equator than it was observed in the previous cycle making the new cycle (24) starting slower than the previous ones.

The torsional oscillation pattern has also been studied using different methods of local helioseismology and different data sets and interesting relationships between the flow and the magnetic activity have been reported. Basu and Antia (2000) analyzed MDI data using ring diagram analysis and found that the amplitude of the zonal flow (torsional oscillation) increases with solar activity. Zhao and Kosovichev (2004) analyzed MDI data using the time-distance method to study the zonal flow and found good agreements with previous helioseismology results. More recently, Komm *et al.* (2009) using ring diagram analysis of 6 years of GONG data found a positive correlation between the unsigned magnetic flux and the zonal flow at depths ranging from the surface to about 16Mm where the zonal flow in active areas were higher than the quiet-sun flow.

1.3.2 Meridional circulation

Meridional circulation is a large scale flow field propagating poleward in the two hemispheres. Together with differential rotation it is the most important ingredient in building the current flux-transport dynamo models. It is supposed

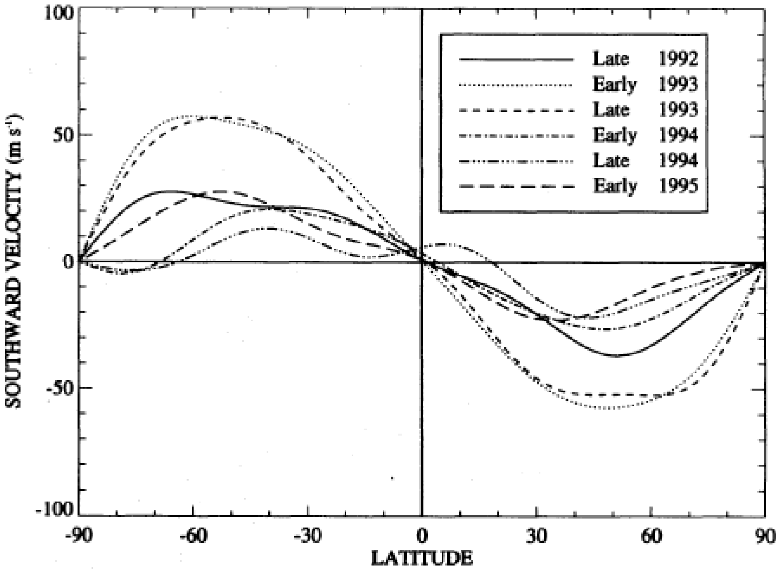

Figure 1.6: Surface meridional circulation derived form Doppler measurements. Source: Hathaway (1996).

to form huge cells in both hemispheres with an amplitude of about 10m/s to 15m/s at the surface to few m/s[1] when penetrating deep in the convection zone to transport the poloidal magnetic field back to the tachocline in order for the cycle to be reproduced. It is also considered as a clock for the solar cycle[2]. Meridional flow has been successfully measured at the surface (figure 1.6) by, for instance, tracing small magnetic features (Komm and Howard (1993), 10m/s) or from Doppler measurements (Hathaway (1996), 20m/s). The detection of this flow field throughout the convection zone has not been accomplished directly so far. However, Hathaway *et al.* (2003) claimed that the equatorial drift of sunspots during the solar cycle, with a mean value of 1.2m/s, is the signature of meridional

---

[1] Mass density at the bottom of the CZ is about 5 times larger than at the surface. To conserve momentum, the velocity at the bottom of the CZ should be 5 times smaller than at the surface.

[2] Suppose a meridional circulation of about v=2m/s at the bottom of the convection zone, in order for the matter to be transported from the pole to mid-latitudes (where first sunspots of a new cycle start to appear) with such a velocity, it needs about $\frac{2\pi R_s/8}{v} \simeq 9$ years which is more or less the extent of a typical solar cycle.

circulation at the base of the convection zone.

Where global helioseismology analysis of low and intermediate modes permitted great achievements on the investigation of the internal rotation of the sun, it was not successfully used to infer meridional circulation because of its very small effect on the acoustic frequencies compared to the high splittings caused by differential rotation. Nonetheless, some theoretical work has been assessed to try to detect the effect of the meridional circulation in global solar oscillation frequency multiplets from long time series (Roth and Stix (2008)). No observational data analysis work has been assessed out of this work yet, but the authors are still optimistic that their analysis could lead to the detection of meridional flow signatures in the acoustic frequencies using time series of several years to reach a frequency resolution of few $10^{-2}\mu$Hz which is now available from long term helioseismic observations.

Local helioseismology is up to now the only way to measure meridional circulation inside the sun. Successful measurements have been assessed from the analysis of MDI data using several techniques e.g. (time-distance; Giles, 1999), (ring diagram analysis; González-Hernández *et al.*, 1999), (Fourier-Hankel analysis; Krieger *et al.*, 2007). Ring diagram analysis of MDI and GONG data suggest the existence of a second cell, called 'counter cell', at high latitudes (González-Hernández *et al.*, 2006; Haber *et al.*, 2002). However, this result is still controversial since the analysis at these latitudes is strongly affected by the variation of the B_0 angle (see article II).

1.4 Discussion

In this chapter I have tried to answer two questions that are the main motivations of my work: '**Why do we need to measure flow fields in the Sun?**' and '**How can we measure flows inside the Sun?**'.

The first question has been pointed out through an overview on the current solar dynamo modeling that I might summarize in the three following points.

- **The differential rotation gradient** **($\nabla\Omega$)** is the most important source term for the generation of the toroidal magnetic field from the 'seed' poloidal magnetic field.

- **Meridional circulation (v_y)** is an important ingredient in the 'flux-transport solar dynamo models'. It advects the magnetic field from the outer layers down to the base of the convection zone and acts as a clock for the solar cycle.
- The seat of the solar dynamo is still questionable. In addition to the popular idea of its location at the tachocline, it has been argued that **the seat of the solar dynamo might be located near the surface where a radial shear has been observed**.

Thus, large scale horizontal flows, i.e. meridional circulation and rotation, are crucial inputs of the solar dynamo models, and hence need to be as accurately defined as possible in order to infer reliable solar dynamo models which are, up to now, the only way to understand the overall mechanism of the solar cycle. Particularly, the sub-surface flows are important to investigate in order to help lifting the veil on the location of the solar dynamo.

To answer the second question I have tried to go through the current measurements of large scale flows, pointing out the fact that most of the achieved work has been carried out using the powerful technique of Helioseismology through local and global investigations of the acoustic waves. Both global and local helioseismology gave valuable results on the investigation of the flows below the surface. It is then motivating to still use helioseismology in several aspects in order to infer and investigate flows below the surface, that I have done by mainly using local analysis of the acoustic waves in order to focus on sub-photospheric flows. However, lots of care has to be taken regarding the sensitivity of helioseismology techniques to several aspects of the solar modeling and observational artifacts that I have tried to emphasize on some of them in this work. But first, one has to get an overview on the theoretical an observational basis of helioseismology in order to understand what we need and what we get from this power tool, so is the purpose of the next chapter.

Chapter 2

Helioseismology

Although to penetrate into the intimate mysteries of nature and thence to learn the true causes of phenomena is not allowed to us, nevertheless it can happen that a certain hypothesis may suffice for explaining many phenomena.

L. Euler

Abstract

An unprecedented tool to probe the solar structure from the core to the upper photosphere originated since the discovery of the acoustic nature of the observed 5 min oscillations at the solar surface in the early 70s. Known as Helioseismology, this tool is still the most reliable source to constrain evolutionary models of the solar interior. The investigation of observed solar oscillations is gathered in two helioseismology sub-fields: Global Helioseismology and Local Helioseismology. Where the first sub-field is used to infer longitudinally averaged flows and structure deep inside the sun, the second provides 3D investigations of the solar flow fields and structure but in narrowed surface regions.

2.1 Introduction

Turbulence in the convection zone perturbs the steady hydrodynamical properties of the fluid resulting on the generation of waves. The two biggest categories of waves are those having pressure gradient as restoring force known as *p-modes* and those having the gravity as restoring force know as *g-modes*. The study of these waves in the sun is dubbed 'Helioseismology'. *g-modes* are confined below the convection zone and reach the surface with an extremely weak energy which makes their amplitude below the noise level, their detection is nowadays one of the biggest challenge in helioseismology (Appourchaux *et al.*, 2009). Whereas *p-modes* have been detected in early 60's and since than are largely observed in the solar surface from velocity and intensity signals. First observations of these waves have been achieved by Leighton *et al.* (1962) who reported a periodic pattern of about 300s at the photosphere (5 min period). Their first interpretation as standing acoustic waves has been suggested 10 years after their detection by Ulrich (1970) and Leibacher and Stein (1970). *p-modes* are trapped inside resonant cavities of different thicknesses below the surface. From the fact that the temperature inside the sun increases with depth, so does the sound speed, the wave is reflected at a certain inner point where its wave vector becomes strictly horizontal. The outer limit of the resonant cavity is the solar surface, where the density decreases drastically and the remaining matter does not allow to carry all the wave component through the solar atmosphere.

In this chapter, I will give an overview of the equations governing the physics of the solar oscillations based on small perturbation theory applied around a static equilibrium state of the stellar plasma. Basic references on this topic are Unno *et al.* (1989) and Christensen-Dalsgaard (2003). I will also discuss the two biggest branches of helioseismology; global and local helioseismology (see the book by Pijpers (2006)) and review the nowadays observational facilities and the commonly used data in helioseismology.

2.2 Theoretical foundations of helioseismology

Solar oscillations have a very small amplitude compared to the characteristic scales of the solar interior. This allows to consider the oscillations as small perturbations around the equilibrium state of the star. Hence, the linear adiabatic oscillations equations can inferred by carrying out a small perturbation analysis of an equilibrium solar model.

The equilibrium model

The hydrodynamical state of the stellar plasma where the magnetic magnetic field is neglected is governed by the mass conservation equation, the momentum equation, the energy equation and the Poisson equation given respectively below.

$$\frac{\partial\rho}{\partial t} + \boldsymbol{\nabla}.(\rho\boldsymbol{v}) = 0 \tag{2.1}$$

$$\rho(\frac{\partial}{\partial t} + \boldsymbol{v}.\boldsymbol{\nabla})\boldsymbol{v} = -\boldsymbol{\nabla}P + \rho g \tag{2.2}$$

$$\rho T(\frac{\partial}{\partial t} + \boldsymbol{v}.\boldsymbol{\nabla})S = \rho\varepsilon - \boldsymbol{\nabla}.\boldsymbol{F} \tag{2.3}$$

$$\nabla^2\phi = 4\pi G\rho \tag{2.4}$$

$$\boldsymbol{F} = -K\boldsymbol{\nabla}T, \tag{2.5}$$

ρ is the density, P the pressure, T the temperature, $\mathbf{v}$ the velocity flow, S the specific entropy, ε the nuclear reaction rate, ϕ the gravitational potential, $\mathbf{F}$ the total energy flux.Each of these quantities gathers tremendous theoretical and observational treatments in order to describe the physical properties of the solar interior from the core to the surface. A short summary of the most important aspects of solar interior modeling will be given in order to bring a clear picture to the physics of the solar interior we are dealing with.

What is a 'standard' solar model?

The Sun is a common star of one solar mass located in the main sequence of the HR diagram at the middle of its life. In order to get the current solar model

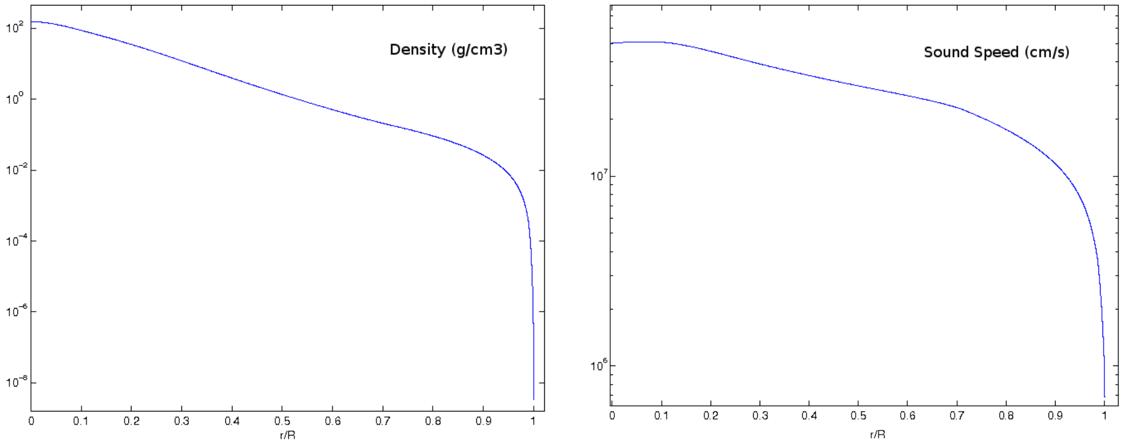

Figure 2.1: Density and sound speed as function of fractional radius[1] derived from a standard solar model.

that describes the properties of its interior as function of radius (1D model), the stellar evolution theory is used.

An evolutionary model of the Sun starts from a chemically homogeneous model.The evolution of the star consists on the change of its chemical composition by means of thermonuclear reactions which are the primary source of energy. These reactions insure the production of helium from hydrogen burning following, among others, the most efficient proton – proton cycle. Another source of change in chemical composition is the microscopic diffusion driven by the structure gradients in the radiative zone. The Sun is supposed in a hydrostatic equilibrium, where pressure and gravity are equally balanced, and is assumed to be spherically symmetric (rotation and magnetic field are ignored). The energy generated from hydrogen burning in the core is firstly transported via radiation by means of continuous emission-absorption of the photons along their way to the surface. The radiative transport depends on the opacity of the materials defined by atomic absorption coefficients for a given chemical composition comprising both pure absorption and scattering[2]. At around 30% below the surface, the radiative transport is not insured anymore because of the dramatic decrease of the

---

[2] The opacity is usually differently determined in two temperature ranges; high and low temperatures. This is because at low temperatures, molecules and grains have to be included in the absorption processes.

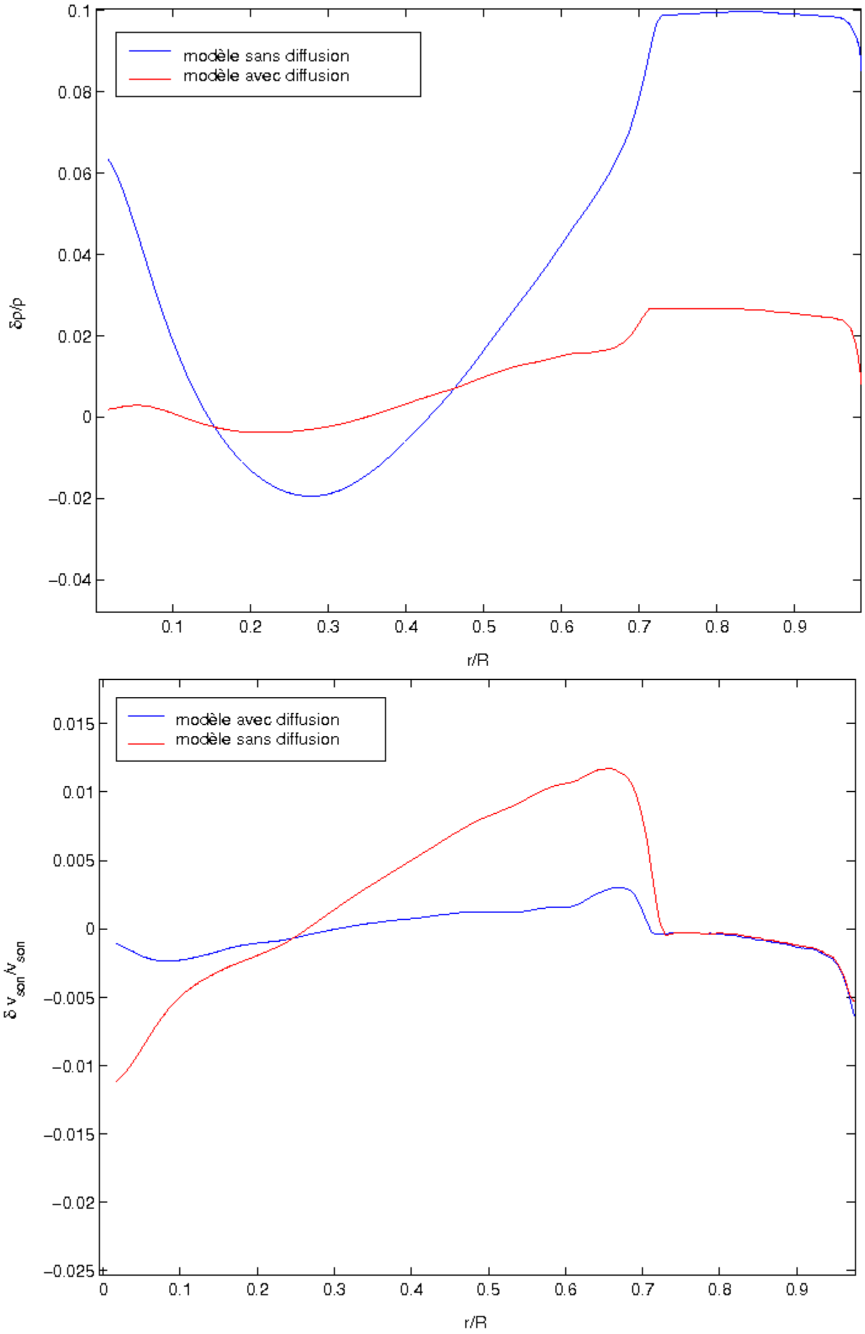

Figure 2.2: Sound speed and density differences as function of fractional radius between seismic observations and solar models with (red) and without (blue) microscopic diffusion.

temperature and the accumulation of heat leading to the apparition of thermal instabilities. These instabilities create convective motions rising adiabatically to the surface. The convection is a very difficult phenomena to model because of its 3D configuration. Most of solar evolutionary models use the Mixing Length Theory (MLT) to get the convective gradient. The MLT consists on describing the convective motions as huge convective cells rising from the bottom of the convection zone until a certain length where their thermodynamical properties are lost. This length is named the Mixing Length and is a free parameter in the construction of a current solar model in addition to the initial helium abundance. In addition, the thermodynamical properties of the stellar plasma are described via the equation of state that gives one of the 3 thermodynamical quantities (pressure, temperature, density) as function of the two others. The basic configuration of the equation of state considers the ideal gas equation and the additional thermodynamical effects are added as corrections to this basic equation.

A 'standard' solar model is calibrated such that at the current age (about 4.6Gyr), radius, mass, luminosity and Z/X (fraction of heavy element abundances and hydrogen abundance) fit with their observed values by adjusting the free parameters i.e., the helium abundance and the mixing length. These quantities are named macroscopic constraints. An exemple of the inferred quantities from a standard solar model is given in figure 2.1 which shows the profile of the density and the sound speed from the upper layers to the core.

Another set of constraints is given by the observed acoustic modes of the Sun. The predicted frequencies of solar oscillations from a standard model can be compared to the observed frequencies in order to evaluate the reliability of the physics of the solar model, this is known as the 'forward problem'. Or, observed frequencies can be used to infer the structure of the Sun, mainly the sound speed and the density, this is known as the 'inverse problem'. In this way, solar oscillations are a real laboratory for the solar interior modeling and have been of a very precious tool to improve our knowledge on the physics of the Sun. For instance, diffusion of chemical elements was neglected in early solar models until helioseismology has proven its crucial role inside the Sun (Christensen-Dalsgaard *et al.*, 1993). Figure 2.2 shows the difference between the sound speed and the density as inferred from the inversion of the observed solar oscillation frequencies and models with and without microscopic diffusion. Clearly, models aith diffusion are much closer to the observation. However, this concordance has been again broken because of the newly revised heavy element abundances that are lower than the abundances used earlier in solar modeling. These abundances bring the difference between the observed sound speed and the predicted one to about 15%. I will talk about this topic in more detail in chapter 3.

For an overview on standard solar models see for instance Provost (1997) and Basu (2007) and for a detailed documentation on stellar evolution see Forestini (1999).

Linear adiabatic oscillation equations

The Eulerian formalism can be used to express small perturbations of each physical quantity around its equilibrium. If this is applied to the equilibrium model (2.1 − 2.5), considered to be static, the linearisation of the system leads to the following set of equations

$$\frac{\partial \rho'}{\partial t} + \boldsymbol{\nabla}.(\rho \boldsymbol{v}) = 0 \tag{2.6}$$

$$\rho\frac{\partial \boldsymbol{v}}{\partial t} + \boldsymbol{\nabla} P' + \rho'\boldsymbol{\nabla}\Phi + \rho\boldsymbol{\nabla}\Phi' = 0 \tag{2.7}$$

$$\rho T\frac{\partial}{\partial t}(\boldsymbol{\xi}.\boldsymbol{\nabla} S + S') = -\boldsymbol{\nabla}.\boldsymbol{F}' + (\rho\varepsilon)' \tag{2.8}$$

$$\boldsymbol{\nabla}^2\Phi' = 4\pi G\rho' \tag{2.9}$$

$$\boldsymbol{F}' = -K\boldsymbol{\nabla} T' - K'\boldsymbol{\nabla} T, \tag{2.10}$$

$\boldsymbol{\xi}$ is the displacement due to the perturbation and $\boldsymbol{v} = \frac{d\boldsymbol{\xi}}{dt}$ is the perturbation velocity. The prime quantities are the Eulerian perturbations (at a given position) of each physical quantity given in the equilibrium model.
In order to simplify the search for the solution, spherical symmetry is assumed. By considering a temporal solution of the form $\exp(i\omega t)$ and treating spatial components in spherical coordinates (see appendix A). The above equations can be simplified by separating their radial and horizontal components. The displacement is given by $\boldsymbol{\xi} = \xi_r \boldsymbol{e}_r + \boldsymbol{\xi}_h$, ξ_r is the radial component and $\boldsymbol{\xi}_h = (0, \xi_\vartheta, \xi_\phi)$

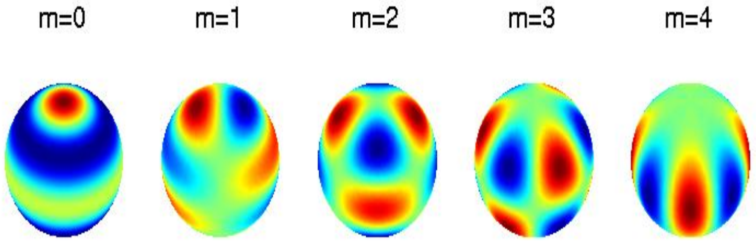

Figure 2.3: Spherical harmonics for $\ell = 4$ and a given m.

is the horizontal component. Hence, the inferred set of equations will have the following solution

$$q(r,t,\vartheta,\phi) = \sqrt{4\pi}\tilde{q}(r)Y_l^m(\vartheta,\phi)\exp{(i\omega t)} \tag{2.11}$$

$\tilde{q}(r)$ is the radial component of the solution and may contain n nodes[1] along the radius, n is called the radial number. Y_l^m are spherical harmonics defined through the Legendre functions P_l^m as

$$Y_l^m(\vartheta,\phi) = (-1)^m c_{l,m} P_l^m(\cos\vartheta)\exp{(im\phi)} \tag{2.12}$$

$c^2 = \frac{(2l+1)(l-m)!}{4\pi(l+m)!}$ l is the spherical harmonic degree and m is the azimuthal order, ϕ is the longitude, and ϑ the colatitude. Some spherical harmonics for different pairs of (l,m) are given in figure 2.3.

From this solution form, the displacement can be written such as:

$$\xi = \sqrt{4\pi}R\{[\xi_r(r)Y_l^m(\vartheta,\phi)\boldsymbol{e}_r+\xi_h(r)(\frac{\partial Y_l^m}{\partial\vartheta}\boldsymbol{e}_\vartheta+\frac{1}{\sin\vartheta}\frac{\partial Y_l^m}{\partial\phi}\boldsymbol{e}_\phi)]\exp{(-i\omega t)}\}, \tag{2.13}$$

where

$$\xi_h(r) = \frac{1}{r\omega^2}(\frac{1}{\rho}P' - \Phi'). \tag{2.14}$$

---

[1] A node is where $\tilde{q}(r) = 0$.

For the solar case, the characteristic time scale of the oscillations which is about few minutes to few hours is much smaller than the characteristic time scales of the energy[1] which are very long except at the surface where they vanish. This fact allows to consider the oscillations to be adiabatic (no heat exchange with the surrounding fluid). In other terms, the specific entropy is constant. This approximation allows to write the forth order set of adiabatic oscillation equations given by

$$\frac{1}{\rho}(\frac{d}{dr}+\frac{g}{c_s^2})P' + (N^2-\omega^2)\xi_r = 0 \tag{2.15}$$

$$\frac{1}{r^2}\frac{d}{dr}(r^2\xi_r) + \frac{1}{\Gamma_1}\frac{d\ln P}{dr}\xi_r + (1-\frac{S_l^2}{\omega^2})\frac{P'}{\rho c_s^2} - \frac{L_2}{\omega^2 r^2}\Phi' = 0 \tag{2.16}$$

$$(\frac{1}{r^2}\frac{d}{dr}(r^2\frac{d}{dr}) - \frac{L^2}{r^2})\Phi' - 4\pi G\rho(\frac{P'}{\rho c_s^2}+\frac{N^2}{g}\xi_r) = 0 \tag{2.17}$$

were $c_s = \frac{\Gamma_1 P}{\rho}$ is the sound speed, $N^2 = g(\frac{\partial \ln\rho}{\partial r} - \frac{1}{\Gamma_1}\frac{\partial\ln P}{\partial r})$ is the Brunt-Väisälä frequency, $\Gamma_1 = (\frac{\partial\ln P}{\partial\ln\rho})_S$ is the adiabatic coefficient, $S_l^2 = \frac{l(l+1)c_s^2}{r^2} = k_h^2c^2$ is the Lamb frequency, $k_h = \frac{2\pi}{\lambda_h}$ is the local horizontal number when the solution is supposed to be given by a set of plane waves $\propto \exp i(\boldsymbol{k}.\boldsymbol{r}+\omega t)$, $\boldsymbol{k} = \boldsymbol{k}_h + k_r\boldsymbol{e}_r$, and $\lambda_h = \frac{2\pi r}{\sqrt{l(l+1)}}$ is the horizontal wavelength. Together with the appropriate boundary conditions, this set of equations is an eigenvalue problem that admits a discrete set of quadratic frequencies ω^2 as non-zero solutions.

It is worth noticing that this set of equations depends on two structure quantities only, the density (ρ) and the square of the sound speed (c_s^2), so does the set of the inferred eigenfrequencies $w_{nl} = F_{nl}[\rho(r), c_s^2(r)]$. Thus, knowing the observed frequencies one can define an inverse problem where the density and the square of the sound speed can be obtained. The inferred structure quantities are often called 'seismic sound speed and density' and are often used to check how close a given solar model is to the seismic observations (for instance figure 2.2 is based on this comparison).

---

[1] Energy time scales are the radiative transfer time scale also named Kelvin Helmholtz time scale ($\sim 3\times 10^7$ years) and the nuclear time scale ($\sim 10^{13}$ years)

Nature of solar oscillations

By adding some assumptions to the adiabatic oscillation equations, one can get a hint on the nature of solar oscillations. First, we consider the Cowling approximation which consists in neglecting the perturbation of the gravitational field. This is at least a good approximation for high order modes. In addition, we suppose that the eigenfunctions are much rapidly varying than the equilibrium quantities ($\frac{dP'}{dr} \gg \frac{g}{c^2}P'$ et $\frac{d\xi'}{dr} \gg \frac{g}{c^2}\xi_r$). Thus, we derive the following simplified wave equation

$$\frac{d^2\xi_r}{dr^2} = \frac{\omega^2}{c^2}(1 - \frac{N^2}{\omega^2})(\frac{S_l^2}{\omega^2} - 1)\xi_r = -K(r)\xi_r. \tag{2.18}$$

Again, this wave equation can not give accurate results of the eigenvalue problem and is used only to get some basic physical insight on the nature of the solar oscillations. The solution of this wave equation depends on the sign of $K(r)$.

- $K(r) < 0$ ($|N| < |\omega| < |S_l|$): The solution is an increasing or decreasing exponential function
  → evanescent waves

- $K(r) > 0$ ($|\omega| > |N|$ and $|\omega| > |S_l|$ or $|\omega| < |N|$ and $|\omega| < |S_l|$): The solution is an oscillatory function
  → eigenmodes trapped in resonant cavities limited by the two characteristic frequencies N and S_l

  - **1st case** ($|\omega| > |N|$ and $|\omega| > |S_l|$): high frequency oscillations
    → *p-modes* with the pressure gradient as restoring force.
    These modes are trapped inside cavities with an upper turning point being the surface -not enough matter to hold the waves because of the dramatic decrease of the density at the surface- and an inner turning point r_t due to the increase of sound speed. The inner point is located where $\omega = S_l$ and hence at $\frac{c_s(r_t)}{r_t^2} = \frac{\omega}{\ell(\ell+1)}$. Hence, for a given frequency, the turning point is decreasing with increasing the degree ℓ. Therefore,

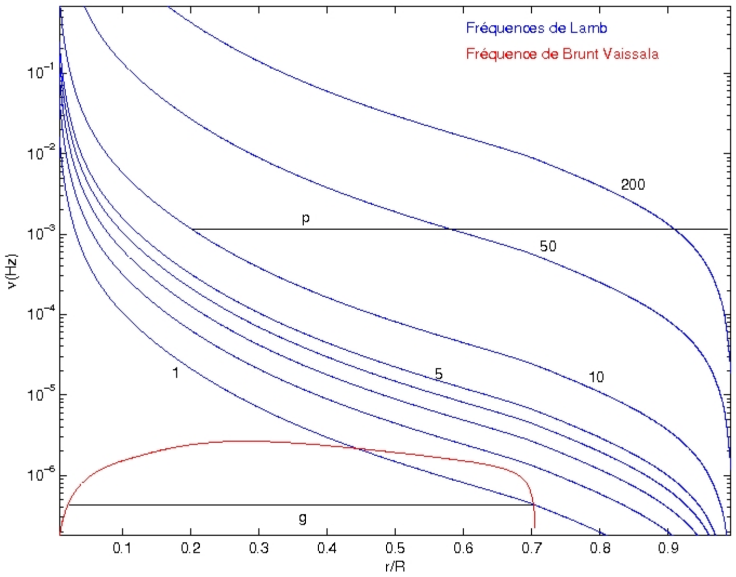

Figure 2.4: Characteristic frequencies N (red) and S_l (black) as function of fractional radius showing the limitation of the resonant cavity for each eigenmode. For p-modes with l=1 – 5, 10, 50, and 200 S_l is shown.

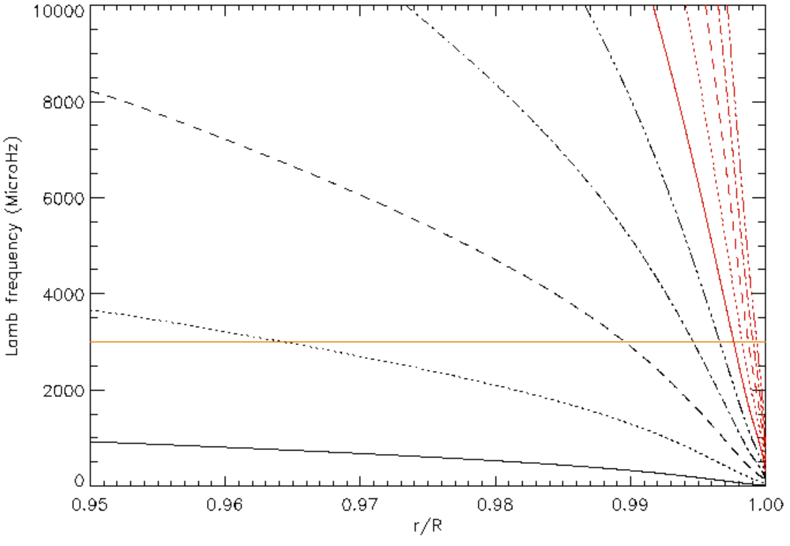

Figure 2.5: Lamb frequency (S_l) as function of fractional radius given for high degree modes. Dark lines (from bottom to top): 100, 200, 300, 400, 500. Red lines (from bottom to top): 600,700,800,900,1000. The horizontal line indicates turning points for modes with a given ℓ and frequency 3000μHz.

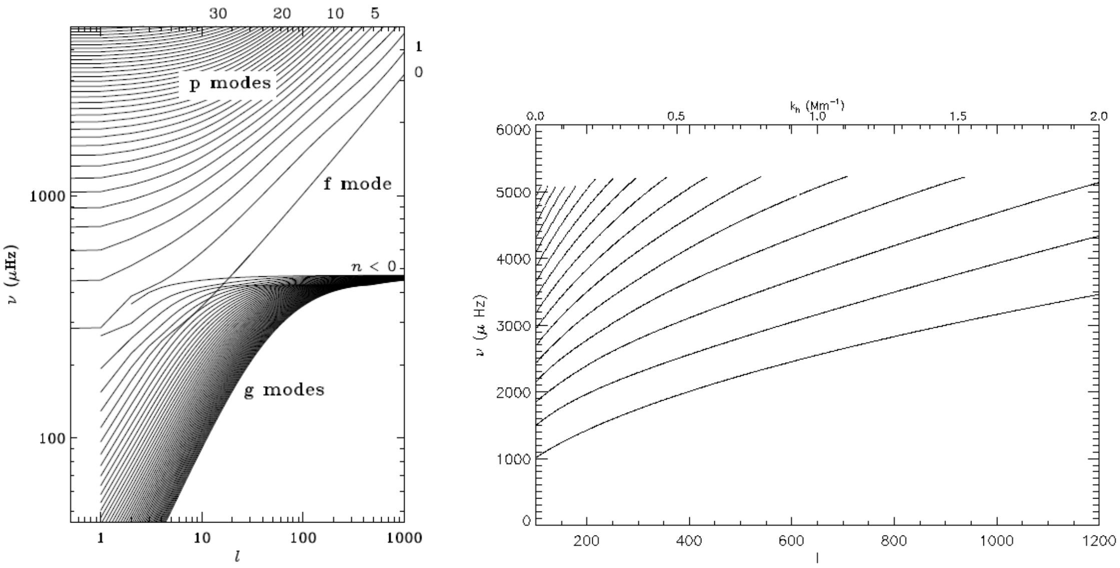

Figure 2.6: Left panel: theoretical $\ell - \nu$ diagram in logarithmic scale of solar eigenmodes showing *p-* *f-* and *g-modes* (Christensen-Dalsgaard, 2003). Right panel: Theoretical $\ell - \nu$ diagram for high degree p-modes. The top x axis gives the horizontal wavenumber in Mm^{-1}, $k_h = \sqrt{\ell(\ell+1)}/R$.

low degree modes propagate deep in the sun (figure 2.4) whereas high degree modes are trapped near the surface (figure 2.5).

- **2nd case** ($|\omega| < |N|$ and $|\omega| < |S_l|$): Low frequency oscillations $\longrightarrow$ *g-modes* with the gravity as restoring force.
  These modes are trapped below the convection zone and hence can be a very efficient holder of information about the solar core. However, these waves reach the surface with a very weak energy (amplitude of few mm/s) making them hard to observe. Nonetheless, many efforts are now provided to detect these modes from the nowadays available long helioseismoic time series. Lately, García *et al.* (2007) and García *et al.* (2008) claimed to detect *g-modes* in GOLF data and reported a faster rotating core than the rest of the radiative zone.

The quantification of solar oscillations is reflected in well distinguished ridges when representing the eigenfrequency as function of the spherical harmonic degree ℓ. This diagram known as $\ell - \nu$ diagram (ν being the frequency) equivalent to $k - \nu$ diagram[1] (k being the horizontal wavenumber), shows parabolic ridges proportional to $\sqrt{k}$ in the case of pressure modes, each corresponding to a positive radial order n going from the lower ridge (n=1) to the highest. $n = 0$ corresponds to surface gravity waves known as fundamental modes (*f-modes*). Ridges corresponding to *g-modes* are usually quantified by a negative radial order n, for instance, n=-1 represents the first ridge of *g-modes*. Figure 2.6 shows the $\ell - \nu$ diagram for all the discussed modes derived from resolving the set of solar oscillation equations using a standard solar model. I also plotted the $\ell - \nu$ diagram for high degree *f-modes*[2] (first ridge) and *p-modes* (until n=15) because the local helioseismology analysis that I will discuss in chapter 5 considers only these modes.

p-modes have been observed in the Sun for a wide range of spherical harmonic degrees and have been explored in order to infer the structure and dynamics of the layers in which they propagate, in the same way as seismic waves are used to probe the structure of the Earth. Knowing now the properties of p-modes, it is clear that the study of the solar internal layers is limited by their penetration depths. Hence, high degree p-modes with their turning points located close to the surface are the most sensitive to the near-surface layers and might be precious to study the dynamics and structure of these regions. Because of their very short wavelengths (high frequencies), these modes are not observed in the whole solar disk and hence need to be resolved locally by using what is known as 'Local helioseismology techniques'. On the other hand, the inner regions can be probed by intermediate and low degree modes that can be seen in the whole Sun, hence their name 'global modes', and are studied via 'Global helioseismology analysis'.

Solar oscillations in the presence of flow fields

Up to now, the oscillations were treated in a static fluid whereas it is known that the Sun is rotating in addition to having other more complex but weaker flows than rotation. The presence of a velocity field in the Sun perturbs the

---

[1] More precisely, k is commonly associated with $\omega = 2\pi\nu$ for a better homogeneity.

[2] From now on, *f-modes* will not be distinguished from *p-modes* except for particular discussions.

eigenmodes and hence shifts the eigenfrequencies of a mode (n,ℓ) as inferred from the resolution of the set of equations (2.15 – 2.17). The frequency shift can be inferred by considering a velocity of the form $\boldsymbol{v} = \boldsymbol{v}' + \boldsymbol{v}_0$, where $\boldsymbol{v}_0$ is the velocity of the fluid and $\boldsymbol{v}'$ is the Eulerian perturbation velocity when carrying out the small perturbation analysis around an equilibrium model given by the continuity equation (2.2) and the momentum equation (2.2). This analysis leads to the following expression between the frequency shift (frequency perturbation) and the fluid velocity (e.g. chapter 8 of Christensen-Dalsgaard, 2003).

$$\Delta\omega = -i\frac{\int_V \rho_0 \boldsymbol{\xi}^*.(\boldsymbol{v}_0.\boldsymbol{\nabla})\boldsymbol{\xi} dV}{\int_V \rho_0 |\boldsymbol{\xi}|^2 dV}, \tag{2.19}$$

$\boldsymbol{\xi}$ is given in equation 2.13, $\boldsymbol{\xi}^*$ is its complex conjugate, and V is the volume affected by the wave perturbation. Moreover, $\boldsymbol{v}_0$ can be written in spherical coordinates such as $\boldsymbol{v}_0 = v_x \boldsymbol{e}_\phi + v_y \boldsymbol{e}_\vartheta + v_r \boldsymbol{e}_r$; where the two first terms on the RHS stand for the horizontal velocity (v_x being the east-west velocity, v_y the north-south velocity) and v_r the vertical velocity. v_r is known to be very small in the Sun compared to the horizontal velocities[1] and hence can be neglected in the expression of $\boldsymbol{v}_0$. Flows in the Sun are dominated by rotation (Ω) which is about 14°/day at the equator. By considering this strong flow, v_y can be neglected and we can write $\boldsymbol{v}_0 = \Omega \boldsymbol{e}_\phi$. I have briefly discussed this case in § ' internal rotation' of section 1.3 and will not focus on it again in this section.

One way to infer weaker flows than rotation from this formalism is to study their effect on localized regions of the Sun tracked with surface rotation rates (see § surface rotation in section 1.3), i.e. subtracting the rotation to reveal weaker flows in x (residual of the rotation or the so called zonal flow) and y directions (meridional circulation). If the region is small enough so that it can be seen as being flat, one can treat the waves there as plane waves so that the shift in the frequency of the mode (n,ℓ) can be written such as

$$\Delta\omega = k_x.u_x + k_y.u_y \tag{2.20}$$

where $k_x = m/R$ and $k_y = (l^2 - m^2)^{1/2}/R$ (Hill *et al.*, 1991) are the components

---

[1] This is true except for a strong downflow below active regions.

of the horizontal wave vector and (u_x, u_y) the velocity field strengths acting on the mode (n,ℓ) in the two spatial directions. This can lead to infer the following expressions of the (u_x, u_y) from the equation 2.19.

$$u_x^{n\ell} = \beta^{n\ell} \int_0^R K^{n\ell}(r) v_x(r) dr \tag{2.21}$$

$$u_y^{n\ell} = \beta^{n\ell} \int_0^R K^{n\ell}(r) v_y(r) dr, \tag{2.22}$$

where $K^{n\ell}$ is a function specific to the mode (n, ℓ) describing the sensitivity of the mode to the physical properties of the plasma, named 'kernel'. K^{nl} is unimodular i.e. $\int_0^R K^{n\ell}(r)dr = 1$. It is not surprising that both $u_x^{n\ell}$ and $u_y^{n\ell}$ have same expressions with same sensitivity functions since the analysis is carried out assuming a spherical symmetry, hence a rotation around an axis perpendicular to the (x,y)-plane (the solar surface) bringing either x to y or y to x leaves the configuration identical. $K^{n\ell}$ and $\beta^{n\ell}$ are given such as

$$K^{nl} = \frac{(\xi_r^2 + L^2\xi_h^2 - 2\xi_h\xi_r - \xi_h^2)r^2\rho}{\int_0^R (\xi_r^2 + L^2\xi_h^2 - 2\xi_h\xi_r - \xi_h^2)r^2\rho dr} \tag{2.23}$$

$$\beta^{nl} = \frac{\int_0^R (\xi_r^2 + L^2\xi_h^2 - 2\xi_h\xi_r - \xi_h^2)r^2\rho dr}{\int_0^R (\xi_r^2 + L^2\xi_h^2)r^2\rho dr}, \tag{2.24}$$

ξ_r and ξ_h are the vertical and horizontal components of the displacement and $L^2 = \ell(\ell+1)$. The concerned modes in the made assumption of the spatial limitation are only high degree modes (with shorter wavelengths than the size of the region) usually with $\ell > 100$. For these modes, the radial displacement is negligible compared to the horizontal displacement. In this case β can be simplified such as $\beta = 1 - \frac{1}{L^2}$, hence it is very close to one. In chapter 4, I carried out a study on the effect of the change in some physical solar properties on the kernels for high ℓ modes. It appeared that they are weakly sensitive to many aspects of the used solar model (opacity, convection, equation of state etc.) and are mostly affected by the physics of the outermost layers.

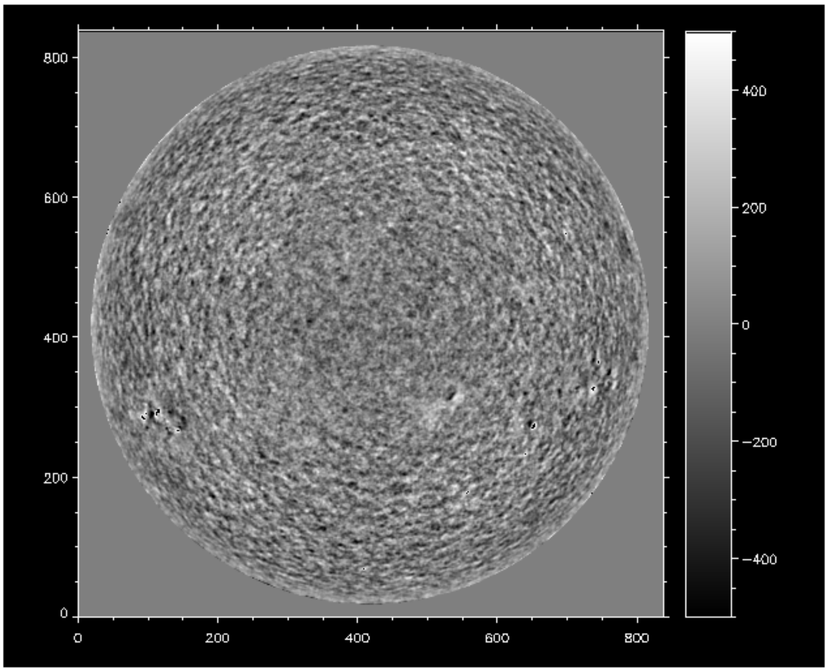

Figure 2.7: GONG Dopplergram taken on 2002.11.10 at 23:52.

Equations 2.21 and 2.22 show that if one can get access to $u_x^{n\ell}$ and $u_y^{n\ell}$ from the observation then the horizontal velocities v_x^r and v_y^r can be inferred. This resumes the basic idea of a helioseismology technique called 'ring diagram analysis' where the observed local modes can give access to frequency shifts in the two spatial directions. This technique is presented in detail in chapter 5 and will be our tool to infer the large scale horizontal flows.

2.3 Observational Helioseismology

The propagation of acoustic waves displaces and compresses the gas in the Sun. The displacement generates a velocity signal along the line of sight detected by measuring the Doppler shift of absorption lines in the solar spectrum, commonly named Dopplergrams (an example of a Dopplergram is given in figure 2.7). The compression of the gas causes brightness fluctuations that can be detected in white-light (intensity) images. The velocity signal of p-modes does not exceed 20 cm/s per mode even at the peak of 3mHz (5min period) and intensity fluctuations are about 10^{-6} of the total intensity. Hence, the detection of such signals requires very sensitive detectors that are now used in instruments on board spacecrafts and ground-based networks (see Brown, 1996, for details on the helioseismic observational techniques). Today, time series of velocity and intensity images are mainly provided by the the Michelson Doppler Imager (MDI[1]; Scherrer *et al.*, 1995) on board the SOlar and Heliospheric Observatory (SOHO) and the ground based Global Oscillation Network Group (GONG[2]; Harvey *et al.*, 1996) with 6 instruments spread around the terrestrial globe to compensate for the diurnal effect. GONG instruments were using CCD cameras with a resolution of 256pix × 256pix from 1995 until 2001 since when they have been upgraded to a resolution of 1024pix × 1024pix[3]. GONG provides roughly[4] continuously full disk high resolution images whereas MDI provides continuous low resolution images for low and intermediate-ℓ *p-modes* and performs about 2 months/year a dynamics program that provides high resolution images (1024pix × 1024pix) suitable for the exploration of high degree modes. Images are taken each minute for both MDI and GONG. In addition to these ongoing facilities, the helioseismology community is also looking forward to the launch of the Solar Dynamics Observatory (SDO) space craft expected end of 2009 in which the Helioseismic and Magnetic Imager (HMI[5]) will provide us with dopplergrams that have a spatial resolution 4 times higher than that of MDI and a shorter exposer time (50sec instead of 1min). These three ongoing and incoming helioseismic imaging facilities are illustrated in figure 2.8. Another type of helioseismic data is provided by instruments that observe the Sun as a star to detect very low degree modes[6]. This type of data is mainly provided by the Global Oscillations at Low Frequency experiment

---

[1] http://soi.stanford.edu

[2] http://gong.nso.edu

[3] When CCD cameras of GONG have been upgraded, the name of the network changed to GONG+. However, I will use both GONG and GONG+ appellations but both will refer to the same high resolution images. In my work, I did not use any low resolution GONG data.

[4] 'Roughly' because it depends on the duty cycle (usually varying between 80% and 95%).

[5] http://hmi.stanford.edu

[6] Modes with degrees higher then 3 can not be resolved from these observations because of the cancellation of positive and negative areas of either intensity or velocity.

(GOLF[1]; Gabriel *et al.*, 1995) on board SOHO and from the ground-based Birmingham Solar Oscillations Network (BISON[2]; Chaplin *et al.*, 1996). This data is provided for more than a decade and has been lately extensively used to look for *g-modes* in addition to the exploration of very low degree modes that are precious for studying the inner layers of the Sun notably the core (Basu *et al.*, 2009). For the exploration of the sub-surface layers' dynamics I am mainly using time series of GONG high resolution velocity images that are available from 2001 up to now but also some MDI data for some specific work. I also used GOLF data provided by G. Grec in 2007 for comparisons on the exploration of the effect of the change in the chemical abundances on the estimation of low degree p- and *g-modes*.

2.4 Processing observational helioseismic data

In helioseismic imaging, the eigenmodes of the Sun are either resolved from the whole image by inferring only 'global modes' of low and intermediate ℓ modes, that have horizontal wavelengths long enough to propagate in the whole Solar surface, or by taking a portion of an image where only high modes limited by the spatial extension are resolved. These two categories of processing the helioseismic data define the two main branchs Global and Local Helioseismology.

Global helioseismology

Time series of velocity or intensity images are used to get the frequencies of solar normal modes quantified by their 3 numbers (ℓ, m, n). First, the image is remapped onto latitude-longitude map. Then, a spatial filtering is performed for each image (each time) using spherical harmonic decomposition $(Y_{l,m}(\vartheta, \phi))$[3]. This leads to series of a signal T given for each mode (ℓ, m) at each time. Finally, the frequency of each mode is inferred from the Fourier transform in time of the generated time serie $T_{\ell,m}(t)$. The radial number n of each mode can be defined from the $l - \nu$ diagram which gathers modes with the same radial order in a

---

[1] http://golfwww.medoc-ias.u-psud.fr/

[2] http://bison.ph.bham.ac.uk/

[3] Equation 2.13 shows that the displacement of the wave perturbation can be written in the basis of spherical harmonics so does the velocity.

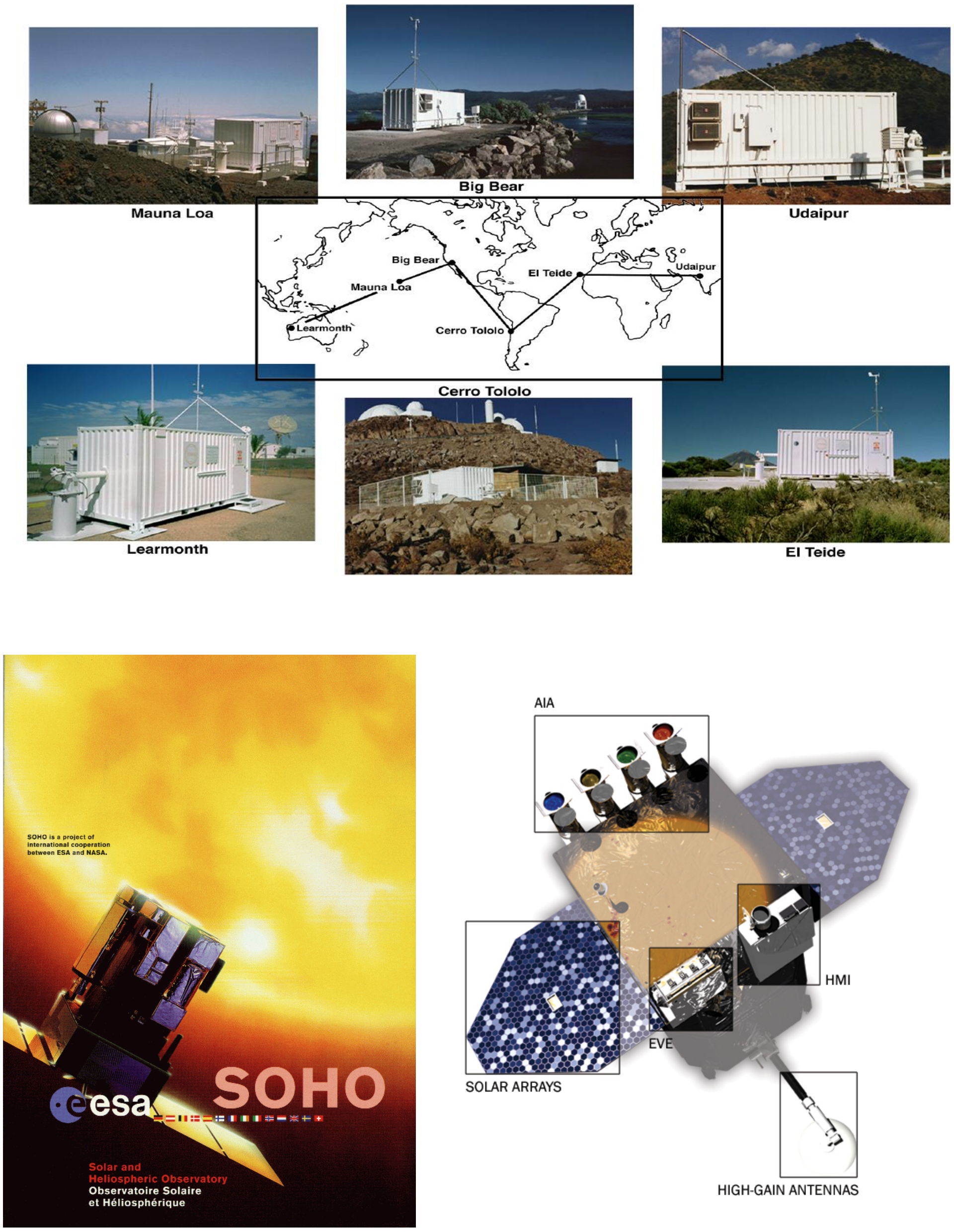

Figure 2.8: Operating and approved helioseismic facilities. GONG ground-based network (up) and SOHO and SDO spacecrafts (below)

common ridge. Hence a spectrum of quantified solar p-modes with frequencies $\omega_{l,m,n}$ is obtained. The length of the original time series increases the frequency resolution of the inferred acoustic oscillation spectrum. This way of determining frequencies of the normal modes and their methods of exploration are gathered in a helioseismology sub-field known as 'Global Helioseismology'. Extensive details on the determination of solar global mode frequencies are given in the review of Christensen-Dalsgaard (2002).

In addition to the measurement of the internal rotation as introduced in the previous chapter, global helioseismology data has been extensively used to constrain 'standard solar models' either by direct comparisons with the theoretical frequencies of the modelor by inverting the data to get structure quantities. Inversion of the global helioseismic data has been successfully applied to infer the sound speed and density profiles inside the sun (Antia and Basu, 1994b), the depth of the convection zone (Basu and Antia, 1997) and the Helium abundance (Antia and Basu, 1994a). In the next chapter, Il will use these constraints to study solar models with different chemical abundances, notably the newly determined solar abundances with lower C, N and O than the old determinations that lead to a solar model presenting a high discrepancy between its helioseismic characteristics and the observations. Up to now, no real solution has been attributed to this issue.

Local helioseismology

Global modes are of a great utility for the study of the dynamics and the structure of the Sun. However, they do not bring a complete view of the several complexities of the star. Indeed, global modes are propagating along the whole observed range of longitudes which makes accessing any physical change along this dimension impossible. In addition, the rotation deduced from global modes can only be symmetric about the equator. Moreover, the analysis is not or weakly sensitive to weak (weaker than rotation) large scale velocity fields such as meridional circulation. Any localized behavior of the waves, for instance, due to the presence of a strong magnetic field can not be detected by the global modes. In order to fill out these insufficiencies a young field of helioseismology was born where the acoustic

Table 2.1: Comparison between Global and Local Helioseismology.

Comparison between Global Helioseismology	Local Helioseismology
Samples the full disk	Samples localized regions of the solar disk
Only low and intermediate modes are resolved	Valid for high degree modes
Only eigenfrequencies with a specific degree ℓ are used to infer the dynamics and the structure	Several aspects of the wave field can be investigated
Spherical harmonic decomposition is only used	Several ways to describe the waves
The longitude structure is not resolved	Longitudinal structure can be resolved
No access to the north-south asymmetry	North-south asymmetry can be studied

waves are studied locally: Local Helioseismology. Table 2.1 gives a concise summary on the comparison between global and local helioseismology. The study of the behavior of the local wave can infer local 3D structure and flows that directly affect these waves along their propagating way (beneath the surface). Local helioseismology is developing very fast thanks to the gathered efforts on developing new techniques and to the excellent sets of data that are now available. Seen as a complementary field to global helioseismology, local helioseismology is now a very actively developing field to interpret the local behavior of the wave field not only by using the eigenfrequencies but also by considering other aspects of the wave such as the amplitude and the phase. Nonetheless, local heliosiesmology is still in its early stages of development and its results are hardly interpreted mainly because the forward problem is not well defined yet. Indeed, the forward problem in local helioseismology which should describe wave fields in a complex medium with complex structure and fields is not fully defined contrary to the more or less simple forward problem in global helioseismology where waves are only sensitive to global parameters defined by a standard solar model as seen in the first section of this chapter. Though, this problem is getting more and more clarified thanks to several theoretical works (Hanasoge, 2008; Hanasoge *et al.*, 2006).

The birth of local helioseismology can be related to the first works on the observation of the behavior of p-modes in a highly magnetized location (a sunspot) (Abdelatif *et al.*, 1986). Further works by Braun *et al.* (1988) confirmed that 40% to 50% of the acoustic signal is absorbed by sunspots. Then, Hill (1988) emitted the idea that local 3D spectra of the acoustic waves can hold precious information about the sub-surface 3D flows in the studied region, hence the first local helioseismology technique was born. The local acoustic oscillation spectrum of the sun has a ring shape in the $k_x - k_y$ plane (cuts at a specific frequency), were k_x and k_y are the components of the horizontal wave vector in x and y directions, thus, the derived name of the technique 'ring diagram analysis'[1]. Several other techniques appeared afterwards by either complementing each other, or bringing new investigations and discoveries of the very complex upper layers of the sun. I can list here, time distance technique, acoustic holography, Fourier-Hankel decomposition etc. Since this thesis mainly handles with the ring diagram analysis, I direct the reader to the review on local helioseismology techniques by Gizon and Birch (2005) for more details. A more concise review by Birch (2008) can also be consulted where the current issues of the field are also outlined. Finally, the table 1 in Duvall (1998) can be consulted for original reference papers of the existing local helioseismology techniques.

2.5 Discussion

In this chapter, I pointed out the fact that the standard solar model with numerous physical processes included in it is constrained by the observed solar oscillations. For instance, the structure quantities inferred from the inversion of the frequencies of the observed modes (mainly density and sound speed) can be compared to those of a given solar model to test its reliability on the description of the different properties of internal regions of the Sun. Also interesting is the fact that the inversion process itself depends on the used solar model through sensitivity kernels, notably when talking about the inversion of flow fields inside the Sun. Hence, the inversion results can be used to probe the solar model but

---

[1] Extensive details about the ring diagram technique are given in chapter 5.

are themselves related to a solar model. Thus, one has to be aware about how sensitive the inversion process is to the used model. In the second part of this thesis, I have tried to assess these two aspects in two particular issues. First, I used the helioseismic diagnostic in order to probe different standard solar models, from the outer layers to the core, that have been built from using different chemical element mixtures. Second, I used several standard solar models to check the sensitivity of the inversion of high degree mode frequency shifts to infer flow fields below the surface to solar model ingredients. This sensitivity is studied by using kernels that correspond to the different solar models.

Moreover, the summary on the most common solar eigenmodes and their properties made clear the fact that the study of solar internal layers via the investigation of these modes depends on their nature and their penetration depth. Thus, intermediate and low degree modes, that can propagate in the whole solar surface, are sensitive to the inner layers. Hence they are precious to infer the structure of these regions from the observed eigenfrequencies and rotation from their splittings via what is known as 'Global helioseismology analysis'. Whereas, high degree p-modes with their turning points located close to the surface are the most sensitive to the near-surface layers. Because of their very short wavelengths, these modes are not observed in the whole solar disk and hence need to be resolved locally by using what is known as 'Local helioseismology techniques'. Ring diagram analysis is one of these techniques which has a similar principle on the inference of flow fields as that of the inference of rotation from global helioseismology analysis since both use the shift in the solar frequencies caused by the underlying dynamics to deduce the velocity flows. However, with ring diagram analysis, we are able to investigate the frequency shifts in both horizontal directions, and hence both east-west and north-south flows can be inferred. This technique will be described in detail in the third part and the inferred flows from ring diagram analysis will be analyzed in the fourth part using continuous high resolution velocity images of 1 min cadence taken for about 7 years by the GONG network.

Part II

Sensitivity of low and high degree modes to the change is solar modeling

Chapter 3

Effects of the mixture of solar chemical elements from outer layers to the core

> *It doesn't matter how beautiful your theory is, it doesn't matter how smart you are. If it doesn't agree with experiment, its wrong.*
>
> Richard Feynman

Abstract

Since 2004, the revolutionary revision of the solar abundances, which is confirmed to be better but lower than the old used abundances threw away the nice concordance between the standard solar model and helioseismology. No real explanation or solution to this issue has been found so far. In addition to the detected discrepancy in the radiative and the convective zone, the change in solar abundances affects deeper zones as well. This chapter resumes my work on the effect of the change in solar abundances on the low degree p-modes and g-modes which are the best helioseismological indicators of the inner solar layers.

3.1 Building calibrated solar models with different mixtures

The solar surface abundances of the Sun are major inputs in the standard solar models because they are crucial for the stellar opacity. Their recent determination from a better modeling of the turbulence at the surface led to less abundant heavy elements than those inferred from a 1D modeling of the solar surface turbulence (Asplund *et al.*, 2005). However, solar models constructed using these low abundances do not match the helioseismological constraints contrary to the models that include old abundances[1]. I have studied this issue by building a set of calibrated solar models with different solar abundances using the stellar evolution code; Code d'Evolution Stellaire Adaptatif et Modulaire (CESAM). I generated the opacity tables relative to the new solar mixture as well as to a set of solar mixtures where the abundances of some heavy elements in the new mixture have been changed, notably, the neon abundance has been changed by several amounts to focus on the suggestion that increasing the neon could resolve the problem (see the recent review by Basu *et al.* (2009)). I got the high temperature opacity tables of each set of abundances using the online OPAL opacity project[2] and implemented them into the CESAM code using an interpolation code developed by G. Houdek. Low temperature opacities corresponding to the new mixture have been kindly constructed for us by D. R. Alexander. These opacities turned out to weakly affect the solar modeling in the outer regions of the convective zone where they are used. Description of the physics used in constructing these models as well as the calibration values are given in the first paragraph of ARTICLE I.

---

[1] References for the different estimations of the solar abundances are given in the reference list of the paper at the end of the chapter

[2] http://adg.llnl.gov/Research/OPAL/opal.html

3.2 Solar mixture effect in convective and radiative zones

Comparisons of the helioseismic constraints of the radiative and convective zones consisting on sound speed, depth of the CZ and Helium abundance are given in figures 1 and 2 of ARTICLE I. Clearly seen is that the new abundances are generating a solar model which is inconsistent with seismic results. The increase of neon by a value of 0.5dex was the best choice for minimizing the discrepancy. However, latest revisions of the neon abundance in the interstellar medium suggest that the solar neon abundance should be revised upwards by about 0.22dex from the new abundances (Wang and Liu, 2008) which is still not enough to eliminate the discrepancy.

In a recent review by Asplund *et al.* (2009), the authors present results of solar abundances that are slightly higher than their previous calculations but are still much lower than the old abundances. Hence, the discussed discrepancies are still considerable (Serenelli *et al.*, 2009).

3.3 Solar mixture effect down to the core

I also studied the effect of the change in the solar abundances on the helioseismic characteristics of the solar core which are frequencies of low degree *p-modes* and *g-modes* through small low degree p-mode frequency spacings that are known to be a powerful diagnostic of the solar core. Figure 3.4 showns the small and big separations in the acoustic oscillation solar spectrum generated from 13 years of GOLF data that has been kindly produced by G. Grec exclusively for this chapter. It is also known that the small spacings are slightly dependent on the solar atmosphere which is dramatically simplified in the solar models. Roxburgh & Vorontsov (2003) have demonstrated that the ratio of the small to large separations of acoustic oscillations is essentially independent of the structure of the outer layers. Thus, we have chosen this ratio to be the helioseismic indicator in this study. The following combinations of acoustic modes penetrating differently towards the center, and thus very sensitive to the inner layers, have been chosen as follows

$$\frac{\delta\nu_{02}(n)}{\Delta\nu(n,\ell=1)} = \frac{\nu_{n,\ell=0}-\nu_{n-1,\ell=2}}{\nu_{n,\ell=1}-\nu_{n-1,\ell=1}}, \tag{3.1}$$

$$\tag{3.2}$$

$$\frac{\delta\nu_{13}(n)}{\Delta\nu(n+1,\ell=0)} = \frac{\nu_{n,\ell=1}-\nu_{n-1,\ell=3}}{\nu_{n+1,\ell=0}-\nu_{n,\ell=0}},$$

$$\tag{3.3}$$

$$\frac{\delta\nu_{01}(n)}{\Delta\nu(n,\ell=1)} = \frac{2\nu_{n,\ell=0}-(\nu_{n,\ell=1}+\nu_{n-1,\ell=1})}{\nu_{n,\ell=1}-\nu_{n-1,\ell=1}}.$$

The frequencies have been computed using the NOSC[1] code (Provost (2008)) for the set of solar models generated from CESAM using several combinations of the solar heavy element abundances. Also averaged values of the upper quantities have been taken between $16 \leq n \leq 24$, this corresponds to a frequency range of about 2500 – 3600 μHz. The low limit of this range insures that the behavior of the frequency is almost asymptotic, the high limit corresponds to observed modes with very high accuracy. For higher frequencies, the accuracy decreases rapidly. The results of these calculations from different solar models are shown in figure 3 of the paper. The small frequency spacings are clearly far from their observed values (squares in the figure) for the new abundances model contrary to the old abundances model. The difference decreases with increasing the neon abundance. I also point out that the predicted g-mode frequencies are sensitive to the change in the solar abundances.

---

[1] Nice OScillation Code

3.4 Summary

Details on this study are given in the following A&A paper and the results can be summarized as follows:

- As seen by several authors, the solar model calculated from the new (low) heavy element abundances do not agree with the different helioseismological estimations (helium abundance, depth of CZ and sound speed profile). Thus, a difference up to 1.5% in sound speed is observed between this model and the observations. This difference bring us back to almost the difference that was shown between models without microscopic diffusion and helioseismic measurements.
- Small spacings are very sensitive to the change in the solar abundances.
- g-mode frequencies are sensitive to the change in the solar abundances, where the frequency difference between the low abundances model and the new abundances models goes up to 4μ Hz. However, modes with frequencies around 250μHz seem to be the less sensitive to the change in solar abundances with a frequency difference between the same two models less than 2μ Hz.
- The increase of the neon abundance by about 0.5dex does decrease the abundances. however, other slight adjustments (diminution) of C, N, O, Si, Mg and Ar are needed in addition to a slight increase of the solar age in order to reach the suitable concordance.
- The sulfur abundance also affects the helium abundance and the depth of the convection zone of the model.

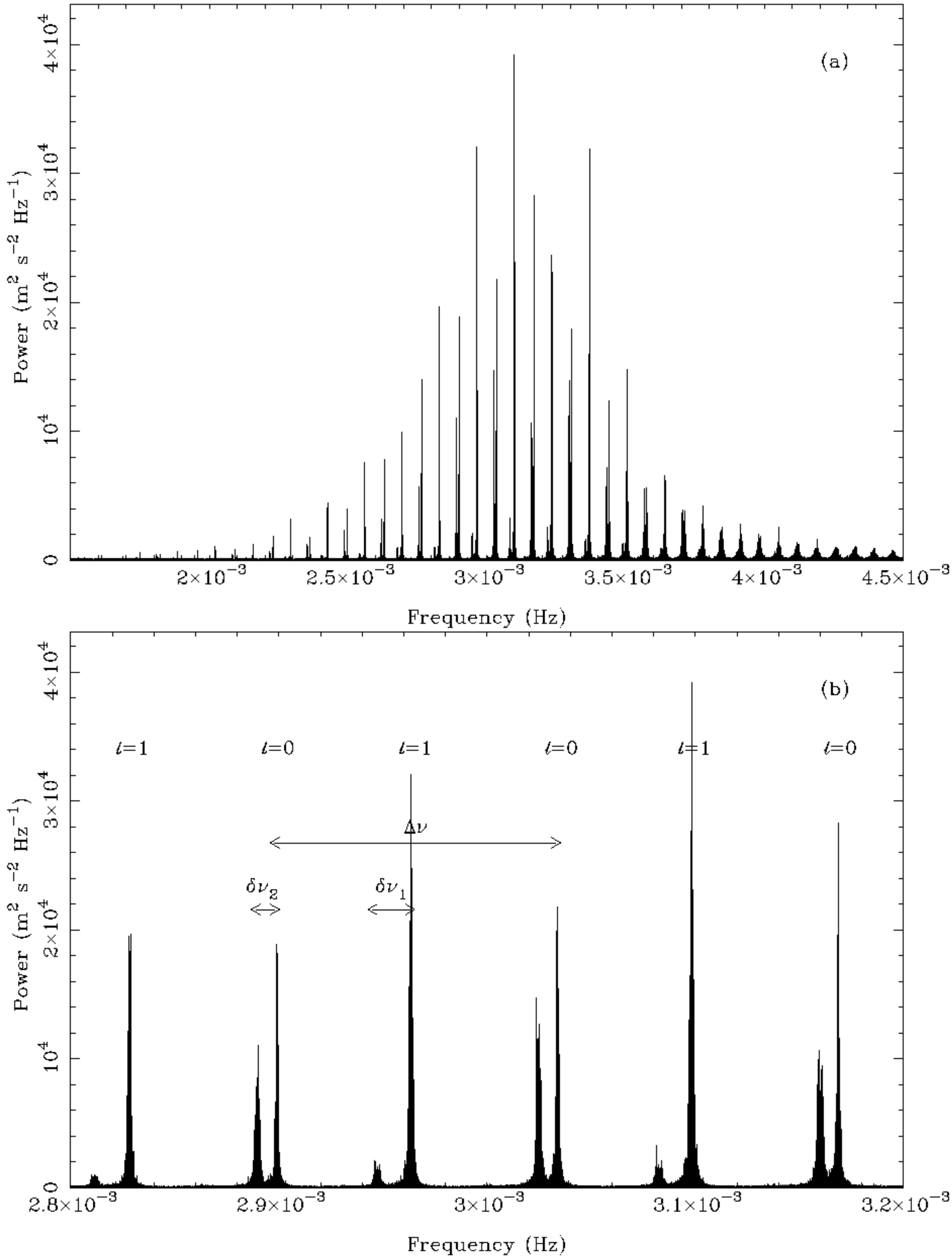

Figure 3.1: Upper panel: Solar oscillation power spectrum derived from 13 years of GOLF data. Lower panel: Small region of the spectrum where the small ($\delta\nu_1, \delta\nu_2$) and big ($\Delta\nu$) separations are clearly seen. Source: (Grec, 2009).

ARTICLE I

TITLE

Sensitivity of low degree oscillations to the change in solar abundances

AUTHORS

A. Zaatri, J. Provost , G. Berthomieu ,
P. Morel , and T. Corbard

REFERENCE

Astronomy and Astrophysics 469, 1145 – 1149 (2007)

ERRATUM: In figure 4 of the paper, the frequency is in μHz and not in Hz as mentioned on the axis label.

A&A 469, 1145–1149 (2007)
DOI: 10.1051/0004-6361:20077212

Astronomy & Astrophysics

Sensitivity of low degree oscillations to the change in solar abundances

A. Zaatri[1,2], J. Provost[1], G. Berthomieu[1], P. Morel[1], and T. Corbard[1]

[1] Département Cassiopée, UMR CNRS 6202, Observatoire de la Côte d'Azur, BP 4229, 06304 Nice Cedex 4, France
e-mail: `zaatri@obs-nice.fr`
[2] Centre de Recherche en Astronomie, Astrophysique et Géophysique, BP 63, Route de l'Observatoire, Bouzaréah, 16340, Alger, Algérie

Received 31 January 2007 / Accepted 11 April 2007

ABSTRACT

Context. The most recent determination of the solar chemical composition, using a time-dependent, 3D hydrodynamical model of the solar atmosphere, exhibits a significant decrease of C, N, O abundances compared to their previous values. Solar models that use these new abundances are not consistent with helioseismological determinations of the sound speed profile, the surface helium abundance and the convection zone depth.

Aims. We investigate the effect of changes of solar abundances on low degree p-mode and g-mode characteristics which are strong constraints of the solar core. We consider particularly the increase of neon abundance in the new solar mixture in order to reduce the discrepancy between models using new abundances and helioseismology.

Methods. The observational determinations of solar frequencies from the GOLF instrument are used to test solar models computed with different chemical compositions. We consider in particular the normalized small frequency spacings in the low degree p-mode frequency range.

Results. Low-degree small frequency spacings are very sensitive to changes in the heavy-element abundances, notably neon. We show that by considering all the seismic constraints, including the small frequency spacings, a rather large increase of neon abundance by about (0.5 ± 0.05) dex can be a good solution to the discrepancy between solar models that use new abundances and low degree helioseismology, subject to adjusting slightly the solar age and the highest abundances. We also show that the change in solar abundances, notably neon, considerably affects g-mode frequencies, with relative frequency differences between the old and the new models higher than 1.5%.

Key words. Sun: helioseismology – Sun: abundances – Sun: interior

1. Introduction

The precise measure of characteristics of the observed p-modes has been used to probe most of the layers inside the sun. For example, seismic sound speed and density determinations can be used to constrain the interior of the sun anywhere except at the surface and in the core. Helioseismology also constrains the surface helium abundance and the depth of the convection zone. However, the small number of p-modes (only low degree p-modes) able to reach the solar core is not sufficient to probe this region using inversion techniques. The solar core is crossed by thousands of g-modes, able to bring much information from this region. The g-modes have not yet been unambiguously identified because of their evanescent nature through the convection zone and low amplitude at the surface but ongoing work is devoted to try to extract them for the existing long time series of SOHO data and to propose new observational and strategies to detect them.

New determinations of solar heavy element abundances using a 3D, NLTE analysis of the solar spectrum has been provided by Asplund et al. (2005; AGS). Previous 1D, LTE determinations are available (Grevesse & Noels 1993 – GN; Grevesse & Sauval 1998 – GS). Relative to GN abundances, the new AGS abundances are, among others, lower in C, N, O, Ne elements by respectively 0.16 dex, 0.19 dex, 0.21 dex and 0.24 dex. Consequently, the new chemical determination gives a smaller metallicity Z/X compared to the older ones. The new determination of solar elements is more accurate than the older one (Grevesse et al. 2005), but it has been shown that it leads to solar models that disagree with the helioseismological determinations of solar internal structure parameters (e.g. Turck-Chièze et al. 2004; Bahcall et al. 2005; Guzik et al. 2005).

In this paper we study the sensitivity of the solar core properties, through low degree p-modes and g-modes, to the change of solar mixture. The chemical solar abundances that we used are those of Grevesse & Noels (1993), Grevesse & Sauval (1998) and Asplund et al. (2005). The other mixtures that we chose include the solar abundances of Asplund et al. (2005) changing mainly the neon abundance. This set of solar mixtures allows us to study the influence of the neon abundance on small frequency separations and to test the possibility of improving the accordance between models that use new abundances and helioseismic observations (Antia & Basu 2005; Bahcall et al. 2005). This is indeed possible because neon photospheric abundance cannot be determined directly due to the lack of suitable absorption lines in the solar spectrum induced by the noble gas nature of neon. The estimations of the solar Ne abundance are still controversial (Drake & Tesla 2005; Young 2005; Schmelz 2005). Here we analyze how the models fit both the global constraints (seismic sound speed, surface helium abundance and convection zone depth) and the small frequency separations in the low degree p-mode frequency range. We use the determination of these

Table 1. Global characteristics of the computed solar models. A(Ne) is the neon abundance in dex, $(Z/X)_S$ is the surface metallicity, $T_c^7 = T_c \times 10^{-7}$, T_c the central temperature in Kelvin. P_0 is the characteristic period (in minutes) of low degree gravity modes. The different models are computed with the following solar abundances: M-GN: GN; M-GS: GS; M-GS*: GS with sulfur abundance of GN; M-AGS: AGS; M3, M4, M5, M6, M7: AGS with the indicated change of the neon abundance; M8: in addition to the change of neon in AGS, C, N, O, Mg and Si have been increased until the maximum of their error bars (see Asplund et al. 2005) and Ar by 0.40 dex.

	A(Ne)	$(Z/X)_S$	Y_S	r_{ZC}	T_c^7	P_0
M-GN	8.08	0.0245	0.2437	0.7133	1.574	35.08
M-GS	8.08	0.0232	0.2462	0.7165	1.574	35.03
M-GS*	8.08	0.0231	0.2429	0.7153	1.571	35.15
M-AGS	7.84	0.0166	0.2279	0.7292	1.549	35.68
M3	8.10	0.0179	0.2329	0.7237	1.555	35.49
M4	8.29	0.0192	0.2381	0.7181	1.559	35.29
M5	8.35	0.0198	0.2402	0.7162	1.561	35.21
M6	8.40	0.0203	0.2417	0.7144	1.563	35.15
M7	8.47	0.0212	0.2445	0.7119	1.565	35.04
M8	8.35	0.0213	0.2439	0.7142	1.566	35.05

mode frequencies obtained from the GOLF experiment by Gelly et al. (2002) and more recently by Lazrek et al. (2007) who have corrected these frequencies for the solar cycle effect. The sensitivity of gravity modes to the new abundances have also been estimated. Preliminary results of this work have been presented by Zaatri et al. (2006).

2. Solar models with new abundances

We have computed solar models with different sets of heavy element abundances by using the stellar evolution code CESAM (Morel 1997). We use OPAL opacity tables[1], calculated for each mixture, and Alexander and Ferguson opacity tables at low temperatures ($T < 6000$ K). Nuclear reaction rates are from NACRE compilation (Angulo et al. 1999) and equation of state tables are those of OPAL (Iglesias & Rogers 1991). We assume the convection treatment given by Canuto & Mazitelli (1991). All the models include the microscopic diffusion of the chemical elements according to the Michaud & Proffitt (1991) description. Models are calibrated for a solar age $t = 4.6$ Gyr at the solar radius, the solar luminosity ($R_\odot = 6.9599 \times 10^{10}$ cm, $L_\odot = 3.846 \times 10^{33}$ erg/s, Christensen-Dalsgaard et al. 1996) and the solar surface metallicity Z/X of the various mixtures.

Table 1 summarizes the characteristics of the solar models at both the surface and the core and their chemical composition is given. The surface helium abundance and the location of the base of the convection zone Y_s and r_{ZC} are to be compared to their seismic determinations $Ys = 0.2485 \pm 0.0034$, $r_{ZC} = (0.7133 \pm 0.001)R_\odot$ by Basu & Antia (2004). These authors have demonstrated that these seismic determinations are not sensitive to the change in solar abundances.

Figure 1 shows relative differences between seismic sound speed and the one determined from our different solar models. Figure 2 shows a comparison between Y_s and r_{ZC} values of the computed models and their seismic determinations. The worse concordance between the model using Asplund et al. abundances and the seismic model is shown by a relative difference in sound speed that peaks at 1.5% just below the convection zone. The surface helium abundance and the location of the base of the convection zone are also very far from their seismic values.

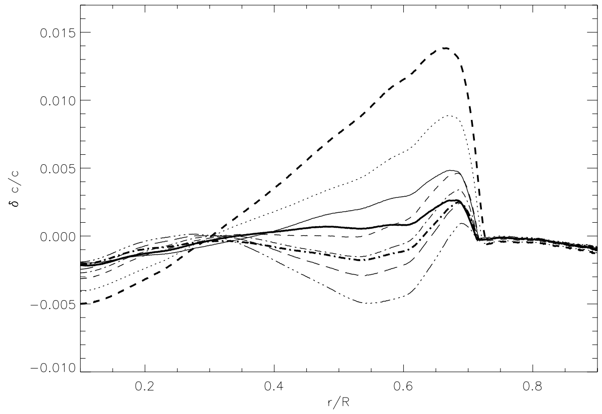

Fig. 1. Relative sound speed differences between the Sun and the models: M-GN (heavy full), M-GS (full), M-AGS (heavy dashed), M3 (dotted), M4 (short-dashed), M5 (dashed-dotted), M6 (long-dashed), M7 (dashed-3*dotted), M8 (heavy dashed-dotted).

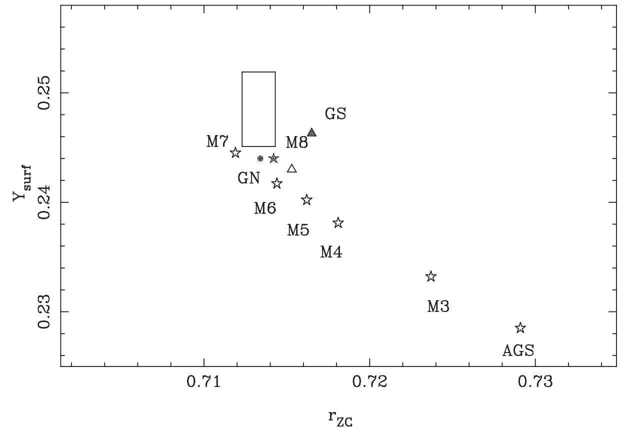

Fig. 2. Characteristics of the solar envelope, surface helium abundance (Y_S) and the location of the base of the convection zone (r_{ZC}), for the models: M-GN (filled circle), M-GS (filled triangle), M-GS* (open triangle), M-AGS (open star), M3 to M7 which is a set of models that use AGS mixture by varying its neon abundance (open star) and M8 (filled star). The box represents the seismic values with their errors (Basu & Antia 2004).

Models M3, M4, M5, M6 and M7 give an idea of how large the neon abundance increase has to be in order to reduce this discrepancy. In all these models the neon has been pushed out of its error bar (±0.06 dex). Before looking for an optimal value of neon, we notice that the larger the neon abundance, the larger the surface helium abundance, the larger the convection zone depth and the higher the sound speed. The augmentation of neon in M4 makes the model's sound speed close to the seismic profile but keeps Y_s and r_{ZC} far from their seismic box, even if they become better than the M-AGS ones. A slightly higher increase of neon (e.g. M7) improves the surface envelope characteristics (Y_s, r_{ZC}) but makes the sound speed much higher than the seismic one. Therefore, a compromise has to be found for the neon abundance value to satisfy Y_s, r_{ZC} and sound speed constraints. We estimate the neon abundance to be 8.39 ± 0.05 dex, subject to some remaining differences between the models and the observation. First, the lowest values of this range lead to models that have Y_S and r_{ZC} values about 2σ far from their seismic values. Second, its highest values infer models with relative differences between their sound speed profile and the seismic one that

---

[1] `http://www-pat.llnl.gov/Research/OPAL/`

are just three times lower than the relative difference between M-AGS and seismic sound speed profiles at their peaks.

In order to see the influence of the other heavy elements abundances on the change of the considered model characteristics (Y_S, r_ZC and sound speed) we constructed the M8 model. This model has a neon abundance that is situated at the bottom of our given neon increase interval (8.35 dex) and has C, N, O, Si and Mg abundances that are increased until the maximum of their error bars (see Asplund et al. 2005). The abundance of argon has also been increased by 0.4 dex, as this element is another noble gas of the solar mixture. We deduce that the sound speed of the M8 model does not change much compared to the model that has the same increase of neon (M5), except at the deeper layers of the sun. However, the values of Y_S and r_ZC become closer to their seismic values compared to those of the M5 model. This means that the increase of other heavy element abundances inside their error bars simultaneously improves the agreement between the three considered seismic determinations and those of the models. This can lead to a reduction of the supposed values of neon as they give good agreement in sound speeds to (8.34 ± 0.05) dex. For this range, relative differences between seismic and theoretical Y_S and r_ZC still have a maximum of 2σ.

For comparison we have considered the models M-GN and M-GS with the previous mixtures GN and GS. The model M-GN has a convective zone depth close to the seismic one but a too small surface helium abundance. On the contrary, model M-GS has a good surface helium content but a thinner convective zone. Since in Fig. 2, the position of the M-GS model does not follow the general trend of the other models, we have looked in more detail at the differences between the two mixtures. We noted that the sulfur abundance of GS mixture (7.33 dex) is larger than the GN value (7.21 dex), due to improved oscillator strengths (Biemont et al. 1993), and than the AGS value (7.14 dex). We computed a model M-GS* with the GS mixture but with GN sulfur abundance. It appears that such a variation of sulfur notably lowers the surface helium abundance of the model.

3. Fit to the low-degree small frequency spacing constraints

Small low degree frequency spacings are a well known diagnostic of the solar core. In order to compare our theoretical results to the observational ones, we use the latest results of Lazrek et al. (2007) and those of Gelly et al. (2002) in the measurement of low degree solar frequencies from the GOLF experiment. We examine the small frequency spacings $\delta\nu_{02}$, $\delta\nu_{13}$ and $\delta\nu_{01}$ which are combinations of acoustic modes penetrating differently towards the center and that are thus very sensitive to this region.

$$\delta\nu_{02}(n) = \nu_{n,\ell=0} - \nu_{n-1,\ell=2},$$

$$\delta\nu_{13}(n) = \nu_{n,\ell=1} - \nu_{n-1,\ell=3},$$

$$\delta\nu_{01}(n) = 2\nu_{n,\ell=0} - (\nu_{n,\ell=1} + \nu_{n-1,\ell=1}).$$

However, the small spacings are slightly dependent on the solar atmosphere which is highly simplified in the solar models. Roxburgh & Vorontsov (2003) have demonstrated that the ratio of the small to large separations of acoustic oscillations is essentially independent of the structure of the outer layers. We thus renormalize the small spacings by considering the ratios $\delta\nu_{02}(n)/\Delta\nu(n,\ell = 1)$, $\delta\nu_{13}(n)/\Delta\nu(n + 1,\ell = 0)$ and $\delta\nu_{01}(n)/\Delta\nu(n,\ell = 1)$ where the large separation is given by:

$$\Delta\nu(n,\ell) = \nu_{n,\ell} - \nu_{n-1,\ell}.$$

We then compute both for our models and for the observations the mean of these renormalized small frequency spacings $\overline{\delta\nu_{02}}$, $\overline{\delta\nu_{13}}$ and $\overline{\delta\nu_{01}}$ for radial orders from 16 to 24. This corresponds to a frequency range about 2500–3600 μHz. The low limit of this range ensures that the behavior of the frequency is almost asymptotic and the high limit corresponds to observed modes with very high accuracy. For higher frequencies, the accuracy decreases rapidly. Figure 3 gives both renormalized and non renormalized mean small spacings for the models of Table 1 and for the observations. The dimensions of the symbols in the upper panel of Fig. 3 reflect the uncertainty on the plotted quantities corresponding to an uncertainty of 0.01 μHz for the numerical frequencies. It shows that the renormalization gives results closer to the observations because it eliminates the differences between surface properties of the models and the sun. The remaining discrepancies are due to differences in the structure of the deep solar interior.

As expected, Fig. 3 shows that the small frequency spacings of the M-AGS model are far from the observations, contrary to those of the M-GN and M-GS models. We note that the M-GS model is closer to the observations than the M-GN model, contrary to the M-GS* model. The small frequency spacings of the models that use an AGS mixture with different values of the neon abundance decrease as the neon increases in almost a regular way. The model M7, which uses the highest value of neon abundance in our considered set of models, is shown to have the best agreement between its small spacings and the observations. However, this model has a much higher sound speed than the seismic one (see Fig. 1), which makes it a less acceptable model. We also show that a slight increase of some other heavy elements has an effect on the change of small frequency spacings as well. We find that for the model M8 the three considered renormalized small spacings are closer to their observational determinations than those of the model M5.

However the small spacings are also sensitive to the solar age, due to the change in time of the mean molecular weight in the nuclear core. For example, Morel et al. (1997) showed that an increase in age of 100 Myr gives a decrease of 0.1 μHz of both $\overline{\delta\nu_{02}}$ and $\overline{\delta\nu_{13}}$, with a small relative increase of sound speed of around 10^{-3} and a slight increase of the thickness of the convection zone of 0.002 $R_\odot$ and no noticeable change of the surface helium abundance. We added, in Fig. 3 a GN model which is calibrated at 4.65 Gyr to see the influence of the solar age on small frequency spacings.

After showing the influence of solar abundances on low degree small frequency spacings, we still believe that in order to resolve the new abundances, a compromise between the neon abundance, the small frequency spacings and the constraints of the preceding paragraph can be reached by slightly adjusting some heavy elements inside their error bars and the age of the sun. Our suggested value of neon (8.34 ± 0.05) is confirmed by considering the low degree small frequency spacing constraint.

4. Gravity modes

Adiabatic frequencies of the models have also been computed for the range from 100 to 800 μHz and for low degrees ($0 < \ell < 6$) including both g-modes and mixed modes. The periods of low frequency gravity modes are proportional to the characteristic period P_0 which is given in Table 1 ($P_0 = 2\pi^2/\int_0^{r_\mathrm{ZC}} (N/r)\mathrm{d}r$, where N is the Brunt-Väissälä frequency). The lowest P_0 difference between M-GN and the other models is obtained for M8, leading to the closest g-mode frequencies. The frequency

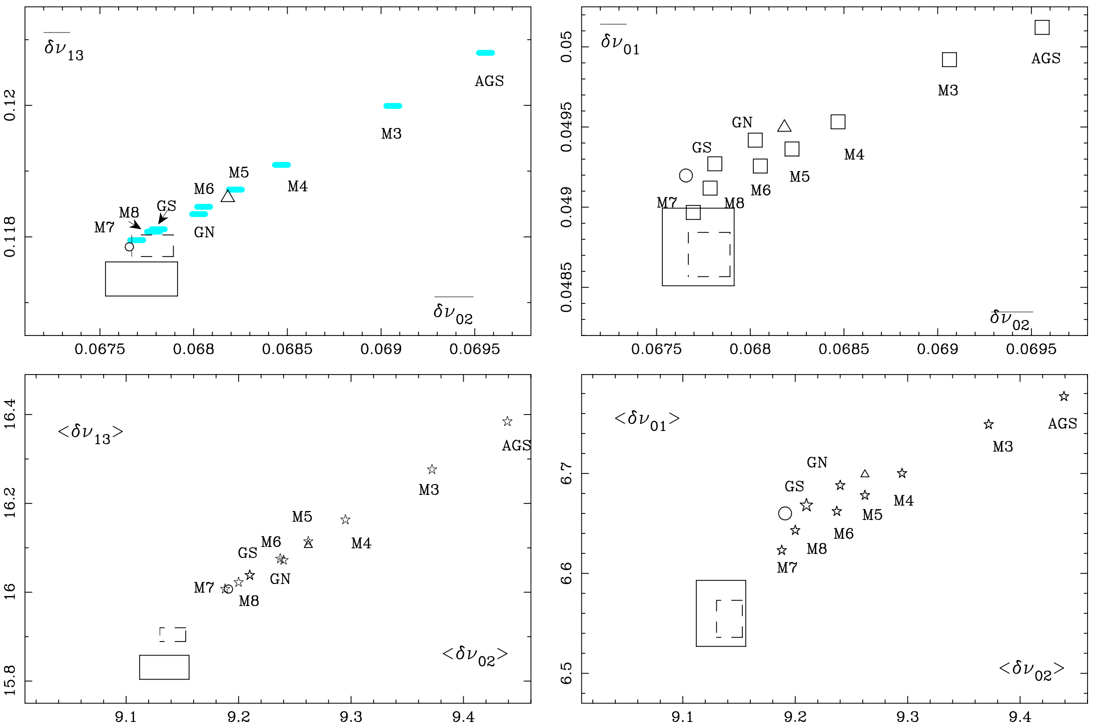

Fig. 3. *Upper panel left*: renormalized mean frequency small spacing $\overline{\delta\nu}_{13}$ as a function of the renormalized mean frequency small spacing $\overline{\delta\nu}_{02}$ for the different models compared to GOLF observations (full box Gelly et al. 2002; dashed box Lazrek et al. 2007). *Upper panel right*: same for renormalized mean frequency small spacing $\overline{\delta\nu}_{01}$ as a function of the renormalized mean frequency small spacing $\overline{\delta\nu}_{02}$. *Lower panel*: for comparison the same quantities are given before renormalization (in μHz), namely $\langle\delta\nu_{13}\rangle$ and $\langle\delta\nu_{01}\rangle$ as a function of $\langle\delta\nu_{02}\rangle$. The small circle corresponds to a M-GN model calibrated at 4.65 Gyr, the open triangles correspond to M-GS* model.

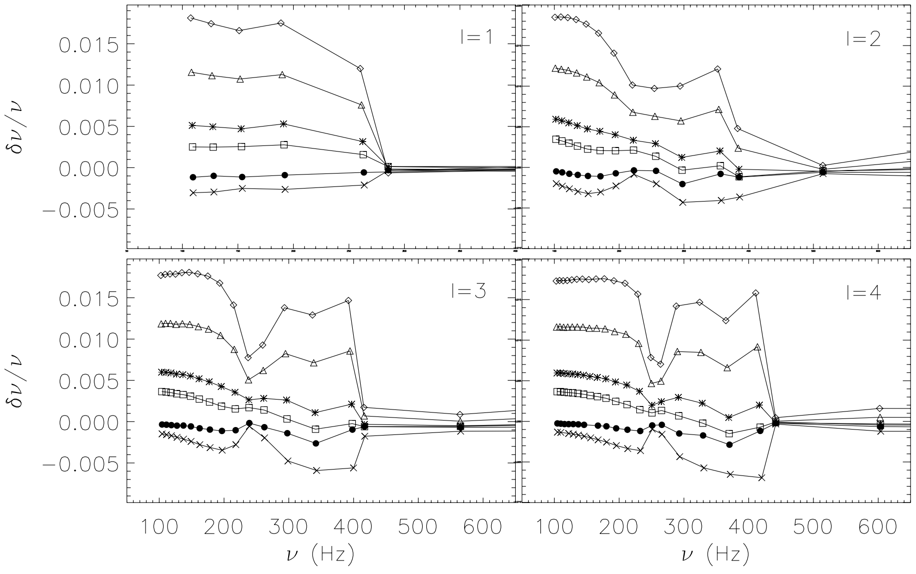

Fig. 4. Relative frequency differences between the gravity modes and the first low frequency p-modes of M-GN and M-AGS (⋄), M3 (△), M4(∗) , M5 (□), M7(×), M8(•).

differences between the M-GN and the other models are given in Fig. 4. We note that the g-modes are more influenced by the change of abundances than the low frequency p-modes. As expected the value of $\delta\nu/\nu$ at very low frequency is close to its asymptotic value $\delta P_0/P_0$. The biggest frequency difference is obtained for M-AGS for which low g-mode frequencies are 1.5% lower. This difference has a minimum for all the models around 250 μHz. It has been shown that the g-modes around this frequency have a mixed character (Provost et al. 2000) and are sensitive to both the sound speed and the Brunt-Väissälä frequency variations. Their frequencies do not depend much on any change in the models. The lowest difference in the frequencies compared to M-GN is obtained for M8 which is expected since they have very similar structure parameters.

5. Discussion and conclusion

We study the sensitivity of low degree frequency spacings to the change on solar heavy element abundances. We constructed several solar models with different solar mixtures. The spacings are considered as helioseismic constraints of the solar core as they are very sensitive to this deep region. Therefore, they are used to test the reliability of the solar models in addition to the envelope constraints (convection zone depth and helium surface abundance) and the sound speed profile. Surface effects have been removed from these spacings by using a renormalization prescribed by Roxburgh & Vorontsov (2003). Their observational values have been taken from the recent GOLF measurements (Lazrek et al. 2007; Gelly et al. 2002).

We found that low degree small frequency spacings are very sensitive to the metallicity of the models. The mean spacings of a model using Asplund et al. (2005) abundances are much higher than the ones of a model using Grevesse & Noels (1993) values and are incompatible with those determined from the GOLF observations. Similar results were found by Basu et al. (2007) by comparing BISON observations of low degree solar oscillations with models using different abundances and numerical codes. They conclude that low surface metallicity models can be ruled out. These two studies strengthen the fact that new solar abundances lead to solar models which disagree with helioseismology measurement in the core as well as in the other regions of the solar interior.

We confirm, as was also mentioned by several authors, that the sound speed profile, convection zone depth and helium surface abundance of a model using the revised abundances are also far from their helioseismic determinations, unlike the ones of a model using the old abundances.

In addition to these two main models we constructed five other models that use new solar abundances with a significant change of the neon abundance. This has been done following the Antia & Basu (2005) suggestion to resolve the new abundances. We found that the small spacings are very sensitive to the neon abundance value and decrease almost regularly when the neon increases. The discrepancy between models and observations is reduced simultaneously for the small frequency spacings and the other constraints when the neon abundance is considerably increased. However, the neon abundance that gives the best agreement between the models and the helioseismic determinations is hard to reach as it is a compromise solution between all these quantities. For instance, a model using a neon value increased by 0.45 dex (M4) makes its sound speed very close to the seismic sound speed but keeps its envelope characteristics (convection zone depth and helium surface abundance) far from their observational values. A model using a neon abundance increased by 0.63 dex (M7) has the opposite effect.

As expected, the search for the neon abundance value that gives a good agreement between models using new abundances and the seismic constraints including the small frequency spacings becomes easier if C, N, O, Si, Mg and Ar abundances are also slightly increased. Other elements may also play a significant role. We show for example that an increase of sulfur abundance, as is the case for the GS mixture, noticeably increases the surface helium abundance and lowers the small frequency spacings.Also, the solar age is a crucial feature in the determination of low-degree frequencies. Indeed, we tested a model using old abundances with an age 50 Myr older than the age we have used to compute all the models (4.6 Gyr) and found that this change brings the spacings closer to the observations.

In conclusion, we show that, if the new solar mixture of Asplund et al. (2005) is confirmed, an increase of the neon abundance by (0.5 ± 0.05) dex can resolve the current disagreement caused by this mixture, subject to adjusting slightly the highest heavy-element abundances and the age of the sun in order to satisfy all the seismic constraints, notably the low-degree small frequency spacings. Our estimated increase of neon is slightly higher than that of Bahcall et al. (2005), which is 0.45 ± 0.05. However, in this work only low degree modes are used, while the higher degree modes also provide independent constraints. Also our model, which is the closest to the observations, has a surface metallicity content Z smaller than the value determined by Antia & Basu (2006) from higher degree modes using the dimensionless sound speed derivative in the solar convection zone.

Our last investigation in this work has been the calculation of g-mode frequencies since the detection of g-modes is one of the current challenges of solar observers. As expected, the solar model using new abundances has the highest frequency differences to the model using old abundances, which go up to 4 μHz. We show that modes with frequencies around 250 μHz and degrees larger than 2 are less sensitive modes to the change in the abundances, with differences less than 2 μHz.

Acknowledgements. We thank B. Pichon for his technical help, D. R. Alexander for giving us low temperature opacity tables for the revised mixture and the OPAL group for their online opacity tables code. We are grateful to G. Grec and M. Lazrek for communicating their results in advance of publication and to H. M. Antia for his constructive remarks. We also thank the "Programme Pluri-Formations Astérosismologie" from OCA for the financial support.

References

Antia, H. M., & Basu, S. 2005, ApJ, 620, L129
Antia, H. M., & Basu, S. 2006, ApJ, 644, 1292
Angulo, C., Arnould, M., Rayet, M., and the NACRE collaboration 1999, Nucl. Phys. A, 656, 1
Asplund, M., Grevesse, N., & Sauval, A. J. 2005, Cosmic Abundances as Records of Stellar Evolution and Nucleosynthesis, ASP Conf. Ser., 336, 25
Alexander, D. R., & Ferguson, J. W. 1994, ApJ, 437, 879A
Bahcall, J. N., Basu, S., & Serenelli, A. M. 2005, ApJ, 631, 1281
Basu, S., & Antia, H. M. 2004, ApJ, 606, L85
Basu, S., Chaplin, W. J., Elsworth, Y., New, R., Serenelli, A. M., & Verner, G. A. 2007, ApJ, 655, 660
Biemont, E., Quinet, P., & Zeippen, C. J. 1993, A&AS, 102, 435
Canuto, V. M., & Mazitelli, I. 1991, ApJ, 370, 295
Christensen-Dalsgaard, J., et al. 1996, Science, 272, 1286
Drake, J. J., & Testa, P. 2005, Nature, 436, 525
Gelly, B., et al. 2002, A&A, 394, 285
Gough, D. O. 1991, in Progress of Seismology of the Sun and Stars, ed. Y. Osaki, & Shibahashi (Springer Verlag), 283
Grevesse, N., & Noels, A. 1993, in Origin and Evolution of the elements, ed. Prantzos, Vangioni-Flam and Cassé (Cambridge Univ. press), 15
Grevesse, N., & Sauval, A. G. 1998, Space Sci. Rev., 85(1/2), 161
Grevesse, N., Asplund, M., & Sauval, A. G. 2005, in Element Stratification in Stars: 40 Years of Atomic Diffusion, ed. G. Alecion, O. Richard, & S. Vauclair, EAS Publ. Ser., 17, 21
Guzik, J. A., Scott Watson, L., & Cox, A. N. 2005, ApJ, 627, 1049
Iglesias, C. A., & Rogers, F. J. 1991, ApJ, 371, 408
Lazrek, M., Grec, G., Fossat, E., & Renaud, C. 2006, A&A, submitted
Morel, P. 1997, A&AS, 124, 597
Proffitt, C. R., & Michaud, G. 1991, ApJ, 371, 584
Provost, J., Berthomieu, G., & Morel, P. 2000, A&A, 353, 775
Roxburgh, I. W., & Vorontsov, S. V. 2003, A&A, 411, 215
Schmelz, J. T., Nasraoui, K., Roames, J. K., Lippner, L. A., & Garst, J. W. 2005, ApJ, 634, 197
Turck-Chièze, S., Couvidat, L., et al. 2004, Phys. Rev. Lett., 93, 21
Young, P. R. 2005, A&A, 444, 45
Zaatri, A., Provost, J., Berthomieu, G., Morel, P., & Corbard, T. 2006, in Beyond the spherical Sun, ed. K. Fletcher, & M. Thompson, ESA SP-624, 59

Chapter 4

Effect of solar model ingredients in high ℓ mode kernels

Abstract

Up to now, only Model S (Christensen-Dalsgaard et al., *1996) has been used in the generation of sensitivity kernels for the inversion of horizontal flows, although it does not contain updated physics in the solar modeling. Thus, I was interested in the question how the use of different standard solar models would affect the sensitivity kernels and hence the inversion results. After using several solar models to generate the kernels, it appeared that changing the equation of state, opacities, surface heavy element abundances, or the modeling of convection do not affect the inversion results. However, the modeling of the outermost layers can affect the measurements if an important amount of high radial order modes (high frequency modes) are included in the analysis.*

4.1 Goal of the study

As discussed in section 2.2, the radial dependence of the horizontal flows can be inferred by inverting an integral equation which gives the frequency shifts, induced by the flows, for each mode of radial order n and spherical harmonic degree ℓ (equations 2.21 – 2.22). The goal of the following study is to use several standard solar models to calculate the kernels and β coefficients (given in equations 2.23 and 2.24) in order to see how the used structure models affect the estimation of the horizontal velocity flows (zonal and meridional flows). For this purpose, I used several standard solar models calculated using the CESAM code (Morel, 1997) and estimated their corresponding eigenfrequencies and kernels using the ADIPLS code (Christensen-Dalsgaard, 2008) and the NOSC code (Provost, 2008). The corresponding results are then compared to the standard calculations based on Model S (Christensen-Dalsgaard *et al.*, 1996). Since the analysis involves high degree acoustic modes, only the modeling of the upper layers are concerned. Results of the inferred horizontal flows from the use of the kernels presented in this chapter are discussed in chapter 5. This work has been accepted for publication with the following entries:

TITLE

Sensitivity of the subsurface flow fields inferred from ring diagram analysis to the change on the solar model

AUTHORS

A. Zaatri, J. Provost, T. Corbard, M. Roth

JOURNAL

Astronomy and Space Science

4.2 CESAM models and Model S

The characteristics of the solar models in this study are described in table 4.1. In addition, nuclear reaction rates, atmosphere models and calibration parameters are as given in ARTICLE I and all models include the microscopic diffusion of the chemical elements. The opacities are those of OPAL 96 for the given heavy element abundances (GN and AGS – for details concerning the solar abundances and the opacities see ARTICLE I and references therein). Model S refers to the model which has been fairly extensively used for helioseismic inversions and on which the GONG ring diagram horizontal subsurface flows are based (see part 3). Model S is taken as a reference model in this study. The effect of the change in the equation of state (CESAM models use OPAL equation of state updated in 2001 whereas Model S uses the old tables of 1991) and the opacities could be revealed by comparing the Model S flow fields to the CS1 ones. The effect of the age is studied via the model CS2 (0.1 Gy older than CS1). The model CS3 is calculated to see the effect of the change on the surface heavy element abundances by using the newly estimated abundances (AGS). Finally, the effect of the convection treatment is studied via the model CS4 calculated using (CM, Canuto and Mazitelli, 1991) formulations for convection instead of the commonly used Mixing Length Theory (MLT). In addition to these CESAM models, I used a model similar to Model S kindly provided by J. Christensen-Dalsgaard for this study (I call it Model $\tilde{S}$). Though, Model $\tilde{S}$ has been adjusted to fit very nearly the observed high degree mode frequencies by changing only the outermost layers. The only difference between Model $\tilde{S}$ and Model S resides in the adiabatic coefficient (Γ_1), and hence in the sound speed of the outer 0.1% of the sun.

Figure 4.1 shows the density and sound speed differences between Model S and the other models at the outermost 2% and 0.1% of the sun. Except for the model CS4, all the CESAM models have densities and sound speeds very close to those of Model S. A difference of up to 20% in the sound speed is shown between Model S and Model $\tilde{S}$ in the outermost 0.1% of the solar interior. Because the sound speed and the density of Model S, at the outer most layers, is higher than those of the CESAM models except for the model CS4, the inferred CESAM models frequencies are lower by up to $10 \mu Hz$ than those inferred from Model S.

Table 4.1: Description of the used solar models

Solar model	Model S	CS1	CS2	CS3	CS4
Equation of state	OPAL 1991	OPAL2001	OPAl2001	OPAL2001	OPAL2001
Opacities	OPAL92(GN)	OPAL96(GN)	OPAL96(GN)	OPAL96(AGS)	OPAL96(GN)
Convection	MLT	MLT	MLT	MLT	CM
Age(Gy)	4.6	4.6	4.7	4.6	4.6

Model $\tilde{S}$ shows the highest frequency differences compared to Model S because of the high sound speed difference in the outermost layers (see figure 4.2).

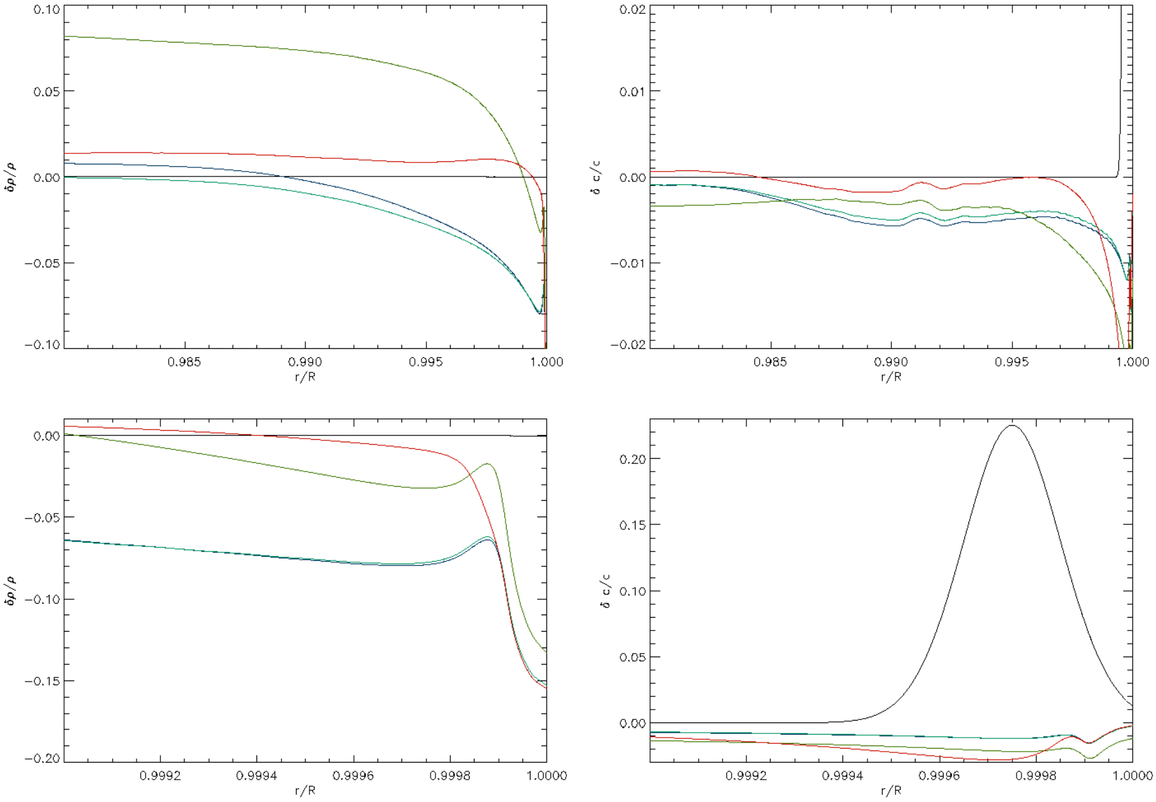

Figure 4.1: Upper panels: Density (left) and sound speed (right) diffrences between Model S and models $\tilde{S}$(black),CS1(blue), CS2(light blue), CS3(green), CS4(red) as a function of fractional radius for the outer 2%. Lower panels: Same as upper panels but for the 0.1% outermost layers.

4.3 Kernels and β coefficients

Examples of the difference between kernels calculated from Model S and the other models are given in figures 4.3 and 4.4 for high degree modes with ℓ=400, 600, 700 and different radial orders n. The differences are given between the reference Model S and the other models. The kernel differences are very similar for all the models except for Model $\tilde{S}$. At the layers of interest, the kernels are dominated by the horizontal wave displacement and the density. Hence, because of the high sound speed at the near surface layers of Model $\tilde{S}$, the horizontal displacement assumes a significant high amplitude that is reflected in the kernels. The coefficient β is very close to one for high degree modes, and is nearly the same for all the models except a slight difference for Model $\tilde{S}$ (figure 4.5). Moreover, the difference between kernels and β coefficients corresponding to Model S and Model $\tilde{S}$ increase with increasing radial order n. This has been expected since for a given order ℓ, modes with higher radial order n have higher frequencies and are more sensitive to the outer-most layers (see figure 2 of Christensen-Dalsgaard *et al.* (1996)).

4.4 Summary

The outcome from the presented study on the effect of the solar model ingredients on sensitivity kernels of high degree modes is that mainly the modeling of the outermost layers matters. In addition, for a given ℓ, mode kernels with the highest radial orders, ie. with highest frequencies, are the most sensitive to the change in the solar modeling because the sensitivity to the outermost layers increases with increasing frequency. However, it is known that the modeling of the outer solar layers from calibrated evolutionary models of the Sun poorly describes the physics of these layers because of their great complexity. Hence, it would be more obvious to use models that are describing more correctly the outermost layers by considering 3D modeling of the turbulence, adding the effect of magnetic field and so on. In chapter 5, I will discuss the effect of the calculated kernels in the inferred horizontal flows from the inversion of frequency shifts obtained from localized power spectra of high degree modes.

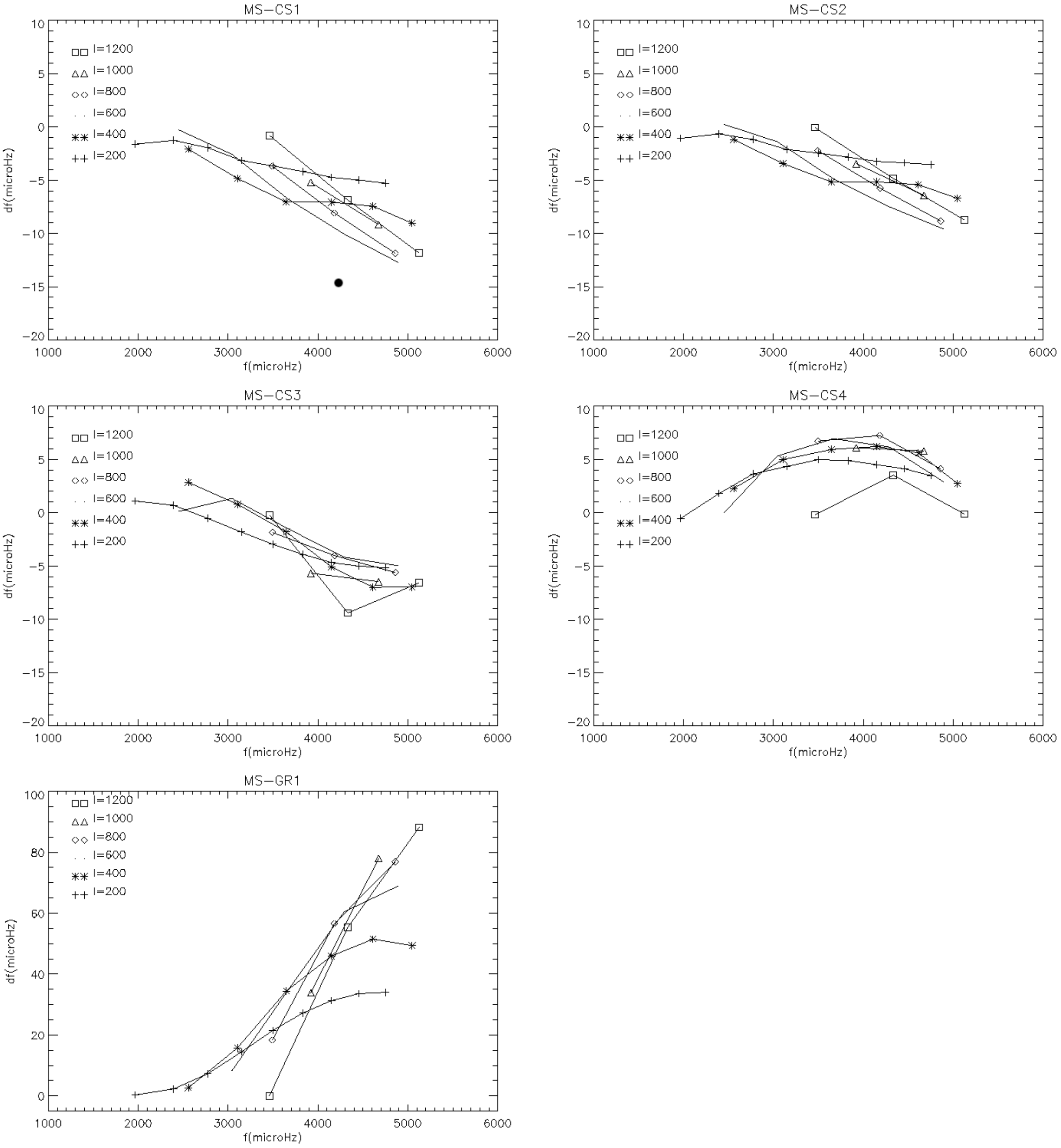

Figure 4.2: Frequency differences between Model S and models CS1, CS2, CS3, CS4, $\tilde{S}$ (noted GR1 in the panel).

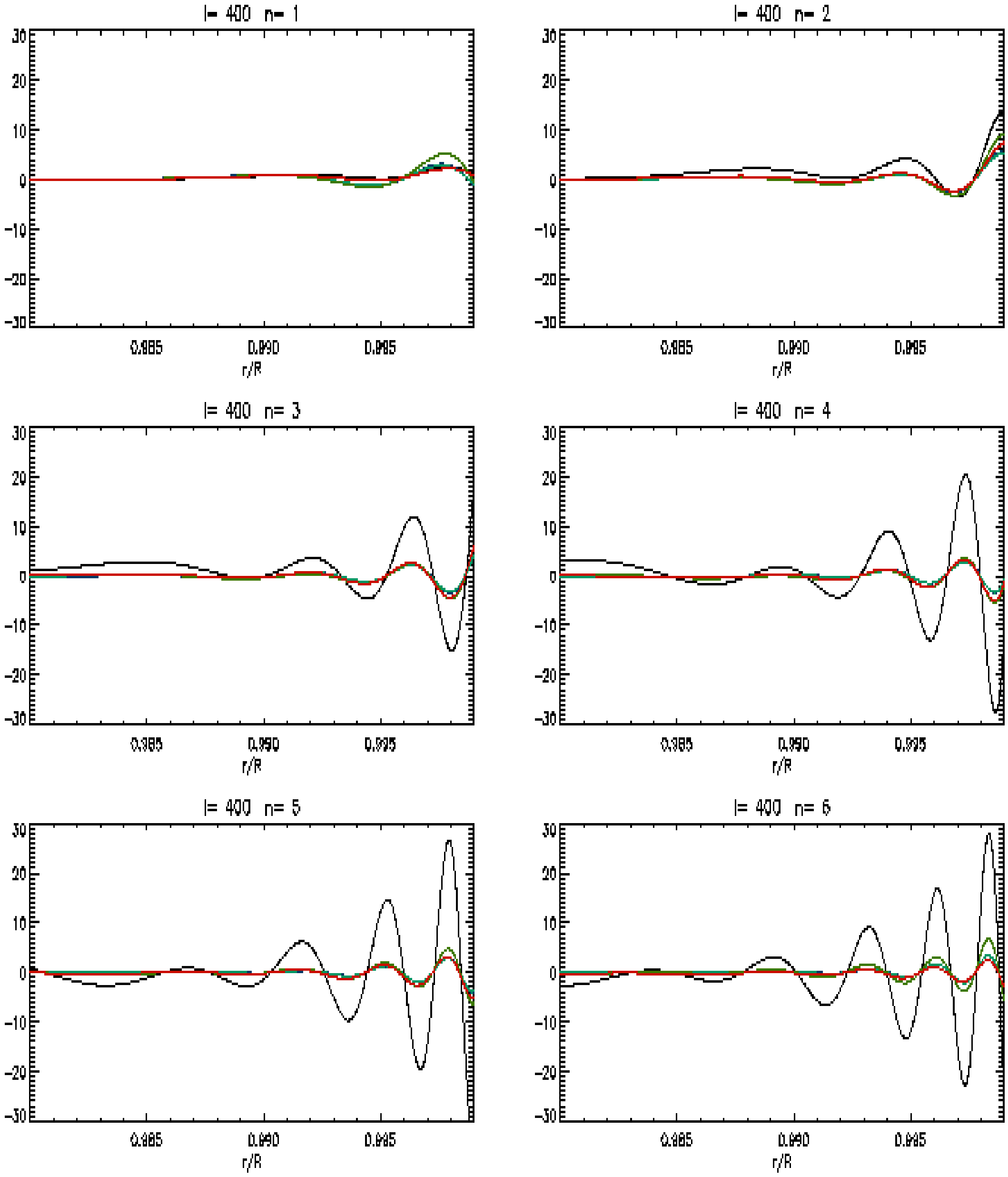

Figure 4.3: Difference between the rotational kernels of Model S and those of models $\tilde{S}$(black), CS1(blue), CS2(light blue), CS3(green), CS4(red) given for degree ℓ=400 and radial orders $1 < n < 6$. The last four colors are hardly distinguishable in the plots because the models are very close to each other but notice that the differences start to appear with increasing the radial value n.

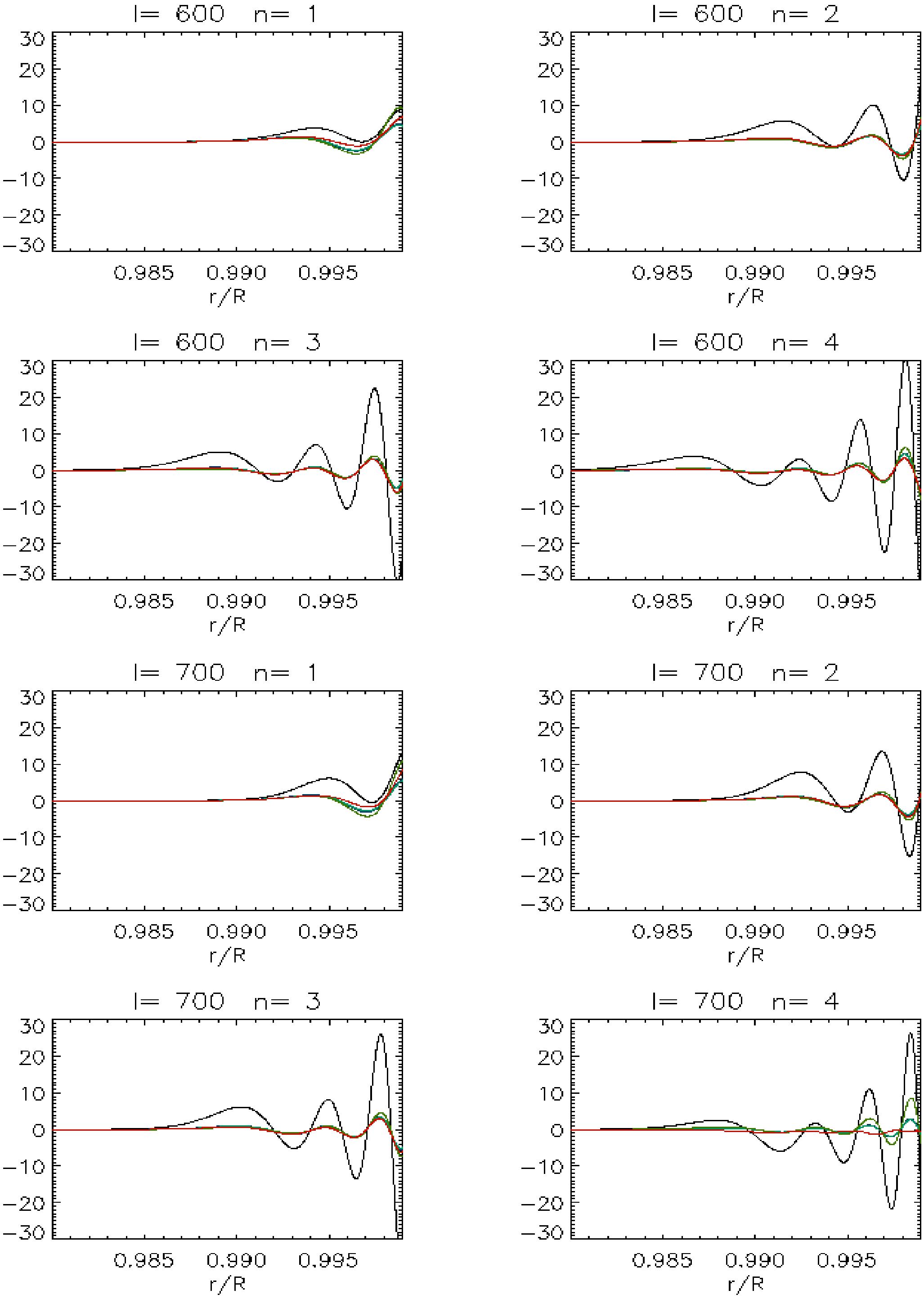

Figure 4.4: Same as figure 4.3 for ℓ=600 and ℓ=700 for radial orders $1 < n < 4$. The maximum radial order for a given ℓ decreases with increasing ℓ as shown from $\ell - \nu$ diagram.

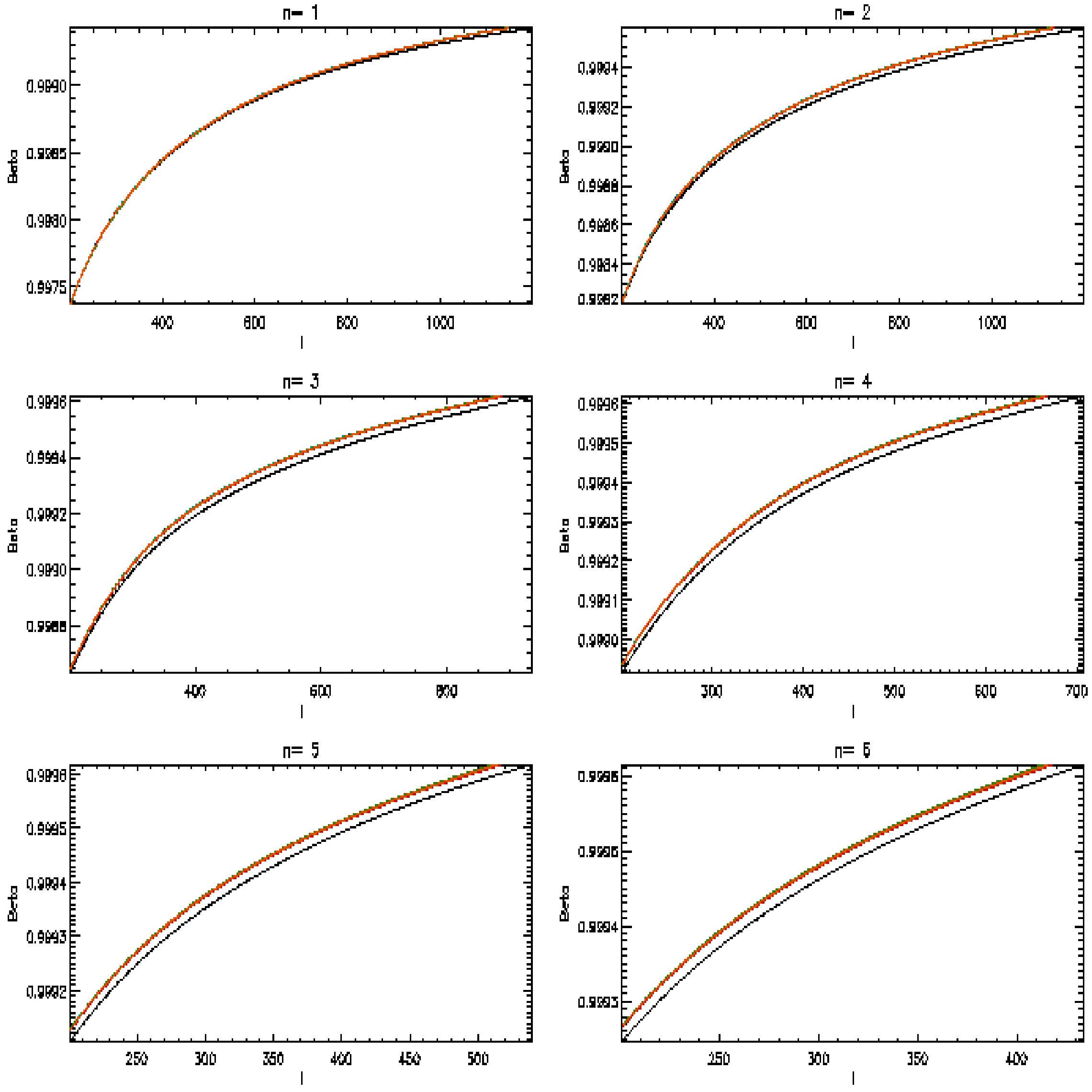

Figure 4.5: β coefficient shown for a set of high degree ℓ modes with different radial orders as derived from several solar models: $\tilde{S}$ (black), Model S and all the CESAM models are overlayed in the red curve.

Part III

Ring diagram analysis

Chapter 5

Ring diagram analysis

> *Remember that in order to analyze any wave it is first necessary to place it accurately in the Kx-ω plane.*
>
> R. F. Stein & J. Leibacher.
> 'waves in the solar atmosphere'

Abstract

Ring diagram analysis is a local helioseismology technique that allows us to infer horizontal flows in the sub-photospheric layers. The data used are sequences of tracked and remapped dopplergrams of localized domains to which Fourier transform can be applied in time and space giving local acoustic power spectra. The power in such spectra is concentrated in rings at a fixed frequency for a set of radial orders. In the 2D spatial frequency domain [k_x,k_y], the rings are not circular because of the underlying flows that act on the waves traveling through the region under study. The displacement of the rings can be obtained by fitting the power spectra. Then, flows down to few Mm can be inferred by inverting the integral equation that links them to the measured ring distortions.

5.1 Introduction

The idea of exploring local disturbances of the acoustic waves in order to infer the dynamics of the propagating medium emerged when Deubner (1975) successfully produced the first observed $\mathrm{k} - \omega$ diagram (2D spectrum) where the ridges fitted well the predicted solar *p-modes* by Ulrich (1970). Deubner *et al.* (1979) suggested to use the shift in *p-mode* ridges as solar tracers to infer rotation at different depths. In 1983, Gough and Toomre studied theoretically the effect of horizontal large scale velocity fields and temperature fluctuations on the $\mathrm{k} - \omega$ diagram. Observational evidence of their predictions was given by Hill *et al.* (1983). All these studies have been carried out in 2D where only the east-west flows can be inferred[1]. In order to keep the information on flows along the north-south direction, Hill (1988) suggested to use the whole image without averaging over y to infer 3D solar oscillation power spectra. In the Fourier space (ν,k_x,k_y), where ν is the frequency and (k_x,k_y) are the two components of the horizontal wavenumber, the 3D spectrum has a trumpet shape and a cut at a specific frequency gives a ring shaped mode power (figure 5.1) which led to name Hill's technique '**ring diagram analysis**'. In the presence of underlying flows, the mode power gets distorted in k_x and k_y directions. The exploration of these distortions permits the measurement of the flows in the two spatial directions. An intuitive idea in Hill (1988) was to model the distorted rings by ellipses and a least square minimization was used to get the velocity field strengths in x and y directions which were related to the ellipse parameters (mainly minor and major axis). The pioneering work by Hill (1988) led to overestimated flows a flow of 100 m/s was found in the y direction) and was not conclusive due to the poor quality of the data that were available and the simplified procedure used for fitting the power spectra. Moreover, since these images were taken at a fixed latitude, it was not possible to reveal any variation on the north-south flow.

Subsequently, Patrón (1994) and Patrón *et al.* (1995) took a set of data cubes from improved Mount Wilson images at different latitudes and longitudes to study the spatial distribution of the flows and used a more powerful tool to fit the 3D

---

[1] To get the 2D spectrum, images are averaged over latitudes (y direction) and the domain in the x direction is taken as large as possible to improve the resolution in k_x.

power spectrum based on the Lorentzian fitting of the solar oscillation spectrum by Anderson *et al.* (1990). The power was not fitted in the (k_x,k_y) plane (the ring) only but also by taking into account the third dimension (frequency). This fitting led to more stable and smaller velocities of about few tens of m/s. Also, an inversion method was used to infer the velocity flows as a function of depth. The inversion was not of a big issue in the ring-diagram analysis, as the problem is similar to that in global helioseismology for the inversion of frequency splittings to get internal rotation which were already well established (e.g. Gough, 1985). This work led to the first estimations of the north-south flow (meridional circulation) as a function of depth from an observational technique. Having confirmed its strength on inferring large scale flows in the Sun, ring diagram analysis has been applied to several sets of data consisting on continuous high resolution Dopplergrams of 1 min cadence provided for periods lasting from a day to several years. One of the first high resolution data sets to whom the ring diagram analysis has been applied to infer large scale flows are MDI data (e.g. Bogart *et al.*, 1997; González Hernández *et al.*, 1998) and Taiwan Oscillation Network (TON) data (Patrón *et al.*, 1998). Most recently, the analysis has been used to infer short-scale flows, notably around and below active regions (Hindman *et al.*, 2006).

When GONG cameras have been upgraded in 2001, a ring-diagram analysis pipeline has been developed in order to continuously analyze the GONG+ data (Corbard *et al.*, 2003). Data products consisting of tables of horizontal flows and their corresponding errors as well as the fit mode parameters (e.g. frequency shifts, amplitude and line width) are available for more than 7 years now[1]. For reviews about the ring-diagram analysis see Hill (1995), Antia and Basu (2007), and González-Hernández (2008).

---

[1] http://gong2.nso.edu/archive/patch.pl?menutype=h

The GONG ring diagram pipeline

the GONG ring diagram analysis pipeline[1] is used to measure the sub-surface horizontal velocity fields derived from ring analysis of GONG Dopplergrams. In addition, I have customized the pipeline in several ways, notably, to investigate the influence that many parameters involved in the ring diagram analysis can have on the estimated flow fields.

- implemention of several planar mappings to study how sensitive the results are to the used projection.The chapter 6 is devoted to this topic.
- implemention of several sets of sensitivity kernels derived from various solar models, mostly those discussed in chapter 4.This aims to study the effect of the change in the standard solor model to the inferred horizontal velocity flows (see section 5.6).
- using an inversion code based on the Optimally Localized averages method, developed by Thierry Corbard, in addition to that based on the Regularized Least Square method already implemented in the pipeline. The resulting velocities from both inversion methods have been compared (see section 5.6).
- Extension of the inversion programs available in the pipeline for the measurement of the horizontal velocity flows to the measurement of their radial gradient (see chpater 8, section 8.4).
- The range in latitudes originally used in the program has been made more flexible by extending the latitude coding to a step of 0.5° instead of 7.5°.
- The pipeline has been adapted to the MDI data.

This customized version of the GONG ring diagram pipeline is now implemented in OCA and KIS where the remapping code of it has also been used to create data cubes analyzed by another local helioseismology technique 'Fourier Henkel Analysis' and the results have been compared to those obtained from the ring diagram analysis from the same data cubes (roth *et al.*, 2009).

---

[1] http://gong.nso.edu/data/DMAC_documentation/RingDiagram

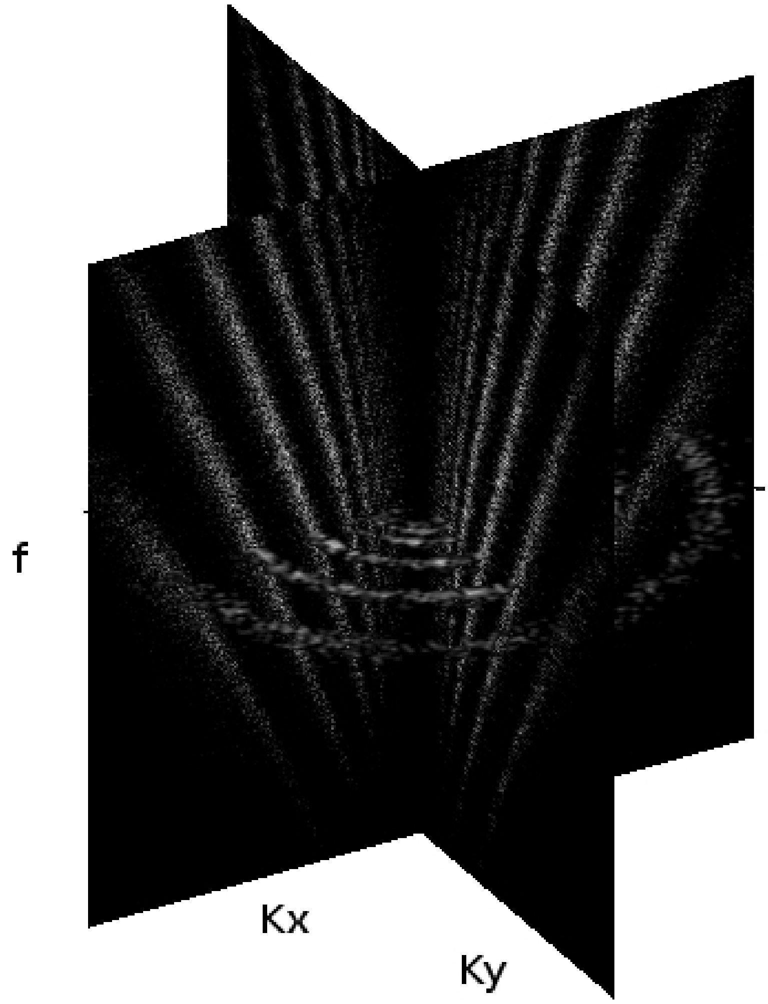

Figure 5.1: Localized solar oscillation power spectrum derived from a data cube of a size (128× 128-pixel, 6480min] with one pixel corresponding to 0.125°. $\mathbf{K_x}$ and $\mathbf{K_y}$ are the components of the horizontal wave number and are given for a maximum value of 2 Mm^{-1}. **f** is the frequency given for a maximum value of 5400 μ Hz. A cut at one frequency shows rings corresponding to the f-ridge (n=0, outer ring) until the p6 ridge (n=6, inner ring).

5.2 Principle of the ring diagram technique

The main idea of the technique is to analyse 3D power spectra of acoustic solar oscillations inferred from time series of localized patches on solar images. The distortion of the ring shape of the 3D spectrum at a given frequency hold information about the existing flows responsible for advecting the wave front[1]. One way of considering the problem is to treat the waves with high horizontal wavenumbers as plane waves when seen on small regions of the solar disk where the plane geometry is approximately valid. Thus, the apparent Doppler shift of the frequencies can be treated as being directly proportional to the horizontal velocity field strength as given by equation 2.20. And because the waves probe the solar interior, the velocity flows as a function of depth can be inferred. However, the spatial limitation allows observations of high degree modes onlywith a turning point located in subsurface layers (see figure 2.5) thus only flows in these shallow regions can be inferred. The processing steps of the ring diagram technique can be summarized as follows:

- building a data cube: It mainly consists on following a region of interest in a sequence of images by tracking it at a solar rotation rate appropriate for its latitude.

- Getting the power spectrum: A 3D Fourier transform is applied to the data cube (x − y − time) to get the 3D power spectrum in $(k_x - k_y - \nu)$.

- Fitting the power spectrum: a Lorentzian function is fitted to the the mode power in polar coordinates ($k = \sqrt{k_x^2 + k_y^2}$, $\theta = \arctan(k_x/k_y)$) at each (ℓ, n). Six fit parameters are inferred; the central frequency and frequency shifts in the two spatial directions x and y, the background, the amplitude and the width of the mode.

- Inversion: the resulting shifts are inverted to infer the horizontal flows (zonal and meridional flows) as a function of depth.

---

[1] If one neglects the second order effect of the magnetic field, the rings would be axially symmetric around the origin $k_x = k_y = 0$ (i.e circular) if no flows were present.

- The variation of the velocity flows as a function of Carrington longitude and latitude can be studied by using patches equally distributed north and south over the solar disk but avoiding regions near the limb strongly affected by foreshortening.

In the following, I will review in detail each of these steps. Most of the discussions will refer to power spectra in different ways, even before introducing them properly. This is because it is important to understand the steps of this data analysis one by one. The shown power spectra have been obtained by analyzing data cubes with a reference image taken on 2006.11.10, unless otherwise mentioned.

5.3 Building a data cube

A data-cube is a sequence of N_t local patches, with a spatial size $N_x \times N_y$, selected from solar disk images taken at a fixed temporal interval Δt. The sequence is defined by its reference patch $N_t/2$ taken at time T_0 and centered at the heliographic coordinates; latitude θ_0 and Carrington longitude ϕ_0. The rest of the patches are taken at $t_{i+N_t/2} = T_0 + i * \Delta t$ with $-N_t/2 < i < N_t/2$. In order to locate the reference patch in the $\mathrm{i_{th}}$ image, it is necessary to:

- Track it in longitude with the solar rotation rate at its given the latitude (latitude of the reference patch).
- The spatial sampling is defined by choosing (on the Sun) a grid of points around the center of each patch.
- Each point of the grid is then located in the solar image using an appropriate interuptions between available pixels.

Dimensions of the data cube

The spatial resolution of the GONG image at the disk center is $\delta x = 0.125°/pixel$ which leads to an extent on the horizontal wavenumber range up to the Nyquist wavenumber of $K_{Ny} = 2\pi/\lambda_{Ny} = 2\pi/(2\delta x) = 2.07Mm^{-1}$, hence the maximum value of the degree ℓ is $\ell \simeq K_{Ny} \times R \simeq 1440$. The spatial resolution in terms of the horizontal wavenumber is given by the limitation of the studied region such as $\delta K = 2\pi/\delta\lambda = 2\pi/N\delta x$ where N is the number of spatial samples and $\delta\lambda$ is the spatial wavelength resolution which is simply the spatial extension of the region. If the number of samples is $N = 128$, ie. an area of 16°, the spatial resolution is $\delta K = 0.0323 Mm^{-1}$, hence the spatial resolution in terms of the spherical harmonic degree is $\delta\ell = \delta K \times R \simeq 22$. Thus, the resolution in ℓ increases with increasing the spatial size of the studied area. This is shown in figures 5.2 and 5.3 where the number of fitted modes from $\ell - \nu$ power spectra inferred from patches with different spatial sizes, increases with increasing the spatial size. Notably, the increase of ℓ resolution allows a better resolution of lower degree modes and lower the degree of the mode deeper is its turning point and hence deeper is the probed area. Also, ridges with higher radial number n (higher frequencies for a given ℓ) can be better seen. However, one has to keep in mind that the analysis we are using is based on the plane wave approximation which is only valid in very limited spatial extents where the curvature of the area ca be neglected. Hence, there is a trade off between the spatial size and the validity of the used approximation. The commonly used spatial size is $16° \times 16°$[1] and is usually named the standard patch. It allows to probe depths down to about 16 Mm. When using the spatial size $30° \times 30°$ one can probe layers down to about 26 Mm (González-Hernández *et al.*, 2006). Most of the work presented here has been performed using the 'standard' aperture unless otherwise noted.

The temporal length of the data-cube in the standard ring analysis is fixed to T=1664min[2]. This choice is made to keep a fixed distribution of patches with a standard aperture in the solar disk during this time span (see section 5.7).The temporal resolution reached from this time span is $\delta\nu = 1/T = 10.016 \mu Hz$. Also GONG images are taken at $\delta t = 1 min$ cadence which gives access to a frequency range up to the Nyquist frequency of $\nu_{Ny} = 1/(2\delta t) = 8333 \mu Hz$.

---

[1] The spatial size of the standard patch is $16° \times 16°$. However, a circular spatial apodization is applied in an extent of 1° transforming the patch to a disk with a radius of 15°. Hence, in most of the text, I will refer to the standard patch with the size of 15° but one has to keep in mind that this is the size obtained after applying the windowing function.

[2] the temporal length 1664min=27.7hr corresponds to a rotation of about 15° at the equator and is commonly called a GONG day.

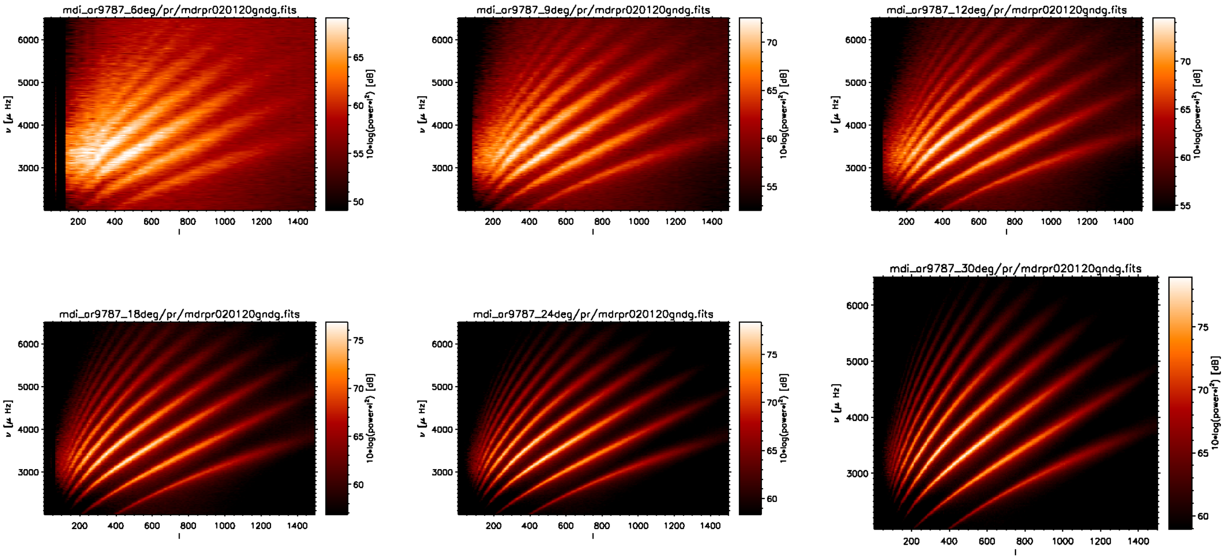

Figure 5.2: Power spectra in a (l, ν)-plane derived from patches with different spatial apertures. From left to right: Upper panels: ($6° \times 6°$, $9° \times 9°$, $12° \times 12°$). Lower panels:($18° \times 18°$, $24° \times 24°$, $30° \times 30°$). The resolution of the ridges increases with increasing the spatial size of the area because the resolution in ℓ increases.

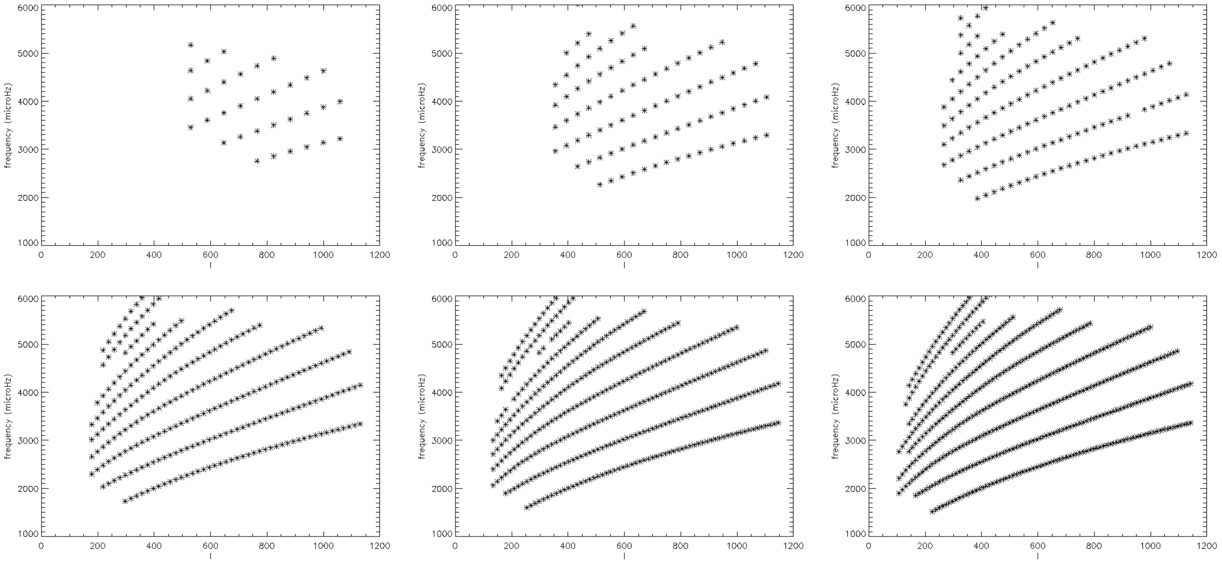

Figure 5.3: Modes fitted to the power spectra given in figure 5.2.

Remapping the local patches

The validity of the ring diagram analysis is mainly related to the reliability of the plane wave approximation in the chosen area. These waves propagate along paths providing the shortest distance between two points. This property is that of what is know as great circles in spherical geometry, ie. circles having the same center as the center of the sphere. It is then very suitable to find geometrical projections that remap the plane with these lines. In addition, power spectra is constructed from each data cube by using 3D Fourier transforms that require equidistance in spatial dimensions (temporal equidistance is insured dorn the constant temporal cadence of the images -1 min-). This second equidistance property is also needed in the search for the suitable mapping. However, a mapping projection insuring the two properties that we are seeking in all directions is not possible and the choice of the best mapping is therefore not obvious. For instance, the gnomonic projection insures a map with points on great circles in all direction, however the distances are not preserved in any of them. The standard implemented projection in the ring pipeline is the transverse cylindrical projection which takes equidistant points on great circle lines perpendicular to the local meridan, this insures our two requirements in the zonal direction only. The difference between a power spectrum in the (k_x, k_y)-plane derived from a data cube where the patches located at latitude 45° have been remapped using the transverse cylindrical projection and a latitude-longitude grid are shown in figure 5.4. Clearly, the equally spaced planar grid in latitude and longitude fails drastically far from the disk center. Hence, the distorted power obtained from unappropriate mapping can lead to important bias since the analysis specifically seeks the distortion of the rings due to the underlying flows. Regarding the prominent role of the geometric mapping in the analysis, I devoted a whole chapter to this topic where I used several types of projections to fit the power spectra distortions and deduce the horizontal velocities from inversion (see next chapter for more details).

Tracking

Large scale flows are mainly dominated by the differential rotation in the Sun (about 2000m/s at the equator). Indeed, shifting of the power spectrum (rings)

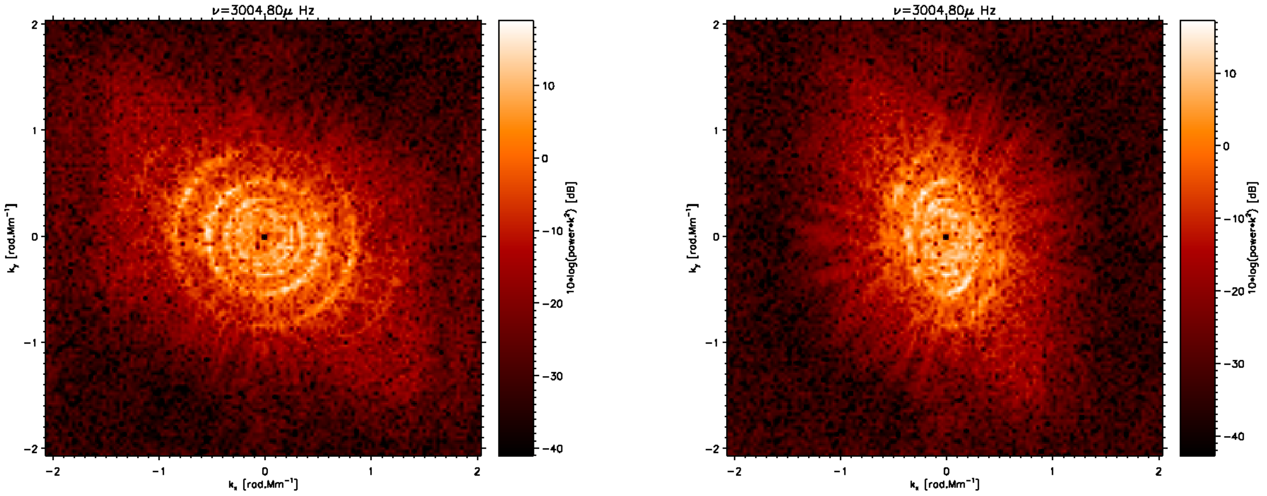

Figure 5.4: Power spectrum in the k_x, k_y plane derived from a patch located at 45° where the patches have been remapped using a great circle mapping (left panel) and an equally spaced latitude and longitude grid (right panel).

due to all the flows that advect the acoustic waves, is predominantly due to this considerable flow field (see figure 5.6). In order to be able to see small amplitude flows such as meridional circulation (about 20m/s at the surface) it is necessary to subtract a considerable amount of rotation from the analyzed data by considering, say, a commonly used surface rotation law. This is done by tracking the area of interest. The commonly used rotation law is that given in equation 1.5. The ring diagram pipeline uses Snodgrass (1984) rotation rates with a sidereal to synodic correction of 31.7nHz.

Camera projection

Once the planar projection is chosen to construct the grid of interest, each point of the grid needs to be localized in the image. In the case of GONG+ data, the images are circular with a constant radius r_0. If (θ, ϕ) are the heliocentric coordinates of the point of interest, their coordinates in the image axis (X, Y) are given by the equations[1]

---

[1] The demonstration of the camera projection equations is given in appendix A.

$$\frac{X - X_c}{r_0} = \frac{\cos\theta \sin(\phi - L_0)}{1 - S\alpha} \tag{5.1}$$

$$\frac{Y - Y_c}{r_0} = \frac{\sin\theta \cos B_0 - \cos\theta \sin B_0 cos(\phi - L_0)}{1 - S\alpha} \tag{5.2}$$

where $\alpha = \sin\theta \sin B_0 + \cos\theta \cos B_0 \cos(\phi - L_0)$, (X_c, Y_c) are the coordinates of the center of the image, B_0 is the inclination of the Earths axis in the ecliptic plane, L_0 is the Carrington longitude of the central point, S is the apparent semi diameter. These quantities can be found in ephemeris tables and are provided in the image header. In practice, the obtained values [X,Y] are usually not integers.

In order to get a grid corresponding to the pixel positions in the image, an interpolation is used (Corbard, 2003).

5.4 Power spectrum of the data cube

Apodization

Before applying the 3D Fourier transform to the remapped and tracked data cube, it is necessary to apply an apodization functionto the cube in both space and time dimensions in order to avoid spatial and temporal aliasing at high frequencies. The GONG ring diagram pipeline uses the cosine bell apodization function in spatial directions on an extend of 1° which transforms the data cubes from 16°/16° to circular patches of a radius of 15°. Table 5.1 displays some power spectra taken in the $[k_x, k_y]$ plane at frequency $3000\mu Hz$ by considering different widths of the spatial apodization; and 1° is a satisfying choice since a bigger width leads to a more dramatic loss of data. In the temporal direction, a multitaper technique has been implemented in an attempt to increase the signal to noise ratio. The inner rings of the power spectrum can be better seen when increasing the number of tapers but has the disadvantage of globally oversmoothing the data (see 5.2). The ring diagram pipeline in its standard run does not use the multitaper technique.

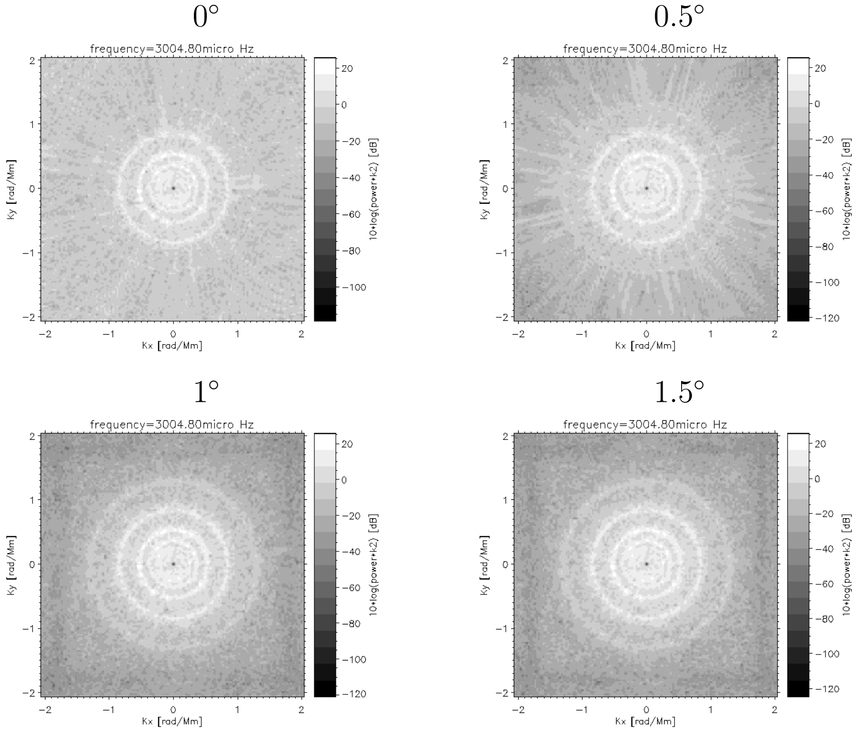
0° 0.5°

1° 1.5°

Table 5.1: Cuts of the power spectra at frequency $3000\nu Hz$ obtained using cosine bell apodization in the (x,y)-plane with different widths. The increase of the width allows to get of the spatial aliasing clearly seen in the upper two panels.

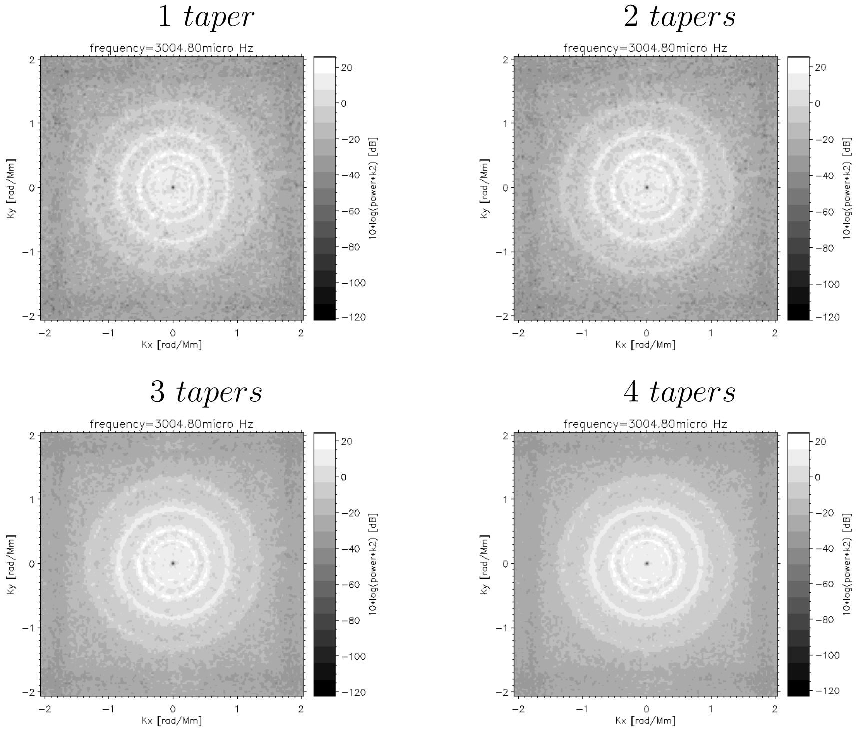
1 *taper* 2 *tapers*

3 *tapers* 4 *tapers*

Table 5.2: Same as table 5.1 but for different temporal apodizations (using different sets of tapers). The increase of the number of tapers, increases the signal to noise ration which allows to better resolve the inner rings but the width of the rings increases because of the oversmoothing.

Power spectrum in Cartesian coordinates $[k_x, k_y, \nu]$

After applying the apodization in space and time, the remapped and tracked data cubes [x,y,t] are Fourier transformed in space and time to produce power spectra of the solar oscillations in the (k_x, k_y, ν)-space, where k_x and k_y are the components of the horizontal wave number and ν is the frequency. The power spectrum shows ridges in all the planes perpendicular to the plane $[k_x, k_y]$. These power spectra are $\ell - \nu$ like diagrams. Consequently, the power spectrum in all the planes parallel to the plane $[k_x, k_y]$, i.e. at fixed frequencies, are ring like diagrams. The whole 3D power spectrum is trumpet like as shown in figure 5.1. The local oscillation power spectra obtained from a standard data cube are shown in the plane (k_x, k_y) for several frequencies and different data cube locations in table 5.3. The visibility of the rings is strongly affected by the location of the data-cube and increases as the observed regions move further away from disk center mainly because of foreshortening (see section 5.7).

Power spectrum in polar coordinates $[k, \theta, \nu]$

Bogart and et al. (1995) presented the idea to see a power spectrum as cylinders[1] wrapping the trumpets with different circumferences fixed by the radius $k = \sqrt{k_x^2 + k_y^2}$ (wave number) for a range of angles $\theta = \cot(kx/ky)$ (azimuth) at all frequencies. The relation between the Cartesian coordinates $[k_x,k_y]$ and the new polar coordinates $[\theta, k]$ at a fixed frequency is $k_x = k \sin\theta$ and $k_y = k \cos\theta$. Hence, equation 2.20 becomes

$$\Delta\omega = k(u_x \sin\theta + u_y \cos\theta), \tag{5.3}$$

θ is simply the direction of propagation. An unwrapped cylinder of this type (at fixed k) results in well distinguished mode powers displayed as nearly parallel straight lines in the plane $[\theta, \nu]$. Hence, each line is associated to a value of k and radial order n. The number of lines is fixed by the number of radial orders n detected. When using a standard patch one can observe the *f-mode* (n=0) and the 5 first *p-modes* (n=$1-5$). Hence, 6 parallel straight lines are seen in the $[\theta, \nu]$

---

[1] Cylinders are parallel to the frequency axis.

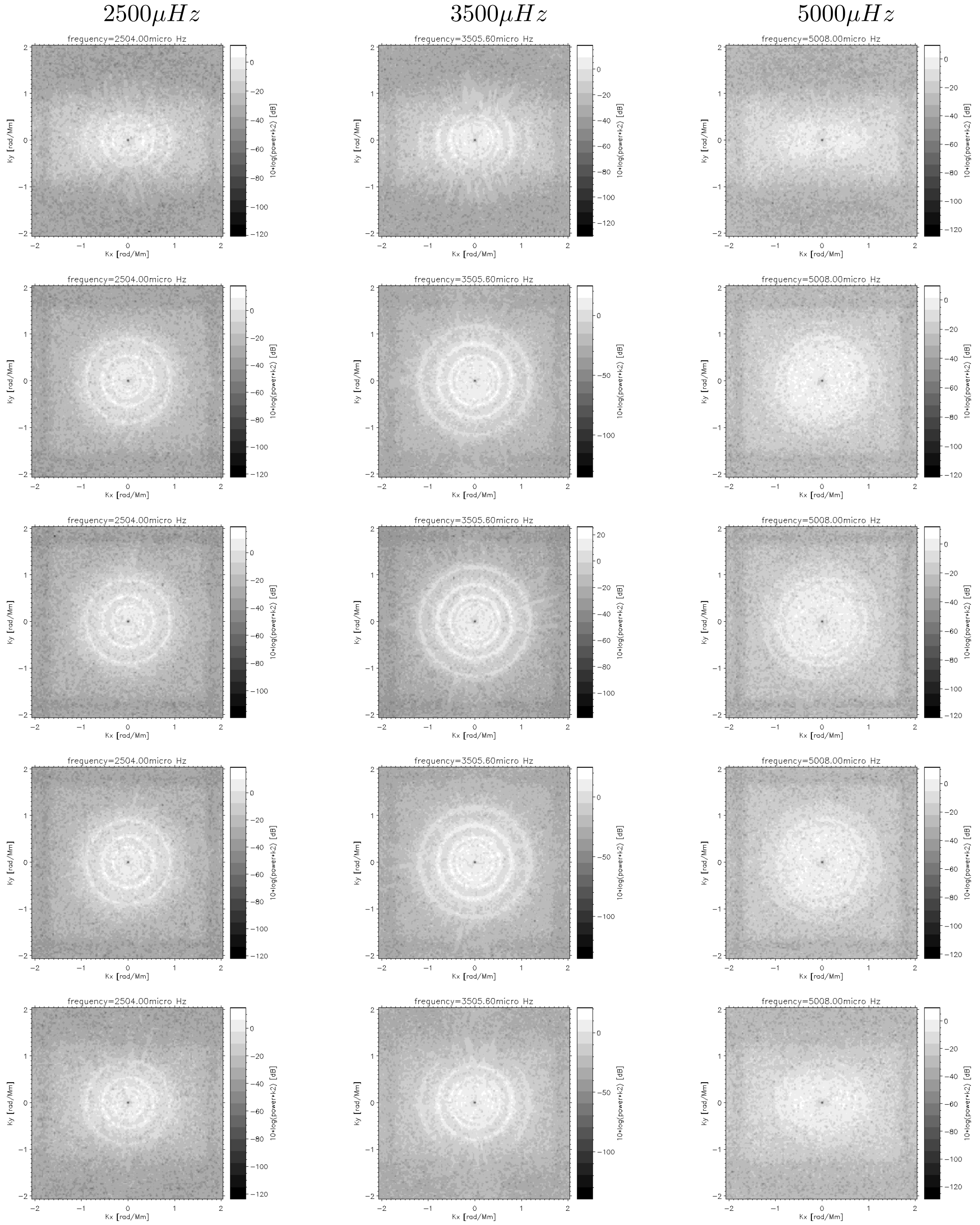

Table 5.3: Ring power spectra of given eigenfrequencies derived from standard patches located at the central meridian and at latitude (from top to bottom) 52.5°,15°,0°,-15°,-52.5°. The visibility of the rings decreased with latitude because of the foreshortening effect. The maximum power is given around 3000 μ Hz (5 min oscillations).

plane. The lines are not strictly straight because of the presence of underlying flows that advect the acoustic waves. This distortion is not easily seen by eye because after tracking, the remaining flows are very weak. In order to show more clearly how the underlying flows distort the lines, I deliberately produced power spectra for various tracking rates: (1) without tracking the patches , (2) by removing around half of the amplitude of the surface rotation, and (3) by using Snodgrass coefficients (see figure 5.6). The power spectra clearly appear to be curved by such flows.

In order to remove the anisotropies in the power distribution mainly due to the position of the data-cube as discussed before or due to any varying sensitivity of the instrument across the field of view, one can perform a Fourier filtering of the power spectrum in the $[\nu,\ \theta]$ plane. This filtering is performed in the frequency range $[150\mu\text{Hz}, 550\mu\text{Hz}]$ in the case of the standard patches, but one has to be aware of increasing this interval if other spatial and temporal dimensions of the data cube are used. The azimuthal dimension is also subsampled, in order to gain in time of data processing, which leads to smoother results as shown in figure 5.5 where power spectra are shown before and after the Fourier filtering and subsampling at different latitudes (2 left columns). The corresponding ring diagram at one specific frequency is also shown. Clearly, the contrast of the most affected parts of the power in high latitude patches (upper and lower panels) by foreshortening is considerably improved. This figure might lead to some confusion if not well understood. Thus, one has to keep in mind that what is shown in the two right panels does not result from the unwrapped rings in the left panel, but rather from unwrapping rings with the same size (same diameter) observed at different frequencies (different radial orders n). For instance, in the shown case, the external ring seen on the left panel corresponds to the third line (from the bottom) in the two right panels (taken around frequency 3000 nHz). The other lines do not correspond to the other rings but rather for rings of other frequencies.

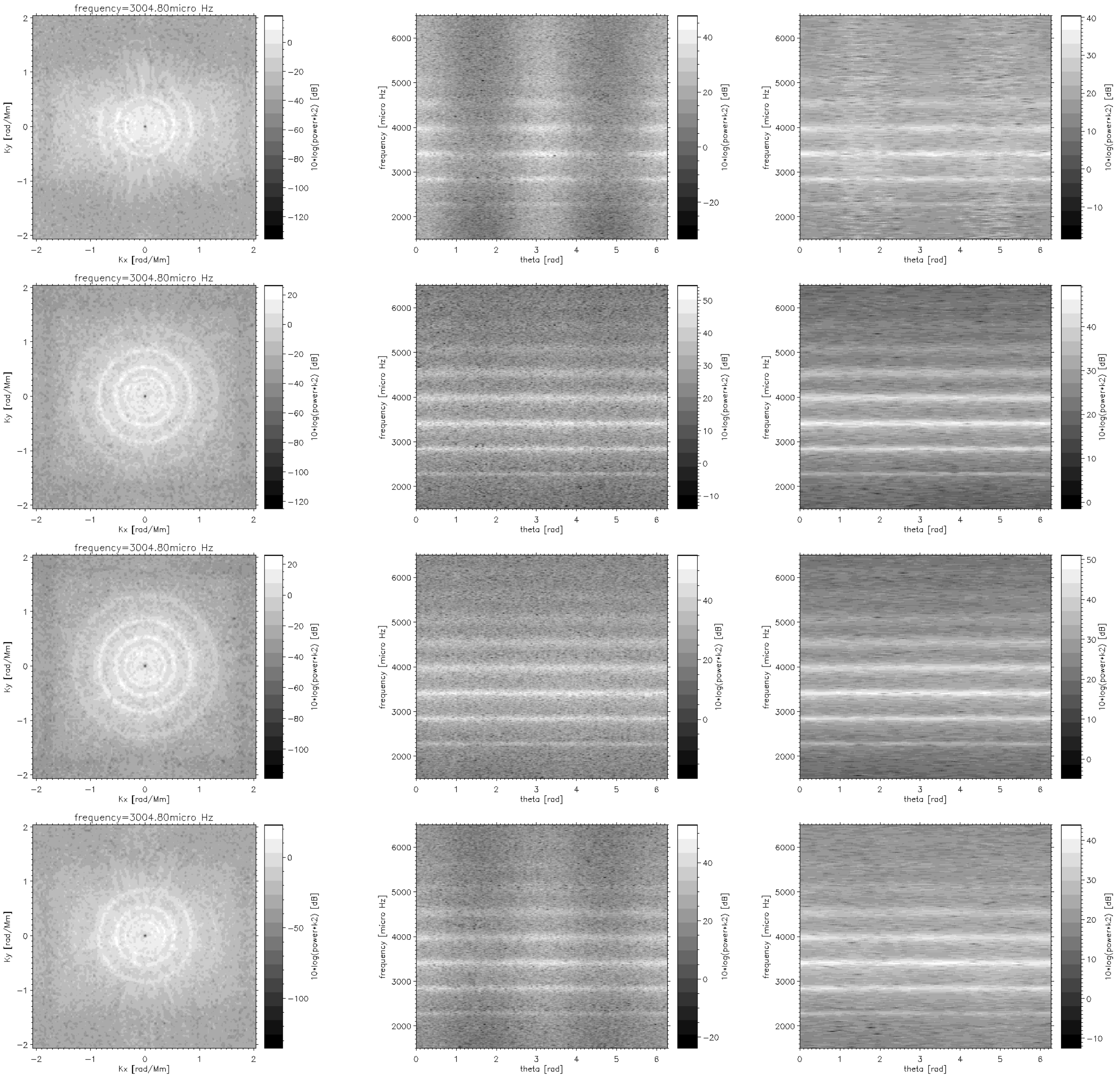

Figure 5.5: Power spectra derived from standard data cubes are shown in: left panels: (k_x, k_y)-plane at $\nu = 3000\mu$Hz. middle panels: polar coordinates ((θ, ν)-plane) at a fixed k. Right panels: Fourier filtered middle panel power spectra. From bottom to top power spectra are produced from data cubes located centered at the central meridian and latitudes [−52.5°,−15°,15°,52.5°].

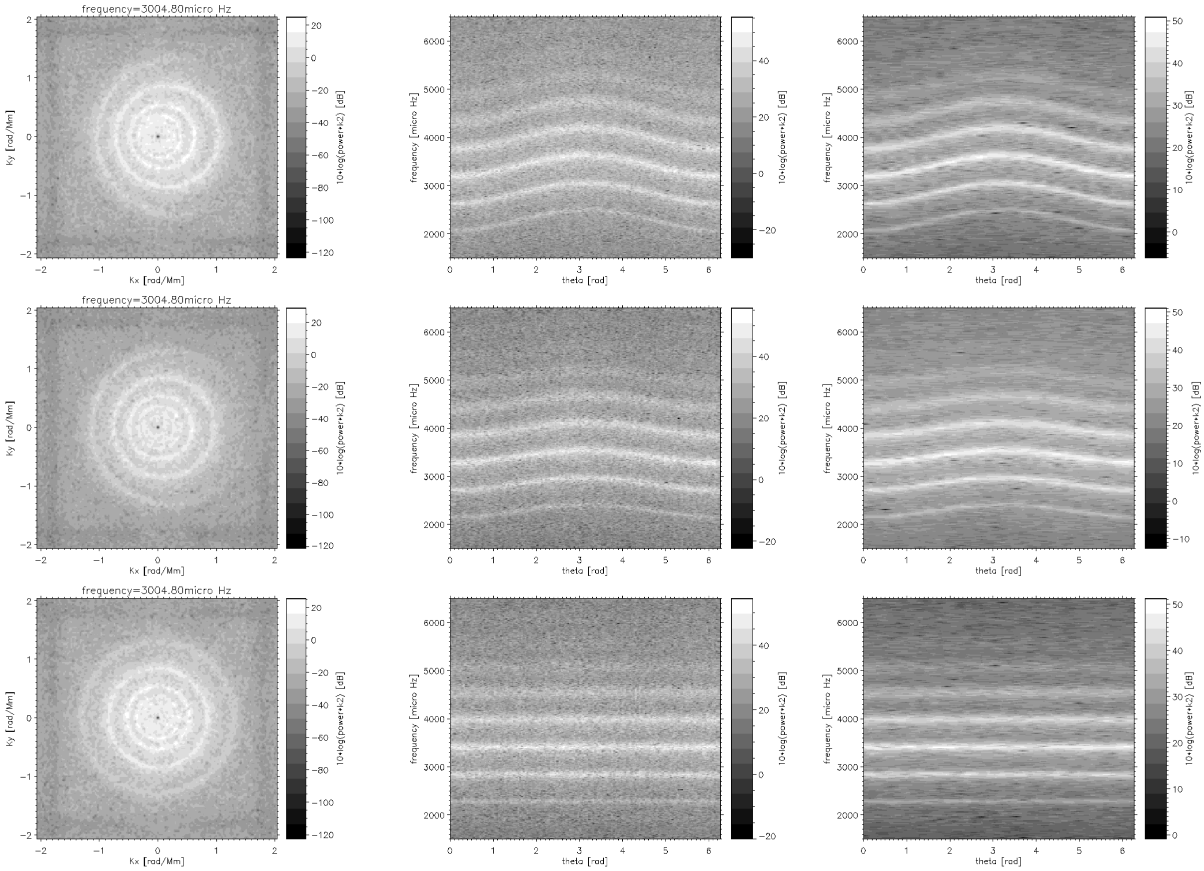

Figure 5.6: Power spectra shown in Cartesian and polar coordinates obtained with different tracking rates. Upper panels: no tracking ($a_0 = a_1 = a_2 = 0$). Middle panels: tracked with $a_0 = 200\mu\text{Hz}$, $a_1 = a_2 = 0$. Lower panels: tracked with Snodgrass (1984) coefficients.

5.5 Fitting the power spectrum

In order to get the horizontal velocity as a function of frequency, a symmetric Lorentzian function[1] is fitted to the observed mode power in the (θ, ν)-plane for each radial order n and wave number k (i.e. ℓ value). The model is given as follows (Haber *et al.*, 2000; Schou and Bogart, 1998)

$$P(\nu, k, \theta) = \frac{\Gamma}{2} \frac{A}{\frac{\Gamma^2}{4} + [\nu - (\nu_0 - \Delta\nu)]^2} + \frac{b}{k^3} \tag{5.4}$$

$\Delta\nu = \Delta\omega/2\pi$ is the frequency shift due to the advection of the wave by the flows, $\Delta\omega$ is given in equation 5.3, hence, $\Delta\nu = (u_x k \sin\theta + u_y k cos\theta)/2\pi$. The profile is specified by six parameters, u_x and u_y[2] , ν_0 is the central frequency, A is the amplitude, Γ is the full-width at half-maximum (FWHM) or simply the line width and, $\frac{b}{k^3}$ is the model background. The model P is fitted to the observation using the maximum likelihood method which seeks the maximum probability for an observed point O_i to be at a model point Pi (defined by θ, k and ν) by maximizing the likelihood function L within the fitting interval or minimizing the function F given by

$$F(u_x, u_y, \nu_0, A, \Gamma, b) = -\ln L = \sum_i (\ln P_i + \frac{O_i}{P_i}) \tag{5.5}$$

where $(\frac{1}{P_i} \exp \frac{O_i}{P_i})$ is the probability density of a single point in the solar oscillation power spectrum (Anderson *et al.*, 1990). The errors attributed to each fitting parameter are given by the diagonal elements of the Hessian matrix.

In figures 5.7 & 5.8 the six fitted parameters are shown as a function of frequency for two standard patches located at the central meridian at two latitudes, 0° and 52.5°. The number of fitted modes in the high latitude patch is much smaller than in the central patch because of foreshortening. I plotted the velocities u_x and u_y as a function of ν/ℓ in order to have a rough idea on the profile

---

[1] Basu and Antia (1999) have shown that the velocity fields obtained by considering an asymmetrical line profile are not substantially different from those obtained using a symmetrical profile.

[2] Since u_x and u_y are directly related to the frequency shift, I will very often refer to them as 'fitted shifts' but one has to be aware that these are velocities (in m/s) and not frequencies.

of the velocity flows in depth[1]. This shows that the extension in depth of the inferred velocities depends on the number of fitted lines (number of radial orders n). Hence, modes with n=0 (f-modes) contribute to the measured velocities on the first few Mm only and modes with the highest n (n=5) contribute to the inferred velocities until around 15 Mm. The use of big aperture patches enables to fit higer order modes and hence allows to get deeper velocity profiles. For instance, González-Hernández *et al.* (2006) have used large aperture patches of $30° \times 30°$ and inferred horizontal velocities until about 26 Mm. In this work, I am mainly interested in the u_x and u_y parameters, however, the other mode parameters are also worth exploring, especially as the inferred modes from ring diagram analysis are high degree modes and hence can provide valuable additional information about the near-surface. Some work has been done such as that of Howe *et al.* (2004) where a long term variation of the high degree mode parameters, amplitude and line width, derived from ring diagram analysis of GONG and MDI data has been explored. In this study, the amplitude and lifetime of the modes at maximum power (around 3mHz) appear to decrease at locations of high magnetic field, whereas higher frequency modes (around 5 mHz) seem to have increasing amplitudes and lifetimes in the presence of magnetic field.

5.6 Inferring flows as a function of depth

The shifts (u_x,u_y) are given for different modes (n, ℓ) trapped in different cavities below the surface. It is then intuitive to think that it is possible to obtain horizontal velocities as a function of depth. This problem is identical to that of global helioseismology where rotational splittings are used to infer the rotation velocity below the surface. In order to resolve such a problem, it is common to define first the 'forward problem' that gives, in our case, the relation between frequency shifts (our observables) and the underlying flows (the quantity we are looking for). Once the forward problem is defined, an inversion method can be applied to define the underlying flows as a function of depth from frequency shifts.

---

[1] This is because the turning point of each mode is given as a function of ν/ℓ (see chapter2).

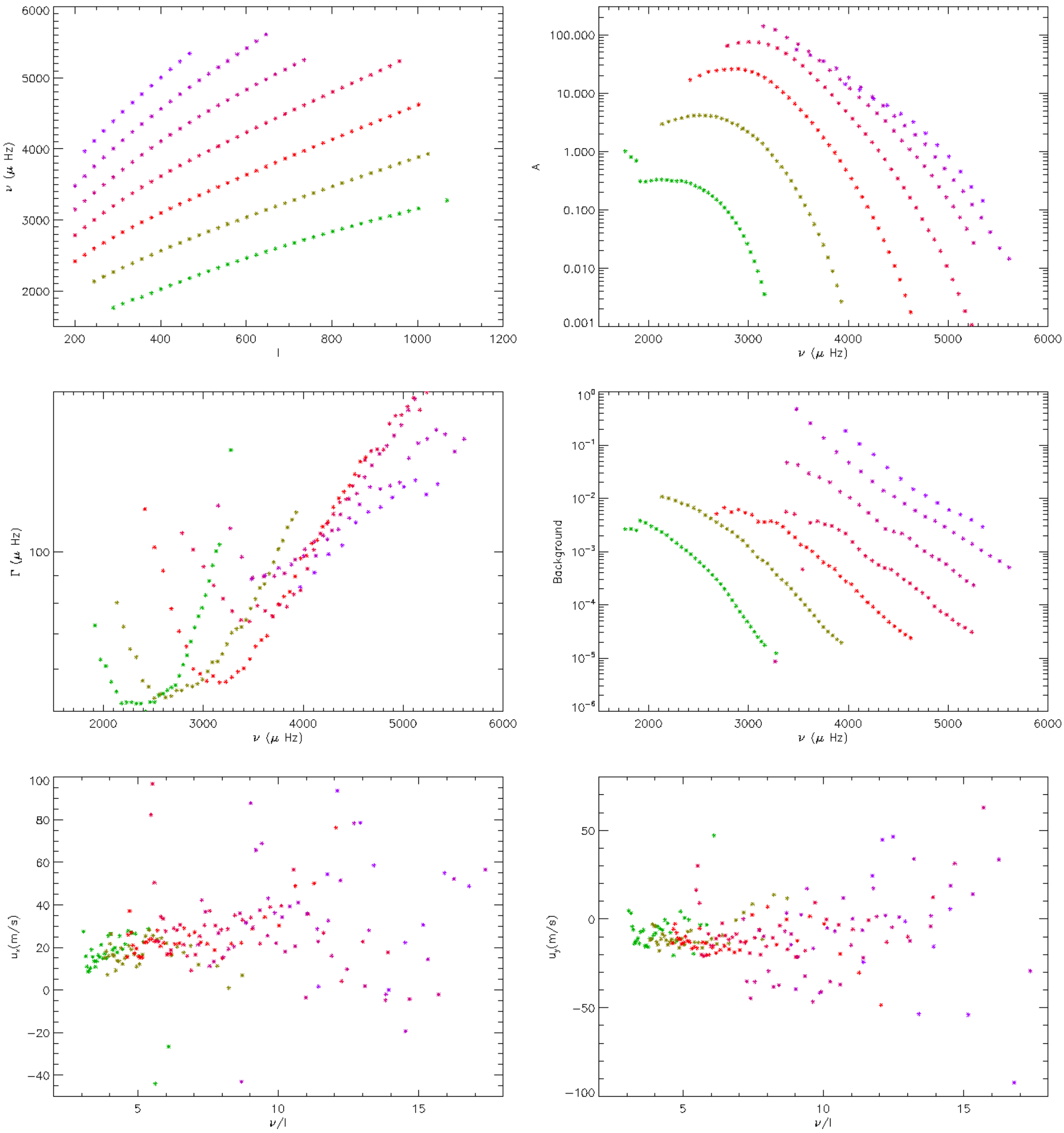

Figure 5.7: Fit parameters obtained from a standard dense-pack located at the central disk (0°,0°). From right to left: The central frequency and the amplitude of the modes function (upper panels), the line-width, and the background (middle panels) are given as a function of the degree ℓ. The frequency shifts in X and Y directions as a function of the ratio ν/ℓ of the frequency over l are given . Color coding gives the radial order of the modes as it is shown in the upper left panel from n=0 (lower rigde) to n=6 (upper ridge).

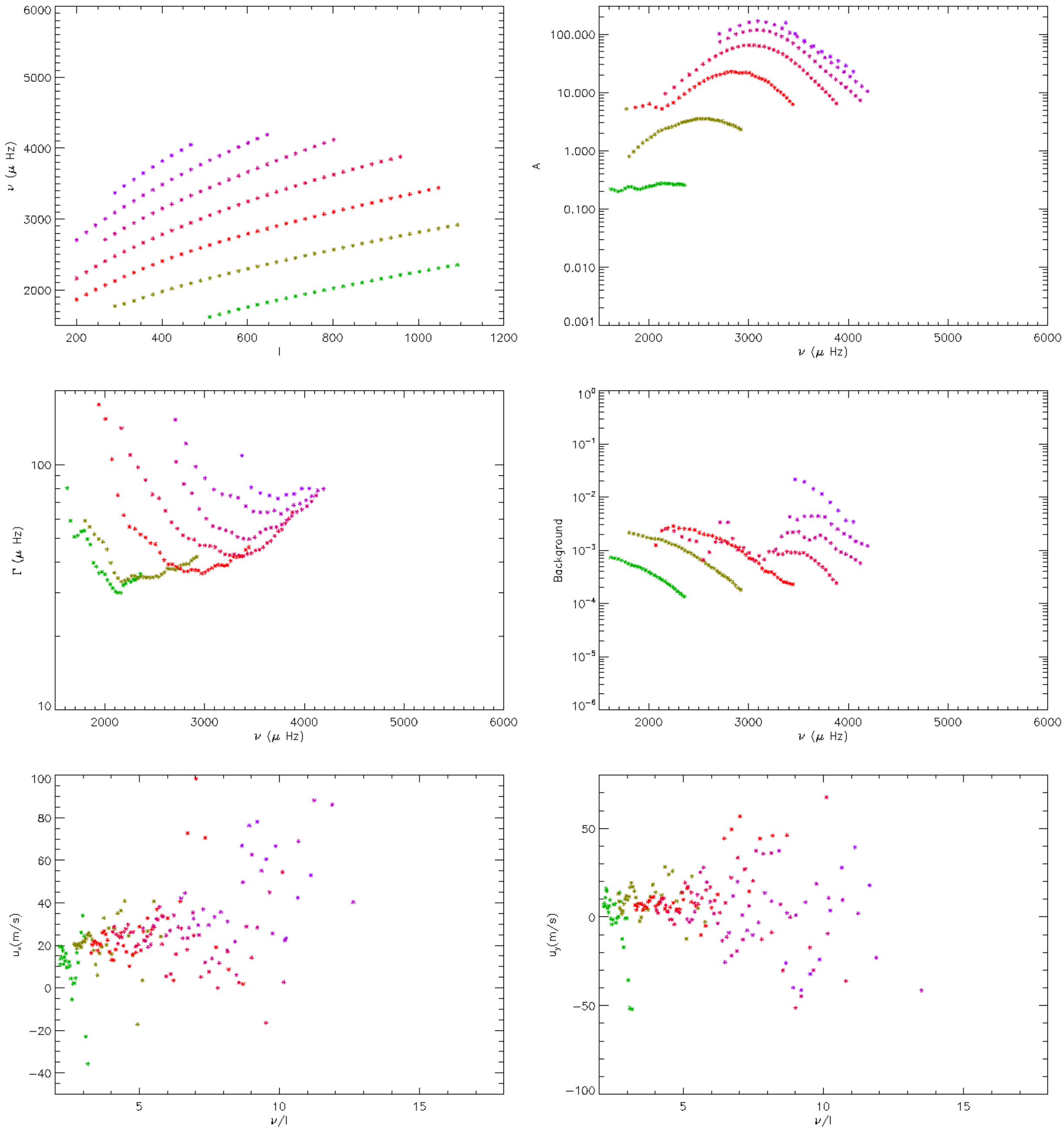

Figure 5.8: Same as figure 5.7 for a patch located at the central meridian with a central latitude of 52.5°.

Equations 2.21 and 2.22 define the 'forward problem' which allows to predict frequency shifts from a given profile of horizontal velocity flows. The problem faced is that we can measure the frequency shifts (observables) but we do not know the profile of the velocity flows in depth. Thus, our goal is to determine the velocity flows from the fitted frequency shifts and knowing the sensitivity functions (K) determined from a theoretical standard model of the Sun by inverting the integral equations (2.22, 2.21).

Inversion

Several inversion techniques have been used in helioseismology to infer the dynamics and the structure of the inner layers of the sun (Christensen-Dalsgaard *et al.*, 1990; Thompson, 1998). Two methods have been implemented in the ring diagram pipeline; the Regularized Least Square method (RLS) and the Optimally Localized Averages (OLA). I will summarize them briefly and discuss the resulting horizontal flows.

Optimally localized averages

The basic idea of this method is to find, for each target radius r_0, a set of coefficients c_i such as:

$$K(r, r_0) = \sum_i c_i(r_0)\beta^i K^i(r) \tag{5.6}$$

K is a unimodular function and is small everywhere except around $r = r_0$. The index i represents an eigenmode (n, ℓ). Thus, by taking into account equations 2.21 and 2.22 one can write

$$\overline{v_{x,y}}(r_0) = \int_0^R K(r, r_0) v_{x,y}(r)dr = \sum_i c_i(r_0) \int_0^R \beta^i K^i(r) v_{x,y}(r)dr = \sum_i c_i(r_0) u^i_{x,y} \tag{5.7}$$

$\overline{v_{x,y}}(r_0)$ is the averaged value of the velocity around r_0 given by a linear combination of the data. The sharpness of the $K(r, r_0)$ function, known as 'averaging kernel', defines the resolution of the method, i.e. the area around r_0 over which the true profile is averaged. Kernels are subject to the constraint of unimodularity. In the perfect case where $\overline{v_{x,y}}(r_0)$ would exactly correspond to $v_{x,y}(r_0)$, $K(r, r0)$ is given by a Dirac distribution and the data are arror-free. But, in reality there is a compromise between the resolution (the width of the averaging kernel) and the errors of the data. Hence, the OLA method uses a regularization parameter to fix the trade-off between the error magnification and the resolution of the kernels. One way to fix this parameter is to use the L-curves. In the case of inverting velocity flows from standard patches, we found that the most appropriate regularization parameter is 0.02. This value is valid for a wide range of the spatial size of the used patches (see figure 5.10). Exemples of OLA kernels are shown in figure 5.9 where the inversion has been prformed from frequency shifts obtained by fitting power spectra derived from data cubes with different spatial sizes. This figure shows that the sharpness of the kernel around the target depth impoves with increasing the size of the patch. This is due to the fact that the number of observed modes increases with increasing the spatial resolution which in turn improves the resolution of the method.

Least squares with second derivative smoothing

Another way to get the solution $(\overline{v_{x,y}}(r))$ is to parameterize it. This is commonly done by considering a piecewise constant function on a grid $r_1 < r_2 < ... < r_N + 1$, where $\overline{v}(r) = v_j$ on the interval $[r_j, r_{j+1}]$ and v_j are defined through a least-squares fit to the data. Hence, one can consider the minimization of the following function:

$$\sum_i [\frac{(u^i_{x,y} - \int_0^R K^i(r)\overline{v_{x,y}}(r)dr)}{\sigma_i}]^2 + \lambda \int (\frac{\partial^2 \overline{v_{x,y}}(r)}{\partial r^2})^2 dr \tag{5.8}$$

The second derivative in the second term on the LHS is the regularization term used to obtain a smooth solution. λ, dubbed smoothness parameter, is included as a trade-off parameter, determining the balance between the resolution and the uncertainties. In the ring diagram analysis of standard patches, this parameter is fixed to 5. I also found that this parameter is still valid for a wide range of spatial sizes of the used patches. The resolution kernels of the RLS method when applied to invert velocity fields from frequency shifts is given for the several sizes of the used tiles in figure 5.11. Also, as small the tile, as wide the kernle around the targeted depth for the same reason mentioned above.

Figures 5.12 and 5.13 show averaged zonal and meridional flows over 8 days. These have been obtained using OLA and RLS inversions of frequency shifts derived from 1 day data-cubes of MDI Dopplergrams of a region with different spatial extensions centered at $-8.3°$ in latitude and $132°$ in Carrington longitude[1]. The two methods provide us with similar velocity profiles. The OLA results are seen to fluctuate more than the RLS results because OLA seeks locally the solution.

On using sensitivity kernels derived from different standard solar models

All the inversions that have been performed so far to infer velocity flows are based on sensitivity kernels calculated using Model S (see chapter 4). In order to see how the change in standard model ingredients included in the calculation of sensitivity kernels might affect the inversion results, we used kernels and β coefficients from other solar models, described in chapter 4, to invert shifts obtained from fitting power spectra. For two standard patches located at the central meridian and at latitudes $0°$ and $15°$, the inferred zonal and meridional flows are shown in figures 5.14 and 5.15. The outcome is that all the CESAM models lead to nearly the same velocity flows as those inferred from Model S. Consequently, we concluded that the measurements of the velocity flows from ring diagram analysis are weakly sensitive to the parameters: age, opacity, equation of state, convection, heavy element surface abundances. However, since the high degree modes are trapped near the surface and hence are more affected by the near-surface modeling, it has been expected that the highest difference compared to Model S would have been that given by Model $\tilde{S}$ where the outermost layers are modified (see figure 4.1). Nonetheless, the difference between these two models are still insignificant where zonal and meridional velocity differences do not exceed 2m/s

---

[1] This data corresponds to the location of active region AR 9787. It is available for download at http://www.mps.mpg.de/projects/seismo/NA4/DATA/data_access.html

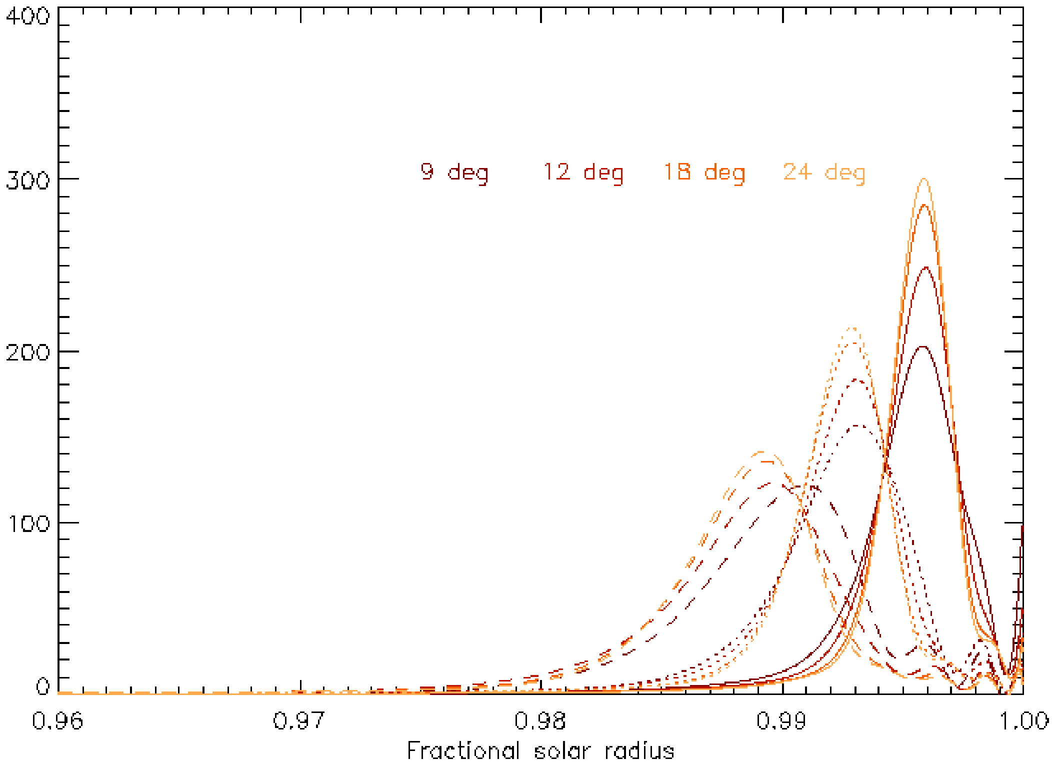

Figure 5.9: OLA Resolution kernels as a function of fractional radius derived from patches with different spatial apertures. Colors give the size of the patch as mentioned in the panel. Kernels derived from the smallest patch have the lowest peaks because they have the largest width (unimodular kernels).

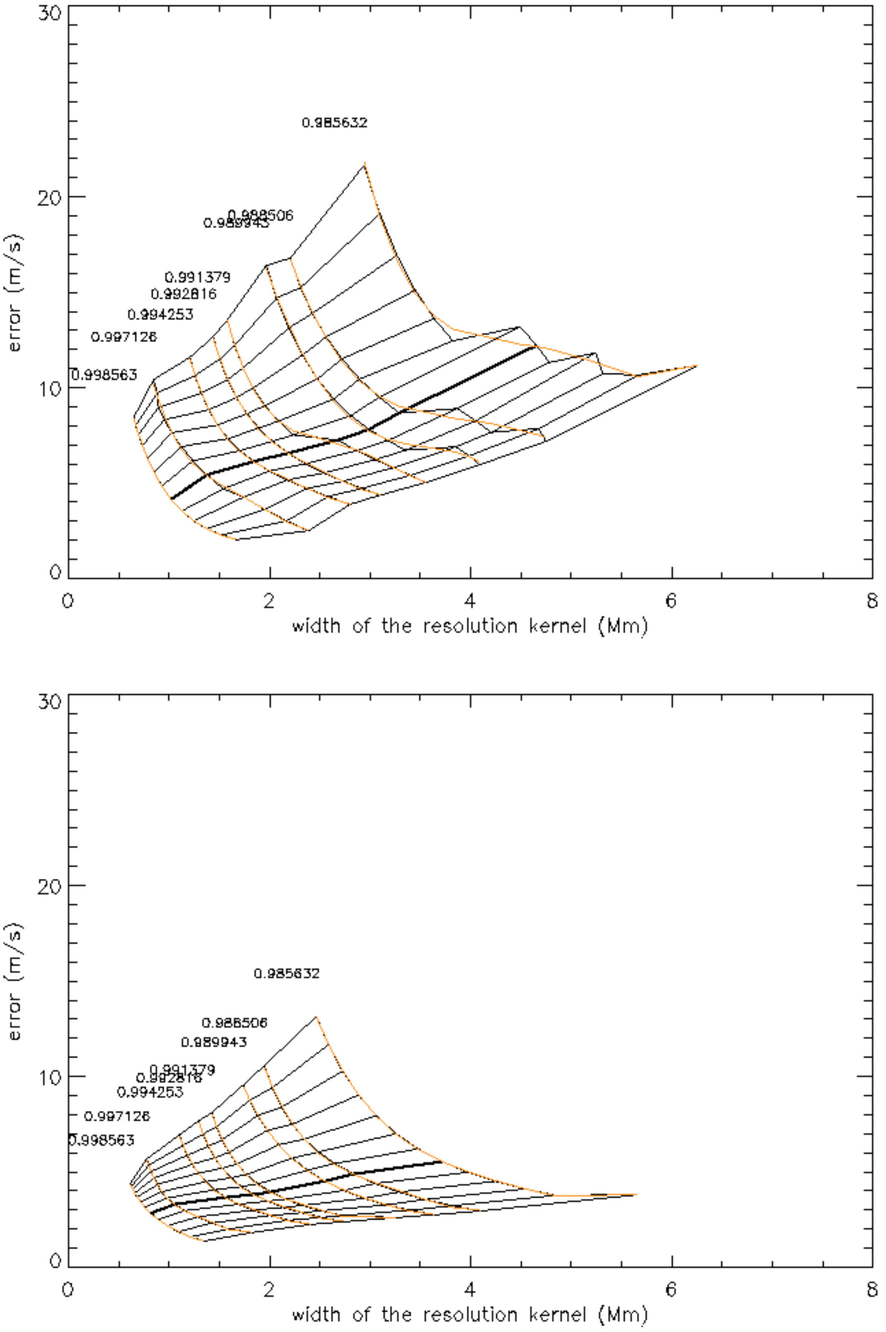

Figure 5.10: Width of the averaging kernels as a function of the errors, known as 'L-curves', derived from patches with different spatial apertures: 24° × 24° (top), 12° × 12° (bottom). L-curves are common tools used in OLA inversion method to find the trade-off between the resolution of the method and the data uncertainties. Black lines are given for the same smoothness parameter and red lines are the isodepth lines, depths are given inside the panels in fractional radius. The dark black line corresponds to a smoothness parameter of a value of 0.02 showing best choice for both spatial sizes.

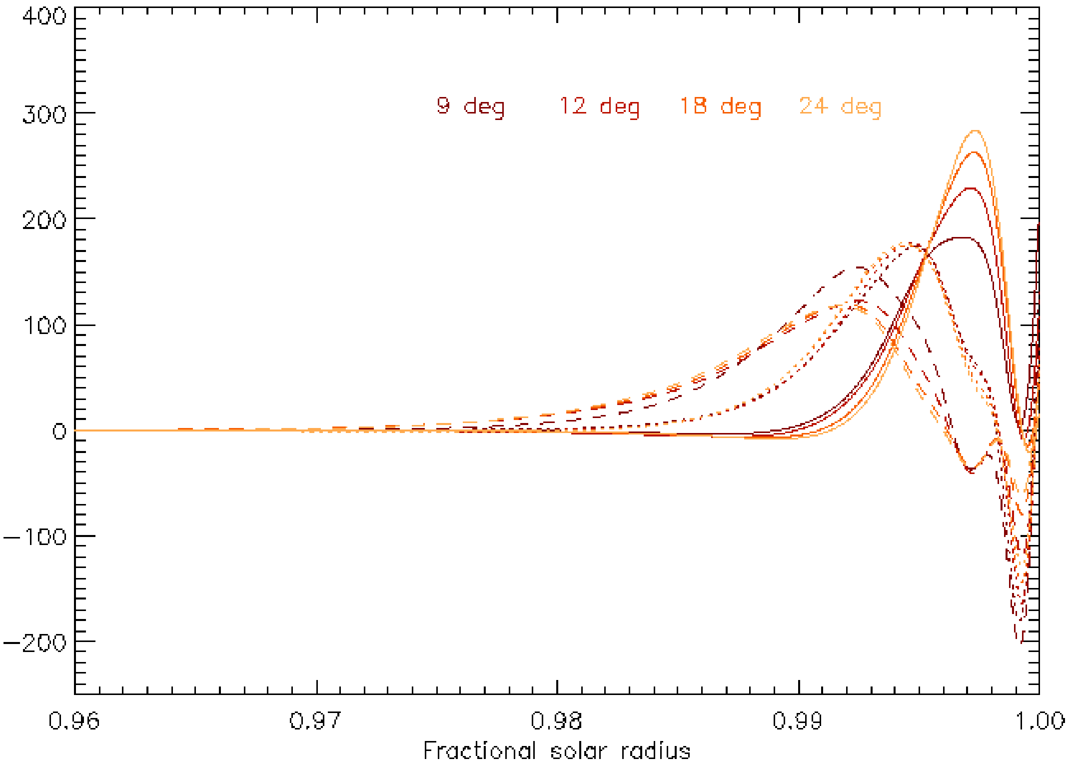

Figure 5.11: RLS resolution kernels as a function of fractional radius derived from patches with different spatial apertures. Colors give the size of the patch as mentioned in the panel. Kernels derived from the smallest patch have the lowest peaks because they have the largest width (unimodular kernels).

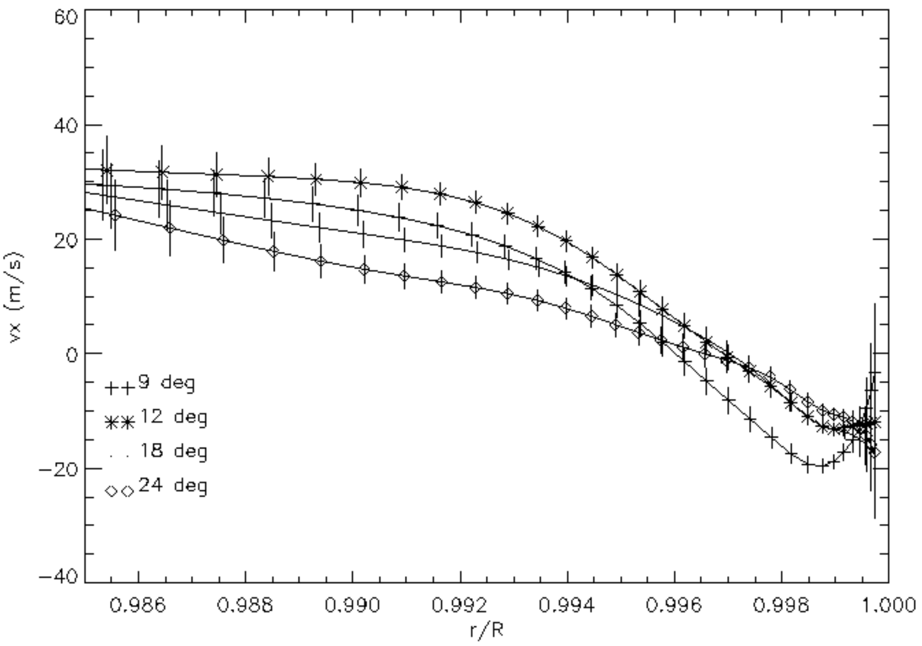

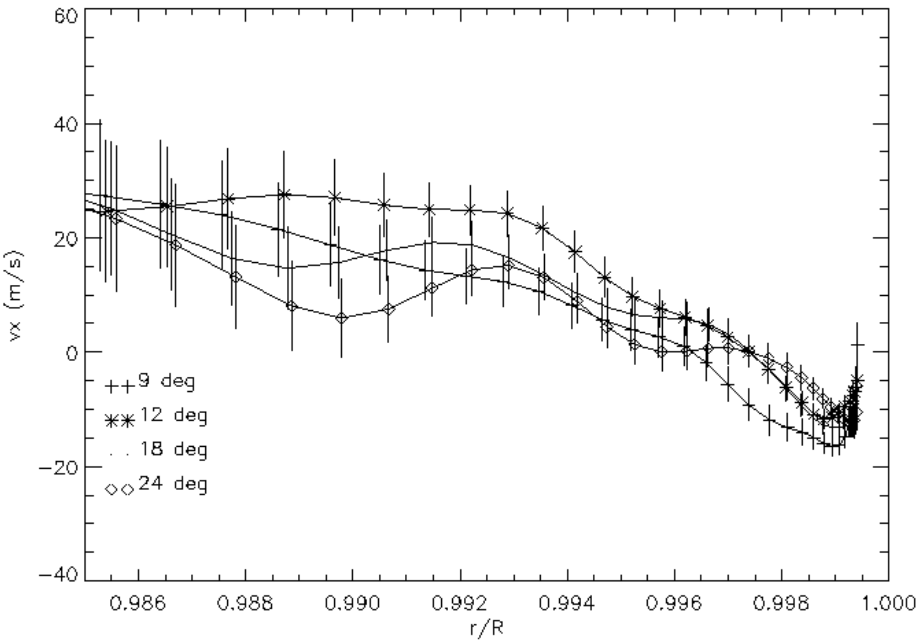

Figure 5.12: Averaged zonal flow over 8 days as a function of fractional radius for patches with different spatial apertures derived from RLS inversion (top) and OLA inversion (bottom).

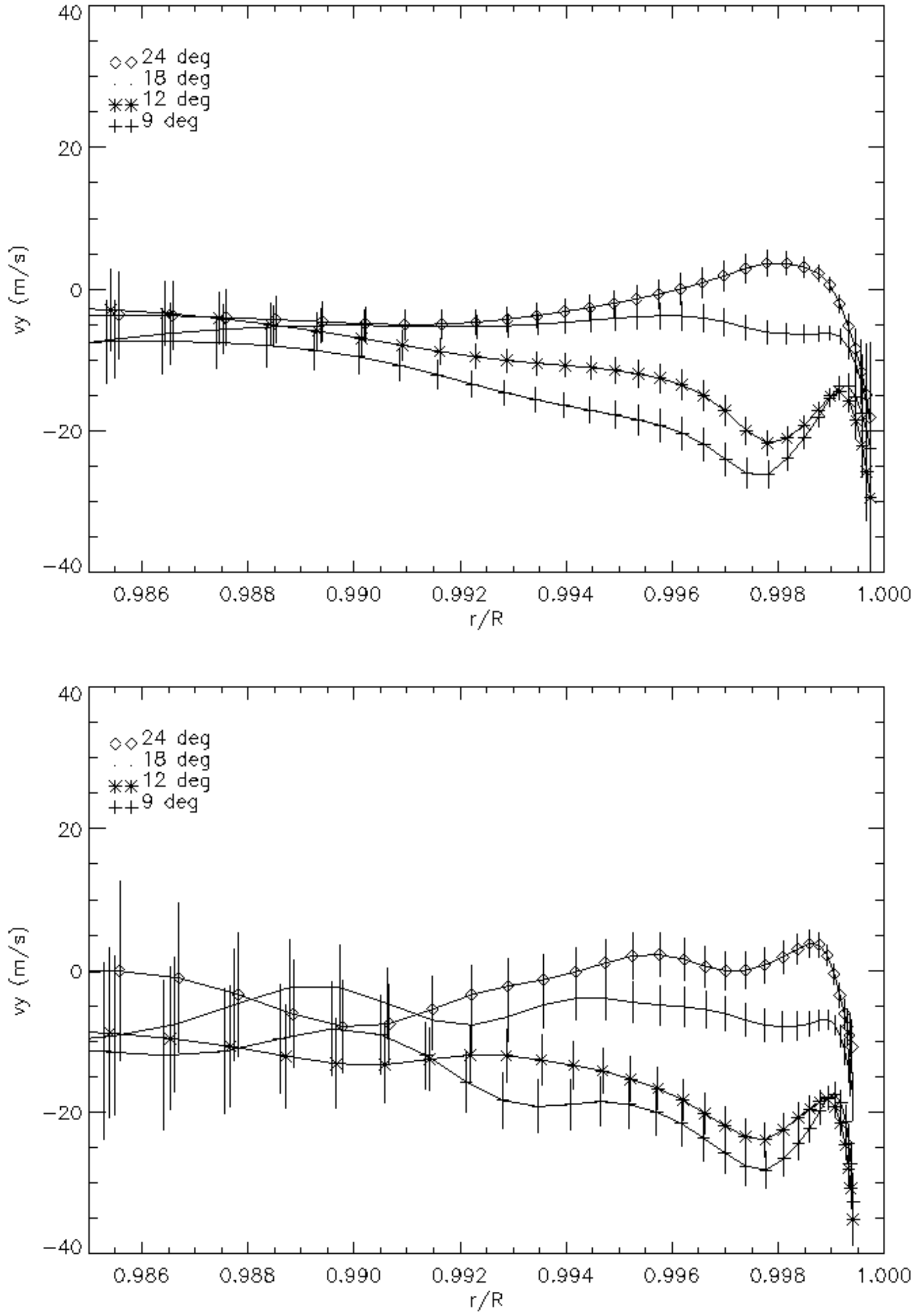

Figure 5.13: Same as figure 5.12 but for the meridional flow.

	-52.5	-45	-37.5	-30	-22.5	-15	-7.5	0	7.5	15	22.5	30	37.5	45	52.5
52.5					+	+	+	+	+	+	+				
45				+	+	+	+	+	+	+	+	+			
37.5		+	+	+	+	+	+	+	+	+	+	+	+	+	
30		+	+	+	+	+	+	+	+	+	+	+	+	+	
22.5	+	+	+	+	+	+	+	+	+	+	+	+	+	+	+
15	+	+	+	+	+	+	+	+	+	+	+	+	+	+	+
7.5	+	+	+	+	+	+	+	+	+	+	+	+	+	+	+
0.0	+	+	+	+	+	+	+	+	+	+	+	+	+	+	+
-7.5	+	+	+	+	+	+	+	+	+	+	+	+	+	+	+
-15	+	+	+	+	+	+	+	+	+	+	+	+	+	+	+
-22.5	+	+	+	+	+	+	+	+	+	+	+	+	+	+	+
-30		+	+	+	+	+	+	+	+	+	+	+	+	+	
-37.5		+	+	+	+	+	+	+	+	+	+	+	+	+	
-45				+	+	+	+	+	+	+	+	+			
-52.5					+	+	+	+	+	+	+				

Table 5.4: Dense pack matrix. The horizontal line indicates the central meridian distance of the data cube, 0 being the central meridian, its Carrington longitude is given by the ephemeris value L0. The vertical line indicates the latitude, 0 being the equator.

with error bars up to 10m/s. However, the effect of the near surface layers on the oscillations increases with increasing the radial order of the mode (see figures 4.3 and 4.4). The HMI instrument aboard the upcoming SDO satellite will provide better spatial resolution allowing us to include higher radial order modes in the analysis. In this context it might become more important to test the influence of our modeling of the outer most layers on the inferred subsurface velocities.

5.7 Inferring flows as a function of latitude and longitude

In order to infer horizontal velocity flows as a function of latitude and longitude, the analysis is applied to several data-cubes where the containing patches are centered in several positions all over the solar disk. Following Haber *et al.* (2002), the solar disk is divided into 189 patches with 15° aperture equally distributed on both hemispheres and on east and west sides of the central meridian. The data-cubes contain 1664 patches (i.e. minutes) where the reference slides are distributed as shown in table 5.4. This table gives the central meridian distance (CMD) and the latitude of the center of each patch of the mosaic. They are separated by 7.5° in helio- latitude and longitude and therefore patches close to

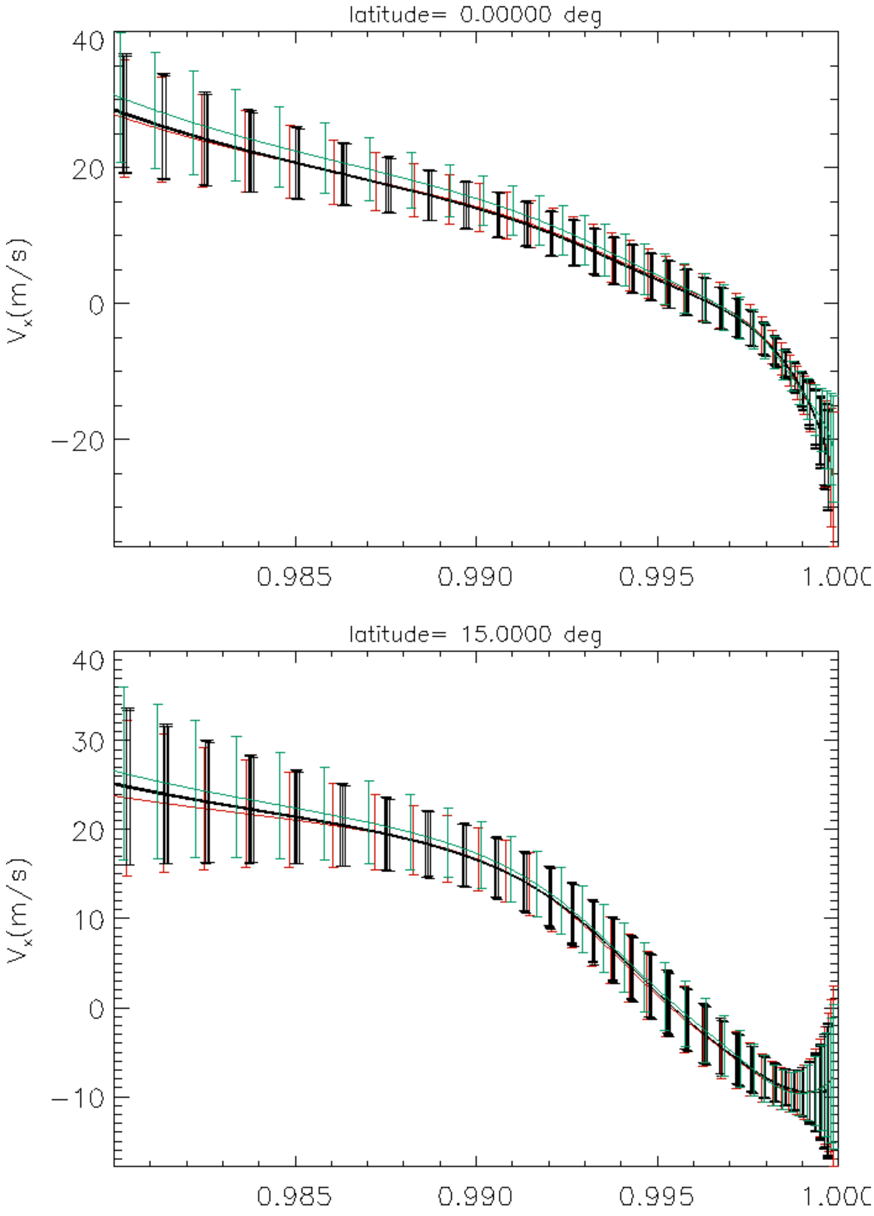

Figure 5.14: Zonal flow inferred from patches located at the central meridian for the mentioned latitudes measured using kernels calculated form: Model $\tilde{S}$(green), Model S (red) and CS1, CS2, CS3, CS4. The various results are all assembled in the black curve.

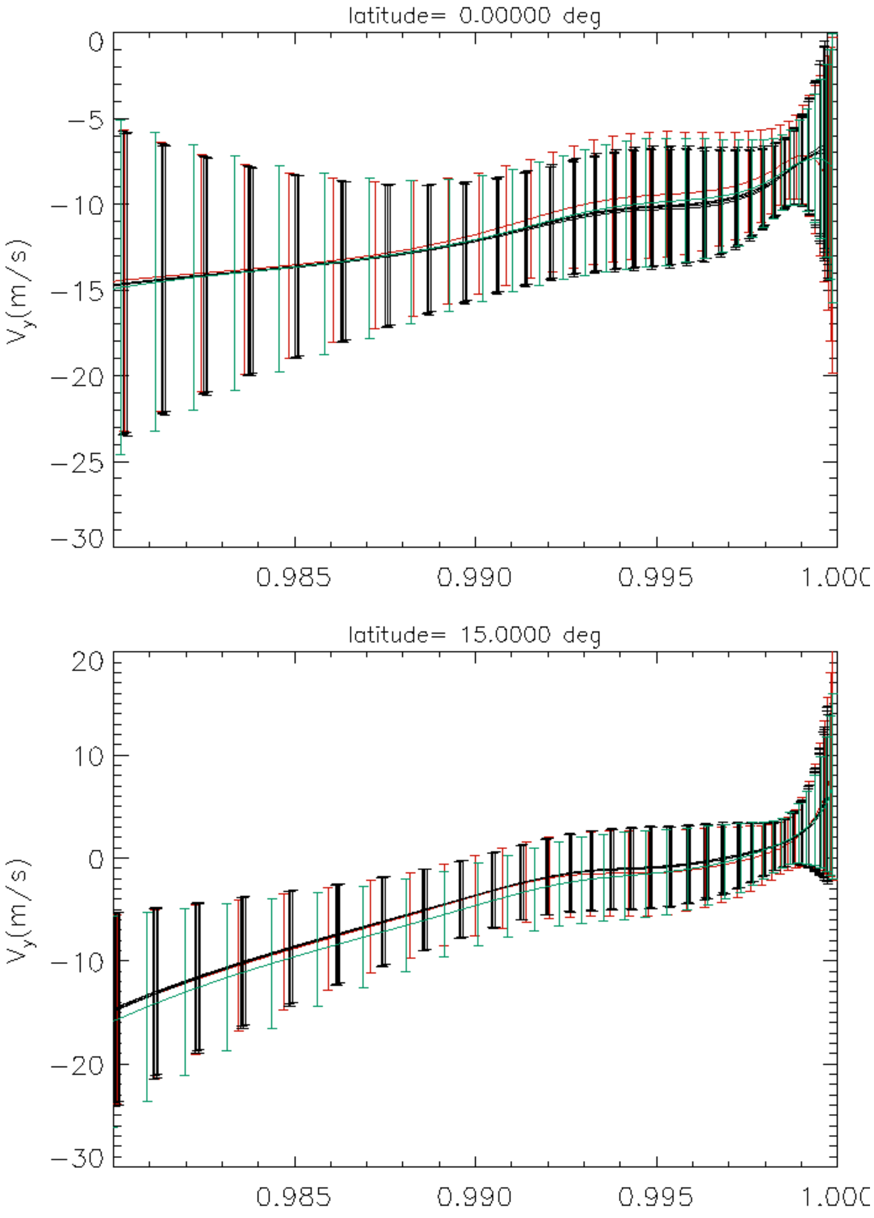

Figure 5.15: Same as figure 5.14 but for the meridional flow.

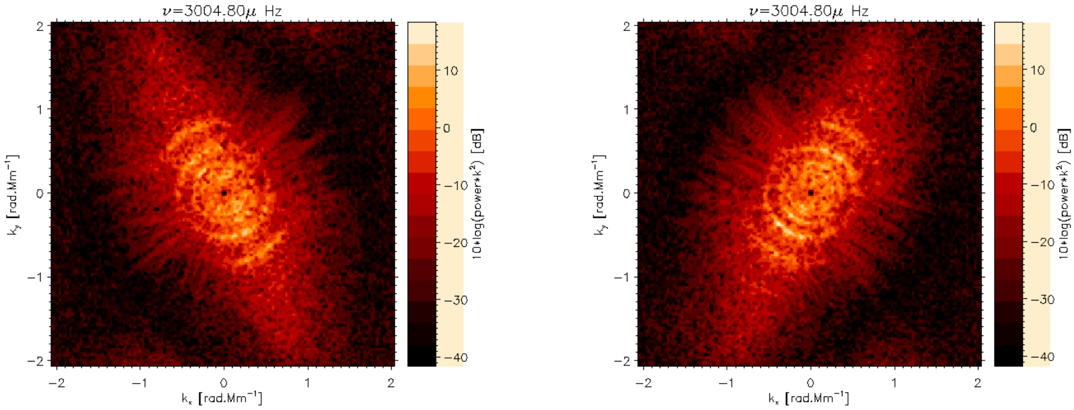

Figure 5.16: left panel: Power spectra in the (k_x, k_y)-plane derived from avoided patches in the dense-pack matrix. left panel: patch located at latitude 52.5° and central meridian distance 52.5°. right panel: latitude 52.5° and central meridian distance −52.5°.

the disk center are overlapped by 7.5° in each direction[1]. The reference image (middle of the serie of 1664 images) is usually taken such as its central meridian is located at a Carrington longitude as close as possible to a multiple of 15°. This distribution, that I will call 'dense-pack matrix', has been chosen in order to avoid as much as possible foreshortening. In figure 5.16, I show power spectra dramatically affected by foreshortening from two patches taken outside the dense-pack matrix. Figure 5.17 shows the inferred velocities from each patch contained in the dense-pack matrix, what is known as 'a daily flow map', but also from those outside the dense-pack matrix. I highlighted (in red) the velocity measurements that provide errors eight times higher than those inferred from the central patch. Clearly, most of these velocities are those derived from the non-used patches that also provide over-estimated flows. Other daily flow maps of the dense-pack matrix are given in figures 2 and 3 of ARTICLE II for two different days at several depths for standard patches and big aperture patches of 30°.

The ring diagram pipeline uses a specific coding of the filenames attributed to the heliographic positions (latitude and Carrington longitude) of each patch in the matrix. This coding was allowing us to code all latitudes between ±52.5° with

---

[1] Close to the disk center only because their extension is not defined in the latitude-longitude grid but rather in the chosen projection (e.g.Postel) leading to more overlap as we go away from disk center.

a step of 7.5° and all Carrington rotations with a step of $o.5°$. I have extended the coding of the latitudes to a resolution of 0.5° in order to be able to use several mosaics. Indeed, Haber's mosaic is not unique and it is of great interest to take other data cube geometries to test the sensitivity of the inferred averaging flows to the considered mosaic. Also, a higher resolution in latitude will allow an automatic processing of the incoming HMI images where the resolution will definitely allow us to sub-divide the current standard patches in order to get a better resolution in the velocities since these are averaged over the whole spatial region.

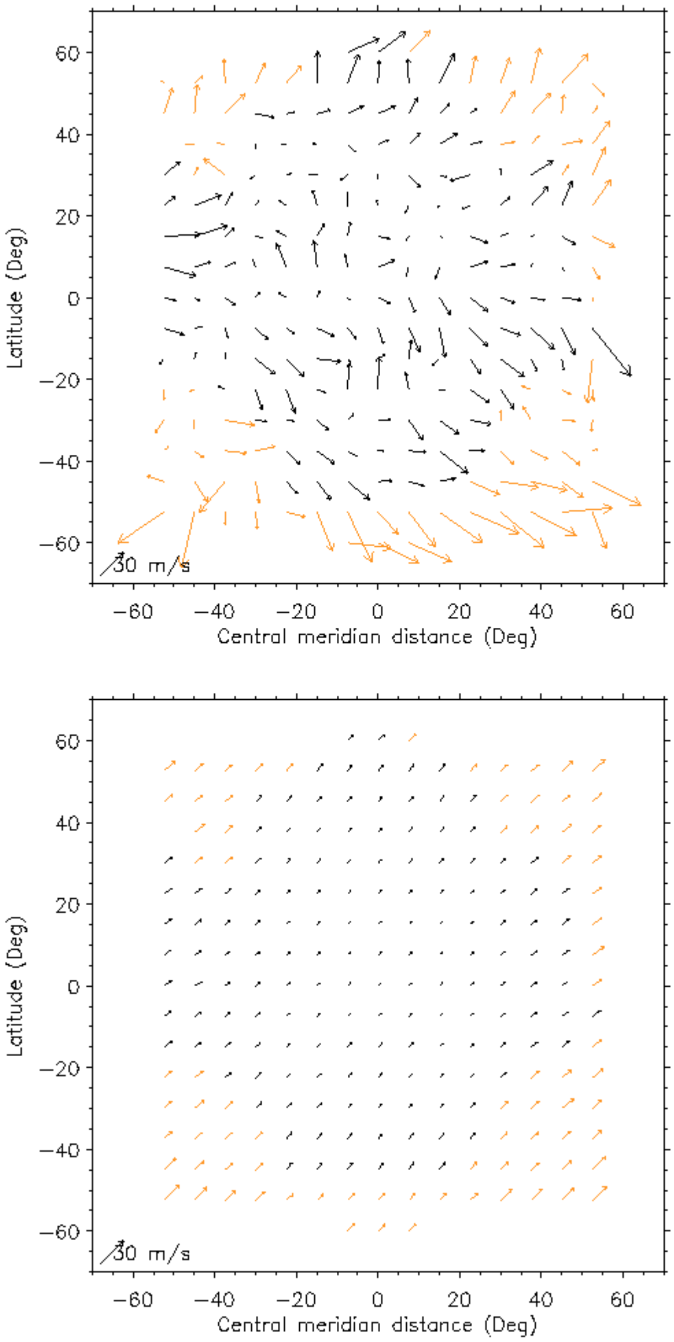

Figure 5.17: Top panel: daily velocity map (2002.11.10) at depth 7.1Mm given for all the considered patches in the dense-pack matrix as well as for the removed data cubes. Red arrows are given for errors 8 times higher than the error obtained from the central patch. Most of the red arrows correspond to the avoided patches. Bottom panel: same as top panel for the velocity errors.

Chapter 6

Sensitivity of the analysis to the change in the geometric mapping

> *I have embarked on this geometric problem... trying to throw light on different aspects each time. I cannot imagine what my life would be like if this problem had never occurred to me; one might say that I am head over heels in love with it, and I still don't know why.*
>
> M. C. Escher

Abstract

The attribution of heliographic coordinates, latitude and Carrigton longitude, or any coordinate associated to a given projection, to any point in a solar image is known as 'remapping'. Because the acoustic waves propagate along great circles at the solar surface, it has been shown that these circles need to be used in the geometrical construction of the plane grid. In order to check how sensitive the ring diagram analysis with respect to the different ways of mappings is, I carried out different types of geometrical projections (Azimuthal equidistant projection, transverse cylindrical projection, gnomonic projection, and stereographic projection) to remap the solar images. All the used projections lead to similar velocity flows estimations with standard patch sizes ($15° \times 15°$*). The difference between the four projections is more noticeable when larger patches (*$30° \times 30°$*) are used.*

6.1 Goal of the study

As it has been emphasized in the last chapter, geometric mapping of the solar images is a crucial step in the ring diagram analysis. Indeed, mapping the solar images onto projected coordinates has to be handled with lots of care since it can cause a nasty artifact in the inferred velocities by adding distortions to power spectrum in addition to those really due to the frequency shift of the oscillations affected by the underlying flows. Hence, it is of a great importance to know how sensitive the analysis is to the geometrical mapping.

In order to study the sensitivity of the subsurface flow measurements to the geometrical mappings, I have used several projections and compared the resulting fitted shifts and inversion velocities. The remapping package of the ring pipeline has been developed by T. Corbard (Corbard *et al.*, 2003). In this package, I have implemented other projections using the mathematical expressions of the heliographic coordinates (latitude, longitude) as a function of the projection coordinates given with an extensive explanation in the PROCEEDINGS III. These projections are accomplished through some combinations of axis rotations of the original coordinate system (heliographic coordinates).The geometrical projections mainly used for Earth mapping are well documented in some books (e.g. Yang *et al.*, 2000) as well as on the www[1].

6.2 Mapping for ring diagram analysis

For local helioseismology analysis, the choice of the projection has to focus on two aspects. First, it needs to insure equidistance because the 3D Fourier transform requires this property[2]. Second, acoustic waves are assumed to be plane waves in the probed region, hence, their propagation paths follow the great circles of the sphere. Nonetheless, when passing from a sphere to the plane, distortions are unavoidable either in distances, areas, or angles. For this study, I used projections that remap at least one of the planar directions onto great circles in addition to

---

[1] http://mathworld.wolfram.com/topics/MapProjections.html

[2] In time, the equidistance is insured by the image timescale.

the equidistance property. The following mappings have been included in this study:

1. **The transverse cylindrical**: Also called Plate Carrée projection, is the projection used in the GONG ring pipeline. This projection has the advantage to map the x direction into great circles and the distances are preserved along it. However, the y direction suffers from distance distortion.

2. **The azimuthal equidistant projection** : Also called Postel projection, is the projection used by the MDI dynamics program. In this projection, all the lines passing through the center of the projection in the map are great circles. However, neither the y direction nor the x direction of the map represent a real distance on the sphere.

3. **Gnomonic projection**: This projection is interesting since all the lines drawn in the resulting map are great circles, which would be ideal for wave paths. However, distances are not preserved in any direction.

4. **Oblique cylindrical**: This projection maps the y direction onto great circles along which the distances are preserved. However, distances along the x direction are distorted.

6.3 Effect of the mapping on frequency shifts

The frequency shifts are obtained by fitting power spectra derived from two different patches, standard ($15° \times 15°$) and big ($30° \times 30°$), that are remapped using three projections (transverse cylindrical, Postel, and Gnomonic). The results are shown in figures 6.1 & 6.2 for shifts on x direction and figures 6.3 & 6.4 for shifts on y direction. Big patches show higher differences between the different projections. This is because the distortion increases far from the center of the patch which is considered to be the center of the projection for all configurations (wider explanation is given in PROCEEDINGS III). The resulting shifts obtained from Postel projection and the transverse cylindrical projection are similar. The gnomonic projection displays the most different results. This is mainly due to the considerable distance distortion in the gnomonic projection even though great circles are insured in all directions.

6.4 Effect of the mapping on the inverted velocities

The effect of mapping the standard and big spatial aperture patches with different projections on the measurement of the daily zonal and meridional flows are given in figures 3 and 4 of PROCEEDINGS III through daily flow maps. Again, the highest differences between the flow measurements of the differently mapped patches are given from the use of big spatial apertures. Unlike the Gnomonic projection, the transverse cylindrical and the Postel provide us with similar results. Also, the difference between the velocities increases with depth. This is most likely due to the fact that the shallowest layers involve all modes, which could average out the effect of the projection whereas the deepest layers involve a very limited range of modes (lowest ℓ and highest n) hence the effect of the projection is more pronounced.

In order to focus on the effect of the change in the planar mapping in each of the horizontal flow components, I averaged zonal and meridional flows over longitude and time (7 days) to get them as a function of latitude and for different depths. Figure 6.5 shows the averaged zonal flow as derived from patches mapped using the transverse cylindrical, the Postel and the Gnomonic projection. The results are very similar for all projections at all depths and latitudes. Even though, more differences are seen from the use of big patches, the zonal flow estimations from the three projections all fit inside the error bars. However, meridional flow measurements given in figure 6.6 show much higher difference from the use of the transverse cylindrical, the Postel and the Gnomonic projection. This has been somehow expected since the transverse cylindrical projection maps only x direction onto great circles where the equidistance is also insured hence distortions are more pronounced in y direction, whereas Postel projection does a better work for both directions, at least for standard patches. In order to see more clearly

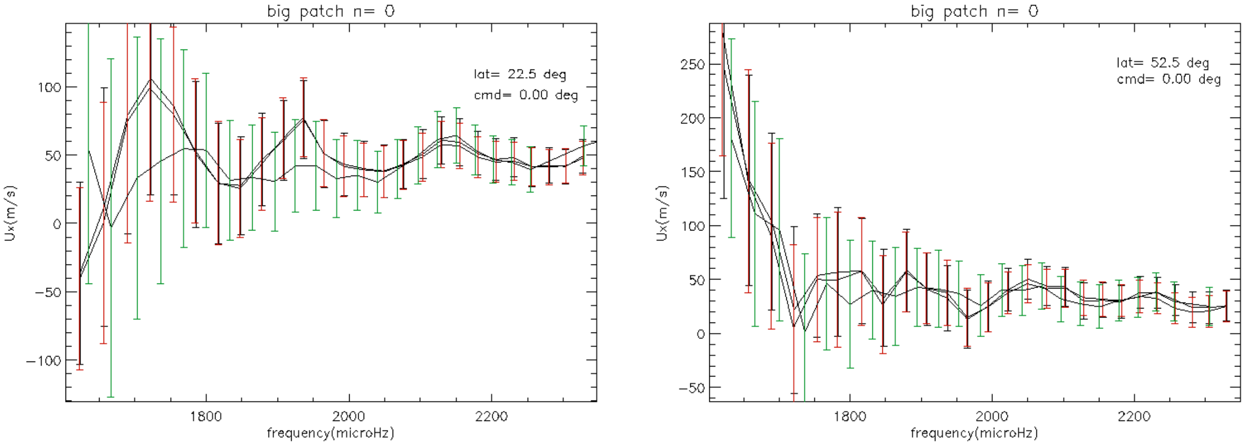

Figure 6.1: Frequency shift in the x direction as function of frequency derived from big patches 30°/30° remapped using the geometrical projections: Transverse cylindrical (black), Postel (red), Gnomonic (green). The position of the patch is mentioned inside each panel.

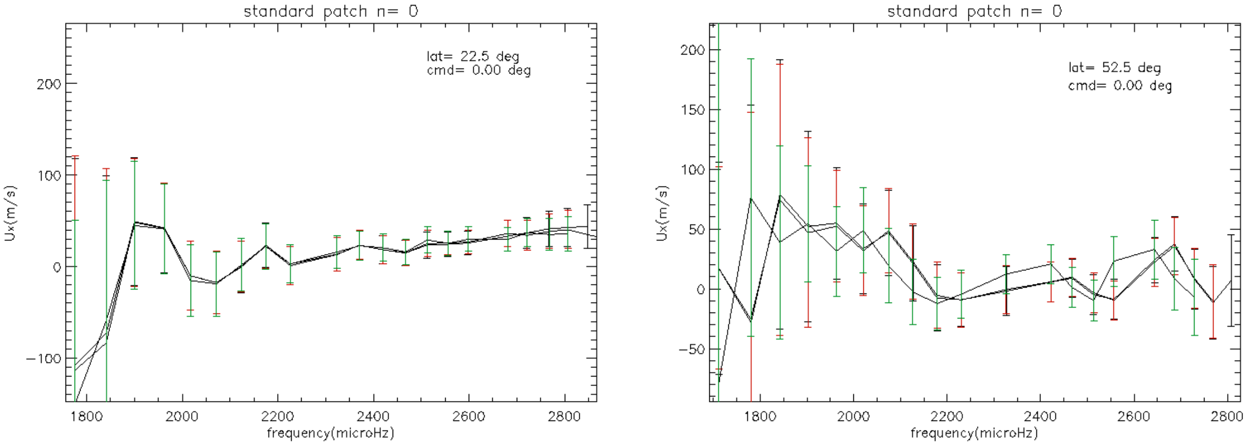

Figure 6.2: Same as figure 6.1 but for standard patches 15°/15°.

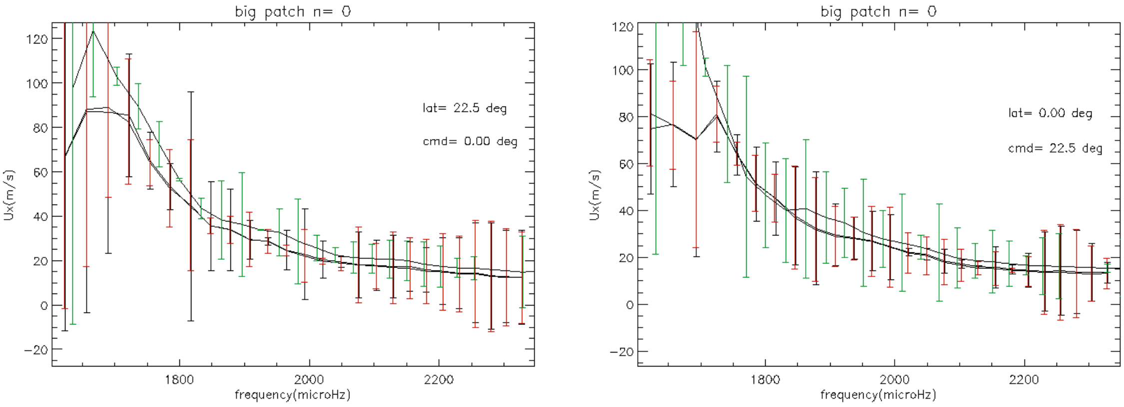

Figure 6.3: Same as figure 6.1 but for frequency shifts in the y direction.

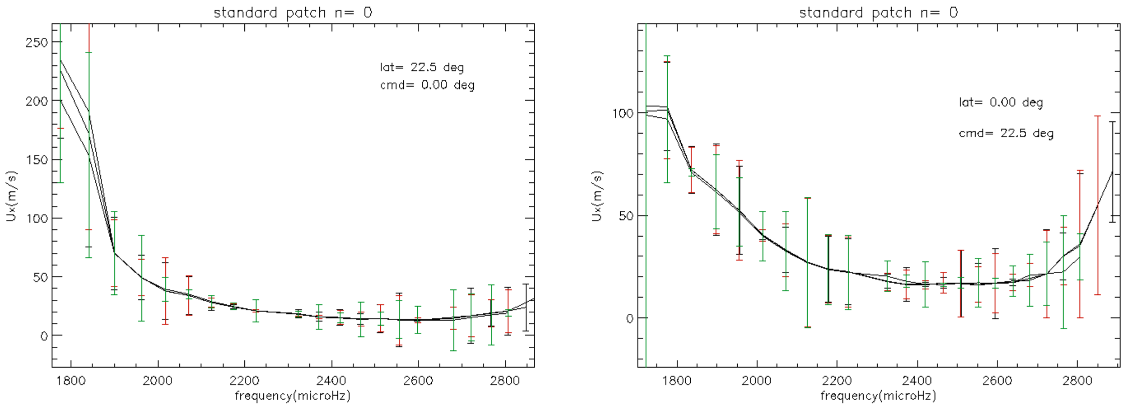

Figure 6.4: Same as figure 6.2 but for frequency shifts in y direction.

this effect, I used the oblique cylindrical projection which does in some sense an opposite work than transverse cylindrical projection. The oblique cylindrical projection maps y direction into great circles with equidistance and distorts the x direction. Contrary to the transverse cylindrical, this configuration might give more accurate results in y direction (meridional) than in x direction (zonal). The meridional circulation obtained from transverse and oblique cylindrical mappings by using the standard patches is shown in figure 6.7. The oblique cylindrical projection gives higher meridional flow, by about 2 m/s at deepest layers for high latitudes, than those inferred from the transverse cylindrical. Thus, one can conclude that the use of the transverse cylindrical projection leads to underestimated measurements of the meridional flow. The best way to infer flows would have been to use patches mapped with a transverse cylindrical and get only zonal flows and use the oblique cylindrical and get only the meridional flows. However, this is very time consuming for the data processing. Nonetheless, the Postel projection provides us with meridional flow measurements close to those obtained from the oblique cylindrical and measurements of the zonal flow close to those obtained from the transverse cylindrical. Consequently, the best choice of the map projection for ring diagram analysis seems to be the Postel projection.

6.5 Summary

In the presented study, several geometric mappings have been applied to solar images. These mappings have been chosen so that at least one of the coordinates axis is remapped onto great circles through which acoustic wave propagate, since these circles provide the shortest way between two points. By applying these mappings to two size patches (standard patches and 30° aperture patches), it turned out that the sensitivity of the flow measurements increases with increasing the probed area. The effect of the mapping is seen in the fitted frequency shifts which is obvious since they can add some distortions to the power spectrum (either by amplifying or minimizing those due to the real solar effect -underlying flows-). This leads to a difference in the inferred daily horizontal flows. The difference is still seen in the averaged flows over few days, which is obvious since the effect is an artifact related to the data processing (independant from time). From the transverse cylindrical projection, one can infer the correct measurement of the zonal flow, since this geometric configuration insures great circle mapping and preseres distances (required for the FFT) along the x axis. Hence, it could be taken as a reference evaluating the zonal flow measurements from other projections. On the hand, the oblique cylindrical projection provides a correct measurement of the flow in the y direction. From the considered projections, it appeared that the best geometric map that provides zonal (meridional) flow close to that obtained from the transverse (oblique) cylindrical projection, is the Postel projection which makes it the best candidate for the projection we are seeking.

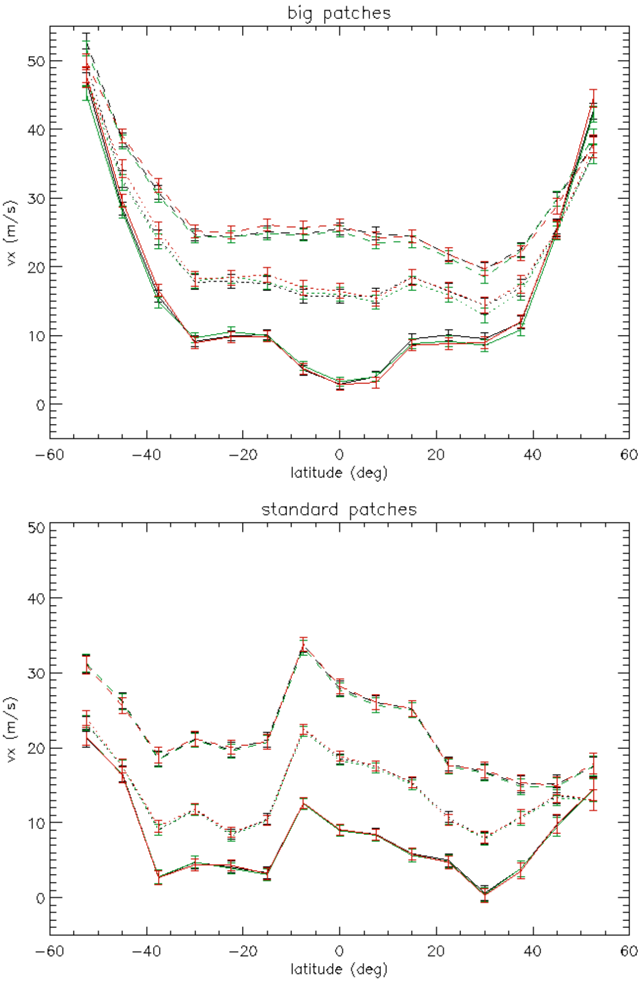

Figure 6.5: Top panel: Zonal flow averaged over 7 days as function of latitude for depths: 3Mm (full), 8Mm (dashed), 12Mm (dotted) derived from big patches (30°/30°) using different map projections : Transverse cylindrical (black), Postel (green), Gnomonic (red). Bottom panel: same as top panel but using standard patches (15°/15°).

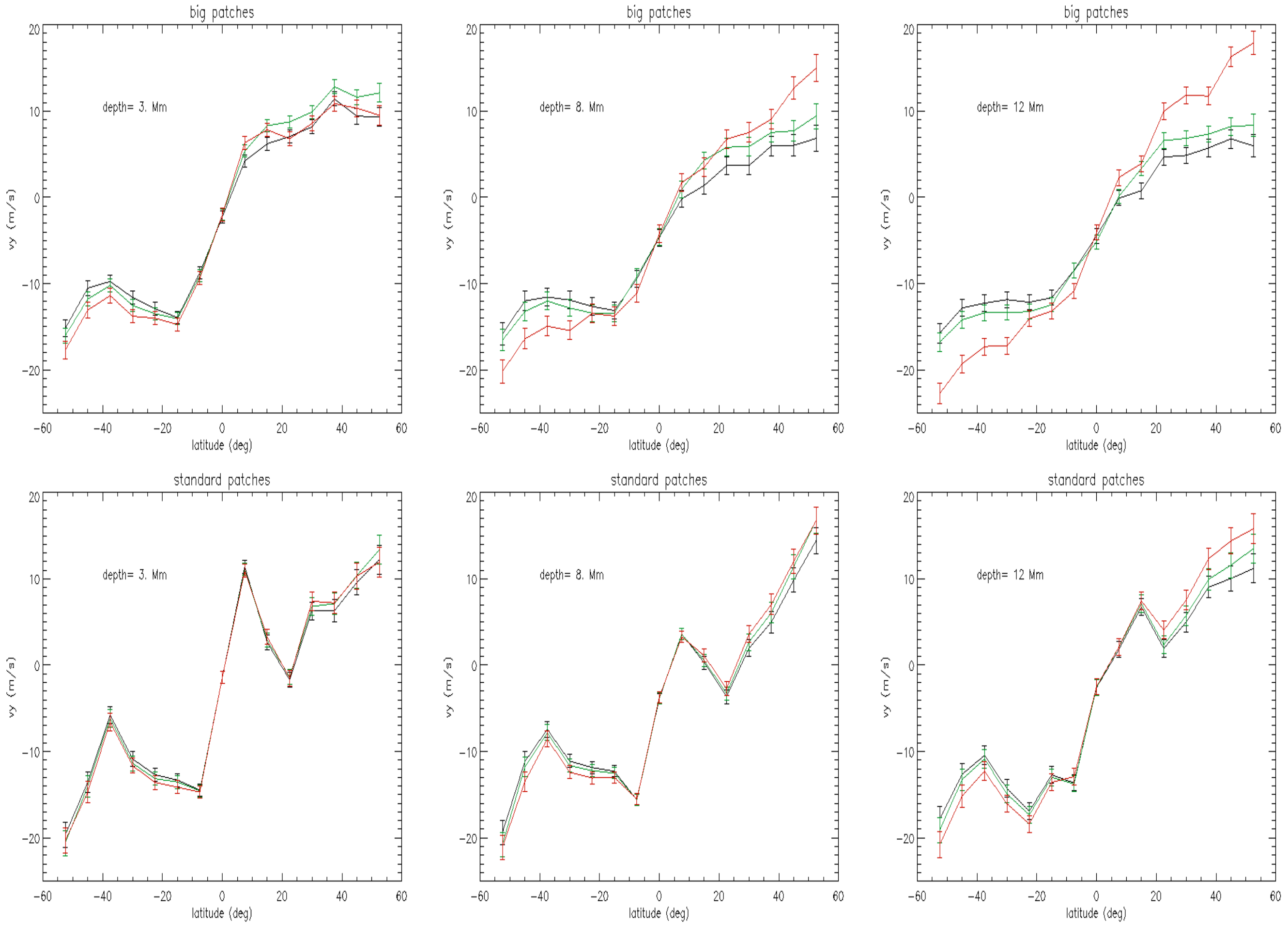

Figure 6.6: Same as figure 6.5 but for the meridional flow.

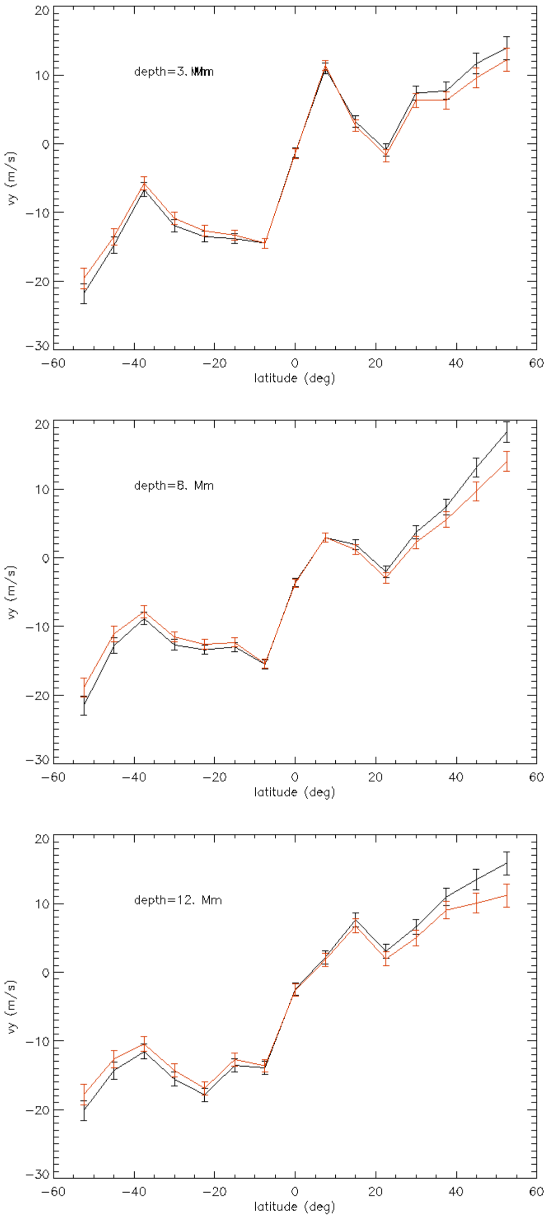

Figure 6.7: Meridional flow as a function of latitude given from transverse cylindrical projection (red) and oblique cylindrical projection for the mentioned depths from standard patches (15°/15°).

PROCEEDINGS III

TITLE

Comparison of geometrical mapping for ring diagram analysis

AUTHORS

A. Zaatri, T. Corbard, M. Roth,
Irene Gonzàlez-Hernàndez and Oskar von der Lühe

REFERENCE

Journal of Physics: Conference Series, Volume 118, Issue 1, pp. 012090 (2008)

Comparison of geometrical mapping for ring diagram analysis

Amel Zaatri [1,2], **Thierry Corbard** [2], **Markus Roth** [3], **Irene González Hernández** [4] **and Oskar von der Lühe** [1]

[1]Kiepenheuer-Institut für Sonnenphysik, Freiburg, Germany
[2]Département Cassiopée, Observatoire de la Côte d'Azur, Nice , France
[3]Max-Planck-Institute für Sonnensystemforschung, Katlenburg-Lindau, Germany
[4]National Solar Observatory, Tucson, USA

E-mail: `amel@kis.uni-freiburg.de, corbard@oca.eu, roth@mps.mpg.de, irenegh@noao.edu, ovdluhe@kis.uni-freiburg.de`

Abstract. Mapping the solar surface is a crucial step in any local helioseismology technique. Because the acoustic waves propagate along great circles at the solar surface, it has been shown that these circles need to be used in the geometrical construction of the plane grid. We study different types of projections based on great circles for the calculation of sub-surface flows from ring diagram analysis of GONG data. Azimuthal equidistant projection, transverse cylindrical projection, gnomonic projection and stereographic projection produce almost the same velocity fields with standard patch sizes ($15^\circ \times 15^\circ$). The difference between the four projections is more noticeable when larger patches ($30^\circ \times 30^\circ$) are used.

1. Introduction

Local helioseismology analysis of high resolution Dopplergrams which are projected from the spherical solar surface onto a plane requires careful projection mapping of the sphere, in order to match heliographic coordinates (latitude and longitude) as precisely as possible with Cartesian image coordinates. Care has to be taken to match the plane coordinate system with geodesics on the solar surface, as acoustic waves propagate along them. A prominent method for detecting sub-surface velocity fields is ring diagram analysis, where frequency shifts of maxima in the three-dimensional power spectra of the Doppler signal within a limited area on the solar surface are analyzed [1]. Within such an area, acoustic waves are treated as plane waves.

The local analysis requires an accurate determination of the heliographic position at each position in the Dopplergram, and solar rotation needs to be corrected for. Two projection algorithms which are based on great circles are used today. The remapping/tracking code of GONG++ ring diagram analysis is based on the transverse cylindrical projection [2], whereas in [3], ring diagram analysis of MDI data is based on the azimuthal equidistant projection, also called Postel projection. As we show in this paper, many projections based on the great circle principle can be used to map the solar surface. However, none of the existing projections is able to avoid distance distortions in the two spatial directions of the plane map.

Different patch sizes have also been used in ring diagram analysis before. Whereas the standard patch size is $15^\circ \times 15^\circ$ [4], bigger patches ($30^\circ \times 30^\circ$) have been used in order to reach deeper sub-surface layers [5]. In this work, we investigate four great circles based projections

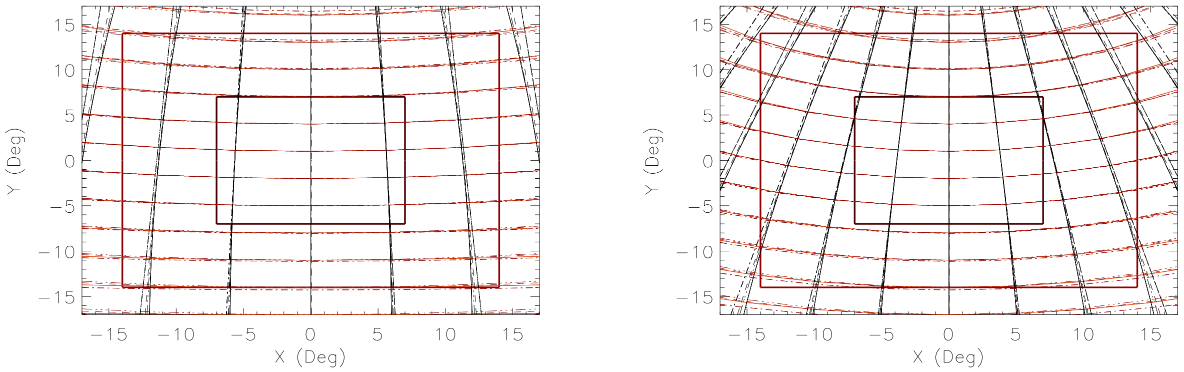

Figure 1. Geometrical maps obtained from the different projections studied here. Transverse cylindrical (full lines), Azimuthal equidistant (dotted), Stereographic (dashed), Gnomonic (dashed dotted). The left panel shows an area centered on the heliographic latitude $\theta_0 = 20°$, the right panel shows $\theta_0 = 50°$. Red lines are lines with same longitudes and black lines are the meridians. The two squares show the sizes of ring diagram analysis patches used here ($15° \times 15°$ and $30° \times 30°$).

(transverse equidistant cylindrical, azimuthal equidistant, stereographic and gnomonic) within areas of interest of various sizes. The daily velocity flows derived from each of these mappings, based on ring diagram analysis of two days of GONG++ data (02/01/2002 and 28/01/2002), are presented and compared.

2. Map projections

The most important criterion for selecting the appropriate mapping of the solar surface in ring diagram analysis is the use of great circles [6]. We describe in this section some of the projections that are generally based on great circles. The projections shown here are not the only possibilities. There are many good references on constructing geometrical maps, which are most frequently used to map the Earth; see for example [7].

All the described projections are presented for an arbitrary center of projection, defined by its heliographic latitude and longitude, (θ_0 , ϕ_0). In the case of ring diagram analysis, this point corresponds to the center of the considered patch. If the latitude of the center of projection differs from zero, the projection is called “oblique”. However, since most of the projections considered here are oblique we shall drop this term in the following to facilitate terminology.

2.1. Transverse cylindrical equidistant projection

The transverse cylindrical projection, also called Plate Carrée projection, is based on a cylinder projection surface where the central meridian is the tangent line between the cylinder and the sphere. The construction of this map can be done by rotating the original coordinate system, expressed in the heliographic latitude and longitude (θ, ϕ), such that the X axis points toward the center of the projection. In order to make the projection transverse, one needs to add a rotation which leads to inverting the roles of the equator and the central meridian. Then, the negative latitudes and the longitudes of the resulting coordinate system are taken as the X and Y Cartesian coordinates of the map. Consequently, all the great circles that are perpendicular to the central meridian at each point are mapped as horizontal lines, along which distances are preserved. However, distances along the vertical lines are not preserved except along the local central meridian. The heliographic coordinates (θ, ϕ) as function of the Cartesian coordinates of the map are derived from the transformation equations

$$\begin{aligned} \theta &= \arcsin\left(\cos X \sin\left(Y + \theta_0\right)\right), \\ \phi &= \arcsin\left(\frac{\sin X}{\cos\theta}\right) + \phi_0, \end{aligned} \tag{1}$$

The plane grids which are generated from this projection when the center of projection is located at two different latitudes are shown in figure 1. This projection, as well as any of the other projections, produces a regular grid in a restricted central area of the solar disk where heliographic and Cartesian coordinates match well.

2.2. Azimuthal equidistant projection

The azimuthal cylindrical projection, also known as Postel projection, is based on a plane projection surface where the center of the projection is the tangent point between the sphere and the plane. This map can be constructed by pointing the Z axis towards the center of the projection. Then, the latitude and longitude of the resulting coordinate system are taken as the polar coordinates r and θ of the projection grid. Consequently, all the lines passing through the center of the projection in the map are great circles and distances are preserved along them. However, neither the Y direction nor the X direction of the map represent a real distance on the sphere. The heliographic coordinates (θ, ϕ) as function of the Cartesian coordinates of the map are derived from the transformation equations

$$\begin{aligned} \theta &= \arcsin\left(\frac{Y}{r}\cos\theta_0 \sin r + \sin\theta_0 cos r\right), \\ \phi &= \arcsin\left(\frac{X}{r}\frac{\sin r}{\cos\theta}\right) + \phi_0, \end{aligned} \tag{2}$$

where $r = \sqrt{X^2 + Y^2}$. The plane grid resulting from azimuthal equidistant projection is also shown in figure 1 for two latitudes of the center point.

2.3. Gnomonic projection

The Gnomonic projection uses the same rotations as the azimuthal equidistant projection, as the center of projection is also the pole of the resulting coordinate system. The Gnomonic projection is a perspective projection that takes the image of each point of the sphere as it is seen from the center of the sphere. In this projection, every line drawn in the resulting map is a great circle. However, the distance between any two points on the map is bigger than their real distance on the sphere, because of the perspective aspect. The heliographic coordinates (θ, ϕ) as function of Cartesian coordinates are

$$\begin{aligned} \theta &= \arcsin\left(\frac{Y}{r}\cos\theta_0 \cos r_1 + \sin\theta_0 \sin r_1\right), \\ \phi &= \arcsin\left(\frac{X}{r}\frac{\cos r_1}{\cos\theta}\right) + \phi_0, \end{aligned} \tag{3}$$

where $r = \sqrt{X^2 + Y^2}$ and $r_1 = \arctan(1/r)$. The Gnomonic projection map is almost the same as the the transverse cylindrical and the azimuthal equidistant maps for regions with the size of the standard patches. But the difference between the three projections becomes noticeable when using bigger patches (see figure 1).

2.4. Stereographic projection

The Stereographic projection is constructed in the same way as the azimuthal equidistant and the gnomonic projection. Thus, the center of projection is taken at the pole of a spherical coordinate system. The stereographic projection is a perspective projection that takes the image of each point as it is seen from the opposite point of the center of projection. In this projection, any straight line through the center of projection is a great circle. The heliographic coordinates (θ, ϕ) as function of the Cartesian coordinates map are

$$\theta = \arcsin\left(\frac{Y}{r}\cos\theta_0 \sin r_1 + \sin\theta_0 \cos r_1\right), \qquad (4)$$
$$\phi = \arcsin\left(\frac{X}{r}\frac{\sin r_1}{\cos\theta}\right) + \phi_0,$$

where $r = \sqrt{X^2 + Y^2}$ and $r_1 = 2\arctan(r/2)$. It is interesting to note that r_1 tends toward r when r is small enough, which transforms the equations of the stereographic projection into those for the azimuthal equidistant projection. This similarity is clearly shown in figure 1 where the stereographic map overlays the azimuthal equidistant map, as we are treating small domains.

3. Application of the ring diagram analysis

We have applied ring diagram analysis to 3D data cubes corresponding to about 27 hours (1664 min) in time and to different field sizes. The starting point is an equidistant (X,Y) grid. A projection transformation is applied to each point of the grid, resulting in a heliographic coordinate, which in turn is used to find the corresponding position in the Doppler map by taking into account the apparent semi diameter and the solar inclination toward the Earth (B_0 angle). These positions are followed in time by compensating for the differential solar rotation. This remapping/tracking part of the technique is described in [2].

We have used all projections described above to calculate two daily flow maps at 189 positions of the solar surface, using GONG data from 02/01/2002 and 28/01/2002. The results have been obtained using a customized GONG++ ring diagram pipeline. We have applied the four projections with the standard patch size ($15° \times 15°$) and with patches which are four times bigger ($30° \times 30°$). The results are presented in figures 2 and 3.

4. Discussion and Conclusions

Figure 2 presents the velocity field for two different days and three different depths for the four studied projections using the standard ($15° \times 15°$) patch sizes. The difference between the projections are most prominent close to the limb, where the flow errors are quite large due to foreshortening. Deeper layers show the most prominent differences in the flows. However, ring diagram analysis is not very efficient at deep layers as low degree modes are not well enough identified because of the small size of the patches. Also, surface layers are suffering from bad estimations of the inversion kernels, which makes the errors significant in these layers. Moreover, most of the differences between the flows that are calculated using the four considered projections are due to both the accuracy of the technique and the observations. This result has been expected as all the projections result in nearly the same geometrical map within an area of the size of the standard patches (see figure 1), and are all based on great circles.

Figure 3 shows the velocity field for the two days and the three depths for the four studied projections when using the larger ($30° \times 30°$) patch sizes. In this case, the differences between the projections are more significant than those for the standard patch size. However, the results are smoother because the treated area is bigger. The differences at the limb, the surface and the deep layers are mainly due to the same errors, as mentioned above for the standard patches.

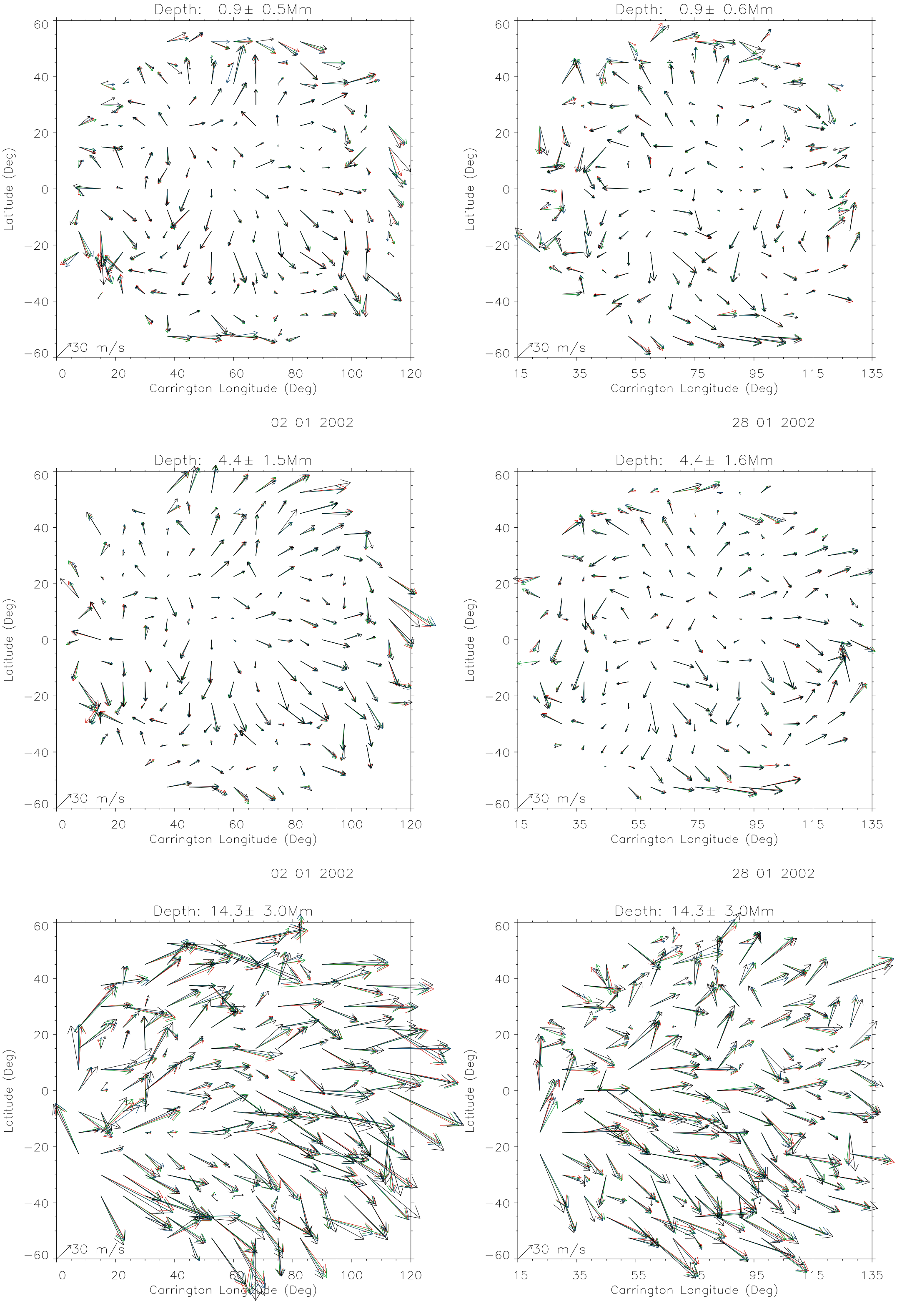

Figure 2. Daily flow maps constructed for two different days and three different depths by ring diagram analysis of 15° × 15° patches. The different colors correspond to the following mappings: transverse equidistant cylindrical (red), azimuthal equidistant and stereographic (green and blue, overlayed), gnomonic (black).

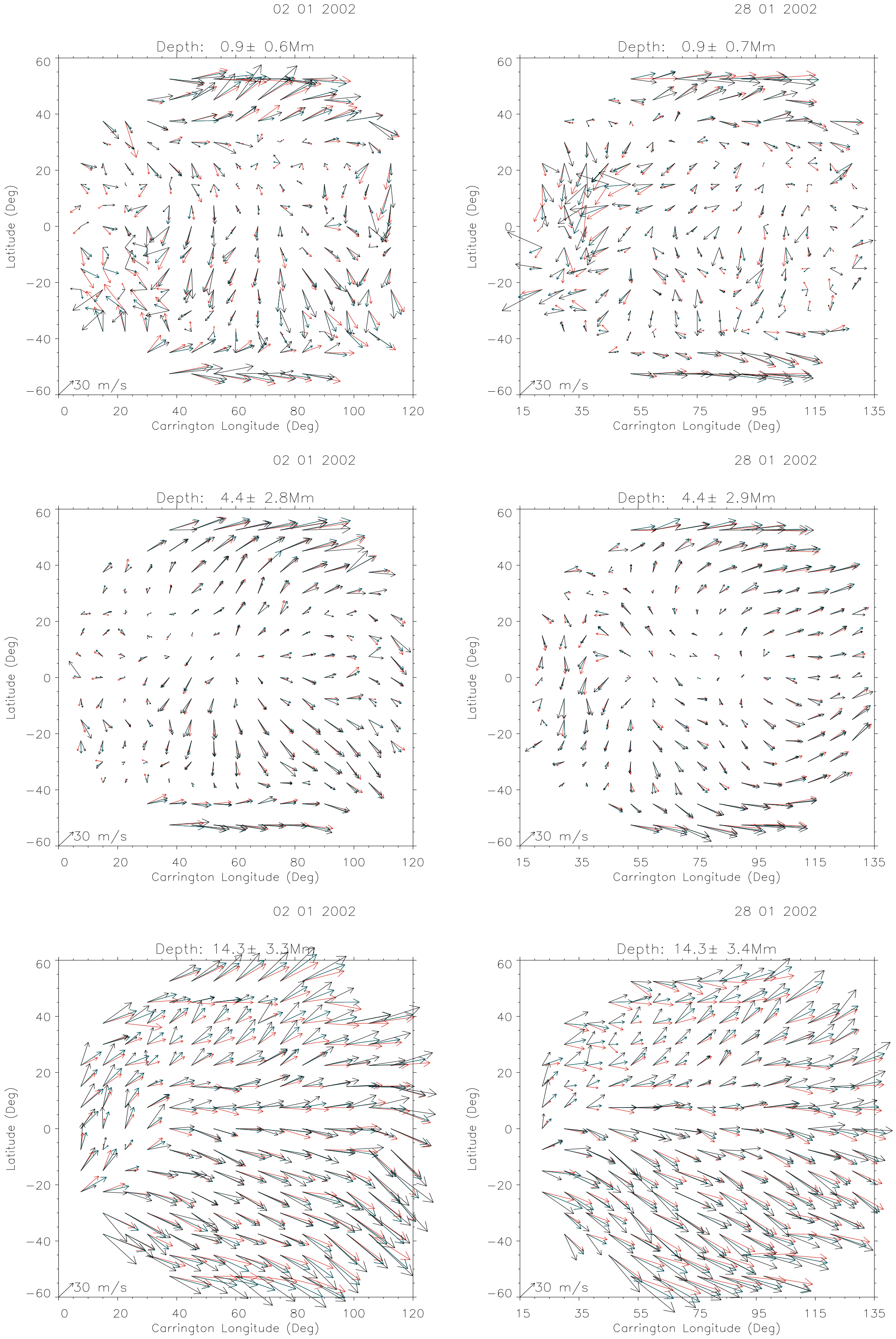

Figure 3. Same as figure 2 for 30° × 30° patches.

Moreover, the deviations observed with big patches may be due to the fact that the ring diagram technique uses a plane wave approximation, which is only valid for areas of limited size. In addition to these technical errors, the gnomonic projection seems to deviate most significantly in comparison to the other projections. This could be due to the fact that there is a stronger difference of this map compared to the others when the big patch size is considered (see figure 1). Indeed, the gnomonic projection produces relative distance distortions in the two directions as large as 6.75% in the limit of $30^\circ \times 30^\circ$ patches, whereas the maximum of the relative distortion for small patches is about 1.73%.

As a conclusion, the azimuthal equidistant, the cylindrical transverse, the stereographic and the gnomonic projections produce very similar results for the horizontal flows when applied to map areas with the standard size of ring diagram analysis patches. A bigger area results in more prominent differences, especially for the gnomonic projection.

References

[1] Hill F., 1988, *ApJ*, 339, 996
[2] Cobard T., Toner C., Hill F., Hanna K. D., Haber D. A., Hindman B. W., Bogard R. S., 2003, in SOHO 12 / GONG+ 2002. Local and global helioseismology: the Present and Futur, ASP 517, p. 255
[3] Bogart R. S., Sa L. A. D., Duvall T. L., Haber D. A., Toomre J., Hill F., 1995, Proc. Fourth SOHO Workshop: Helioseismology, ESA SP- -376, Vol. 2, p.147
[4] Haber, D.A., Hindman, B.W., Toomre, J., Bogart, R.S., Larsen, R.M. and Hill, F. 2002, *ApJ*, 570, 255.
[5] Gonzalez Hernandez I., Komm, R., Hill, F., Howe, R., Corbard, T., Haber, D.A., 2006, Astrophys. J 638, 576
[6] Haber D., Toomre J., Hill F., Gough D., 1995, in GONG'94: Helio- and Asteroseismologyfrom the Earth and space, ASP 76, P. 272
[7] Snyder J.P., Yang Q. H., Tobler W. R., 2000, Technology industrial arts, P. 367

Part IV

Long term variations of the sub-photospheric flows

Chapter 7

Long term variations of horizontal flows

> *I always had to wait for time to finish writing down the epilogue of what really matters.*
>
> T. Maref

Abstract

Ring diagram analysis provides us with daily flow maps at different depths. Nowadays, computational facilities allow us to process a big amount of data in a relatively short time. Hence, the study of the temporal variation of the horizontal sub-surface flows can be performed from a wide set of daily flow maps. The synoptic view in latitude and longitude for different depths is a very practical way to study the behavior of the flows as resolved in the sub-photospheric layers, except for the very high latitude regions. From synoptic maps of horizontal flows, I studied their north-south variation and their relation to the magnetic activity in time. Nonetheless, many artifacts in the long term data need to be understood in order to correctly interpret the behavior of the flows in time. One of those is the so called B_0 *angle.*

								L_0							
1st day	307.5	315	322.5	330	337.5	345	352.5	0	7.5	15	22.5	30	37.5	45	52.5
2nd day	292.5	300	307.5	315	322.5	330	337.5	345	352.5	0	7.5	15	22.5	30	37.5
3rd day	277.5	285	292.5	300	307.5	315	322.5	330	337.5	345	352.5	0	7.5	15	22.5
4th day	262.5	270	277.5	285	292.5	300	307.5	315	322.5	330	337.5	345	352.5	0	7.5
5st day	247.5	255	262.5	270	277.5	285	292.5	300	307.5	315	322.5	330	337.5	345	352.5
6nd day	232.5	240	247.5	255	262.5	270	277.5	285	292.5	300	307.5	315	322.5	330	337.5
7rd day	217.5	225	232.5	240	247.5	255	262.5	270	277.5	285	292.5	300	307.5	315	322.5
8th day	202.5	210	217.5	225	232.5	240	247.5	255	262.5	270	277.5	285	292.5	300	307.5

Table 7.1: Carrington longitudes of the equator patches of the dense-pack matrix shown on eight consecutive days, where the Carrington rotation of the central meridian of the first day is $L_0 = 0$. One Carrington longitude multiple of 15 (one not multiple of 15) is highlighted in green (red) in order to show the number of its appearance in the dense-pack matrix.

7.1 Synoptic horizontal flow maps

A synoptic view of horizontal flows in an extent of one Carrington rotation displaying flows as a function of Carrington longitude [0°,360°] and latitude [$-52.5°$,52.5°] at several depths, is a very instructive way to explore their temporal and spatial variations. In order to construct a synoptic horizontal flow map[1] one needs daily flow maps of about 32 GONG days[2]. Since a patch with the same Carrington rotation appears several times on the disk (more precisely, in the dense-pack matrix), one needs to locate this patch in the consecutive daily flow maps and average the corresponding flows. Depending on the position of the patch in the dense-pack matrix, it can be often seen differently for a sequence of daily flow maps. An example of such a case is given in table 7.1 where all the patches on the equator are entered with their Carrington longitude. Since L_0 is always taken as multiples of 15° in the dense-pack matrix, it appears that patches with Carrington longitudes multiples of 15° are seen 7 times before they leave the dense-pack matrix whereas Carrington longitudes that are not multi-

---

[1] Since Carrington longitude of the solar disk is decreasing with time, synoptic flows have to be seen from right to left.

[2] Since a Carrington rotation starts where $L_0 = 0$, the last patches of the Carrington rotation need to be observed additionally in the first daily flow maps of the following Carrington rotation in order to be correctly averaged. Hence, a construction of a synoptic flow map needs to include daily flow maps of more than 1 Carringon rotation.

ples of 15° will appear 8 times. In this way and since the dense-pack matrix reduces the number of patches in longitude with increasing latitude, one can also see that patches at ±52.5° of latitude will appear either 3 or 4 times depending on their Carrington longitudes. While averaging flows with the same Carrington longitude, it is important to take into account the fact that patches get more and more resolved when they approach the central meridian distance. This can be done by considering a cosine to the fourth function of the central meridian distance in order to reduce the weighting of flows inferred from patches located close to the solar limb (Komm *et al.*, 2004).

Another interesting way to see the synoptic behavior of these flows is to subtract a large scale component of the meridional and the zonal flow which mainly correspond to the quiet Sun in order to be able to focus on flows around and below active regions. I construct synoptic residual flow maps by following Komm *et al.* (2004) where the average of the meridional flow is considered to be approximately given by the derivatives in latitude of the first two even Legendre polynomials. The large scale component of the zonal flow is removed by subtracting a low-order polynomial fit in latitude of the longitudinal average. I plotted in figures 7.1, 7.2, 7.3 a synoptic horizontal flow map and its corresponding residual flow map for Carrington rotation 1997, where the synoptic magnetic map of the same time is shown in the background. The longitudinal component is seen to increase with depth, which is reflecting a mainly negative rotational gradient in the sub-surface layers. The behavior of this gradient is studied in more detail in chapter 8. The displayed Carrington rotation corresponds to the end of 2002, which is part of the high activity period associated to the declining phase of solar cycle 23, and hence, several active regions are seen in the synoptic magnetic map. In the residual maps, flows appear to converge towards active regions. These residual maps will not be part of the presented study, however, interesting long-term investigations related to these maps have been handled so far to closely explore the relationship between the sub-surface flows and active regions (e.g. Komm *et al.*, 2008, 2009).

The shown synoptic flow maps and residual maps have been produced using an ISL package that I wrote for the specific case of the GONG daily horizontal velocity measurements produced for the dense-pack matrix. The package is available online on the HElio- and ASteroseismology European network (HELAS) local helioseismology website and a brief readme file for the installation and the utilization of this package is given in Appendix B. This package also allows to obtain synoptic maps of the flow divergence and vorticity and the vertical velocity. In appendix (see B), I show results of these fluid descriptors and briefly discuss the change in the density profile used to get vertical velocity from the divergence of the flow assuming mass conservation.

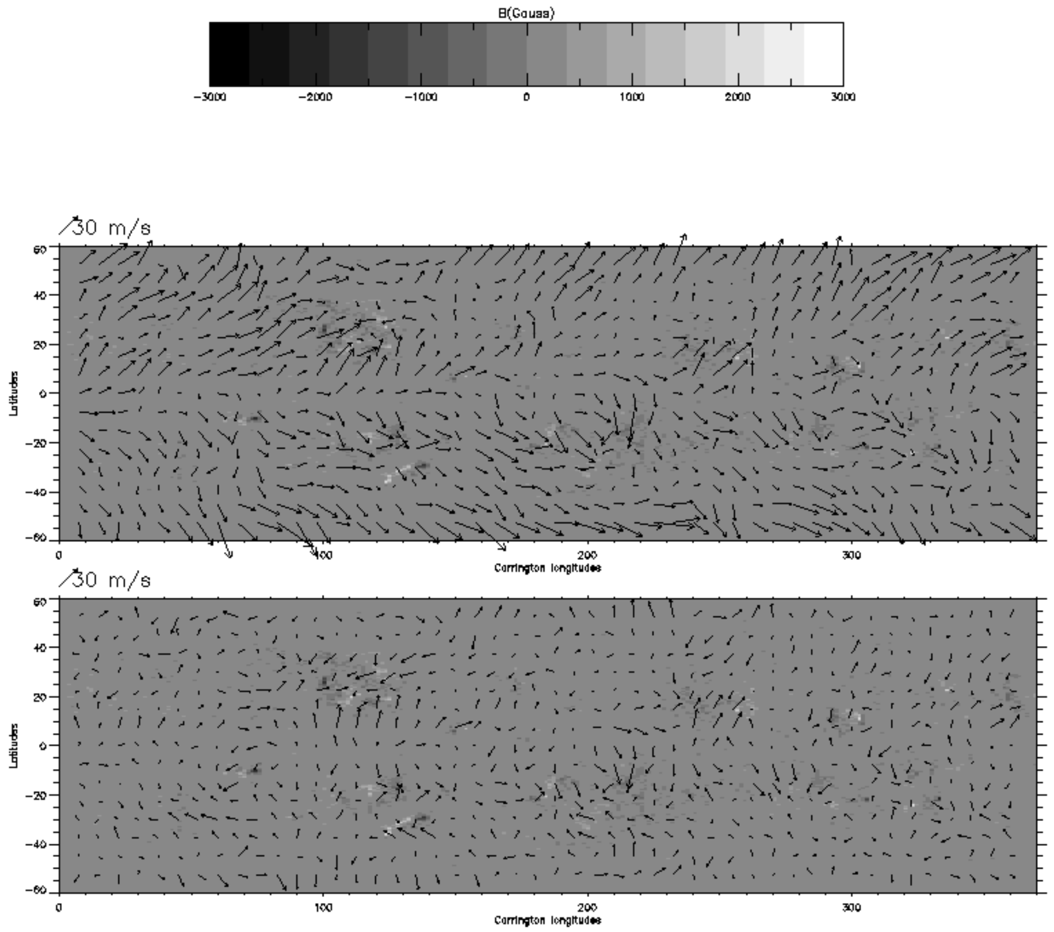

Figure 7.1: Upper panel: Synoptic flow map of Carrington rotation 1997 taken at a depth of 4 Mm. Lower panel: Same as upper panel but for flow residuals.

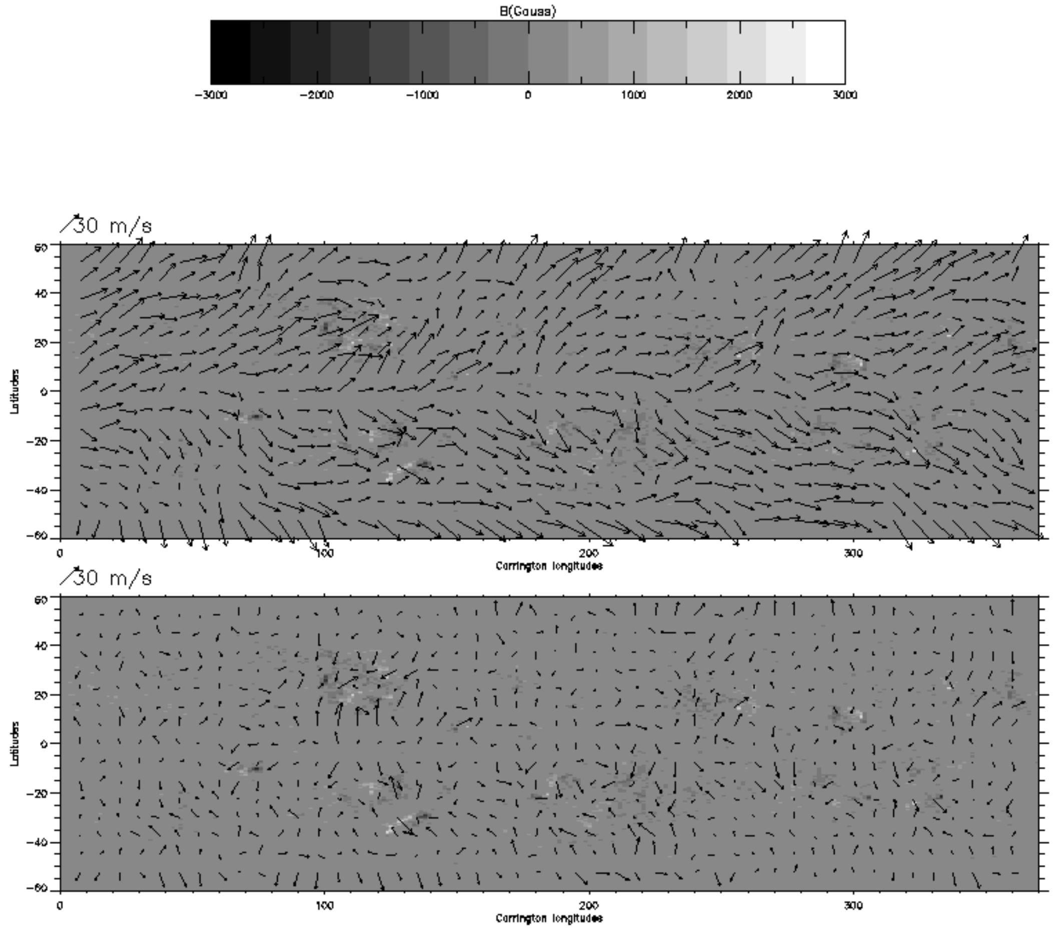

Figure 7.2: Same as figure 7.1 but taken at a depth of 8 Mm.

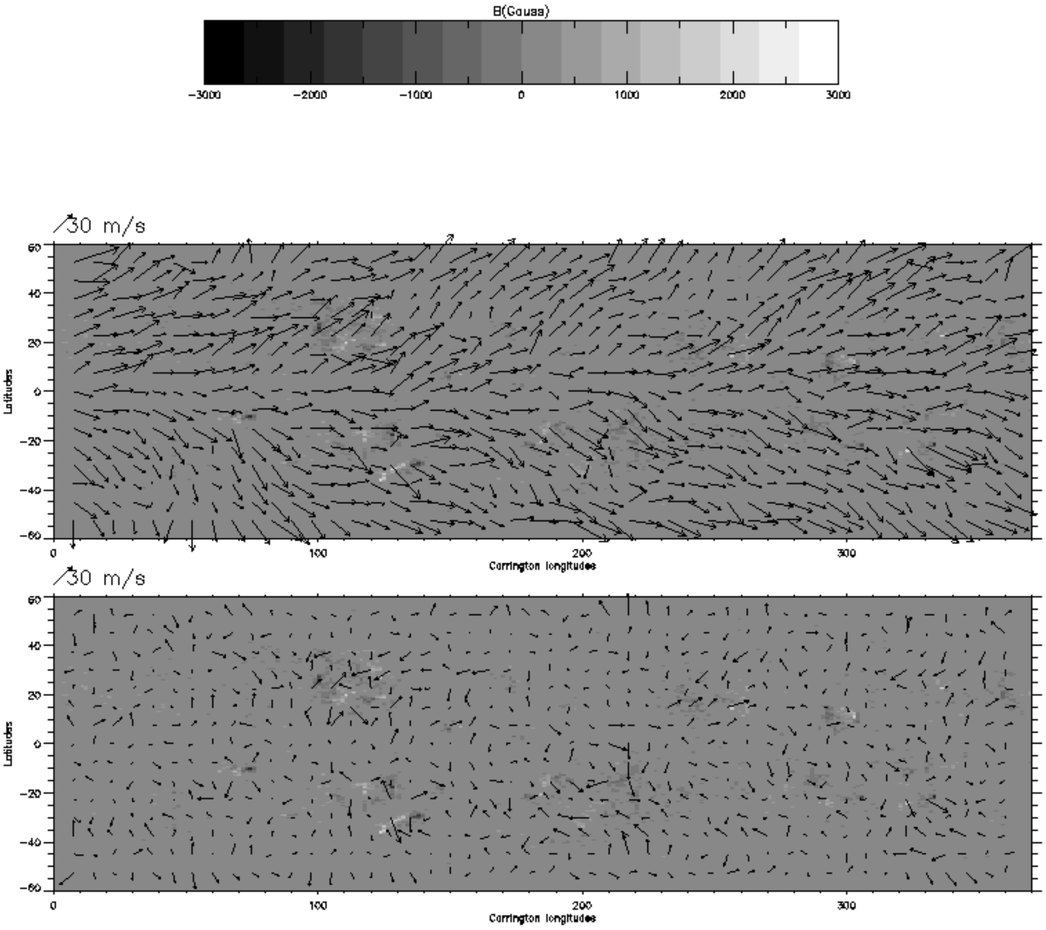

Figure 7.3: Same as figure 7.1 but taken at a depth of 12 Mm.

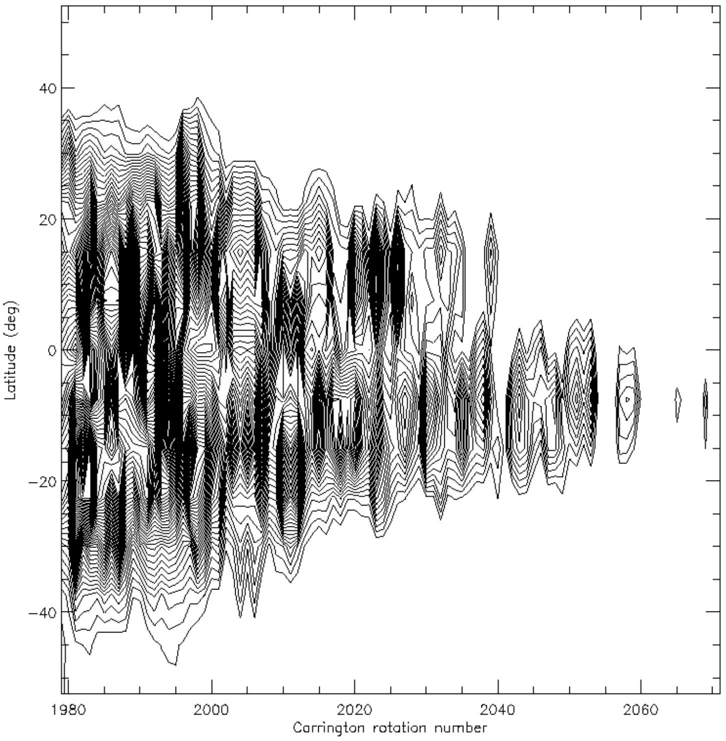

Figure 7.4: Contour plot in time (Carrington rotation number) and latitude (degree) of the unsigned magnetic field in Gauss binned in 15° × 15° spatial extents by considering the dense-pack mosaic.Contours are given for values extending from 10 G to 100 G. The plot shows a butterfly like shape with a more active southern hemisphere than the northern hemisphere. At maximum activity, the southern magnetic activity was extended over a wider latitudinal range than the northern activity. Also, at minimum of the cycle, the activity was predominantly southern.

7.2 Long term variation of the horizontal flows

Ring diagram analysis of the continuous GONG data (July 2001 – July 2008) provides us with a set of velocity flows down to 16 Mm defined at all Carrington longitudes and latitudes up to ±52.5° for the two hemispheres, covering almost the whole declining phase of solar cycle 23. This is an unprecedented set of data allowing to study the behavior of the flows in the time-scale of a solar cycle. Hence, these flows can be confronted to the observed magnetic activity

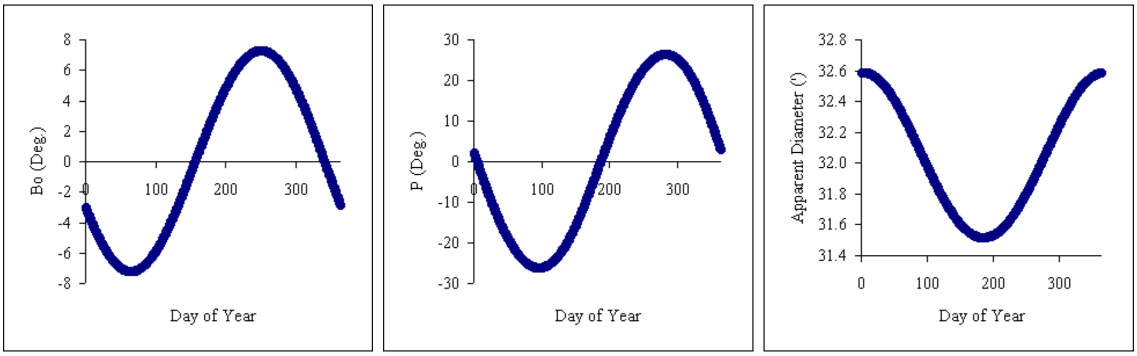

Figure 7.5: Variation of the B_0 angle, the P angle and the apparent Semi diameter over the year[1].

in the attempt to understand the relationship between the dynamics of the Sun, which we know is the source of all magnetic fields and the origin of the solar cycle. In this part, I will summarize my results on the investigation of long term variations of the zonal flow as well as rotation and the meridional flow. One of the most important aspects that attracted my attention is the investigation of the North-South asymmetries of the flows which turned out to follow that of the magnetic activity with a more active southern hemisphere during the studied period (see figure 7.4). Another issue that has imposed itself during the analysis of long-term variations are systematic effects in the measured flows. Indeed, we are analyzing images that are a plane projection of the visible face of the spherical sun. Moreover, we observe these images from a moving point (earth, satellite) with an elliptical orbit and a changing rotation axis over the year. All these effects result in artifacts in the observed image and have to be filtered out in order to get real solar variations. The variation over time of some important sources of systematic errors such as the B_0 angle, the apparent semi-diameter, and the P angle are given in figure 7.5. For instance, errors on the determination of the P angle caused the appearance of a strong circular flow on the solar surface, the so called washing machine effect, in the daily flow measurements, this systematic effect has been found with the GONG data that I am using in this thesis (González-Hernández, 2003). The other systematic effects will be discussed in the following sections.

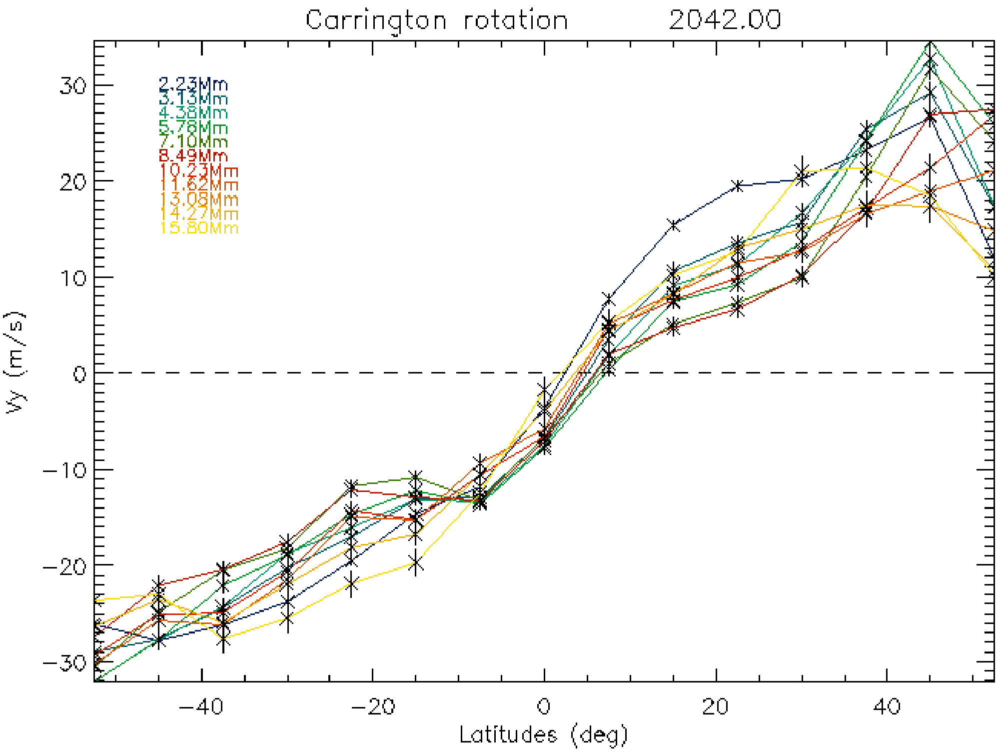

Figure 7.6: Meridional flow averaged over one Carrington rotation (CR= 2024) as a function of latitude at several depth. Color coding of the depth is given inside the panel. The dashed line shows the zero level.

7.2.1 Meridional circulation

The long term variation of the meridional flow has been studied first for an extent of 44 Carrington rotations (CR: 1979 – 2022, July 2001 – October 2004)[1] which corresponds to the maximum activity period of the declining phase of solar cycle 23. Results from this set of data are given in the Article II at the end of the chapter. Moreover, since we have now more coverage of the declining phase of solar cycle 23 from GONG, I have extended this study to a period of 93 Carringon rotations (CR: 1979 – 2071 , July 2001 – July 2008). This period covers about 65% of a typical 11 years cycle, however, solar cycle 23 has got a long solar minimum extending over more than 11 years. In order to see the behavior of the flows at maximum and minimum activity, I subdivided this period to two main periods. The first period, to which I will refer to as a maximum activity period is roughly that corresponding to the period described in Article II (CR: 1979 – 2024) and the second period will be the minimum activity period (CR: 2025 – 2071). Even though, the second period does not only include the minimum cycle period, it covers most of it where the international sunspot number did not extend 10 on average. The distribution of magnetic field in latitude during these two periods is shown in figure 7.4. In the following, I will summarize the most prominent behaviors of the meridional flow during these two periods.

Overall behavior of the meridional circulation in latitude and depth

Before starting to describe the behavior of the meridional flow for a period of few years, it is worth starting to see its common behavior in an extent of one Carrington rotation only. This is given in figure 7.6 for Carrington rotation 2042. The meridional circulation is clearly seen to be poleward in both hemispheres, it mostly vanishes at the equator and reaches its maximum values at the highest latitudes which does not exceed 30 m/s. A slight variation of a few m/s is seen between the surface and the deepest layers. It is also seen that the variation of the flow is not linear in latitude but reveals little bumps at around ±20°. These

---

[1] The start and end dates of each Carrington rotation can be found at: http://soi.stanford.edu/magnetic/cr_table.html

bumps appear to be more pronounced for periods with high activity. González Hernández *et al.* (2008) reported a study on the nature of these bumps suggesting that they might be related to the magnetic activity. Their analysis consisted on subtracting areas containg active regions and averaging the flows only for the residual quiet Sun regions. They found out that even with the most drastic subtraction of the magnetic regions, bumps still persist in the averaged meridional flow and came out with the supposition of the existence of a global pattern or longitudinally-located organized flows.

B_0-angle effect in the temporal variation of the meridional flow

The variation of the meridional flow over seven years (93 CR) of the declining phase of solar cycle 23 is given for selected depths and latitudes in figure 7.7 for the northern and southern hemispheres. The most prominent behavior of the meridional flow is probably the one year periodicity at high latitudes close to the surface. We found that this periodicity is well correlated with the variation of the solar inclination toward the Earth (B_0 angle) which is also shown in the same figure at the top panels and a linear fit of the flows with B_0 is given in each panel, showing the high correlation of the one year periodicity of the flows with the B_0 annual variation. After removing the B_0 angle effect by subtracting the fit of a linear regression between the meridional flow and the B_0-angle variation, the one-year periodicity has disappeared as shown in figure 5 of article II for the first maximum period. Nonetheless, for this period, the correlation between the B_0-angle and the meridional flow is also shown to be above significance level at low to mid- latitudes in a wide depth range (see figure 7.8). Surprisingly, the correlation between B_0 and the meridional flow at low to mid-latitudes completely disappears in the minimum period as it is shown in figure 7.9. This supposes that the correlation between the yearly signal and the flows at these latitudes is not due to a systematic effect of the B_0-angle but might be a real variation of the meridional flow at this period, most likely related to the magnetic activity. This might endorse González Hernández *et al.* (2008) conjecture on the existence of a longitudinal dependence of the meridional flow which might be related to the active longitudes that are well known preferred longitudes for the appearance of active regions.

Also seen is a sign reversal of the meridional flow at high latitudes of the shallowest layers (see figure 1, panel [52.5°,0.6 Mm]) suggesting the existence of a counter cell that persists after correcting for the systematic effect due to B_0-angle variation in time. It is hard to tell whether this counter cell is a real effect or whether it is due to another neglected systematic effect. Beckers (2007) criticized our way of removing the B_0-angle effect from the data, endorsing the fact that this systematic effect has to be combined with the foreshortening effect. His correction led to the removal of the counter flow close to the surface at high latitudes.

We have also studied the correlation between the meridional flow over time and the annual variation of the semi-diameter which is out of phase with the B_0-angle for four Carrington rotations. The sidereal-synodic correction also changes with time and might affect systematically the measurements, however, since it is in phase with the variation of the semi diameter, it was sufficient to use only one of them. By repeating the same correlation study as the one with the B_0 angle, we show that the semi-diameter does not show significant effects on the temporal variation of the meridional flow.

Acceleration of the meridional flow

Another behavior of the meridional flow mentioned from its temporal variation in figure 7.7 is the acceleration of the flow that appears in mid- to high latitudes (see for instance the panel [37.5°,2 Mm] of figure 7.7). This acceleration does not go until the end of the studied period but rather vanishes at the end of the minimum activity period where the meridional flow stabilizes its amplitudes to the highest reached speed of more than 20 m/s poleward. To get a precise picture of the variation of this acceleration with depth and latitude, I show it for the maximum activity period in figure 7.10 and for the minimum activity period in figure 7.11. The meridional acceleration at maximum activity period reaches its strongest value mostly at latitudes higher than 20° north and south and appears to be higher in the southern hemisphere where the whole range of latitudes is subject to this acceleration than in the northern hemisphere. This strong acceleration is also limited in depth. On the other hand, the meridional flow shows a deceleration with time at latitudes lower than 20° in both hemispheres where a strong deceleration of the flow close to the surface is seen in the northern hemisphere. At low activity period, a deceleration of the meridional flow in both hemispheres is clearly seen at high latitudes whereas the acceleration becomes concentrated at latitudes around 30° north and south which usually are the locations where the first sunspots of a solar cycle start to appear. In resumé, the meridional flow shows a fast migration towards the pole at maximum activity and slow migration towards the pole at minimum activity which might be a long term characteristic of the solar dynamo.

North-south asymmetry of the meridional flow

The subsurface meridional flow down to 16 Mm is not symmetric about the equator and its north-south asymmetry varies with activity. Figures 7.12 and 7.13 show the difference between poleward northern and unsigned southern meridional flows at dense-pack latitudes for the minimum and maximum activity periods. During the minimum activity period, the poleward southern meridional flow is stronger than the northern flow at all latitudes and depths, except around latitude 20° close to the surface. This north-south asymmetry increases in the first 5 Mm below the surface whereas deeper layers show a weak north-south asymmetry variation except at the highest latitudes. The predominant southern meridional flow is in concordance with the strong excess of the magnetic field at mid to low latitudes in the southern hemisphere (see figure 7.4). The maximum activity period shows a varying north-south predominance of the meridional flow with latitude and depth. At latitudes poleward of 40°, the meridional flow is stronger in the northern hemisphere at shallower depths and larger in the southern one at greater depths. At latitudes equatorward of 25°, the poleward meridional flow has a larger amplitude in the southern hemisphere except close to the surface as shown at depth 0.6 Mm in figure 9 of article II. These low latitudes with the largest excess of poleward flow in the southern hemisphere also coincide with those of the largest excess of magnetic flux in the southern hemisphere (see figure 9 of article II).

7.2.2 Zonal flows and rotation

The zonal flow is the residual of the rotation after removing a fixed amount of the east-west flow by tracking the dense-pack patches at different latitudes. Figure 7.14 shows the averaged sub-photospheric zonal flow over one Carrington rotation. The east-west residual flow increases with depth reflecting a negative rotational gradient below the surface. At high latitudes, this gradient decreases considerably and vanishes when extrapolating to higher latitudes, which would also suppose a sign reversal of the gradient. This overall behavior of the rotational radial gradient is presented in detail through a long-term study of 7 years of GONG data in chapter 8. Also where figure 7.14 shows a clear north-south asymmetry, were the zonal flow at symmetric latitudes about the equator is southern dominant. These behaviors shown over one Carrington rotation average of the zonal flow last for the whole declining phase of solar cycle 23 and are shown for the first half of this period in figures 6 and 11. The search for systematic errors on the zonal flow measurements through a correlation study between the B_0-angle (the semi-diameter) and the temporal variation of the zonal flow has shown that the flow is weakly affected by the B_0 annual variation (see the correlation coefficients in figure 3 of article II).

Regarding the well known difference between the quiet Sun rotation and the active regions rotation - active regions rotating faster than the quiet Sun -, I carried out a study on the comparison between the rotation recovered from adding the tracking coefficients to the zonal flow at a given latitude, and bright coronal structures that are the most profuse features of the corona and are observed up to significantly high latitudes (compared to sunspots, for instance) and can still be observed at low activity periods of the cycle. These features are tracked in the SOHO Extreme Ultraviolet Imaging Telescope (EIT) images in order to measure the rotation of the corona. Results from this study are given in the following paragraph.

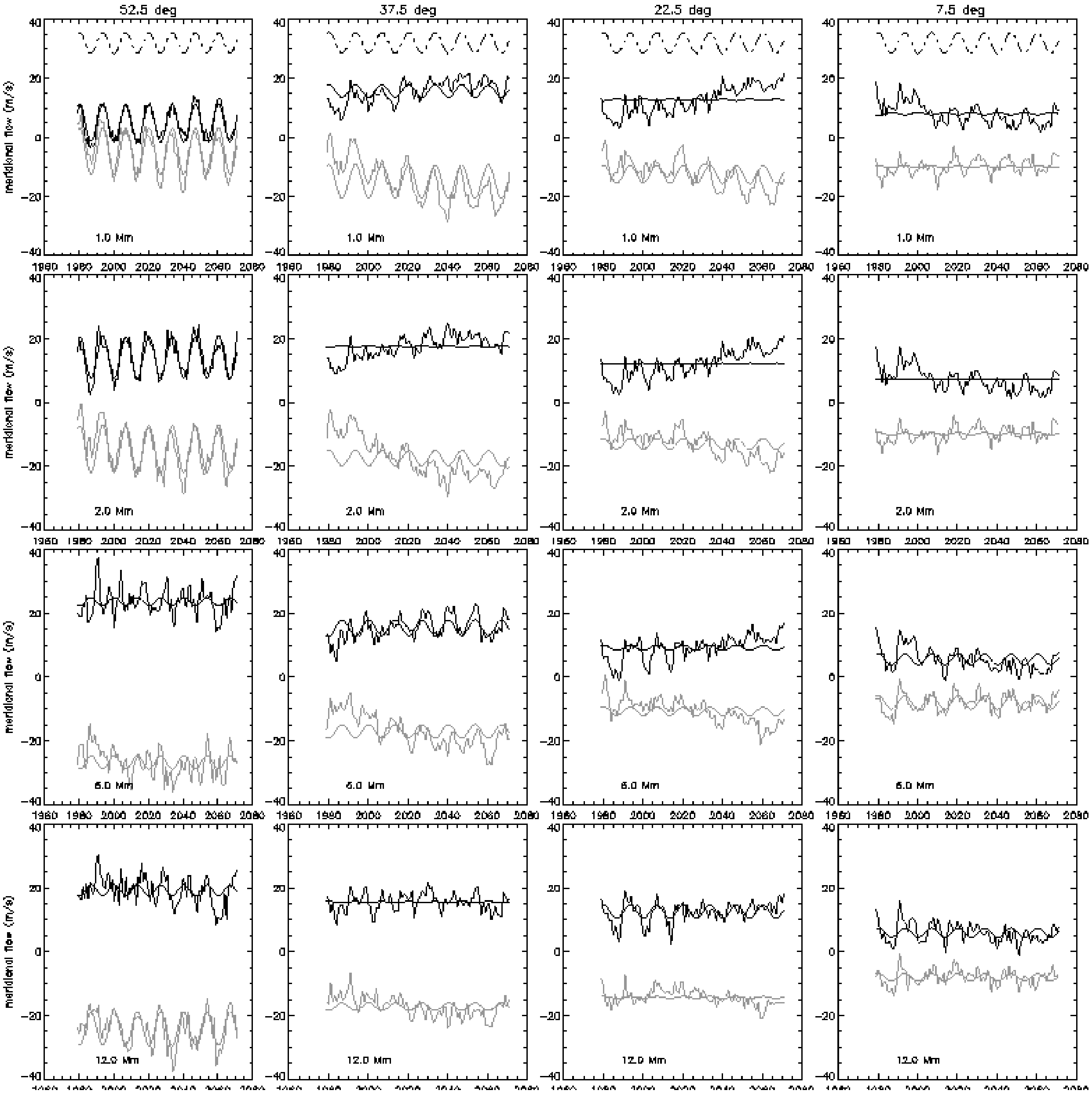

Figure 7.7: averaged meridional flow over longitude as a function of Carrington rotation number (CR: 1979 – 2071, July 2001 – July 2008) for a given latitude and depth in the northern (black) and southern hemisphere (grey). From left to right 52.5°, 37.5°, 22.5°, 7.5°, and from top to bottom 1 Mm, 2 Mm, 6 Mm, 12 Mm. The B_0-angle variation (in degree) is indicated as dot-dashed line in the top row (shifted by 30 m/s in the y direction). Thin solid lines represent linear fits of the B_0 -angle to the flows. Positive (negative) values indicate flows to the North (South). The yearly periodicity of the flow at high latitudes (first left panel) is well correlated with the B_0-angle. The acceleration of the flows appears to be well pronounced for instance in the panel [37.5°,2 Mm] where the meridional circulation reaches its maximum at minimum cycle and keeps this high value for the rest of the studied period.

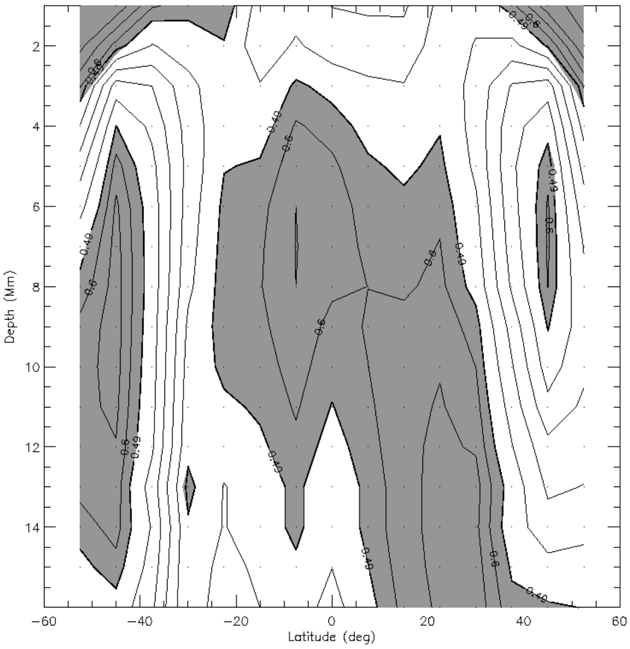

Figure 7.8: Correlation coefficient between the annual variation of the B_0-angle and the temporal variation of the meridional flow for the maximum activity period (CR: 1979 – 2024) as a function of depth and latitude. The grey areas indicate values greater than the 99.9% significance level represented by thick solid contour lines (of 0.49). Solid (dashed) contour lines indicate positive (negative) correlations (0.1, 0.3, 0.6, 0.7, 0.8, 0.9).

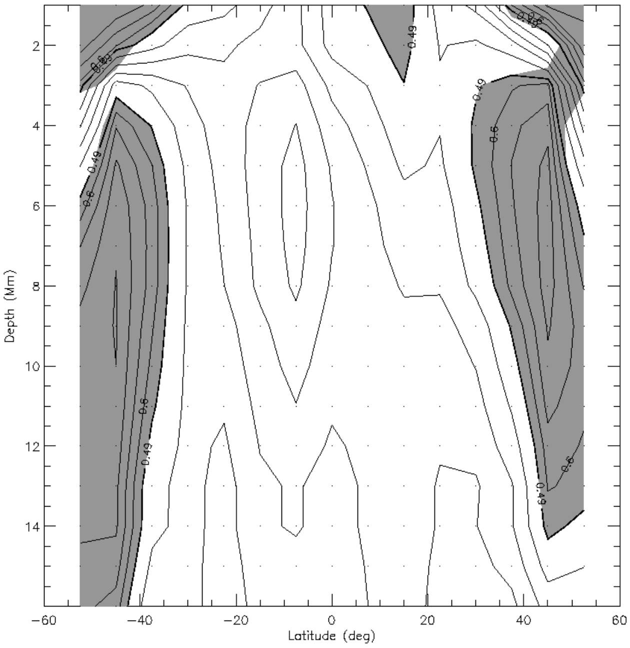

Figure 7.9: Same as figure 7.8 but for the minimum period (CR: 2025 – 2071).

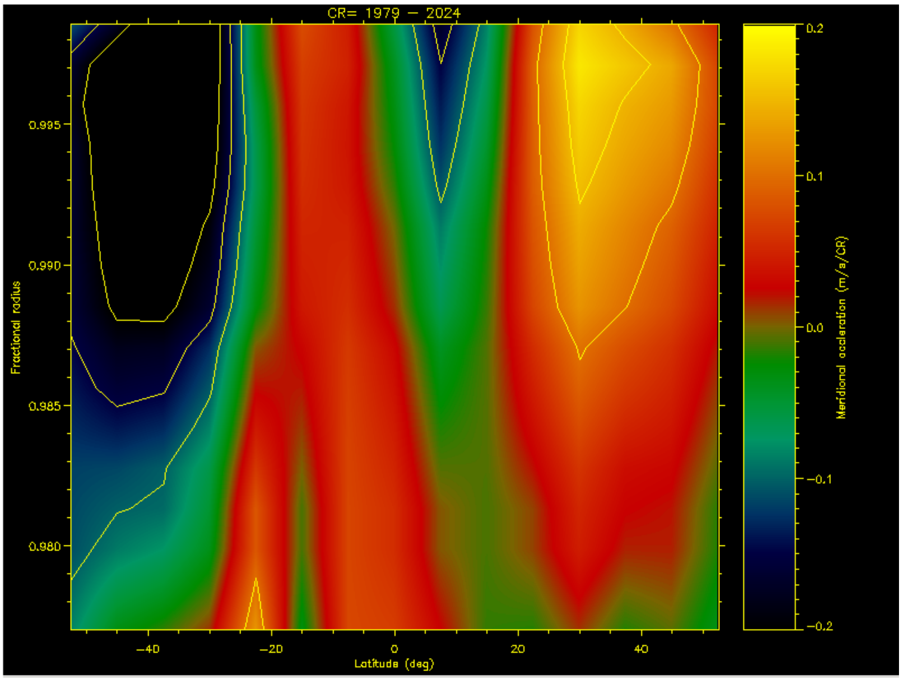

Figure 7.10: Acceleration of the meridional flow in m/s per Carrigton rotation during the maximum activity period (CR: 1979 – 2024) a function of latitude and depth. Contours are given for acceleration -0.2 m/s/CR, -0.15 m/s/CR, 0.15 m/s/CR, 0.20 m/s/CR. The negative (positive) acceleration in the southern (northern) hemispheres indicates an increasing velocity with time. The positive (negative) acceleration in the southern (northern) hemispheres indicates a decreasing flow with time.

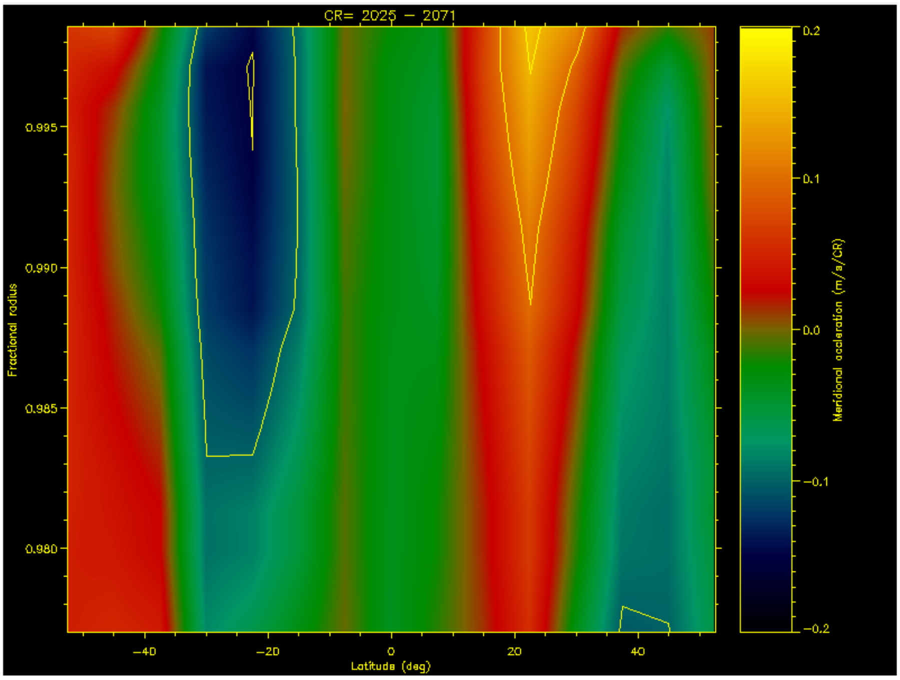

Figure 7.11: Same as figure 7.10 but for the minimum activity period (CR: 2025 – 2072).

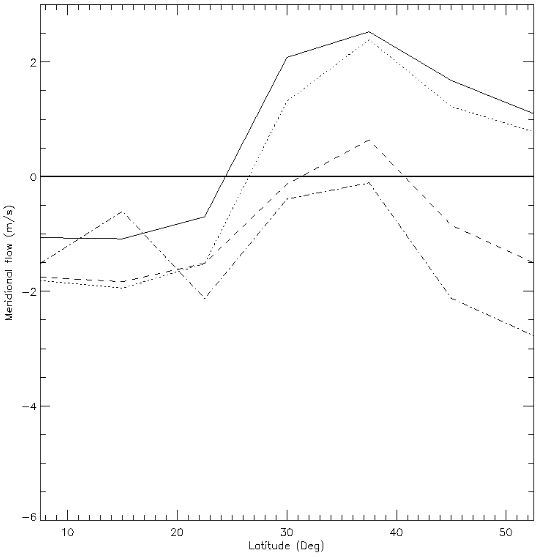

Figure 7.12: Difference between the northern and the unsigned southern meridional flow at maximum activity period as a function of latitude at depths: 1 Mm (full), 2 Mm (dotted), 6 Mm (dashed), 12 Mm (dashed-dotted). The dark thick line shows the zero level. Negative (positive) values stand for a higher (lower) poleward southern flow than the northern flow.

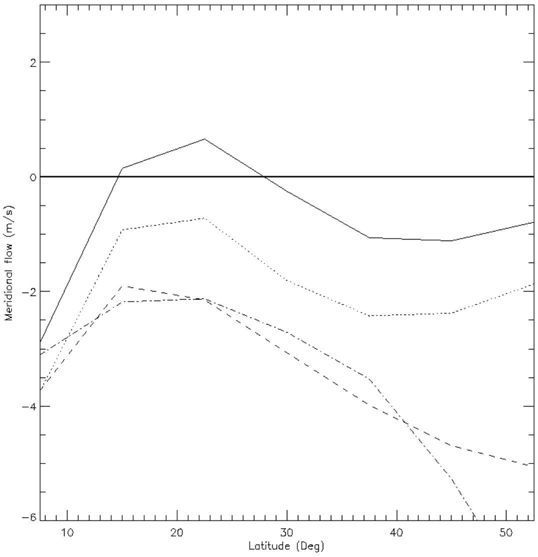

Figure 7.13: Same as figure 7.12 but for the minimum activity period.

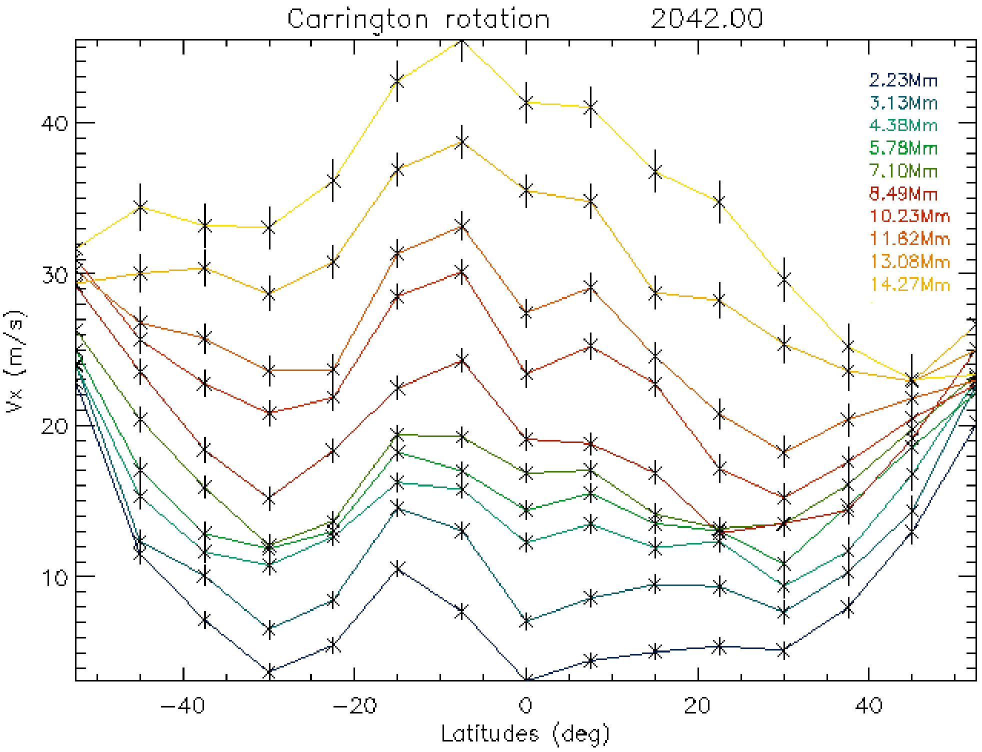

Figure 7.14: Zonal flow averaged over one Carrington rotation (CR= 2024) as a function of latitude at several depth. Color coding of the depth is given inside the panel.

Comparison between the sub-photospheric and coronal rotations

In article III given at the end of the current chapter, I present a study on the comparison between angular velocities of sub-photospheric and bright point coronal structures (SBCS) during the declining phase of solar cycle 23 (August 2001 – December 2006). The sub-photospheric rotation is derived from ring diagram analysis whereas the SBCS were tracked in EIT images in order to infer the solar coronal rotation. The outcome is that the SBCS rotate faster than the shallowest layer considered in this study (3 Mm) by about 0.5° per day. We also inferred the acceleration of the two rotations and saw that SBCS do show an acceleration during the studied period up to 0.005° per month with a maximum acceleration reached at minimum activity period (see figure 2 in article III). However, the sub-photospheric angular velocity does not show such a significant temporal variation except a slight acceleration at high latitudes which corresponds to the torsional oscillation signal during the period 2001 – 2006. This slight difference can be seen through the two arms of the faster than average rotating regions over time in figure 1.5. Coronal activity has also been studied in relation to the torsional oscillation pattern from observations of Fe XIV coronal emission features were it was pointed out that the two phenomena have similar time-latitude properties (Altrock *et al.*, 2008).

We have also performed a north-south study for two periods of the studied epoch and saw again a faster rotating southern hemisphere through the SBCS rotation. This behavior is valid regardless of which hemisphere is more active in terms of SBCS affluence (see figure 3 of article III). The north-south asymmetry of the sub-photospheric layers increases with depth and behaves differently from the SBCS asymmetry during the first and second half period of the studied epoch of the declining phase of solar cycle 23 (see figure 4 of article III). When the north-south asymmetry of the rotation velocity is lower than its temporal average for the subsurface layers, it is higher for the SBCS and vice-versa. All the cited findings on the relationship between coronal activity and sub-surface dynamics may place observational constraints on dynamo models.

7.3 Summary

In this section, I am summarizing the results of my studies on the long term variations of the horizontal flows inside the Sun, which were inferred from ring diagram analysis of GONG data for the declining phase of solar cycle 23. I obtained the results by assembling the dense-pack daily flow maps onto synoptic maps of sub-photospheric horizontal flows as a function of latitudes (up to 52.5° north and south) and Carrington longitudes for depths down to about 16 Mm. These results might be crucial observational constraints for the solar dynamo models aiming to understand the complex mechanism of the magnetic solar cycle.

- The meridional flow shows an acceleration up to 0.2 m/s per Carrington rotation at latitudes poleward of 20° at the maximum activity period of the declining phase of solar cycle 23, with a maximum acceleration close to the surface. This acceleration vanishes at the low activity period for most of the high latitudes range keeping the meridional flow with its strongest amplitude until the end of the studied epoch (July 2001 – July 2008). At the end of the cycle, the maximum meridional acceleration gets concentrated around 20° north and south. Unlike meridional circulation, the zonal flow does not show significant temporal variations during the studied period except for a torsional oscillations like behavior.

- A yearly periodicity of the poleward meridional flow at high latitudes close to the surface has been attributed to a systematic effect due to the annual variation of the B_0-angle. Removing the linear regression of the meridional flow with B_0 from the signal cancels this periodicity. Nonetheless, annual variations on the semi- diameter, as well as the synodic sidereal correction, slightly affect the horizontal measurements.

- The north-south asymmetry of the meridional and zonal flows are predominantly southern with some northern dominances at high activity periods. The magnetic field during the declining phase of solar cycle 23 is also southern dominant. The north-south asymmetry increases with depth more clearly at the minimum activity period for the meridional flow and for most of the studied period for the zonal flow.

- The sub-photospheric rotation is lower than those of the coronal active regions as it is the case for most of the magnetic active regions rotating faster than the quiet Sun. A difference of about 0.5° per day has been found between the angular velocity of the bright coronal structures and that of the sub-surface layer at a depth of 3 Mm. These coronal features show an acceleration during the last phase of solar cycle 23 and have also a southern dominant rotation with a differently behaving north-south asymmetry when compared to the sub-photospheric rotation asymmetry. At latitudes where the north-south asymmetry of the angular velocity increases (decreases) with activity for the SBCS, it decreases (increases) for subphotospheric layers.

ARTICLE II

TITLE

North – South Asymmetry of Zonal and Meridional Flows Determined From Ring Diagram Analysis of Gong ++ Data

AUTHORS

A. Zaatri, R. Komm, I. Irene Gonzàlez-Hernàndez,
R. Howe and T. Corbard

REFERENCE

Solar Physics, vol. 236, Issue 2, p.227-244 (2006)

Solar Physics (2006) 236: 227–244
DOI: 10.1007/s11207-006-0106-5

NORTH – SOUTH ASYMMETRY OF ZONAL AND MERIDIONAL FLOWS DETERMINED FROM RING DIAGRAM ANALYSIS OF GONG++ DATA

A. ZAATRI
Centre de Recherche en Astronomie Astrophysique et Geophysique, B.P. 63 Bouzaréah, Algiers 16340, Algeria

R. KOMM, I. GONZÁLEZ HERNÁNDEZ, and R. HOWE
National Solar Observatory, 950 N. Cherry Ave., Tucson, AZ 85719, U.S.A.
(e-mail: rkomm@nso.edu)

and

T. CORBARD
Observatoire de la Côte d'Azur, F-06304 Nice Cedex 4, France

(Received 17 November 2005; accepted 28 March 2006)

Abstract. We study the North – South asymmetry of zonal and meridional components of horizontal, solar subsurface flows during the years 2001 – 2004, which cover the declining phase of solar cycle 23. We measure the horizontal flows from the near-surface layers to 16 Mm depth by analyzing 44 consecutive Carrington rotations of Global Oscillation Network Group (GONG) Doppler images with a ring-diagram analysis technique. The meridional flow and the errors of both flow components show an annual variation related to the B_0-angle variation, while the zonal flow is less affected by the B_0-angle variation. After correcting for this effect, the meridional flow is mainly poleward but it shows a counter cell close to the surface at high latitudes in both hemispheres. During the declining phase of the solar cycle, the meridional flow mainly increases with time at latitudes poleward of about 20°, while it mainly decreases at more equatorward latitudes. The temporal variation of the zonal flow in both hemispheres is significantly correlated at latitudes less than about 20°. The zonal flow is larger in the southern hemisphere than the northern one, and this North – South asymmetry increases with depth. Details of the North – South asymmetry of zonal and meridional flow reflect the North – South asymmetry of the magnetic flux. The North – South asymmetries of the flows show hints of a variation with the solar cycle.

1. Introduction

We study the zonal and meridional flow in shallow solar subsurface layers: their temporal variability and North – South asymmetry during the declining phase of the solar cycle. For this purpose, we analyze 44 consecutive Carrington rotations of Global Oscillation Network Group (GONG) Doppler images using the GONG ring-diagram analysis pipeline.

Large-scale zonal and meridional flows play an important role in solar dynamo theory (*e.g.*, Charbonneau, 2005). For example, the transport of magnetic flux by the meridional flow is a key ingredient in some dynamo models (Dikpati and Gilman, 2001; Nandy and Choudhuri, 2002). The North – South asymmetry of the meridional flow can cause the polar field in one hemisphere to reverse before the polar field in the other (Dikpati *et al.*, 2004).

Long-term meridional and zonal-flow variability in subsurface layers have been studied using different methods of local helioseismology and different data sets. Zhao and Kosovichev (2004) analyzed Michelson Doppler Imager (MDI) Dynamics Program data with the time-distance method to study the solar-cycle variation of the zonal flow, the so-called torsional oscillation pattern, and the variation of the meridional flow. Haber *et al.* (2002) studied the long-term variation of the zonal and the meridional flow applying the ring-diagram technique to MDI Dynamics Program data. Chou and Dai (2001) and Chou and Ladenkov (2005) applied the time-distance technique to Taiwan Oscillation Network (TON) data to study the meridional flow during the rising and declining phase of the solar cycle. In addition to an essentially-poleward meridional flow, these studies find that the meridional flow converges toward the mean latitude of magnetic activity at depths less than about ten Mm and that it diverges at greater depth. Chou and Ladenkov (2005) find that the amplitude of the divergent flow increases with depth to about 90% of the solar radius and then decreases with depth at least down to about 80% of the radius. Basu and Antia (2003) found changes related to solar activity in the North – South asymmetries of horizontal flows derived from nine Carrington rotations of MDI data covering the rising phase of solar cycle 23. In particular, the antisymmetric component of the meridional flow decreases in amplitude with increasing activity.

The goal of this paper is to study the zonal and meridional flow variability during the declining phase of the solar cycle 23 from mid-2001 to end-2004 with a standard ring-diagram analysis of high-resolution GONG data. However, this is a rather “boring” epoch as far as large-scale flows are concerned since the mean latitude of magnetic activity (about 15°) changes little during this time, moving somewhat toward the equator.

Given the length of the data set and the rather constant distribution of magnetic activity, we can check the derived flows for systematic variations of observational origin that might bias the results. As part of the ring-diagram analysis, effects such as the variation throughout the year of the solar inclination toward the Earth, the B_0-angle, are taken into account. But, the processing cannot correct for a loss in detail that can occur at high spatial frequencies due to this variation. For example, González Hernández *et al.* (2006) found in a large-aperture ring-diagram analysis of high-resolution GONG data that an equatorward meridional cell appears at high latitudes during maximum values of the B_0-angle and that it appears either in the northern or southern hemisphere depending on the sign of the B_0-angle. Finally, we correct the measured horizontal flows for these systematic effects and focus on their temporal variations and North – South asymmetry.

2. Data Analysis

The data used in this work consist of continuous, high-resolution Dopplergrams from the Global Oscillation Network Group (GONG) covering 44 consecutive Carrington rotations from CR 1979 to CR 2022 (July 27, 2001 – October 12, 2004). Full-disk Dopplergrams at one minute cadence are recorded on a 1024 × 1024 pixel CCD (Harvey, Tucker, and Britanik, 1998) and then registered so that the solar image covers an area of 800 pixels in diameter (GONG++ data). In order to measure the horizontal components of the solar subsurface flows as a function of depth, we use one of the local helioseismology techniques called ring-diagram analysis (Hill, 1988; Morrow, 1988). This technique uses high-degree acoustic waves measured in small patches in the plane-wave approximation. This simplification is good enough for studying subsurface layers close to the surface. The wave pattern is advected by a local velocity field and the resulting shift of the wave pattern can be used to determine the subsurface flows (Gough and Toomre, 1983).

We use the dense-pack technique as described by Haber *et al.* (2002) for their analysis of Michelson Doppler Imager (MDI) Dynamics Program data. For GONG++ data, simultaneous images from different sites are merged (Toner *et al.*, 2003), and the time series of merged images is analyzed in “days” of 1664 minutes duration. For each day, the merged full-disk Dopplergrams are remapped into a set of 189 overlapping patches with centers separated by 7.5° in latitude and longitude covering the solar disk from the central meridian to ±52.5° in longitude and ±52.5° in latitude. Each patch of 16° × 16° diameter is tracked at the surface rotation rate (Snodgrass, 1984) in order to remove the differential rotation effect and apodized with a circular function reducing the effective diameter to 15°. Three-dimensional power spectra are constructed from each dense-pack patch using a three-dimensional FFT so that each data cube in spatial and temporal coordinates (x, y, t) is transformed into one described in horizontal wavenumbers (k_x, k_y) and temporal frequency (ν). Two-dimensional slices of the power spectra at a specified temporal frequency show “rings” which are shifted in k_x, k_y by a velocity field. The power spectrum is then fitted with a Lorentzian profile model which incorporates a perturbation term $(k_x v_x + k_y v_y)$ due to the horizontal velocity components. Finally, the Regularized Least Square (RLS) method is used to invert the fitted velocities (Thompson *et al.*, 1996; Haber *et al.*, 2002) in order to derive the horizontal velocity components as functions of depth $(v_x(r), v_y(r))$ for the East – West, or zonal, component and the North – South, or meridional, component. The analysis is described in more detail by Corbard *et al.* (2003) and implemented as the GONG ring-diagram pipeline as described by Hill *et al.* (2003).

In this way, we derive 189 pairs of zonal and meridional velocity at 16 depths from 0.6 to 16 Mm for each 1664-minute day. We combine these daily flow maps to calculate synoptic flow maps for each depth using a weighting factor of cosine central meridian distance to the fourth power. For this work, we average the horizontal flows over the length of a Carrington rotation and study the temporal variation of zonal and meridional flows from more than three years of consecutive GONG++ data.

During the remapping stage, a variety of geometric effects are taken into account that vary with a period of one year, such as the solar inclination toward the Earth (B_0-angle) and the apparent semi-diameter of the Sun. However, the processing cannot correct for a loss in spatial resolution introduced by these effects. For example, a large B_0-angle value means that one solar hemisphere is tilted away from the observer which will increase the geometric foreshortening at a given solar latitude on this hemisphere. In order to check for annual variations introduced by these effects, we calculate the B_0-angle and the apparent semi-diameter for the middle of every Carrington rotation and compare their temporal variation with the variation of the measured zonal and meridional flows. The sidereal-synodic correction is a geometric effect (*e.g.*, Wittmann *et al.*, 1996) that influences the determination of the central meridian distance and can be expressed as a change in the tracking rate (Corbard *et al.*, 2003). While the average value of the sidereal-synodic correction is taken into account at the remapping stage, we calculate its value[1] for the middle of each Carrington rotation and correct the zonal flows for the annual variation of the sidereal-synodic correction.

As a measure of solar activity, we use the NSO Kitt Peak synoptic charts.[2] We rebin the magnetogram data into circular areas with 15° diameter centered on a grid with 7.5° spacing in latitude and longitude to match the dense-pack mosaic.

3. Results

3.1. TEMPORAL VARIATION

Figure 1 shows the temporal variation of the meridional flow in the northern and southern hemisphere at four latitudes and four depths. The meridional flows are mainly poleward in each hemisphere, except at high latitudes and very close to the surface as indicated by the predominantly positive values of the southern flow and the negative values of the northern flow in the first panel (±52.5° and 0.6 Mm). These values indicate an equatorward flow, a so-called counter cell, close to the surface at high latitudes in both hemispheres.

At high latitudes and low depths, these meridional flows exhibit periodic trends recurring on a yearly basis. For comparison, we include the variation of the B_0-angle with time. The B_0-angle has an annual periodicity, and its variation seems to be well correlated with that of the meridional flows in these regions. In order to better visualize this correlation, we include a linear regression of the flow with the B_0-angle on the same chart. Furthermore, correlation coefficients, shown in Figure 2 at the same latitudes and depths, show overall a good correlation between the B_0-angle

[1] see `http://aa.usno.navy.mil/faq/docs/SunApprox.html`

[2] Available at `http://nsokp.nso.edu/dataarch.html`

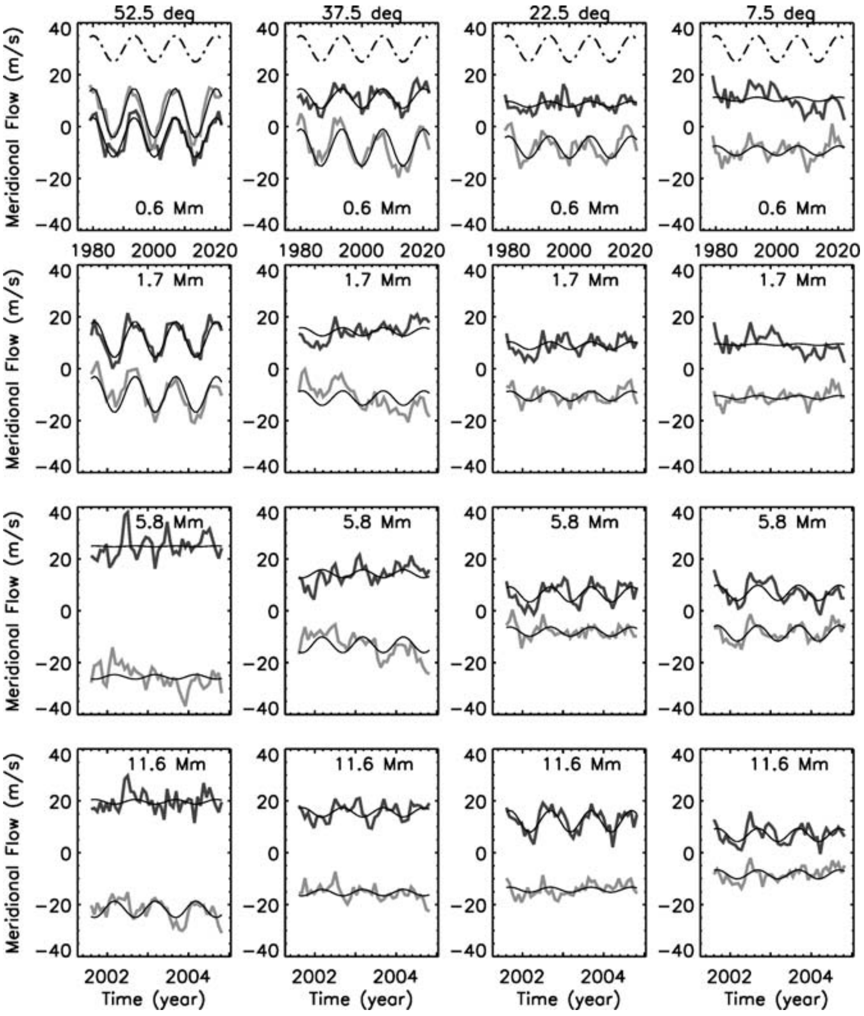

Figure 1. Temporal variation of the meridional flow in the northern (*dark grey*) and southern hemisphere (*light grey*) at four latitudes and four depths. The *line thickness* represents about two standard deviations of the formal uncertainty. Positive (negative) values indicate flows to the North (South). The top row shows, for comparison, the time scale in Carrington Rotations. The B_0-angle variation (in degree) is indicated as dot-dashed line in the top row (shifted by 30 m/s in the y direction). *Thin solid lines* represent linear fits of the B_0-angle to the flows.

and flow variabilities. Large correlation coefficients occur mainly at high latitudes, while the values are generally small close to the equator. The correlation values are very similar in both hemispheres except at shallow layers equatorward of about 30^o and at depths greater than about ten Mm poleward of about 30^o.

For comparison, we also calculate the correlation between the meridional flow and the apparent semi-diameter, which varies with an annual period but about

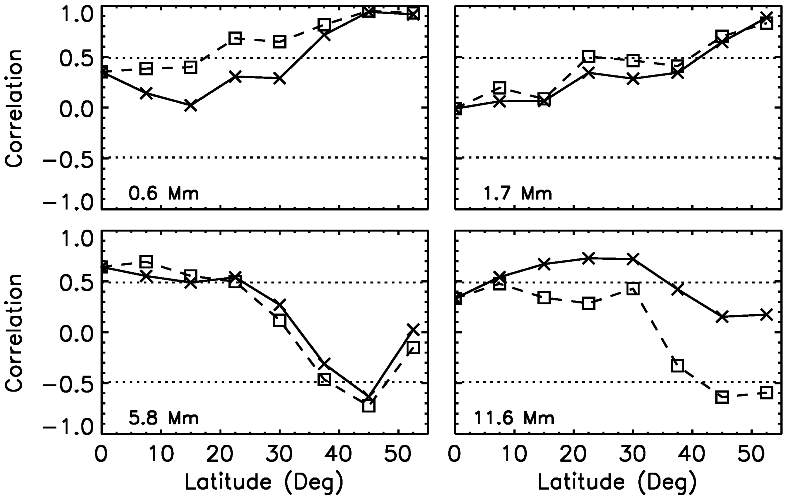

Figure 2. Linear correlation between meridional flow and B_0-angle variation at four depths for northern (*solid line, crosses*) and southern hemisphere (*dashed line, squares*). The *dotted lines* indicate the 99.9% significance levels.

four Carrington rotations out of phase with the B_0-angle. Since the apparent semi-diameter and the sidereal-synodic correction vary in phase, it is sufficient to use only one of them. We then repeat the correlation analysis for the zonal flow.

Figure 3 summarizes the results by showing the coefficients of a linear correlation between B_0-angle (top) and apparent semi-diameter variation (bottom) with the two horizontal-flow components. The correlation between meridional flow and B_0-angle shows a complex behavior with high positive values close to the surface at high latitudes, at depths between about four and ten Mm at latitudes equatorward of about 20°, and at greater depths in the northern hemisphere. In addition, there are regions of large anticorrelation at high latitudes at depths between about four and ten Mm. The temporal variation of the zonal flow is, by comparison, less correlated with the B_0-angle variation. It is significantly correlated with the B_0-angle only in the southern hemisphere at depths between two and 11 Mm. At the same depth range in the northern hemisphere, the correlation is negative and increases in amplitude with increasing latitude but remains below the 99.9% significance level. The correlations between the apparent semi-diameter and the zonal and meridional flow are much smaller compared to the ones with the B_0-angle.

Figure 4 shows the same as Figure 3 but for the errors of the horizontal flows. The errors of both flow components are clearly correlated with the temporal variation of the B_0-angle, with positive values in the southern and negative ones in the northern hemisphere. The correlation values increase with increasing latitude and the most equatorward latitudes with significant correlations occur at a depth of about five Mm. The flow errors show hardly any correlation with the apparent semi-diameter variation.

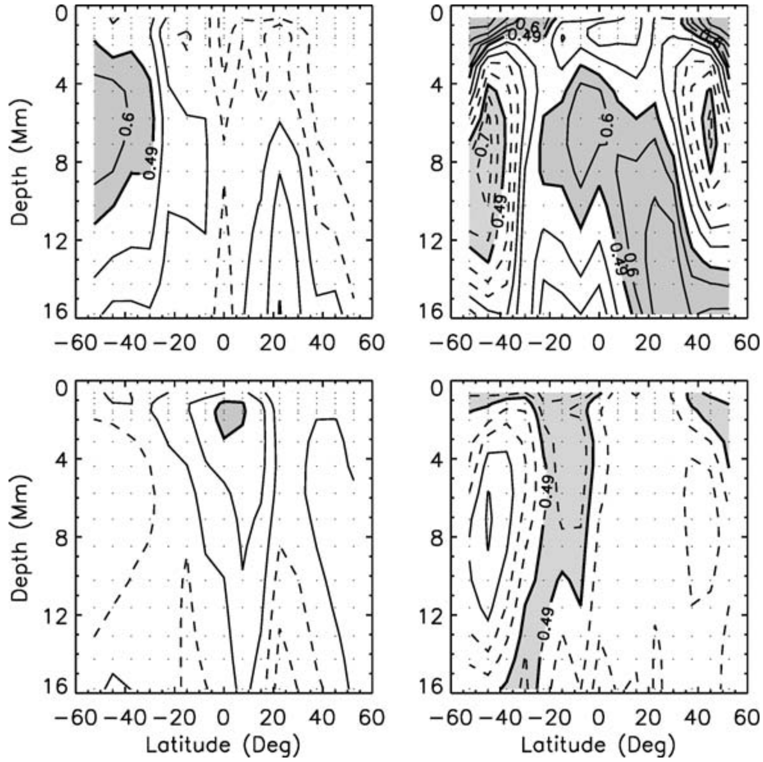

Figure 3. Coefficients of a linear correlation between B_0-angle and apparent semi-diameter variation with the two horizontal flow components as functions of latitude and depth: *Top-left:* B_0-angle and zonal flow; *top-right:* B_0-angle and meridional flow; *bottom-left:* semi-diameter and zonal flow; *bottom-right:* semi-diameter and meridional flow. The *grey areas* indicate values greater than the 99.9% significance level represented by *thick solid contour lines* (of 0.49). *Solid* (*dashed*) *contour lines* indicate positive (negative) correlations (0.1, 0.3, 0.6, 0.7, 0.8, 0.9). Dots indicate the depth-latitude grid of the ring-diagram analysis.

Figure 5 shows the temporal variation of the meridional flow after removing the B_0-angle effect by subtracting the fit of a linear regression between flow and B_0-angle variation. The one-year periodicity has disappeared. Consequently, one can conclude that such a periodicity is purely a systematic effect due to the B_0-angle. However, the “counter cell” still appears at high latitude in shallow layers in both hemispheres. While the meridional flow is nearly constant with time at many locations close to 22.5°, its amplitude noticeably increases with time at 37.5° latitude and decreases at 7.5° at depths of 1.7 and 5.8 Mm in both hemispheres. Fluctuations on time scales shorter than one year seem to be unrelated between the hemispheres.

Figure 6 shows the variation of the zonal flow. The tracking rate has been subtracted and the sidereal-synodic correction has been added. While the correlation between the zonal flow and the B_0-angle is not significant except at high latitudes at some depths in the southern hemisphere, it shows the same pattern with latitude

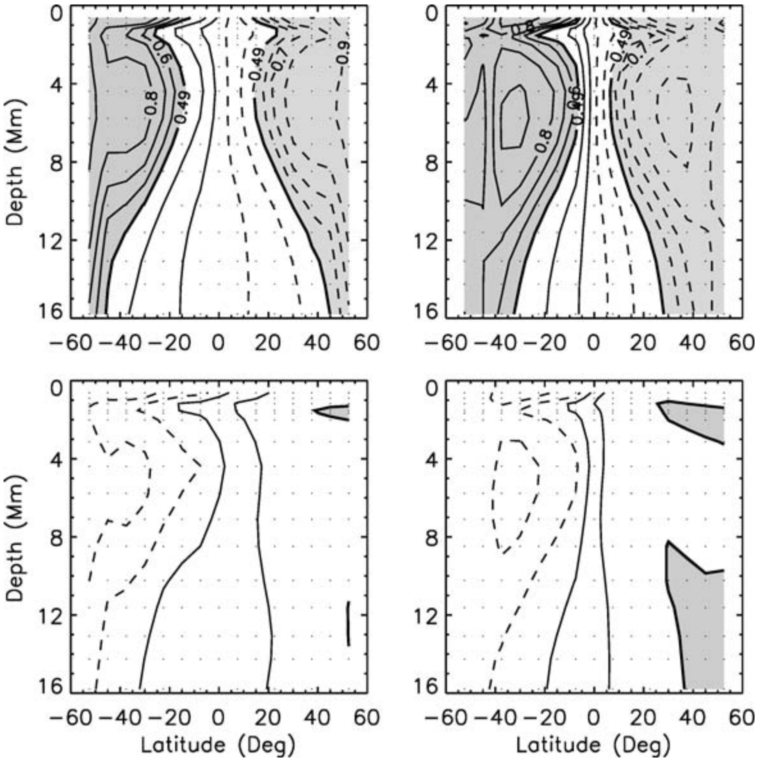

Figure 4. Same as Figure 3 for correlations with flow errors: *Top-left:* B_0-angle and zonal flow error; *top-right:* B_0-angle and meridional-flow error; *bottom-left:* semi-diameter and zonal flow error; *bottom-right:* semi-diameter and meridional-flow error.

and depth as the correlation between the errors of the zonal flow and the B_0-angle. For this reason, we decided to remove the B_0-angle effect from the zonal flow, as shown in Figure 6. The zonal flow values are generally larger in the southern than in the northern hemisphere, which is most apparent at high latitudes. The zonal flow shows strong fluctuations on time scales shorter than one year, which appear to be correlated between the hemispheres at 7.5° and 22.5° latitude. At latitudes poleward of about 40°, the variation of the zonal flow appears to have a larger amplitude compared to more equatorward latitudes.

To estimate the magnitude of these fluctuations, we calculate the rms value of the meridional flow and find an average value of 3.1 ± 0.6 m/s over all latitudes and depths. The average rms value (3.0 ± 1.0 m/s) of the zonal flow is very close to this value, but the zonal-flow average is the result of a bowl-shaped variation with latitude with a value of 2.3 ± 0.3 m/s averaged over latitudes equatorward of 25° and a value of 4.2 ± 0.7 m/s averaged over latitudes poleward of 40°. At face value, this result implies that the zonal flows are “noisier” than meridional flows at high latitudes, while the opposite is true at low latitudes. These fluctuations are much larger than the average error of 0.5 m/s for zonal and meridional flow. Before

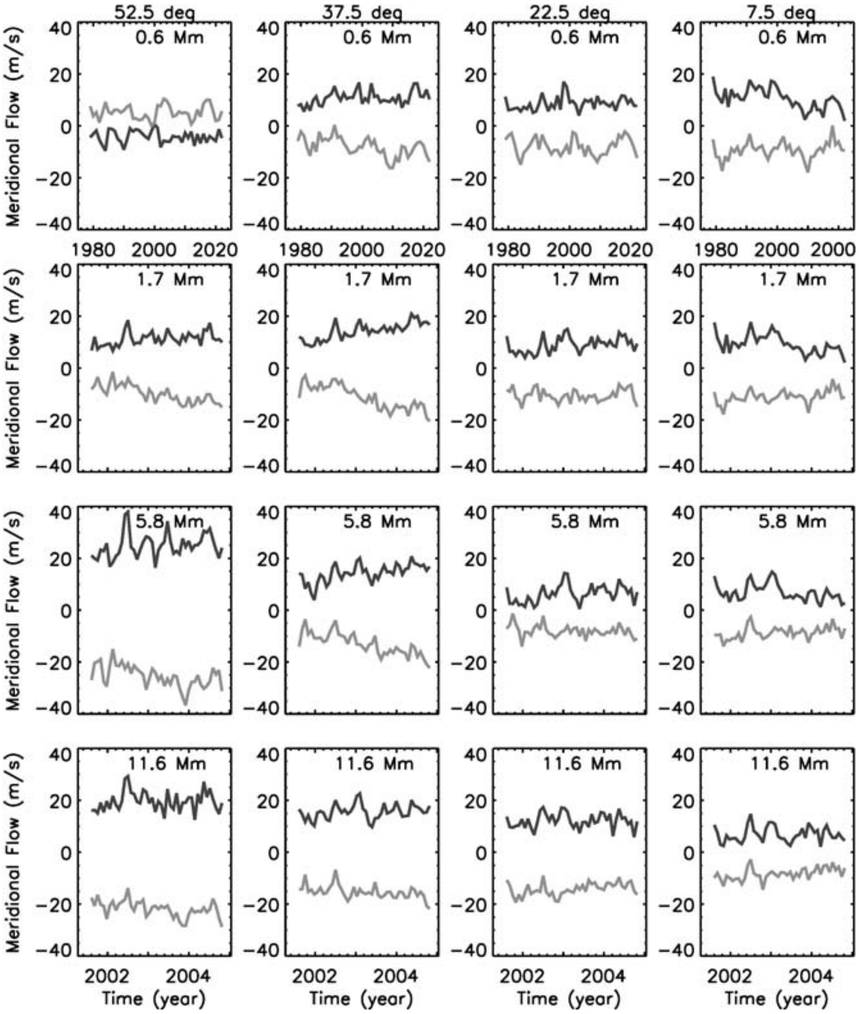

Figure 5. Same as Figure 1 after removing the B_0-angle variation from the meridional flow.

the B_0-angle corrections, the rms fluctuations of both zonal and meridional flow show a bowl-shaped variation with 2.3 ± 0.3 m/s equatorward of 25° latitude and 4.7 ± 0.7 m/s poleward of 40° latitude for the zonal flow and 3.2 ± 0.6 m/s and 5.0 ± 1.4 m/s for the meridional flow. As expected from the correlation results, the correction has the greatest effect at high latitudes.

3.2. NORTH – SOUTH COMPARISON

Figure 7 shows linear correlation coefficients between flows in the northern and southern hemisphere. While the short-term variations of the zonal flow are highly correlated at low latitudes, at latitudes poleward of 45°, the variations are

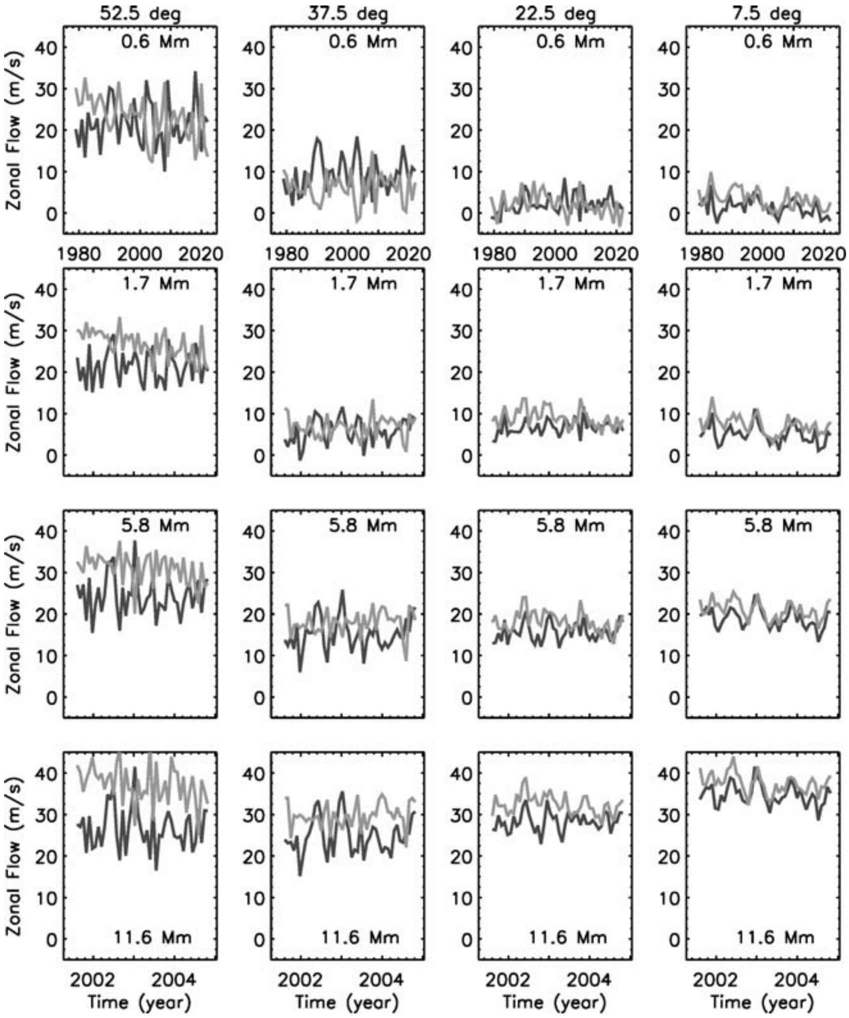

Figure 6. Temporal variation of the zonal flow in the northern (*dark grey*) and southern hemisphere (*light grey*) at four latitudes and four depths after removing the B_0-angle variation. The surface rotation rate (tracking rate) has been subtracted (Snodgrass, 1984) and the sidereal-synodic correction has been added. The *line thickness* represents about two standard deviations of the formal uncertainty. The top row shows, for comparison, the time scale in Carrington Rotations.

significantly anticorrelated between the hemispheres. The range of latitudes with significant correlations is greatest at a depth of about nine Mm. The correlation is close to zero at about 30°. While this correlation might be of solar origin, we cannot rule out that it is due to some other systematic effect. The meridional flow shows hardly any significant correlation between the temporal variation in the two hemispheres. The positive correlation values near 30° at about two Mm reflect the trends seen in Figure 5.

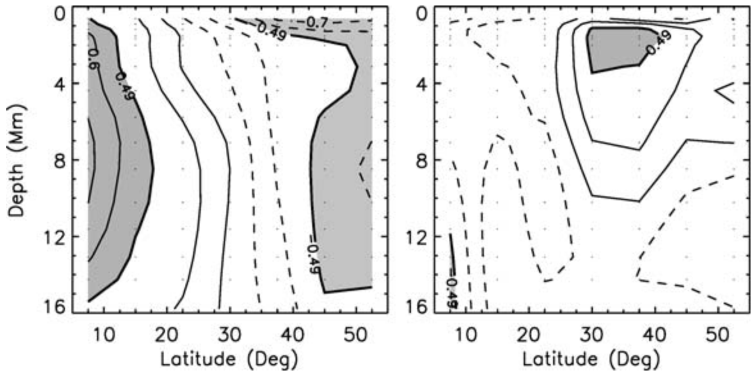

Figure 7. Linear correlations between flows in the northern and southern hemisphere as a function of latitude and depth for zonal (*left*) and meridional flow (*right*). The annual variations due to the B_0-angle have been removed. The grey areas indicate correlations greater than the 99.9% significance level represented by thick solid contour lines (of 0.49). *Solid* (*dashed*) *contour lines* indicate positive (negative) correlations (0.1, 0.3, 0.6, 0.7). The *dots* indicate the depth-latitude grid of the ring-diagram analysis.

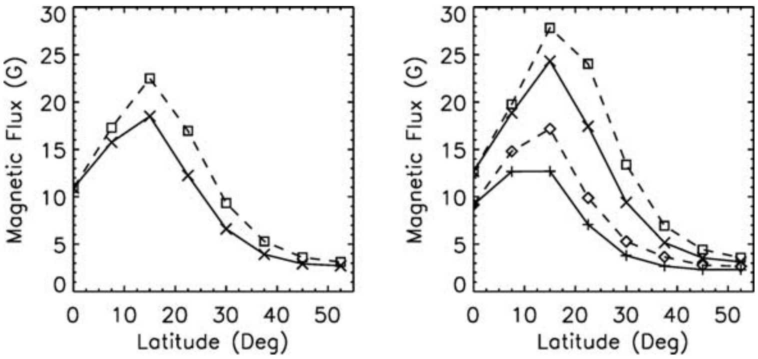

Figure 8. Left: Unsigned magnetic flux averaged over 44 Carrington rotations as a function of latitude for the northern (*solid, crosses*) and southern hemisphere (*dashed, squares*). *Right:* Unsigned magnetic flux averaged over two subsets of 22 Carrington rotations 1979 – 2000 (*crosses, squares*) and 2001 – 2022 (*plus signs, diamonds*) for the northern (*solid*) and southern hemisphere (*dashed*).

Since some variations might be related to the distribution of magnetic flux, Figure 8 shows average unsigned flux values as a function of latitude. The unsigned magnetic flux of CR 1979 – 2022 is on average larger in the southern hemisphere than in the northern one; the greatest differences occur at 15° and 22.5° latitude. To indicate the temporal variation of activity, we divide the data into two subsets of higher and lower average magnetic activity, which cover CR 1979 – 2000 (July 2001 to March 2003) and CR 2001 – 2022 (March 2003 to November 2004). The mean latitude of activity is at about 15° and moves from somewhat poleward of 15° during the high-activity subset to somewhat equatorward of 15° during the low-activity subset. The shift in mean-latitude position is about the same as the distance

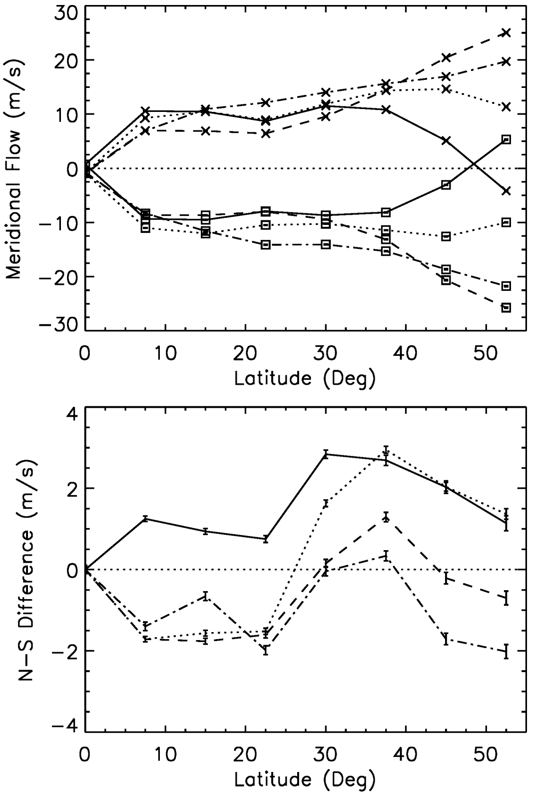

Figure 9. *Top:* Average meridional flow as a function of latitude at four different depths (0.6 Mm: *solid*, 1.7 Mm: *dotted*, 5.8 Mm: *dashed*, 11.6 Mm: *dot-dashed*) for the northern (*crosses*) and the southern hemisphere (*squares*). Positive (negative) values indicate flows to the North (South). *Bottom:* Difference between the meridional flow derived in the northern and southern hemispheres. Positive (negative) values imply greater poleward flow in the northern (southern) hemisphere.

between two dense-pack grid points. The unsigned magnetic flux decreases with time at all latitudes during the period of the observations, which coincides with an increase in the meridional flow at latitudes greater than 30° at most depths (Figure 5) and a decrease in the zonal flow at 52.5° in the southern hemisphere (Figure 6).

Next, we calculate the meridional flow averaged over CR 1979 – 2022 corrected for the B_0-angle variation. The top panel of Figure 9 shows the average flow as a function of latitude at four different depths. The meridional flows in both hemispheres show steep gradients at latitudes of about 35° or 40° and higher. At these latitudes, the flow amplitudes decrease with increasing latitude at shallow depths (below about two Mm), while they increase with latitude at greater depths and then decrease again at depths greater than about 13 Mm (not shown). The counter cell is noticeable close to the surface at the highest latitudes. The bottom panel of Figure 9 shows that the poleward meridional flow has a larger amplitude in the southern

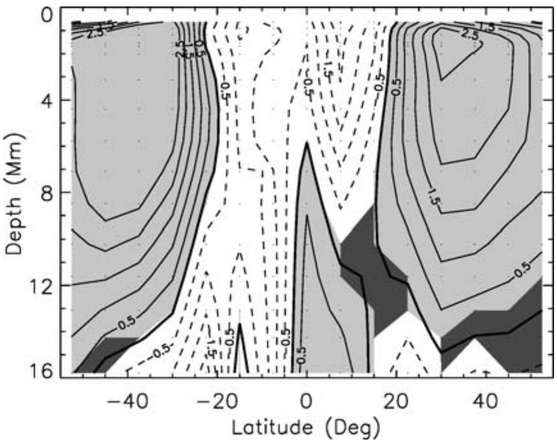

Figure 10. The slope of a linear regression with time of the meridional flow in units of m/s per year. The sign of the flow has been changed in the southern hemisphere so that positive (negative) values imply an increase (decrease) in flow amplitude in either hemisphere. The *dots* indicate the depth-latitude grid. *Solid* (*dashed*) *contours* indicate positive (negative) slopes with a spacing of 0.5 m/s. *Dark grey areas* indicate locations were the slope is less than three times its error; *light grey areas* highlight positive values.

hemisphere for almost all depths at latitudes equatorward of 25°, except close to the surface. At mid-latitudes between 25° and 40°, the meridional flow is larger in the northern hemisphere. The latitudes with the largest excess poleward flow in the southern hemisphere (10° to 25°) coincide with the latitudes of the largest excess magnetic flux in the southern hemisphere. At latitudes poleward of 40°, the meridional flow is stronger in the northern hemisphere at shallower depths and larger in the southern one at greater depth.

We now revisit the long-term variation of the meridional flow and represent it with a linear regression with time. Figure 10 shows the resulting slope as a function of depth and latitude. The mean location of magnetic activity appears to be a dividing line. Near the mean latitude of activity and equatorward of it, the slope is generally negative implying that the flow amplitude is larger during high magnetic activity and decreases during the declining phase of the cycle. Exceptions are the deeper layers in the northern hemisphere. On the poleward side of magnetic activity, the slope is generally positive which indicates that the meridional flow amplitude increases with decreasing activity. Exceptions are the deepest layers especially in the northern hemisphere and the near-surface layers at 0.6 Mm at 52.5° latitude. The positive slopes are generally larger in the southern hemisphere than in the northern one.

The average zonal flow corrected for the B_0 angle variation is shown in Figure 11 as a function of latitude at four depths. The zonal flow increases in amplitude with increasing depth, as expected from measurements of the rotation rate (*e.g.*, Howe *et al.*, 2006). The amplitude shows a local maximum near 15° latitude or less, which

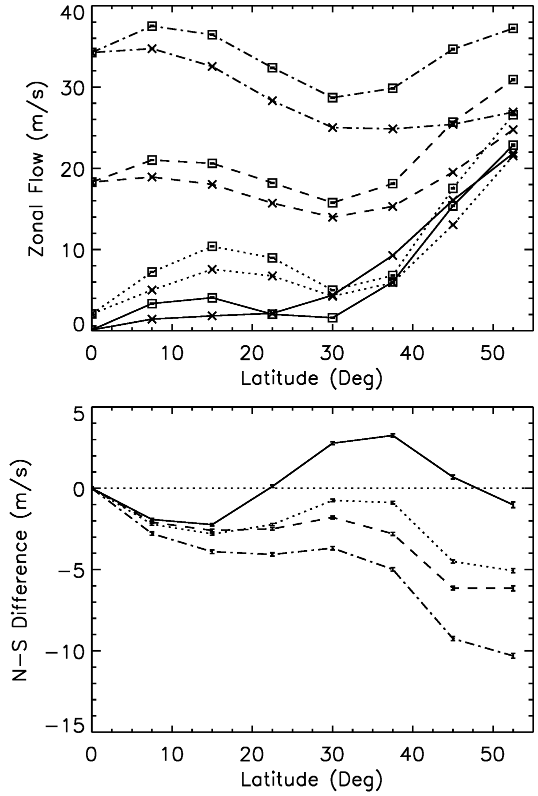

Figure 11. Same as Figure 9 for the average zonal flow. In the *bottom panel*, positive (negative) values imply greater zonal flow in the northern (southern) hemisphere.

coincides with the mean latitude of magnetic flux, and a local minimum near 30°. This latitudinal variation is most likely a consequence of the solar-cycle variation of the zonal flow, the torsional-oscillation pattern. The zonal flow is predominantly faster in the southern hemisphere than in the northern one. The differences generally increase with increasing latitude for latitudes greater than 25°. Furthermore, the difference in amplitude between the hemispheres increases with depth with a local maximum near 15° latitude. The high- and low-activity subsets of CR 1979 – 2000 and CR 2001 – 2022 show essentially the same behavior (not shown). The most obvious difference is that the local maximum is clearly at 15° for CR 2001 – 2022 and closer to 22.5° for CR 1979 – 2000, following the change in mean latitude of activity from higher to lower latitude.

The North – South asymmetry of the zonal flow appears to consist of one component that relates to the distribution of magnetic activity (at latitudes less than 30°) and another one that describes a general increase in asymmetry with latitude. To quantify the second component, we calculate a linear fit with latitude of the North – South difference of the average zonal flow (CR 1979 – 2022). Figure 12 shows the

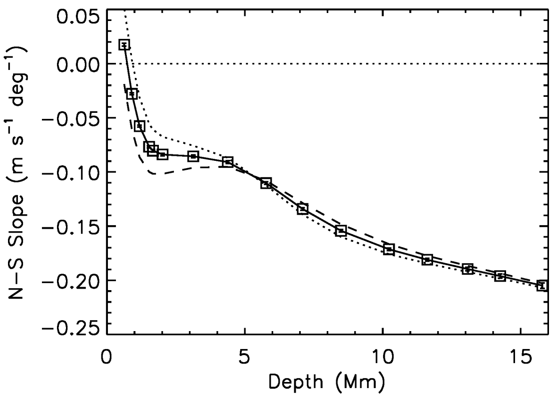

Figure 12. Slope of a linear regression with latitude of the North – South difference of the zonal flow as a function of depth for CR 1979 – 2022 (*solid line, squares*), CR 1979 – 2000 (*dashed line*), and for CR 2001 – 2022 (*dotted line*).

resulting slope as a function of depth. The slope is negative at all depths implying faster zonal flows in the southern hemisphere than in the northern one, except near the surface where there is almost no North – South asymmetry. The magnitude of the slope increases with depth; about half of the increase occurs in the outer two Mm and the asymmetry barely changes between two and five Mm. The two subsets of CR 1979 – 2000 and CR 2001 – 2022 show the same behavior, as expected from the previous paragraph. However, at depths less than about five Mm, the North – South asymmetry of the subset with less magnetic activity (CR 2001 – 2022) is smaller than the one with higher activity (CR 1979 – 2000). This is mainly due to a decrease in zonal flow amplitude in the southern hemisphere at high latitudes (noticeable in Figure 6). At greater depth both subsets lead to similar slopes.

4. Summary and Discussion

We have analyzed 44 consecutive Carrington rotations and explored the horizontal flow components, their temporal variation and their North – South asymmetry. The meridional flow shows an annual variation related to the B_0-angle, as noticed by González Hernández *et al.* (2006). The flow errors also vary in time with the variation of the B_0-angle. Komm *et al.* (2005) found that the velocity errors show a bowl-shaped dependence with latitude most likely due to geometric foreshortening. It is thus not too surprising that the errors show an annual variation in phase with the B_0-angle, since a non-zero B_0-angle will either enhance or diminish the foreshortening at a given solar latitude. Furthermore, since this variation affects the spatial resolution in the North – South direction, this can explain why the meridional flow would also show such a variation, while the zonal flow, a flow in the East – West direction, would be less affected by such a variation. The B_0-angle variation affects flows differently at different layers for a given latitude. This implies that its effect on the observations varies with spatial wavenumber. It is somewhat surprising that the B_0-angle effect can be different between the hemispheres. One reason might be that different mode sets might be fitted in different dense packs and the inversions are performed on mode sets specific to each dense pack and not on the subset of common modes. To correct the horizontal flows for these annual variations, we subtract a linear regression in B_0-angle from the flows.

The meridional flow is generally poleward except near the surface at the highest latitudes where the flow is equatorward. This “counter cell” is present in both hemispheres at all times even after correcting for the B_0-angle effect. The existence of a counter cell at high latitudes in the meridional flow has been reported by Haber *et al.* (2002) analyzing MDI Dynamics Program data. However, the counter cell found in MDI data with a ring-diagram analysis is located at depths greater than about six Mm in the northern hemisphere. González Hernández *et al.* (2006) studied meridional flows with a large-aperture ring analysis of GONG++ data at depths about 60% deeper than those accessible with a standard ring-diagram analysis. They found that a counter cell appears at great depths during times of maximum B_0-angle and that it appears either in the northern or southern hemisphere depending on the sign of the B_0-angle. With counter cells unique to each data set or analysis method, we cannot rule out that the near-surface counter cell reported here is due to some systematic effect.

The average meridional flow has a larger amplitude in the southern hemisphere equatorward of the mean latitude of magnetic activity and a larger amplitude in the northern hemisphere poleward of the mean latitude. This is a consequence of a meridional flow that is composed of a poleward average component and a secondary one that converges toward the mean latitude of activity, as found in previous studies (*e.g.*, Haber *et al.*, 2002; Zhao and Kosovichev, 2004; Komm *et al.*, 2005), and a North – South asymmetry in magnetic flux with more activity in the southern hemisphere. The average meridional flow amplitude has a large gradient with depth at latitudes poleward of 40° compared to its variation with depth at lower latitudes. The amplitude of the meridional flow increases with decreasing magnetic acitivity at latitudes greater than about 25° which is poleward of the mean latitude of activity. This agrees with the variation at high latitudes observed by Basu and Antia (2003). At more equatorward latitudes, the meridional flow amplitude is larger during the epoch of high activity, which is a consequence of the convergence toward the mean latitude of activity. This “steepening” with increasing activity has been found by Haber *et al.* (2002) and by Zhao and Kosovichev (2004) in their analyses of MDI Dynamics Program data and this result also agrees with Chou and Ladenkov (2005) who found in deeper layers that the amplitude of the divergent flow correlates with the sunspot number variation.

The amplitude of the zonal flow is usually larger in the southern hemisphere than in the northern one during these 44 Carrington rotations except in the layers close to the surface. This leads to a North – South asymmetry of the average flow that is close to zero near the surface and increases with depth, similar to the one derived from one year of GONG++ data by Komm *et al.* (2005). The current results show that the North – South asymmetry at depths less than about five Mm decreases with decreasing activity during the declining phase of the solar cycle. Basu and Antia (2003) found a similar North – South asymmetry in the zonal flow derived from MDI data and there are hints of a similar solar-cycle variation in their work.

The meridional and zonal flow patterns and their North – South asymmetry are strongly related to the distribution of magnetic activity and hence to the solar cycle. The GONG++ data set used here is the longest consecutive data set available for local helioseismology, but it still covers only about 30% of an 11-year cycle. The systematic variations of non-solar origin show the importance of continuous coverage, which will be possible with the Helioseismic and Magnetic Imager instrument onboard the Solar Dynamics Observatory and the on-going operation of GONG.

Acknowledgements

This work was supported by NASA grant NNG 05HL41. This work utilizes data obtained by the Global Oscillation Network Group (GONG) program, managed by the National Solar Observatory, which is operated by the Association of Universities for Research in Astronomy (AURA), Inc. under a cooperative agreement with the National Science Foundation. The data were acquired by instruments operated by the Big Bear Solar Observatory, High Altitude Observatory, Learmonth Solar Observatory, Udaipur Solar Observatory, Instituto de Astrofísica de Canarias, and Cerro Tololo Interamerican Observatory. NSO/Kitt Peak data used here are produced cooperatively by NSF/NSO, NASA/GSFC, and NOAA/SEC. SOLIS VSM data used here are produced cooperatively by NSF/NSO and NASA/GSFC. The ring-fitting analysis is based on algorithms developed by Haber, Hindman, and Larsen with support from NASA and Stanford University. We thank the referee for helpful comments.

References

Basu, S. and Antia, H.M.: 2003, *Astrophys. J.* **585**, 553.

Charbonneau, P.: 2005, *Living Rev. Solar Phys.* **2**, No. 2 (`http://solarphysics.livingreviews.org` lrsp-2005-2).

Chou D.-Y. and Dai, D.-C.: 2001, *Astrophys. J.* **559**, L175.

Chou D.-Y. and Ladenkov, O.: 2005, *Astrophys. J.* **630**, 1206.

Corbard, T., Toner, C., Hill, F., Hanna, K.D., Haber, D.A., Hindman, B.W., and Bogart, R.S.: 2003, in H. Sawaya-Lacoste (ed.), *Local and Global Helioseismology: The Present and Future*, (ESA SP-517), ESA, Noordwijk, Netherlands, p. 255.

Dikpati, M. and Gilman, P.: 2001, *Astrophys. J.* **559**, 428.

Dikpati, M., de Toma, G., Gilman, P.A., Arge, C.N., and White, O.R.: 2004, *Astrophys. J.* **601**, 1136.

González Hernández, I., Komm, R., Hill, F., Howe, R., Corbard, T., and Haber, D.A.: 2006, *Astrophys. J.* **638**, 576

Gough, D.O. and Toomre, J.: 1983, *Solar Phys.* **82**, 401.

Haber, D.A., Hindman, B.W., Toomre, J., Bogart, R.S., Larsen, R.M., and Hill, F.: 2002, *Astrophys. J.* **570**, 885.

Harvey, J., Tucker, R., and Britanik, L.: 1998, in S.G. Korzennik and A. Wilson (eds.), *Structure and Dynamics of the Interior of the Sun and Sun-like Stars*, (ESA SP-418), ESA, Noordwijk, Netherlands, p. 209.

Hill, F.: 1988 *Astrophys. J.* **339**, 996.

Hill, F., Bolding, J., Toner, C., Corbard, T., Wampler, S., Goodrich, B., Goodrich, J., Eliason, P., and Hanna, K.D.: 2003, in H. Sawaya-Lacoste (ed.), *Local and Global Helioseismology: The Present and Future*, (ESA SP-517), ESA, Noordwijk, Netherlands, p. 295.

Howe R., Komm, R., Hill, F., Ulrich, R., Haber, D.A., Hindman, B.W., Schou, J., and Thompson, M.J.: 2006, *Solar Phys.* **235**, 1.

Komm, R., Howe R., Hill, F., González-Hernández, I., Toner, C., and Corbard, T.: 2005, *Astrophys. J.* **631**, 636.

Morrow, C.A.: 1988, Ph.D. Thesis U. Colorado and NCAR, NCAR Coop. Thesis No. 116.

Nandy, D. and Choudhuri, A.R.: 2002, *Science* **296**, 1671.

Snodgrass, H.B.: 1984, *Solar Phys.* **94**, 13.

Thompson, M.J., *et al.*: 1996, *Science* **272**, 1300.

Toner, C., Haber, D.A., Corbard, T., Bogart, R.S., and Hindman, B.W.: 2003, in H. Sawaya-Lacoste (ed.), *Local and Global Helioseismology: The Present and Future*, (ESA SP-517), ESA, Noordwijk, Netherlands, p. 405.

Wittmann, A.D., *et al.*: 1996, *Solar Phys.* **168**, 211.

Zhao, J. and Kosovichev, A.G.: 2004, *Astrophys. J.* **603**, 776.

ARTICLE III

TITLE

Comparison of the sidereal angular velocity of subphotospheric layers and small bright coronal structures during the declining phase of solar cycle 23

AUTHORS

A. Zaatri, H. Wöhl, M. Roth, T. Corbard and R. Brajŝa

REFERENCE

Astronomy and Astrophysics, Volume 504, Issue 2, pp.589-594 (2009)

A&A 504, 589–594 (2009)
DOI: 10.1051/0004-6361/200912130

Astronomy & Astrophysics

Comparison of the sidereal angular velocity of subphotospheric layers and small bright coronal structures during the declining phase of solar cycle 23

A. Zaatri[1,2], H. Wöhl[1], M. Roth[1], T. Corbard[2], and R. Brajša[3]

[1] Kiepenheuer-Institut für Sonnenphysik, Schöneckstr. 6, 79104 Freiburg, Germany
e-mail: `[amel;hw;mroth]@kis.uni-freiburg.de`
[2] Université de Nice Sophia-Antipolis, CNRS, Observatoire de la Côte d'Azur, BP 4229, 06304 Nice Cedex 4, France
e-mail: `corbard@oca.eu`
[3] Hvar Observatory, Faculty of Geodesy, University of Zagreb, Kačićeva 26, 10000 Zagreb, Croatia
e-mail: `romanb@geof.hr`

Received 22 March 2009 / Accepted 24 June 2009

ABSTRACT

Context. We compare solar differential rotation of subphotospheric layers derived from local helioseismology analysis of GONG++ dopplergrams and the one derived from tracing small bright coronal structures (SBCS) using EIT/SOHO images for the period August 2001–December 2006, which correspond to the declining phase of solar cycle 23.

Aims. The study aims to find a relationship between the rotation of the SBCS and the subphotospheric angular velocity. The north-south asymmetries of both rotation velocity measurements are also investigated.

Methods. Subphotospheric differential rotation was derived using ring-diagram analysis of GONG++ full-disk dopplergrams of 1 min cadence. The coronal rotation was derived by using an automatic method to identify and track the small bright coronal structures in EIT full-disk images of 6 h cadence.

Results. We find that the SBCS rotate faster than the considered upper subphotospheric layer (3 Mm) by about 0.5 deg/day at the equator. This result joins the results of several other magnetic features (sunspots, plages, faculae, etc.) with a higher rotation than the solar plasma. The rotation rate latitudinal gradients of the SBCS and the subphotospheric layers are very similar. The SBCS motion shows an acceleration of about $0.005° \mathrm{day}^{-1}$/month during the declining phase of solar cycle 23, whereas the angular velocity of subsurface layers does not display any evident variation with time, except for the well known torsional oscillation pattern. Finally, both subphotospheric and coronal rotations of the southern hemisphere are predominantly larger than those of the northern hemisphere. At latitudes where the north-south asymmetry of the angular velocity increases (decreases) with activity for the SBCS, it decreases (increases) for subphotospheric layers.

Key words. Sun: rotation – Sun: helioseismology – Sun: corona – methods: data analysis

1. Introduction

The solar angular rotation velocity is a function of latitude, time, and height above or depth below the solar photosphere. This phenomenon is known as the solar differential rotation. The most commonly established latitudinal dependence of the angular velocity is given by the empirical relation $\Omega(\theta) = A + B\sin^2\theta + C\sin^4\theta$, where θ is the latitude, A is the equatorial rotation, B and C are the differential rotation coefficients, and C is usually neglected for low and mid-latitude measurements. In terms of amplitude, the rotation of the quiet Sun regions, given for instance by Doppler-shift measurements of Fraunhofer lines, is found to be slower than the rotation of the photospheric magnetic tracers (individual sunspots, sunspot groups, faculae, supergranules, etc.). Moreover, magnetic features exhibit different angular velocities depending on their evolution, age, and size (see a review by Beck 2000). So far, this difference is explained by magnetic features being rooted at different depths (Ruždjak et al. 2004). Several local and global helioseismology analyses of solar acoustic modes, such as time-distance helioseismology analysis (e.g., D'Silva 1996) and f-mode analysis (e.g., Corbard & Thompson 2002), have confirmed that the angular velocity increases with depth in the upper layers of the convection zone, at intermediate latitudes.

The coronal angular velocity has been measured using several coronal structures such as coronal green lines (e.g., Altrock 2003; Badalyan et al. 2006), radio emission flux (e.g., Mouradian et al. 2002), and coronal holes (e.g., Insley et al. 1995). Many of these features show two rotational modes where high-latitude regions rotate more rigidly than low-latitude regions. However, part of this behaviour has been related to the lifetime of the structure and not specifically to that of the corona (see a review by Schröter 1985). Moreover, small bright coronal structures (SBCS, hereafter) have been used to estimate the coronal rotation from data recorded by the EUV imaging telescope (EIT) on board the solar and heliospheric observatory (SOHO). These features are mostly short-lived structures with a lifetime up to 54 h (Brajša et al. 2008) and are formed at a height of about 8000–12 000 km above the photosphere (Brajša et al. 2004). Brajša et al. (2001, 2002) explored these structures using 284 Å EIT filtergrams with a 6 h cadence, whereas Karachik et al. (2006) used 194 Å EIT filtergrams with 12 min cadence. Both authors confirm the differential rotation of the corona through the SBCS with a close relation to the differential rotation of atmospheric magnetic features. Moreover, the SBCS are interesting features to be used for the rotation estimation along the cycle since they appear at both minimum and maximum cycle phases, in contrast to other activity features that are absent at minimum activity or, for instance, coronal holes with their polar concentration at that period. Their relation to the photospheric magnetic field has been studied by Pres & Phillips (1999), who find that the time evolution of bright coronal points observed with EIT/SOHO is correlated with the rise and fall of the magnetic field given by the MDI/SOHO magnetograms.

In this paper, we compare the rotation velocity of subphotospheric layers (from 3 Mm to 15 Mm) obtained from ring-diagram analysis of GONG++ data using the GONG ring-diagram analysis pipeline[1] (Corbard et al. 2003) with the one measured by tracing the SBCS observed in EIT/SOHO images (at 284 Å) using the automatic method described in Brajša et al. (2001). The purpose of this comparison is to get a complementary view of the relation between coronal features and their root layers below the photosphere. Moreover, we investigate the latitudinal gradient of the angular velocity to check the assumption of the two rotational modes and the variation of the latitudinal profile of the coronal rotation during the declining phase of the solar cycle 23 as reported by Altrock (2003). Finally, a comparison between the rotations of the northern and the southern hemispheres is shown for both SBCS and subphotospheric layers.

2. Data reduction

2.1. Rotation of subphotospheric layers

Subphotospheric angular velocity is measured using ring-diagram analysis which is a local helioseismology technique based on frequency-shift measurements of high-degree acoustic-modes to infer horizontal velocity flows at different subphotospheric depths (Hill 1988). By dividing the full-disk image into 189 overlapping patches with centres separated by 7.5° in latitude and longitude with a latitude range of [–52.5, 52.5] and a central meridian distance range of the same extent, each region is remapped and tracked at the surface rotation rate of its central latitude in consecutive images with a 1 min cadence. The resulting data cubes are Fourier-transformed, and the resulting power spectra are fitted with a Lorentzian profile to derive frequency shifts that are directly related to horizontal velocity components by assuming a plane wave approximation. The horizontal velocity as function of depth is then deduced using inversion methods.

We considered the depth range [3 Mm, 15 Mm]. We avoided extending the radial depth to upper layers since surface measurements of the flow are affected by poor estimation of the inversion kernels because of the complexity of the photospheric layers. Deeper measurements were not possible because the small size of the patches only gives access to high spatial frequencies (high spherical harmonic degree). The sidereal angular velocity for each local area (latitude, Carrington longitude) was recovered by adding the measured east-west flow (zonal flow) to the tracking rate. Finally, the rotation rate at each latitude is given by averaging over all the available Carrington longitudes for each month. The synodic-sidereal correction was taken into account for each day.

2.2. Rotation of small bright coronal structures

The data reduction to determine the motions of bright coronal structures was described in detail by Brajša et al. (2001). Although not just coronal bright points (CBP) were selected in the cited paper, this abbreviation was used. In fact, besides points also small loops and small active regions were selected. We prefer to call the used tracers small bright coronal structures (SBCS) now. The interactive method has up to now only been applied to images obtained in 1998 and 1999, because it is very time consuming. An automatic method was developed later to cover more images from most of the years of an activity cycle. The main idea was to automatically select small structures in three consecutive images and find whether they belong to a stable structure within 12 h so they only show small changes in latitude and in longitude. Slight differences were applied to the parameters of the automatic reduction program (Brajša et al. 2001). First, the circumferences of the allowed structures was changed to the range of 30 to 80 pixels, which equals 80 to 210 arcsec. The range of relative intensities was 100 to 600 units. Most important was a change in the allowed difference in latitude from one image to the next from 1 degree to 0.8 degree and the application of a differential rotation for the allowed motions in longitude: the limits were 9.5 to 16.5 degrees per day of the synodic rotation, but these limits were reduced by $-3.0{*}\sin^2(\theta)$, where θ is the latitude.

The conversion of synodic rotation rates to sidereal was performed for each observing time separately. Filtering after a first fit to the differential rotation law with $C = 0$ was applied in the same way as described in Sect. 4.2 of Brajša et al. (2001). This filtering was applied only when data from certain periods (e.g. months, years or longer periods) are combined. Thus the sum of all structures used is slightly different when adding monthly numbers and comparing with annual sums. At the beginning the data were selected for all latitudes in each month and only differential rotation parameters fitted using $C = 0$. To adapt the reduction to the GONG++ data, a new program was added, where the results were sampled for overlapping bins of 15 degrees width in latitude and a stepping of 7.5 degrees. Thus a data cube was derived with rotation rate results and their errors for 15 latitude bins and 65 months from August 2001 until December 2006.

3. Solar differential rotation

We measured the subphotospheric and coronal rotation velocities for the period August 2001–December 2006, which corresponds to the declining phase of solar cycle 23. GONG++ data covers all the months with a good duty cycle. The variation in the zonal flow (i.e. rotation residual) as derived from ring-diagram analysis of GONG++ data during this period has been studied in detail by Komm et al. (2009) with 3 extra months in 2007. They find a positive correlation between the unsigned magnetic flux and the zonal flow and report a higher zonal flow in patches with activity than for the quiet Sun patches. They do not find any particular long-term pattern of the zonal flow except the well-known pattern of torsional oscillations (Howard & LaBonte 1980). However, a slight increase in the zonal flow in patches with activity was observed at minimum activity. Figure 1 shows the sidereal angular velocity given by the coronal and subphtospheric measurements for the latitudinal range [−52.5°, 52.5°]. From ring-diagram analysis measurements, we see that deep subsurface layers rotate faster than those closer to the surface with a decreasing radial gradient as the latitude increases. The radial gradient variation in the rotation velocity estimated

---

[1] `http://gong2.nso.edu/archive/patch.pl?menutype=h`

Table 1. Unsigned differential rotation parameter B derived from the linear fit of the rotation averaged over 3 time frames (Aug. 2001–Dec. 2006; Aug. 2001–Mar. 2004; Apr. 2004–Dec. 2006) and $\sin^2(\theta)$ for all latitudes [−45°, 45°], southern hemisphere [−45°, 0°] and northern hemisphere [0°, 45°].

	August 2001–December 2006			August 2001–March 2004			April 2004–December 2006		
	All latitudes	North	South	All latitudes	North	South	All latitudes	North	South
SBCS	2.72 ± 0.04	2.77 ± 0.04	2.64 ± 0.04	2.70 ± 0.03	2.70 ± 0.04	2.69 ± 0.04	2.73 ± 0.07	2.82 ± 0.07	2.59 ± 0.08
3 Mm	2.77 ± 0.01	2.74 ± 0.01	2.73 ± 0.01	2.77 ± 0.01	2.77 ± 0.02	2.70 ± 0.02	2.77 ± 0.01	2.72 ± 0.02	2.76 ± 0.02
6 Mm	2.78 ± 0.01	2.77 ± 0.01	2.73 ± 0.01	2.78 ± 0.01	2.80 ± 0.02	2.70 ± 0.02	2.78 ± 0.01	2.74 ± 0.02	2.76 ± 0.02
15 Mm	2.88 ± 0.01	2.90 ± 0.01	2.80 ± 0.01	2.88 ± 0.01	2.93 ± 0.02	2.77 ± 0.02	2.88 ± 0.01	2.87 ± 0.02	2.82 ± 0.02

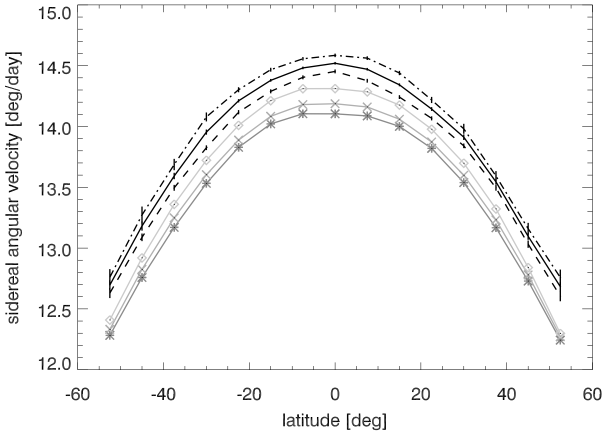

Fig. 1. Rotation velocity derived from ring-diagram analysis at 3 Mm (asterisk), 7 Mm (cross), 15 Mm (diamond) (lines from dark to light grey) and SBCS tracing (black) averaged over the periods: August 2001–March 2004 (dashed), April 2004–December 2006 (dashed dotted).

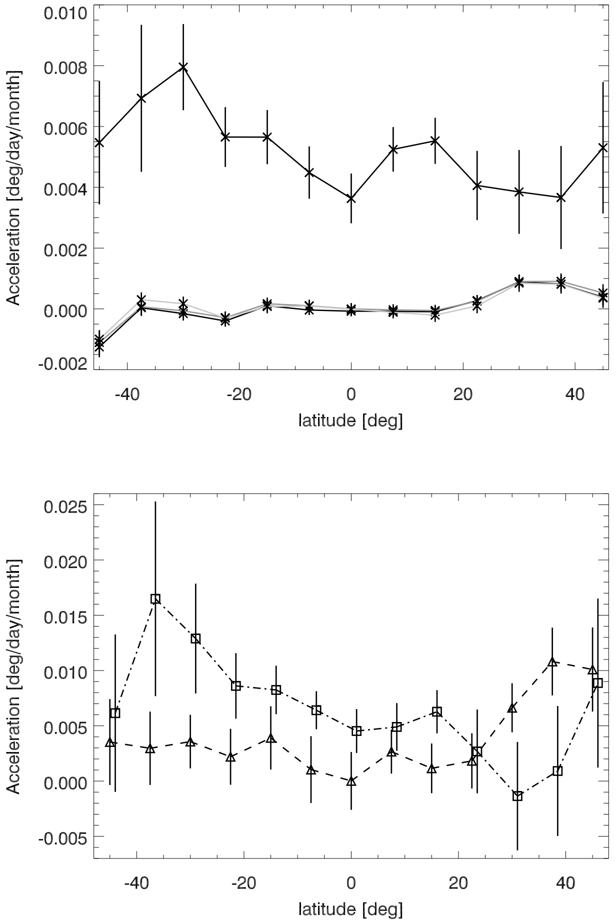

Fig. 2. *Upper panel*: slope of the linear fit of the rotation with time derived from ring analysis at 3 Mm, 6 Mm and 15 Mm (from dark to light grey) and SBCS tracing (black) for the period Aug. 2001–Dec. 2006. *Lower panel*: slope of the linear fit of the SBCS angular velocity with time for the periods: Aug. 2001–Mar. 2004 (dashed line, triangles); Apr. 2004–Dec. 2006 (dashed-dotted line, squares). Squares are shifted by 1° to avoid overlapping of error bars.

from ring-diagram analysis of the same data was studied in detail by Zaatri & Corbard (2009), who report that the use of higher latitudes can lead to a reversal of the radial gradient from negative to positive. Moreover, Fig. 1 shows a smaller northern radial gradient than the southern gradient at high latitudes. From SBCS tracing, the rotation rate is found to be higher than for all the considered subsurface layers by about 0.5° day^{-1} at the equator (this corresponds to a velocity of about 70 m/s, and a frequency of about 16 nHz) compared to that of the subsurface layer at 3 Mm depth. This difference is in good agreement with the angular velocity difference between the photospheric active regions and their surrounding quiet solar plasma (e.g., Koch 1984).

The upper panel of Fig. 2 shows the angular acceleration of the SBCS and of the subsurface layers. The subphotospheric layers have no significant acceleration compared to that of the SBCS. However, it is worth mentioning that the absence of acceleration at low latitudes and the week acceleration at latitudes higher than 20° (up to 10^{-3} deg/day/month) is consistent with the torsional oscillation pattern for the years 2001–2006 (see Fig. 30 of Howe 2009). The SBCS rotation shows a positive increase with an acceleration of about 0.005° day^{-1}/month. This acceleration also depends on activity as shown by the lower panel of Fig. 2. At higher activity, the acceleration is clearly seen to be lower than the lower activity for the southern hemisphere; however, it shows a more complicated latitudinal and activity variation in the northern hemisphere. It is worth mentioning that the photospheric magnetic features are also rotating faster at low activity, as seen from several observations (e.g., Brajša et al. 2006).

Lastly, we investigated the latitudinal gradient of the rotation by measuring the differential rotation coefficient B. We avoided taking the highest latitude ±52.5° where the SBCS are almost absent at low activity, leading to angular velocities which are mostly interpolated values. Table 1 gives the B values for both SBCS and three subphotospheric layers, and B is seen to increase with depth at the outer part of the convection zone. Moreover, neither the small SBCS nor the subphotospheric layers show any significant variation with the activity of the latitudinal gradient of their angular velocity.

4. North-south asymmetry

We investigated the north-south asymmetry of the coronal rotation velocity through the SBCS angular velocity change between the northern and southern hemispheres by evaluating the difference between two symmetric bins. For instance, a rotation velocity averaged over a bin centred at 15° is subtracted from that derived from a bin centred at −15°, the difference value is shown at latitude 15°. This quantity is evaluated for the unsigned latitude range [7.5°, 45°] in the upper panel of Fig. 3. The north-south asymmetry of the coronal rotation reveals a faster southern hemisphere during the period under analysis. Also shown is a latitudinal dependence of this property with an increasing north-south difference in rotation from the equator to about 20°, where the amplitude is more pronounced with strong activity. At latitudes higher than 20°, this asymmetry continues to increase at the low activity level (end of cycle 23), whereas it is more irregular at the beginning of the declining phase and becomes even positive around 30°. To see whether the asymmetry in the coronal rotation velocity is related to the coronal activity, we investigated the activity asymmetry via the asymmetry index given by $(N - S)/(N + S)$ for each pair of symmetric bins where N is the number of structures in the northern bin and S is the number of structures in the southern bin. The asymmetry index and its statistical mean error are evaluated on a monthly basis and shown in Fig. 3. The figure shows that the northern coronal activity prevails during the first half of the declining phase of solar cycle 23 and the southern activity is more dominant during the second half of this period. This agrees with the flare activity during this cycle, which favoured the north at maximum activity and the south during the declining phase (Joshi et al. 2007). Figure 3 clearly shows that, in the first half of the declining phase of solar cycle 23, the northern hemisphere, which is more active, rotates more slowly than the southern hemisphere, and it remains slower at the end of the cycle even though it becomes less active than the southern hemisphere. This disagrees with several studies reporting that the active hemisphere rotates more slowly than the less active one (Obridko et al. 2001).

Figure 4 shows the difference between the northern and southern rotation velocities for three subsurface layers at depths of 3 Mm, 7 Mm, and 15 Mm. As for the SBCS, subsurface rotation velocity is predominantly southern except at the intermediate latitudes of the upper subsurface layers during the low activity epoch. This southern dominance also characterised the photospheric magnetic activity during solar cycle 23 as shown from sunspot indicators (See Li et al. 2008, and references therein). Besides, Zaatri et al. (2006) have analysed the first three years of our GONG++ dataset and found that the zonal flow pattern and its north-south asymmetry are strongly related to the distribution of magnetic activity. Moreover, a clear increase of this asymmetry with depth is seen for the whole period. This confirms, for a longer period, the results by Zaatri et al. (2006) who found the same north-south asymmetry depth dependence for the zonal flow. Unlike the SBCS, the north-south asymmetry in the subsurface rotation velocity shows a slight increase with decreasing activity, at low latitudes. At latitudes higher than 20° and close to solar cycle maximum, the subsurface asymmetry is slightly changing until around 40°. During the low activity epoch, the rotation velocity of the southern hemisphere gets very close to the northern velocity and even smaller around latitude 30° for the upper subsurface layers.

Some hints of the north-south asymmetry are also given from the latitudinal gradient in Table 1 where the subsurface layers show more varying B values with depth in the northern hemisphere than in the southern hemisphere for both activity levels. The SBCS have a more pronounced north-south variation of B at low activity than at high activity.

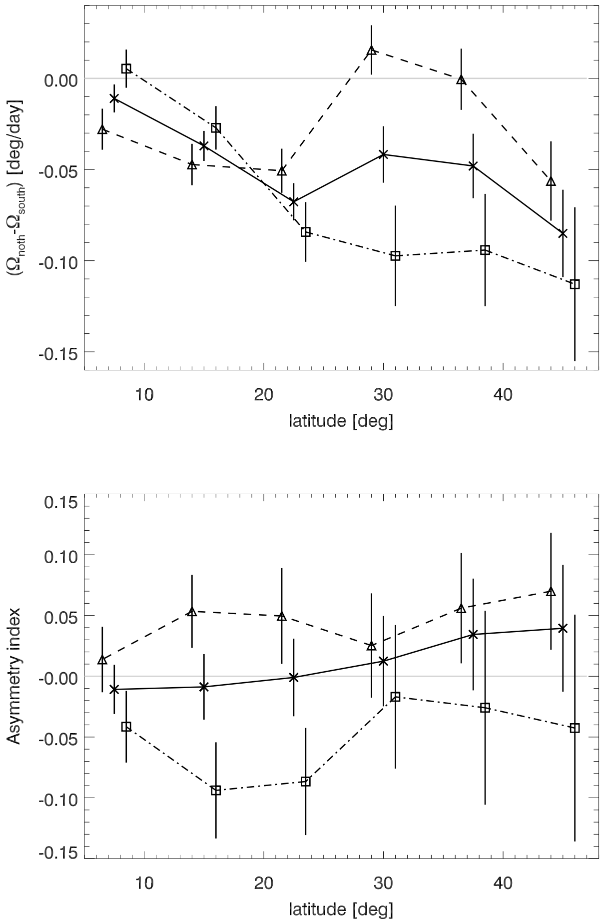

Fig. 3. *Upper panel*: difference between the northern and southern angular velocity of SBCS averaged over the periods August 2001–December 2006 (full lines), August 2001–March 2004 (dashed, triangles), April 2004–December 2006 (dashed-dotted,squares). *Lower panel*: asymmetry index of the coronal activity derived from the number of observed SBCS in the north (N) and in the south (S) given by the formula (N-S)/(N+S) by summing the structures over the periods given in the upper panel. The thin grey line shows the zero level. Triangles and squares are shifted by 1° to the left and right to avoid overlapping the error bars.

5. Discussion and conclusion

In this work, we compared the rotation of the corona as revealed by tracing its most profuse features, the SBCS, and that of the uppermost layers of the convection zone. We report the following results:

(i) There is a difference of about 0.5° day^{-1} between the angular velocity of the SBCS and the upper considered subphotospheric layer at 3 Mm below the surface. This difference decreases while considering deeper layers due to the increase of the angular velocity with depth at intermediate latitudes. At the highest latitudes of our considered range $[-52.5°, 52.5°]$, the radial gradient of the rotation velocity decreases considerably and the difference between the angular velocities of the SBCS and the various subsurface layers becomes very similar.

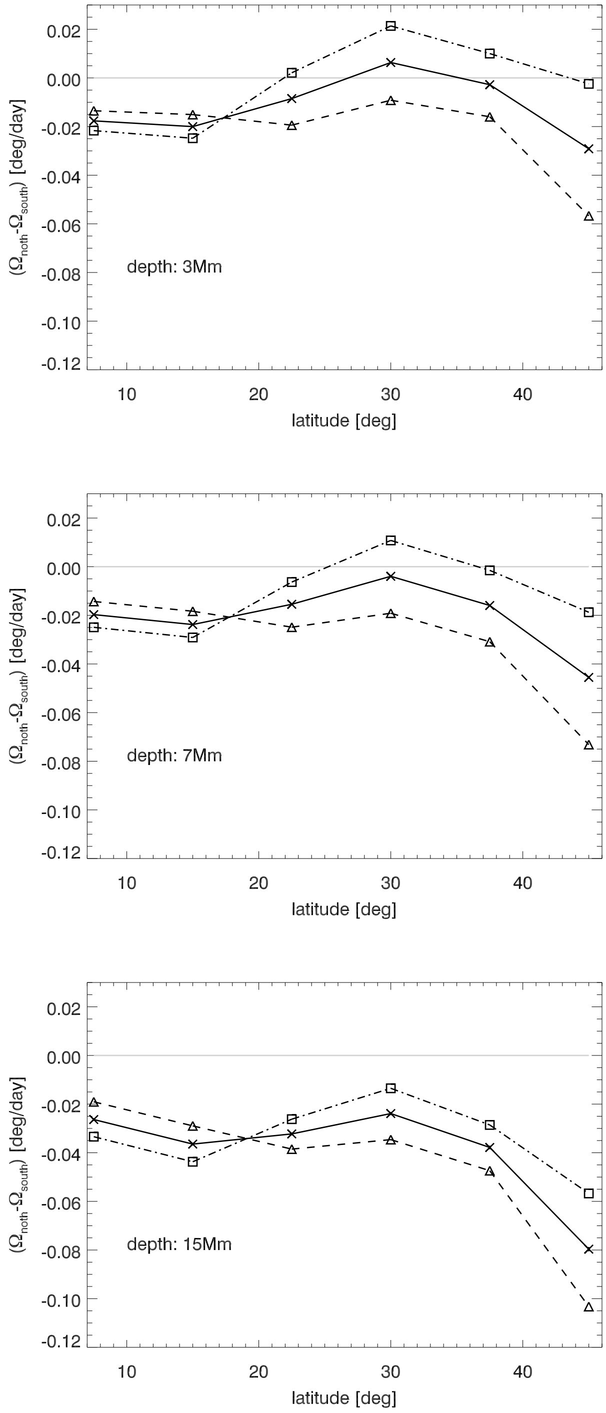

Fig. 4. Difference between the northern and southern averaged angular velocity of subsurface layers as a function of unsigned latitude and for depths 3 Mm, 7 Mm and 15 Mm. Shown are the periods: August 2001–December 2006 (full lines), August 2001–March 2004 (dashed), April 2004 – December 2006 (dashed-dotted). The thin grey line shows the zero level.

(ii) The temporal variation of the SBCS angular velocity during the declining phase of the solar cycle 23 shows an acceleration of about 0.005° day $^{-1}$/month on average and reaches its maximum during the low activity period (end of cycle 23) in the southern hemisphere. It is not clear whether this acceleration is related to the chosen tracers or if it is the property of the corona and whether it is specific to the studied period. So far, there have been no studies of the coronal rotation using other activity features for the last years of solar cycle 23. However, results from other periods have reported a deceleration that makes the coronal rotation tend to that of the photosphere at solar minimum (e.g. Giordano et al. 2008, for the period 1996–1997), whereas Mehta (2005) did not find any evidence of the coronal rotation variation during four consecutive solar cycles (19 to 22). The angular velocity does not show a significant temporal variation except a slight acceleration at high latitudes which corresponds to the torsional oscillation signal during the period 2001–2006.

(iii) The latitudinal dependence of the angular velocity from the two measurements was studied through the differential rotation parameter B as given by the most commonly used rotation law at intermediate latitudes θ ($\Omega(\theta) = A + B\sin^2\theta$). We found a very similar latitudinal gradient B of coronal and subphotospheric rotations, except that the unsigned value of B slightly increases with depth. From this point of view, we do not see any particularity in the latitudinal behaviour of the coronal rotation as mentioned by several authors from long-term coronal features observations, notably, the widely mentioned existence of two different rotational modes with a more rigid rotation of the corona than for the photosphere at low latitudes (Altrock 2003). Clearly, the SBCS behave more like magnetic photospheric features which endorses the hypothesis of the formation of EUV bright points as being caused by the heating derived from the dissipation of electric currents that are formed in the solar atmosphere from the displacement of footpoints of magnetic flux tubes by the photospheric plasma motion (see Santos et al. 2008, and references therein).

(iv) For both corona and subphotospheric layers, the southern hemisphere rotates predominantly faster than the northern hemisphere. The north-south velocity difference increases with depth. This result was already shown in Zaatri et al. (2006) and is now confirmed for a longer period including the very low activity period of cycle 23. Also, when the north-south asymmetry of the rotation velocity is lower than its temporal average for the subsurface layers, it is higher for the SBCS and vice-versa. Clearly, the southern coronal hemisphere rotates faster than the northern hemisphere regardless of which hemisphere is more active. It would be interesting to see whether this persists on a time scale of multiple cycles as opposed to the relatively short time scale of our study.

Acknowledgements. A. Zaatri and M. Roth acknowledge support from the European Helio- and Asteroseismology Network (HELAS) which is funded by the European Commission's Sixth Framework Programme. The research of R. Brajša leading to the results presented in this paper has received funding from the European Community's Seventh Framework Programme (FP7/2007-2013) under grant agreement No. 218816. The work on SBCS analysis was performed with the support of the Alexander von Humboldt Foundation and is related to the SOHO-EIT Proposal Brajša 206: "An analysis of the solar rotation velocity by tracing coronal features" (`http://umbra.nascom.nasa.gov/eit/proposals/`) submitted in March 1999 by R. Brajša, B. Vršnak, V. Ruždjak, D. Roša, H. Wöhl, and F. Clette. SOHO is a project of international cooperation between ESA and NASA. We would like to thank the EIT team for developing and operating the instrument. We thank F. Clette, J.-F. Hochedez, S.F. Gissot and J. de Patoul for providing the EIT images used and helpful discussions. This work utilises data obtained by the Global Oscillation Network Group (GONG) programme, managed by the National Solar Observatory, which is operated by the Association of Universities for Research in Astronomy (AURA), Inc. under a cooperative agreement with the National Science Foundation. The data were acquired by instruments operated by the Big Bear Solar Observatory, High Altitude Observatory, Learmonth Solar Observatory, Udaipur Solar Observatory, Instituto de Astrofisica de Canarias, and Cerro Tololo Interamerican Observatory.

References

Altrock, R. C. 2003, Sol. Phys., 123, 23

Badalyan, O. G., & Sýkora, J. 2006, Adv. Space Res., 38, 906

Beck, J. G. 2000, Sol. Phys., 191, 47

Brajša, R., Wöhl, H., Vršnak, B., et al. 2001, A&A, 374, 309

Brajša, R., Wöhl, H., Vršnak, B., et al. 2002, A&A, 392, 329

Brajša, R., Wöhl, H., Vršnak, B., et al. 2004, A&A, 414, 707

Brajša, R., Ruždjak, D., & Wöhl, H. 2006, Sol. Phys., 237, 365

Brajša, R., Wöhl, H., Vršnak, B., et al. 2008, Cent. Eur. Astrophys. Bull., 32, 165

Corbard, T., & Thompson, M. J. 2002, Sol. Phys., 205, 211

Corbard, T., Toner, C., Hill, F., et al. 2003, in Proceedings of SOHO 12/GONG+ 2002, Local and global helioseismology: the present and future, ESA SP-517, 255

D'Silva, S. 1996, ApJ, 462, 519

Giordano, S., & Mancuso, S. 2008, ApJ, 688, 656

Hill, F. 1988, ApJ, 333, 996

Howard, R., & LaBonte, B. J. 1980, ApJ, 239, 33

Howe, R. 2009, Living Reviews in Solar Physics, 6, lrsp-2009-1 http://www.livingreviews.org/lrsp-2009-1

Insley, J. E., Moore V., & Harrison, R. A. 1995, Sol. Phys., 160, 1

Joshi, B., Pant, P., Manoharan, P. K., & Pandey, K. 2007, ASP Conf. Ser., 368, 539

Karachik, N., Pevtsov, A. A., & Sattarov, I. 2006, ApJ, 642, 562

Koch, A. 1984, Sol. Phys., 93, 53

Komm, R., Howe, R., Hill, F., & González Hernández, I. 2009, Sol. Phys., 254, 1

Li, K. J., Gao, P. X., & Zhan, L. S. 2009, Sol. Phys., 254, 145

Mouradian, Z., Bocchia, R., & Botton, C. 2002, A&A, 394, 1103

Mehta, M. 2005, Bull. Astr. Soc. India, 33, 323

Obridko, V. N., & Shelting, B. D. 2001, Sol. Phys., 201, 1

Pres, P., & Phillips, K. J. H. 1999, ApJ, 510, L73

Ruždjak, D., Ruždjak, V., Brajša, R., & Wöhl, H. 2004, Sol. Phys., 221, 225

Santos, J. C., Büchner, J., Madjarska, M. S., & Alves, M. V. 2008, A&A, 490, 345

Schröter, E. H. 1985, Sol. Phys., 100, 141

Zaatri, A., & Corbard, T. 2009, in proceedings of GONG 2008/SOHO XXI meeting ASP Conf. Ser., in press

Zaatri, A., Komm, R., González Hernández, I., Howe, R., & Corbard, T. 2006, Sol. Phys., 236, 227

Chapter 8

Solar subsurface radial gradient of angular velocity

> *... the $\alpha\Omega$ dynamo [More precisely, it should be called $\alpha\nabla\Omega$ dynamo as only the derivatives of Ω matter]...*
>
> M. Stix
> The Sun: An Introduction

Abstract

The sub-surface axisymmetric part of the rotational radial gradient has been measured using global helioseismology of surface gravity modes that penetrate down to about 15 Mm. This study revealed a hint of a sign reversal at mid- to high latitudes. Ring diagram analysis allows a better resolution of the sub-surface layers from very high degree modes and is able to resolve both northern and southern hemispheres. These capabilities allow to get enriched information about the radial gradient except at high latitudes where the foreshortening effect crucially degrades the measurements. This chapter discusses the long term behavior in depth and latitude of the radial rotational gradient inferred from ring diagram analysis of 7 continuous years of GONG data. With this study, we hope to bring more insights to the solar dynamo models where the rotational gradient is a crucial ingredient, notably at the sub-photosphere where a shear layer might also also contribute to the solar dynamo.

8.1 Goal of the study

The radial gradient of angular velocity is calculated from numerical differentiation, using 3-points, of the zonal flow in the depth range [1 Mm, 14 Mm] for the whole range of the dense-pack latitudes. Zonal flows are taken from 93 synoptic maps (CR = 1979 – 2071, i.e. July 2001 – July 2008) constructed as described in the previous chapter and averaged over Carrington longitudes for each CR, latitude and depth. The studied period is the declining phase of solar cycle 23 from its maximum with a high magnetic activity to its minimum corresponding to the end of the cycle. In this chapter, I will discuss the long term variation of the gradient in both hemispheres and the north-south symmetrized gradient and make a small comparison with the gradient inferred from f-mode splitting inversion (Corbard and Thompson, 2002). Finally, another way to measure the radial gradient by inverting frequency shifts will be shortly discussed.

8.2 Rotational radial gradient in the two hemispheres

Hereafter, I discuss the most prominent behavior of the temporal variation of the radial gradient in depth and latitude at both northern and southern hemispheres.

General behavior of the radial gradient:

The variation over time of the radial gradient at latitudes up to 52.5° north and south is shown in figure 8.1 at depths between 2 Mm and 12 Mm. The radial gradient is mostly negative and its variation in latitude and depth is overly homogeneous in time except for a particular behavior at the beginning of 2007 at mid latitudes of the southern hemisphere where an uncommon strong gradient appeared (-1000 nHz/R close to the surface). At the shallowest layers, the gradient shows strong discontinuities with latitude where the equator displays the strongest gradient no weaker than 600 nHz/R in amplitude. The gradient decreases again between 15° and 30° then increases on average for latitudes up to 45° where it starts to considerably decrease to reach the weakest amplitudes in latitude. As we go deeper, the amplitude of the gradient decreases at all latitudes and the latitudinal discontinuity gets less pronounced until the gradient becomes roughly constant (about -300 nHz/R) from the equator to latitudes up to 40° where it decreases more pronounced in the northern hemisphere than in the southern hemisphere. This general behavior in latitude and depth is shown from the temporal average of the radial gradient over the whole period (93 CR), displayed in figure 8.2. Moreover, figure 8.3 shows the difference between the averaged northern gradient and the averaged southern gradient at considered depths. This north-south difference is positive everywhere meaning that the amplitude of the southern radial gradient is stronger than the northern one at all latitudes and depths. This difference increases with latitude at all depths and increases with depth in the first 1% than decreases in deeper layers. This result joins the study of the north-south asymmetry in chapter 7, where the zonal flow was also seen to be stronger in the southern hemisphere than in the northern hemisphere, so does the magnetic activity in the declining phase of solar cycle 23.

Sign reversal of the gradient at high latitudes:

The averaged gradient does not show a sign reversal at depths down to 14 Mm in the range of dense-pack latitudes (up to 52.5°). Nonetheless, by extrapolating to higher latitudes 52.5° it might be possible to find a sign reversal there. Figure 8.4 displays latitudinal derivative of the averaged gradient at the highest latitudes (latitude $> 30°$) as a function of depth, where the highest value is reached around 0.995R and becomes constant in depth together with reaching its lowest value at 0.990R. This could lead us to suppose that, most likely, the sign reversal of the gradient at high latitudes might appear in depths around 0.995R where the the gradient gets very steep with latitude contrary to the deeper layers where the gradient becomes more rigid in latitude. This joins (Corbard and Thompson, 2002) who studied the radial gradient from f-modes and conjectured that the sign reversal might appear at the first 5Mm below the surface. Moreover, figure 8.4 shows a higher slope at the northern hemisphere than the southern hemisphere. This supposes that the sign reversal of the gradient in the northern hemisphere might appear at lower latitudes than in the southern hemisphere. Nonetheless, we do see some sign reversals at the highest latitude (52.5°) randomly appearing at particular carrington rotations as shown in figure 8.5. This figure clearly shows that most of the positive radial gradient appears in the northern hemisphere and is more concentrated at deep layers. Surprisingly, at periods where the positive radial gradient appears, it is either northern or southern, i.e. it never appears in both hemispheres simultaneously for the same period.

Strong negative gradient close to the surface:

In order to better see the extent of the strong negative gradient at the shallowest layers, I plotted in figure 8.6 contour plots of the gradient with absolute values equal to 500 nHz/R and higher, in time and depth. In the equatorial regions, this strong gradient is observed in the whole studied period (93 CR) from the surface down to 0.8% at the equator and down to 0.7% at latitudes ±7.5°. At latitudes 15° and 22.5° north and south, such a strong gradient is not visible at all time and is only located at the first 0.5%. The extension in depth of the strong gradient increases again at latitudes 30° and 37.5° until about the same extension as in the equatorial regions. In addition, at these latitudes, an exception is seen at the beginning of 2007 (CR: 2055 – 2058) where the strong southern radial gradient goes as deep as about 13Mm with an amplitude of 500 to 600 nHz/R.

A singularity in the behavior of the gradient at the beginning of solar minimum:

In the following, I will focus on the strong unusual radial gradient that went as deep as about 2% of the Sun, observed at periods corresponding to the beginning of solar cycle minimum. Figure 8.7 shows the radial gradient as a function of depth for a restricted period, corresponding to solar cycle minimum, of 20 Carrington rotations lasting from 2049 to 2069. It appears from this figure that the strong negative gradient that goes as deep as about 13 Mm in the southern mid-latitudes increases downwards in amplitude, whereas the most common behavior of the gradient is to decrease in amplitude downward at all latitudes as seen from figure 8.2. The Carrington rotation that follows the period of this reversed gradient (around 2057) shows again a negative radial gradient with an amplitude decreasing downward but with a much stronger amplitude than usual. Indeed, figure 8.8 where the radial gradient at Carrington rotation 2057 is plotted as a function of depth and latitude, shows that the strong gradient in the southern mid-latitudes has an amplitude as high as 1000 nHz/R and is even much stronger than the equatorial gradient, which is found elsewhere to be the strongest gradient in latitude (see figures 8.1, 8.2).

In order to find any eventual explanation to this singularity, I looked on several solar observations that could report any anomaly during the period where this gradient reversed, starting from CR 2051 (see figure 8.7) which correspond to the end of the cycle, i.e. beginning of solar cycle minimum. I found that sunspot 930 which appeared few degrees below the equator at the end of Carrington rotation 2050 and at the beginning of Carrington rotation 2051, caused one of the strongest solar flares of the last 30 years, albeit the solar activity was very weak. It appeared on the front side on the 5th of December 2006 creating an X9 class flare, followed by an X6 class flare (Dec. 6th) and an X3 class flare (Dec. 13th). These strong flares have been reported by several solar spacecrafts such as the GOES[1] solar x-ray imager[2]. The first flare was so strong that auroras were seen at very low terrestrial latitudes (central Europe) and the Global Positioning System (GPS) were significantly impacted. Many news regarding sunspot 930 have been reported in the NASA website[3]. It is hard to decide whether the two events of the reversed gradient and the production of the strong solar flare are related to each other or whether the reversed gradient is related to the solar minimum itself. For further studies, it might be worth checking more carefully the correlation between the reversed gradient and the production of solar flares in other locations and periods. Moreover, a longer term perspective would be to see whether this reversed gradient followed by a very strong negative gradient will appear in the incoming solar minimum and whether it could explain in some sense the large extent of the solar minimum period of solar cycle 23.

---

[1] Geostationary Operational Environmental Satellites

[2] http://goes.ngdc.noaa.gov/data/plots/2006/GOES-200612_special.pdf

[3] http://search.nasa.gov/search/search.jsp?nasaInclude=sunspot+930

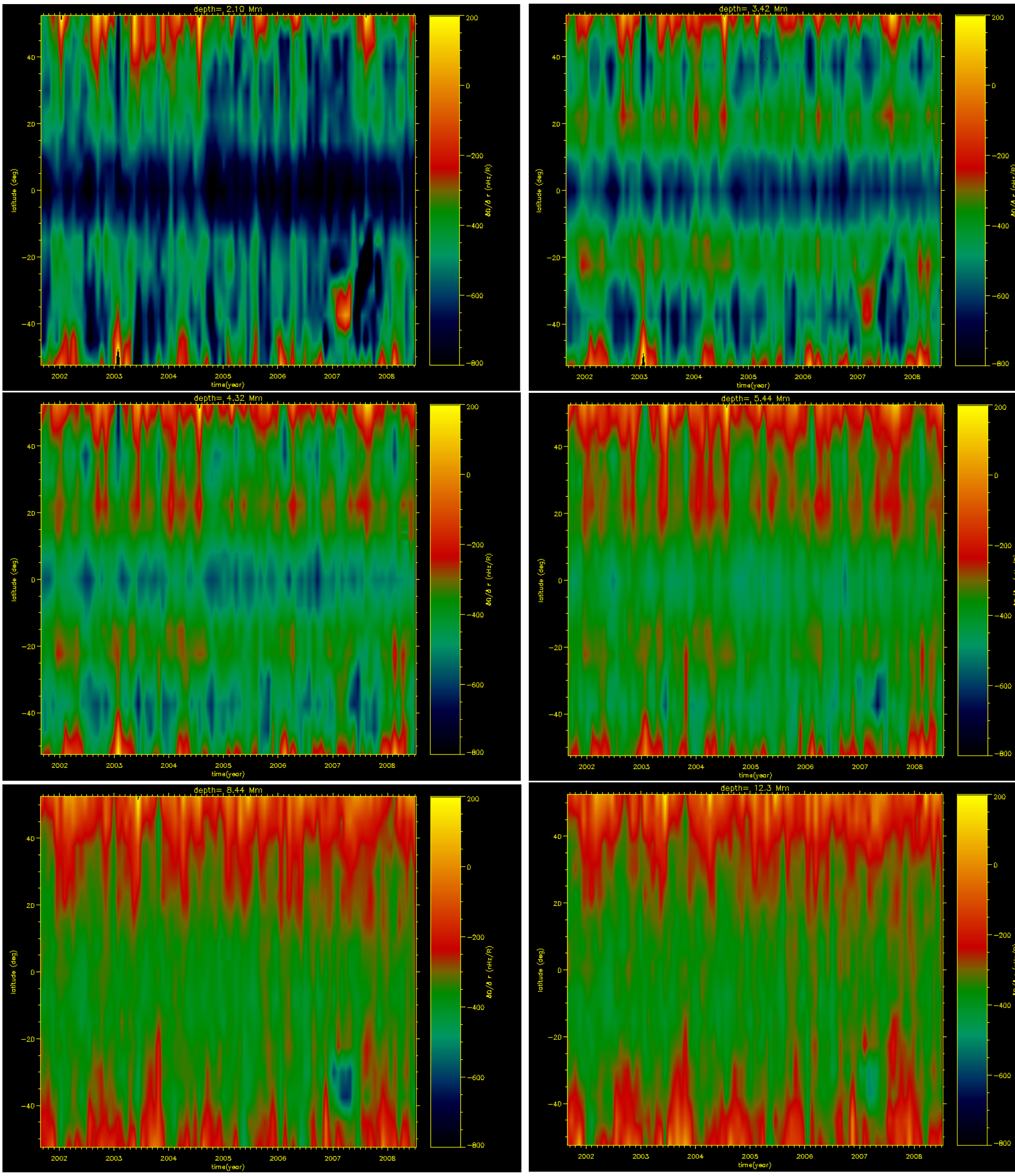

Figure 8.1: Radial gradient of angular velocity in nHz/R as a function of time (July 2001 – July 2008 , CR = 1979 – 2071) and latitude at a given depth. From top to bottom and from left to right, depths are: 2.1 Mm, 3.42 Mm, 4.32 Mm, 5.44 Mm, 8.44 Mm, 12.3 Mm.

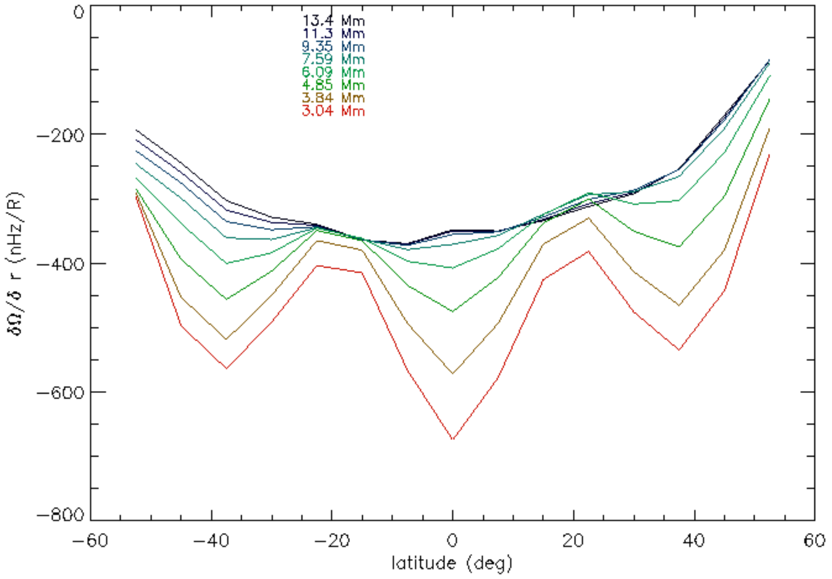

Figure 8.2: Averaged radial gradient of angular velocity in nHz/R over 93 Carrington rotations as a function of latitude at given depths. The gradient looks similar in both hemispheres except at high latitudes where the northern gradient gets weaker than the southern one at all depths.

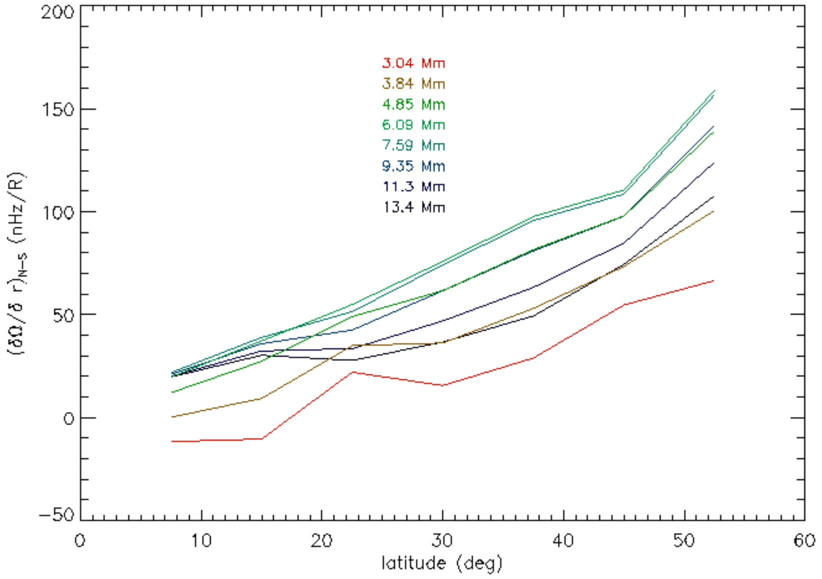

Figure 8.3: North-South difference of the averaged radial gradient of angular velocity in nHz/R over 93 Carrington rotations as a function of latitude at given depths. The difference is positive at all depths and latitudes meaning that the southern hemisphere has a stronger radial gradient (in amplitude) than the northern hemisphere.

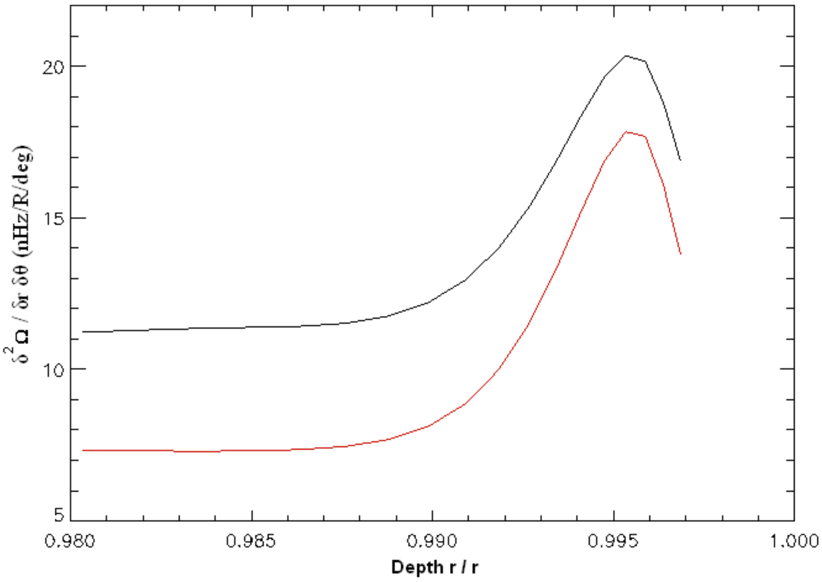

Figure 8.4: Latitudinal derivative of the averaged radial gradient of the averaged radial gradient of angular velocity of figure 8.2 at latitudes higher than 37.5° as a function of depth. The value is derived from the slope of a linear fit of the averaged gradient, of the northern (black) and southern (red) hemispheres, with the highest latitudes [37.5,45,52.5].

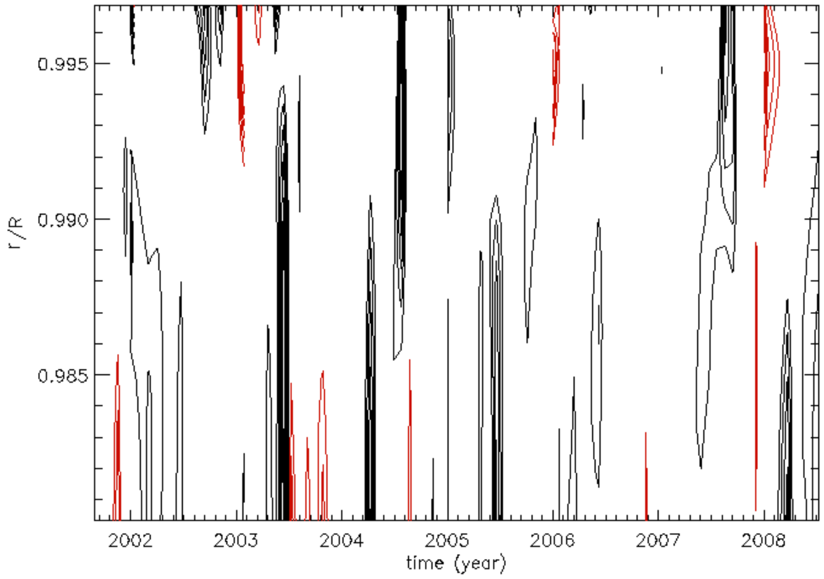

Figure 8.5: Contour plots of the positive radial gradient of angular velocity in nHz/R as a function of time (93 CR) and depth, in the northern hemisphere (black) and the southern hemisphere (red) at latitude 52.5°. Most of the positive gradient is accuring in the northern hemisphere. It is sometimes detected in the southern hemisphere but never in both hemispheres at the same time.

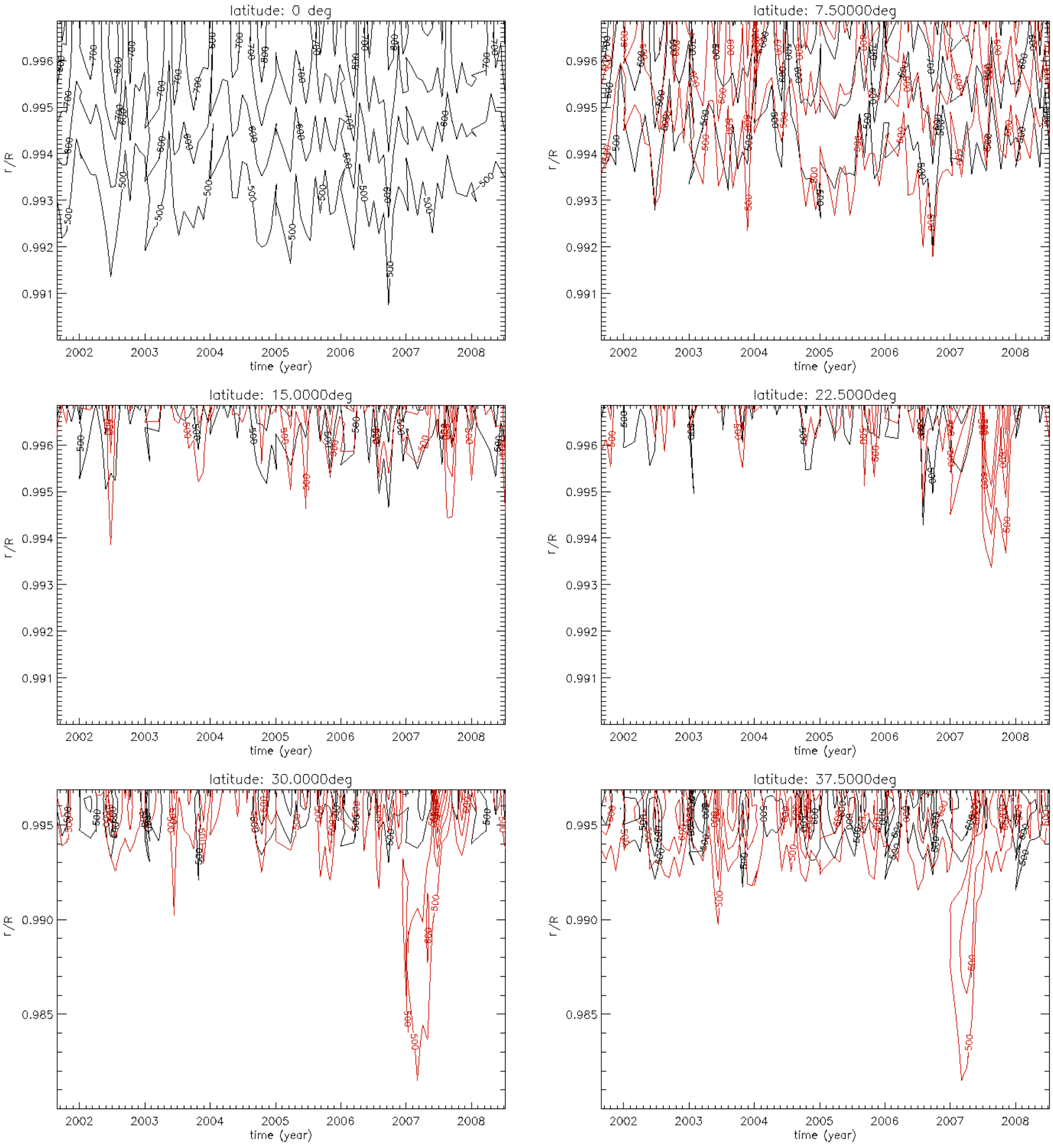

Figure 8.6: Contour plots of strong radial gradient of angular velocity (with amplitudes 500 nHz/R and higher) given as a function of time (July 2001 – July 2008, CR= 1979 – 2071) and depth for a given latitude. In the same panel symmetric latitudes about the equator are given; southern latitude (red), northern latitude (black). From top to bottom and from left to right latitudes are: 0°, 7.5°, 15°, 22.5°, 30°, 37.5°. Note that the y-axis in the bottom panels differs from those in the top panels.

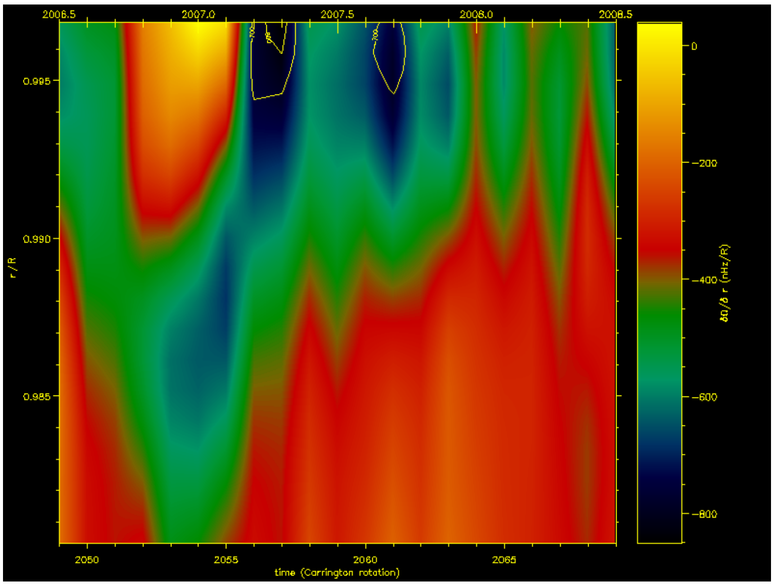

Figure 8.7: Radial gradient of angular velocity in nHz/R at latitude 37.5° as a function of depth and time CR=[2049 – 2069], the top axis gives time in fractions of the year. At around Carrington rotation 2057, a strong negative gradient appears and is preceded by a reversed radial gradient around 2054 with increasing amplitude in depth instead of decreasing as for its usual behavior.

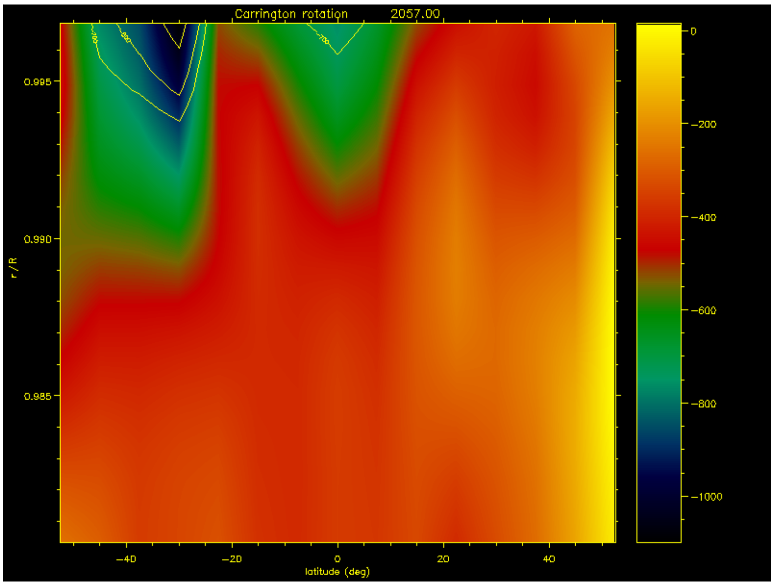

Figure 8.8: Radial gradient of angular velocity in nHz/R as a function of latitude and depth for Carrington rotation 2057. The high gradient in the southern hemisphere is much stronger than the gradient at equatorial regions for the same range of depths.

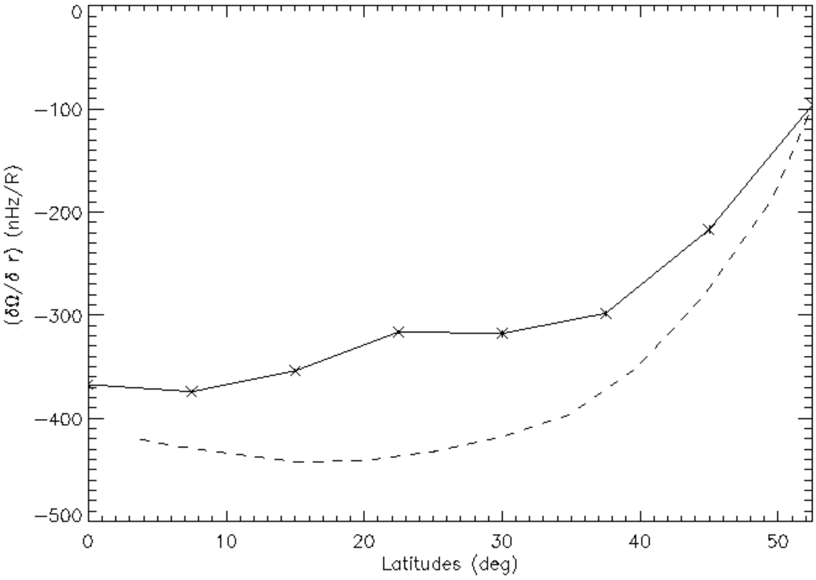

Figure 8.9: Radial gradient derived from a linear fit of angular velocity as a function of latitude. f-mode splitting inversions (dashed) and ring diagram analysis (full).

8.3 North-South symmetrized radial gradient of angular velocity

The radial gradient of the angular velocity has been studied from f-mode splittings inversion down to about 15 Mm (Corbard and Thompson, 2002). This analysis has only access to the axisymmetric component of the rotation. In order to confront these results to those obtained from ring diagram analysis, I calculated the axisymmetric gradient by averaging zonal flows of symmetric bins relative to the equator. Results from this study are discussed in PROCEEDINGS III given at the end of this chapter, where a period of 80 Carrington rotations lasting from 07/2001 to 07/2007 has been considered. Figure 1 of the proceedings paper shows the behavior of the north-south symmetrized radial gradient as function of depth for the positive dense-pack latitudes. Like figure 8.2, this figure shows that the radial gradient becomes roughly constant when reaching a depth of about $0.99R$. This result is also shown from f-mode analysis, albeit, this analysis infers a radial gradient of -400 nHz/R whereas our analysis leads to a radial gradient of about

-300 to -350 nHz. Since the radial gradient is constant from $0.99R$ and deeper, one can infer it from a linear fit of the angular velocity. This is given by the full line in 8.9. This gradient is found to be different from the one estimated using a linear fit of the angular velocity obtained from f-modes splitting inversion (dashed line). We believe this is due to the different modes included in the two techniques. Ring diagram analysis allows using both f-modes and p-modes (up to n=6) with radial degrees going from 200 to around 1000 whereas f-modes inversion contains only f-modes with radial degree lower than 300.

An attempt on using patches centered at latitude 60° is discussed in the proceedings III. These high latitude patches do show a positive axisymmetric gradient from the analysis of six Carrington rotations. Nonetheless, because of the strong foreshortening effect at these latitudes, this analysis may lead to ambiguous results. In the near future, the analysis of high resolution images that will be provided by the HMI experiment aboard the SDO satellite will tell us more about the location and the strength of the positive gradient at high latitudes.

8.4 Inversion of the velocity gradient

Following Thompson (1990) it is also possible to invert the radial velocity gradient directly from the observed shifts by taking equations 2.21, 2.22, and considering an integration by part such as

$$u^{n\ell}_{x,y} = \beta^{n\ell} v_{x,y}(R) - \beta^{n\ell} \int_0^R \tilde{K}^{n\ell}(r) \frac{dv_{x,y}(r)}{dr} dr \tag{8.1}$$

$$\tilde{K}^{n\ell}(r) = \int_0^r K^{n\ell}(r')dr'$$

where $K^{n\ell}$ and β are given in equations 2.23, 2.24. $\tilde{K}^{n\ell}$ is the mode sensitivity kernel relating the radial velocity gradients to the frequency shifts. This inversion also requires to know the velocity at the surface given in the first term of the LHS of equation 8.1. I have implemented this inversion into the ring diagram pipeline to infer radial gradients of angular velocity and meridional circulation. The resolution kernels inferred from OLA inversion of the frequency shifts derived

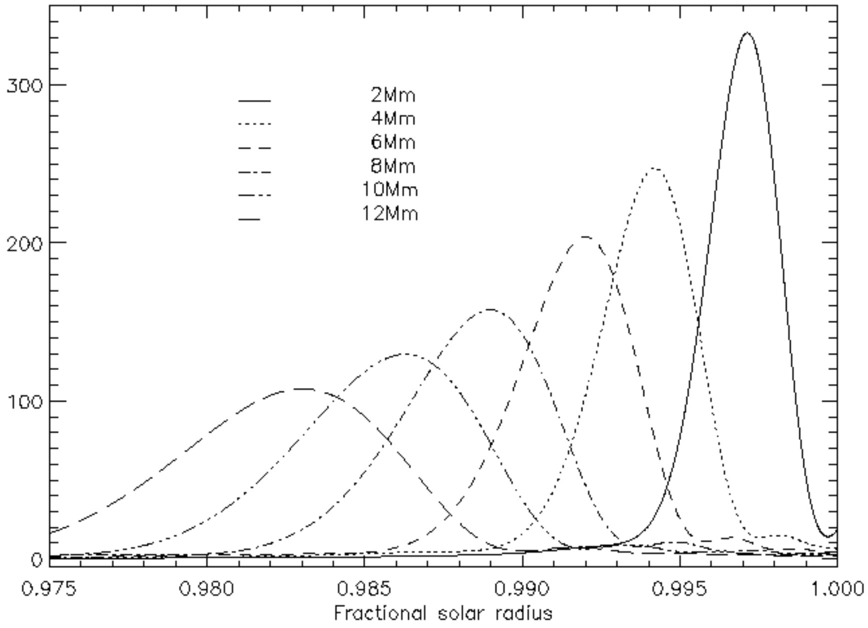

Figure 8.10: Resolution kernels of OLA inversion of the radial gradient of the zonal and meridional flows.

from a standard data-cube are shown in figure 8.10 and look well peaked. Hence, the results of the inversion are promising. Up to now, the inversion has been applied to one data cube only for a performance test. In the near future, the whole available GONG data will be used to invert the meridional and zonal radial gradient to perform a long term study.

8.5 Summary

Results on the study of the radial gradient of angular velocity from ring diagram analysis of 7 years of GONG data can be summarized as follows:

- The radial gradient is mostly negative at all depths at latitudes up to 52.5° north and south. Its highest amplitude is reached at the equator whereas the lowest amplitude appears at the highest latitude.

- The amplitude of the radial gradient decreases downward until about 0.99R where it becomes mostly constant with depth with a value between 300 nHz/R and 350 nHz/R between the equator and ±40°.

- The southern radial gradient has a stronger amplitude than the northern gradient at all latitudes.
- From extrapolation one can hint that the radial gradient is likely to change sign at higher latitudes than 52.5° most likely at the first 0.5% below the surface. In addition, the northern gradient is supposed to change sign at lower latitudes than the southern gradient.
- A singularity happened at the end of solar cycle 23 (beginning of year 2007) where a radial gradient higher than 350 nHz/R went deeper than 0.99R at mid latitudes, with an amplitude increasing downward. The period where this deep reversed gradient happened was followed by a period of a strong gradient of about -1000 nHz/R, much stronger than the equatorial gradient.
- At the period where the reversed gradient happened, a strong solar flare appeared close to the equator, even though the period is part of a solar minimum.
- The radial graident obtained by the linear fit of the angular velocity derived from ring diagram analysis and that obtained from f-mode inversion show similar trends as a function of latitude but with slightly different amplitudes. f-mode inversion infers a lower constant gradient at low latitudes (-450 nHz/R) than our results. This is most likely due to the fact that ring diagram analysis includes modes with higher degree in addition to the use of modes with radial orders up to 6 whereas f-mode inversion includes only mode with $\ell < 300$ and $n = 0$ only.
- The inversion of the radial gradient of angular velocity and meridional circulation from frequency shifts of ring diagram analysis reveals promising results and will be performed for a long term study.

PROCEEDINGS III

TITLE

The solar subsurface radial gradient of angular velocity as revealed by ring diagram analysis

AUTHORS

A. Zaatri, T. Corbard

REFERENCE

ASP Conference Series, in proceedings of the GONG 2008/SOHO XXI meeting (2008), In press.

FULL TITLE
*ASP Conference Series, Vol. **VOLUME**, **YEAR OF PUBLICATION***
NAMES OF EDITORS

The solar subsurface radial gradient of angular velocity as revealed by ring diagram analysis

Amel Zaatri [1,2], Thierry Corbard [2]

[1]*Kiepenheuer-Institut für Sonnenphysik, Schöneckstr. 6-7, 79104 Freiburg, Germany*

[2]*Département Cassiopée, UMR CNRS 6202, Observatoire de la Côte d'Azur, BP 4229, 06304 Nice CEDEX 4, France*

Abstract. We have estimated the radial gradient of angular velocity in the very subsurface layers of the sun for the period 07/2001 - 07/2007 which covers 80 Carrington rotations, starts at the maximum of cycle 23 and ends at its minimum. This analysis confirms that, on average, the radial gradient of angular velocity remains negative and roughly constant between 0.980 and $0.991R_\odot$ below 40° of latitude. The extension of ring analysis up to 60° over 2 periods covering 3 Carrington rotations each shows a positive gradient at this latitude which tends to confirm the sign reversal revealed by the analysis of MDI f-modes (Corbard & Thompson 2002). Finally, we report an enhancement of the radial gradient around 35° and $0.990R_\odot$ at the beginning of 2007 which corresponds to the beginning of the new cycle 24.

1. Introduction

The radial gradient of angular velocity has previously been inferred in the solar interior using global properties of f or p-modes. By analyzing f-modes collected over 7 years of MDI observations $(1996-2001)$, Corbard & Thompson (2002) have found an evidence of sign reversal at latitudes higher than 50° but confined in a thin layer extending only 5 Mm beneath the visible surface. By analyzing depth dependence of the horizontal flows during a single Carrington Rotation (CR 1988: 2002 March 30-April 25) for each latitude and longitude of a standard ring diagram analysis, Komm et al. (2004) found a very significant correlation between the surface magnetic flux and the amplitude of the horizontal flows vertical gradient. More recently (Antia et al. 2008) analyzed f and p-modes (up to $l = 300$) covering the whole solar cycle using GONG and MDI data $(1996-2007)$ and observed again a close relation between the temporal behavior of this gradient and solar activity.

In this work, we attempt to look more closely at this sub-surface radial shear by using the high degree p-modes through ring diagram analysis of 7 years of GONG data covering a period between the maximum and the minimum of the solar cycle 23 (July 2001 - July 2007, CR=[1979,2059]). The modes we are exploring allow us to reach a depth of about 16 Mm (about 2% under the visible solar surface). We restrict our study to layers deeper than 3 Mm in order to avoid possible bias that could arise from less reliable estimation of the inversion kernels close to the photosphere boundary. In addition to the use of

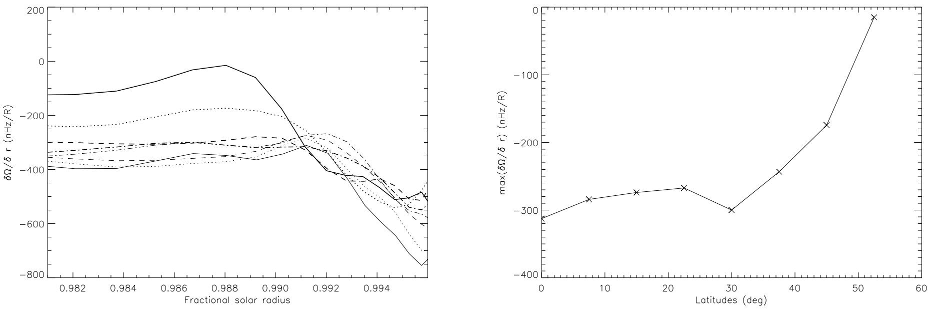

Figure 1. Left panel: radial rotation gradient averaged over 7 years as function of depth for eight latitudes (0, 7.5, 15, 22.5, 30, 37.5, 45 and 52.5° from bottom to top at $0.980R_\odot$) . Right panel: maximum value of the radial gradient at each latitude.

usual patches up to 52.5° of latitude, we have tried to explore patches centered at 60° in order to check for the sign reversal of the radial gradient of angular velocity at high latitudes.

2. Data analysis

Ring diagram analysis has been used to infer zonal velocity flows (Hill 1988; Corbard et al. 2003). Patches of $16^\circ \times 16^\circ$ have been remapped, tracked , appodized to an extend of 15° and Fourier transformed to get local 3D power spectra. Frequency shifts are inferred by fitting the power spectra using a Lorentzian profile. Then, the shifts are inverted using an optimal localized average method to get flows as function of depth. Each patch is averaged over the time period during which it is visible. In order to reduce doertening effects less weight is given to a patch when it is located close to the limb. Then patches located at the same latitude are averaged over a whole CR.

3. Variation of the radial gradient of angular velocity over 7 years of GONG data

The radial gradient of angular velocity has been estimated at depths from $0.980R_\odot$ to $0.997R_\odot$ from a numerical derivation of the azimuthal part of the north-south symmetrized horizontal flows for each of the 80 CR and for 8 latitudes in the range [0°-52.5°]. Figure 1 (left panel) shows that the radial derivative of the time and longitude averaged angular velocity is negative at all the taken depths and latitudes. Between $0.980R_\odot$ and about $0.991_\odot$ and for latitudes below 40° the radial gradient of angular velocity roughly constant with a value around -350 $nHz/R_\odot$. Above 40° this value tends towards zero. On the opposite, above $0.991R_\odot$ (i.e. 7Mm), its amplitude increases quickly at all latitudes as we approach the surface. Figure 1 (right panel) shows the maximum value (i.e. its minimum amplitude) reached by the radial gradient as a function of latitude. This value is almost constant for latitudes lower than 40°. For higher latitudes, it decreases in absolute value and reaches almost zero at 52.5°.

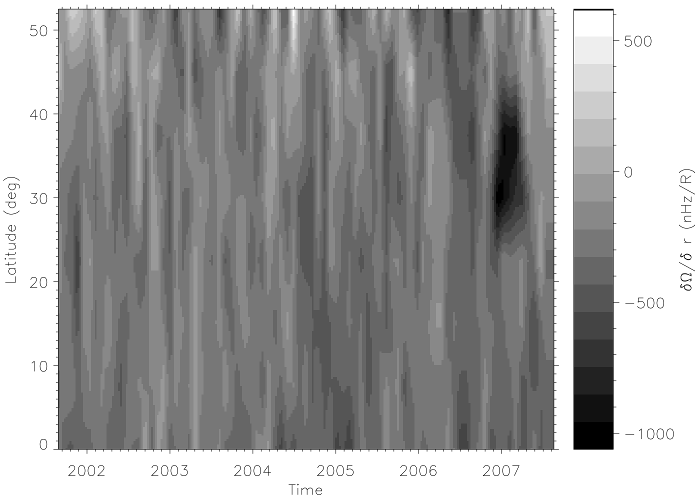

Figure 2. Temporal variation of the radial gradient of angular velocity at $0.990R_\odot$

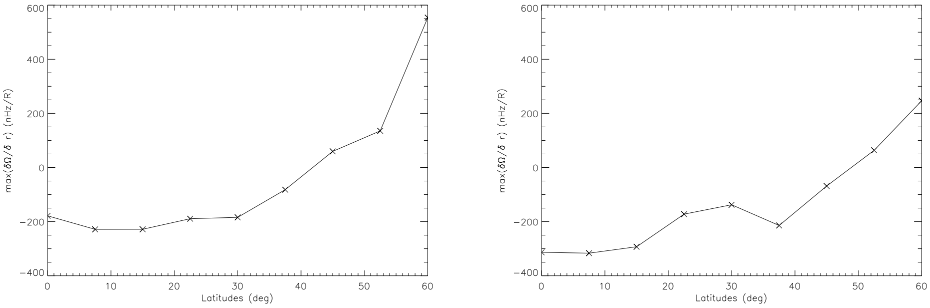

Figure 3. Same as Fig. 1. Left: the radial gradient is averaged over 3 CR (1983-1985) at the maximum solar activity. Right: the radial gradient is averaged over 3 CR (2057-2059) at the minimum solar activity.

We also notice from Fig. 1 that the depth for which the minimum amplitude of the gradient is reached increases with latitude.

Figure 2 shows the temporal variation of the gradient near $0.990R_\odot$. It shows some fluctuations around the average behaviour discussed above but a noticeable exception is seen at the beginning of 2007 when a unusually strong gradient is detected near 35° of latitude. We notice that such enhanced gradient appears also in the analysis of (Antia et al. 2008) but rather around year 2005. Such features could be related to the starting of the new solar cycle 24 and might deserve more investigations.

4. Using high latitude patches

The most poleward patches considered in standard ring diagram analysis mosaic of the solar disk are centered at 52.5°. This choice has been made in order to avoid foreshortening effects that can bias the ring analysis. We have extended the mosaic to patches centered at 60° from the equator and no more than 15° from the central meridian. We have checked that the number of fitted modes does not decrease dramatically for these patches showing that it should still be possible to make some inference about these latitudes.

We have used this new mosaic for a restricted data set of 6 Carrington rotations. The 3 first CR cover the maximum of cycle 23 at the end of 2001-beginning of 2002 (CR 1983-1985) and the second 3 CR cover the minimum of the cycle at mid 2007 (CR 2057-2059). The radial gradient has been estimated by deriving the averaged angular velocity over 3 CR in both cases. Figure 3 shows that a positive gradient is detected at the extended latitude and that it is more important for the period with higher activity. The inferred gradient fluctuates however quite a lot when evaluated on few months only. In future work, we should look at the correlation with activity over more CR by averaging patches with similar activity levels rather than taking simple longitude averages.

5. Conclusion

In this work we confront results obtained previously from global helioseismology on the radial gradient of angular velocity in the immediate sub-surface layers to the one obtained by averaging, over time and longitudes, local horizontal flows inferred using ring-diagram analysis. Because local helioseismology is based on the analysis of modes of higher spherical harmonic degrees, we can potentially reach higher spatial resolution. This allow us for instance to show that the radial gradient is clearly not constant everywhere in a layer covering 2% of the solar radius beneath the surface (see Fig. 1). On the other hand, local helioseismology is strongly affected by foreshortening effects when one analyses patches located at high latitudes or close to the limb. We have shown here however that results obtained at 60° are compatible and show also the sign reversal previously revealed by global f-mode analysis. Our analysis exhibits also an enhanced gradient located at 35° and $0.990R_\odot$ at the beginning of 2007. If confirmed, this could be of particular interest because this corresponds to the beginning of a new cycle and the latitude at which the first signs of activity emerge. Ring analysis results remain however quite noisy when averaged over only few months and therefore more analysis over longer periods will be needed in a more complete work in order to address their statistical significance.

References

Antia, H. M., Basu, S., & Chitre S. M. 2008, ApJ, 681, 680

Corbard, T., & Thompson, M. J. 2002, Sol. Phys., 205, 211

Corbard, T., Toner, C., Hill, F., Hanna, K. D., Haber, D. A., Hindman, B. W., & Bogart, R. S. 2003, in: GONG+ 2002. Local and Global Helioseismology: the Present and Future, ed. H. Sawaya-Lacoste, ESA SP, 517, p. 255

Komm, R., Corbard, T., Durney, B. R., González Hernández, I., Hill, F., Howe, R., & Toner, C. 2004, ApJ, 605, 554

Hill, F. 1988, ApJ, 333, 996

Conclusions

Hereafter, I will first summarize results obtained in this thesis and touch upon on perspectives of some future work at the latest.

Summary

Results in this thesis have again shown the doubtless strength of helioseismology as a tool to explore solar dynamics and structure both globally and locally. The processed work in this thesis as well as the most important findings are summarized here starting by the efforts provided on the investigation of solar structure in the light of helioseismic constraints followed by the exploration of long-term variation of the zonal and meridional flow, inferred from ring diagram analysis of GONG data, during the declining phase of solar cycle 23. In the following, I will highlight each result in bold followed by a short summary on more details about the idea behind and the work done to reach it.

1. The new solar abundances, lower than those previously used to build standard solar models, lead to a considerable disagreement with helioseismic constraints of the radiative and convective zones. I extended the helioseismic diagnostic to the use of small frequency spacings of

low degree modes to constrain the inner zones modeling down to the core, where the discrepancy appeared to be strong as well. As yet, no plausible solution has been found to raise the discrepancy.

In order to study the effect of changing the solar mixture in the standard solar models, I used the CESAM stellar evolution code in which I implemented new OPAL opacity tables of several sets of heavy element abundances, notably the new solar mixture, to build several standard solar models. The outcome from this study was that the inner regions of the solar interior are also strongly affected by the change in solar abundances, where small frequency low degree spacings of solar models based on the new mixture are much higher than those obtained from old mixture models and essentially higher than the small frequency spacings observed with GOLF/SOHO instrument. Also, the calculated g-mode frequencies are affected by the change in solar abundances. This work has confirmed that the increase of Neon abundance by about 0.5 dex could raise the discrepancy from the convection zone to the core, however this value has not been confirmed from observations. The discrepancy between helioseismology and the solar models based on the new abundances has no explanation, as yet. This issue is a challenge to review and improve solar model physical processes, for instance, in terms of angular momentum transport including rotation and magnetic field that are not fully treated in the stellar evolution theory.

2. Sensitivity kernels of high degree modes are weakly sensitive to most of the solar modeling ingredients. Nonetheless, they show a slightly more pronounced sensitivity to the upper most layers modeling. It might then be appreciable to get a better modeling of these layers than that provided by standard solar models.

Sensitivity kernels of high degree modes are important inputs for the ring diagram analysis which is the local helioseismology technique used to infer subsurface flows in this thesis. Up to now, only model S constructed in 1996 with the contemporary physics of the solar interior processes has been used to generate these functions. However, many aspects of the solar modeling have been improved since then. In order to see whether the change in solar models affects the sensitivity kernels, I generated a set of sensitivity kernels using different solar models constructed from the CESAM code. This study confirmed that sensitivity kernels of high degree modes are very weakly influenced by the change in solar modeling ingredients such as, the age, the solar abundances, the opacities and the treatment of the convection zone. However, the modeling of the outer most layers of the Sun (last 0.1%) affect kernels relative to high degree modes with high radial orders. The effect of this change on the measurement of the underlying flows from the inversion of locally measured frequency shifts also revealed a very weak effect of the change in the solar modeling, where the biggest effect is also due to the outer most layers modeling but is still inside the measurements error bars. This study might, however, become more important with the upcoming HMI/SDO data which will provide us with better spatial resolution. The inferred result from this new data will be in turn moe sensitive to our modeling of the outer most layers.

3. Ring diagram analysis of high degree modes at localized parts of the solar disk offers a precious access to the study of sub-photospheric large scale flows longitudinally, latitudinally as well as radially. Although, the technique is subject to many artifacts that can crucially degrade the sought solar signal by distorting the 3D power spectrum of solar oscillations. Correctly mapping the solar images onto heliographic grids can avoid one of the major sources of non desirable distortions of the power spectrum. Using the Postel projection seems to bring the best results regarding this issue.

Continuous data provided by the GONG network since July 2001 which covers most of the declining phase of solar cycle 23, was our stimulating factor to continue using ring diagram analysis in order to infer long term variations of the horizontal flows. Indeed, having precise measurements of the rotation and meridional circulation from maximum to minimum activity can bring precious insights on the solar dynamo theory in order to better understand the puzzling process of the solar cycle. However, the ring diagram technique has to be handled with lots of care since many artifacts could interfere with the horizontal flow measurements and might lead to some misleading information about the solar dynamics. In this thesis, I have tried to focus on one of the sources that might be harmful for the analysis in the sense that it could bring additional distortions to the local power spectrum of high degree solar oscillations leading to systematic errors in the determination of the frequency shifts and hence in the sub-surface flows. This source is the remapping of solar images onto a heliographic coordinates grid. Despite the obvious fact that one has to use projections based on great circles along which acoustic waves propagate, I came out with the fact that the better choice of the geometric mapping is the Postel projection which gives the best results in the x direction (zonal flow) and in the y direction (meridional circulation).

4. One efficient way to studying long term variations of horizontal flows is to see them in a synoptic picture as a function of Carrington longitude and latitude for several depths at a given Carrington rotation. During this thesis, I have developed a code to generate these synoptic maps from daily horizontal flows measured by the ring diagram analysis of GONG data.

From ring diagram analysis of seven continuous years of GONG data, long term investigations of the sub-photospheric flows can be performed in time, latitude (±52.5°) and depth down to 15 Mm from the maximum to the minimum of the cycle. In order to easily produce synoptic maps from daily horizontal flows of the dense-pack mosaic for several Carrington rotations, I developed a program to produce these maps as well as those corresponding to the flow residual that allow focusing on flows around active regions. Moreover, the code generates related fluid characteristics such as the divergence as well as the vertical velocity derived from mass conservation that can be obtained for a given density profile. The code is adapted to the actual range of latitudes and central meridian distances (±52.5°) given by the dense pack matrix but can be easily extended or adapted to other mosaics such as the ones that will become possible with the HMI/SDO high resolution data. The synoptic maps are also overlayed to rebinned unsigned magnetic field measurements obtained from magnetic synoptic maps of MDI or

GONG in order to study the relationship between magnetic activity and horizontal flow fields.

5. The analysis of 7 continuous years of GONG data has allowed us obtaining several interesting results about the variation of meridional and zonal flows with time. Especially, their north-south asymmetry has been studied. These are observational ingredients that should be taken into account when modeling the very complex solar cycle processes. The most important findings on the long-term study of the horizontal flows are summarized in the following points.

- First investigations of the long term variations of horizontal flows have shown an annual periodicity in the variation of the meridional circulation, a north-south flow, at high latitudes that turned out to be well correlated with the B_0 angle. The zonal flow, an east-west flow, is much less sensitive to this systematic effect.

- Meridional circulation got a strong acceleration during the declining phase of solar cycle 23 whereas the zonal flow only shows the well known torsional oscillation variation with time.

- Rotation of the subsurface layers recovered from the zonal flow and tracking rotation rate, is shown to be slower than the small bright coronal points rotation. The north-south asymmetry of both rotations reveals a faster rotating southern hemisphere than the northern hemisphere. The investigated part of solar cycle 23 also shows that the southern hemisphere was more active than the northern hemisphere. In addition, at latitudes where the north-south asymmetry of the angular velocity increases (decreases) with activity for the SBCS, it decreases (increases) for subphotospheric layers.

- The rotational radial gradient is overly negative for the dense-pack mosaic. It mainly reaches its strongest value at the equator and the lowest value at the highest latitudes where the sign reversal can be expected. The northern hemisphere shows a less strong negative gradient than the southern hemisphere which supposes that the sign reversal in the north might appear at

> lower latitudes than in the south. Moreover, a strange bifurcation of the radial gradient appeared at the beginning of solar minimum where also an uncommon strong solar flare erupted at the same period.

Perspective

The long term study of horizontal zonal flows inferred from ring diagram analysis of continuous GONG data covering the whole declining phase of solar cycle 23 has already revealed many interesting results. Nonetheless, as more results we get, as more new questions we ask. Here, I summarize some incoming investigations that are planned for the near future.

1. Further improvements of the synoptic flow maps

The dense-pack matrix is a practical way to study the flows at different latitudes and Carrington longitudes. However, the fixed distribution of patches in central meridian distance (in a Carrington coordinates grid) is based on the assumption that regions at all latitudes rotate at a the same rotation rate. Thus, a patch centered at 52.5° latitude and at the central meridian which would have rotated only 12° in one GONG day, is supposed to be centered at the central meridian distance of 15° in the subsequent day. Consequently, this attributes to the tracked region a portion of 3° in width which was not part of the first patch on one side and removes an original portion with the same width on the other side of the patch. This issue can be resolved if a grid in central meridian distance was built by considering the differential rotation over one Carrington rotation such as that suggested by Ulrich and Boyden (2006). This is worth investigating in the future to get a more proper construction of synoptic flow maps.

2. Radial gradients of the meridional and zonal flows inferred from the inversion of frequency shifts.

The direct inversion of the radial gradients of the zonal and meridional flows from frequency shifts has been successfully applied to one data cube. When having accurate estimates of the velocity fields at the surface, this procedure is more robust than computing radial graidents from the inverted flows. In the near future, this inversion will be applied to the whole GONG data available to infer daily radial gradient flow maps and perform a long-term study in latitude and depth that will be confronted to the magnetic activity.

3. Investigating the relationship between rotational radial gradient and the flare activity.

I mentioned a singular concurrence between a bifurcation in the monotonous behavior of the rotational radial gradient and a strong eruption of an active region that happened at the beginning of the solar cycle minimum. A more advanced statistical study along the seven studied years on this relationship between flare productivity and rotational radial gradient might bring precious insights for the space weather forecast.

4. Investigating the relationship between longitudinal meridional flow variation and active longitudes

Our finding on the correlation between the meridional circulation and the annual variation of B_0 has been confirmed to be different between minimum and maximum cycle. The correlation observed around the equator is most likely due to another source than the B_0 variation which would obviously affect only high latitude regions. Since the relation between the variation of the meridional flow and the solar activity has been confirmed by the acceleration of the meridional circulation in the period of solar minimum, this periodicity at low latitudes might also be related to the magnetic activity. One of the possibilities is that there exists a direct relation between the meridional flow variation and the well know active longitudes. In the near future, an advanced study on the relationship between meridional circulation and the active longitudes will be performed.

5. Using the incoming HMI/SDO data

The Solar and Dynamics Observatory is planned for launch on the 3rd of February 2009. The Helioseismic and Magnetic Imager (HMI) will be the successor of MDI/SOHO but with continuous production of dopplergrams, 4 times higher resolution (4kX4k), and a shorter time cadence (45 sec). It is our plan to use this data that will definitely push our actual knowledge on the flow fields of the

Sun from ring diagram analysis to a much higher level. For instance, in the presented study, our latitudinal coverage was limited to less than ±55° because of the foreshortening effect combined to the actual resolution that prevent us from performing high latitudinal investigations. The HMI images will allow us reaching much higher latitudes might, for instance, lift the veil on the location of the sign reversal of the rotational gradient. This will allow addressing the question of the shear layer near the surface in order to bring other constraints on the internal circulation, the transport of the angular momentum and dynamo processes. Also, the detailed analysis I have performed in this work reviews the influence that many parameters involved in our models and methods can have on the estimated flow fields. Some have turned out to have negligeable effects given the present resolution and quality of the data but all are expected to become truly significant with the upcoming HMI high resolution and high cadence data. Moreover, shorter temporal sampling also means a higher Nyquist frequency that will allow us to resolve the acoustic oscillation power spectrum in regions never explored before. Undoubtedly, the upcoming HMI/SDO will again revolutionize our knowledge about the structure and dynamics of our Sun with the very precious tool of helioseismology.

Appendix A

A.1 Projection to the camera plane

Let us define any point on the sun as observed from Earth in the coordinate system $R"(x", y", z")$. The relation between $R"$ coordinates and those of the heliographic coordinates ($R(X, Y, Z)$) can be obtained by rotating X and Y by an angle L_0 around Z leading to the system $R'(X', Y', Z)$ and then rotating (X',Z) around Y' by an angle B_0, where L_0 and B_0 are the coordinates of the center of the solar disk as observed from Earth. Then, any point on the Sun (R coordinate system) defined by its heliographic latitude and longitude (θ, ϕ) will have the following cartesian coordinates in the $R"$ coordinate system

$$x" = \sin\theta \sin B_0 + \cos\theta \cos B_0 \cos(\phi - L_0) \tag{A.1}$$

$$y" = \cos\theta \sin(\phi - L_0) \tag{A.2}$$

$$z" = \sin\theta \cos B_0 - \cos\theta \sin B_0 \cos(\phi - L_0) \tag{A.3}$$

In figure A.1 (distances are exagerated for clarity), one can consider the projection plane to be $(y", z")$. From the triangel oRI one can get :

$$\epsilon = R\frac{r_0}{D}, \tag{A.4}$$

D being the distance Sun-Earth, R is the solar radius, r_0 is the radius of the solar image and ϵ is a negligible distance.

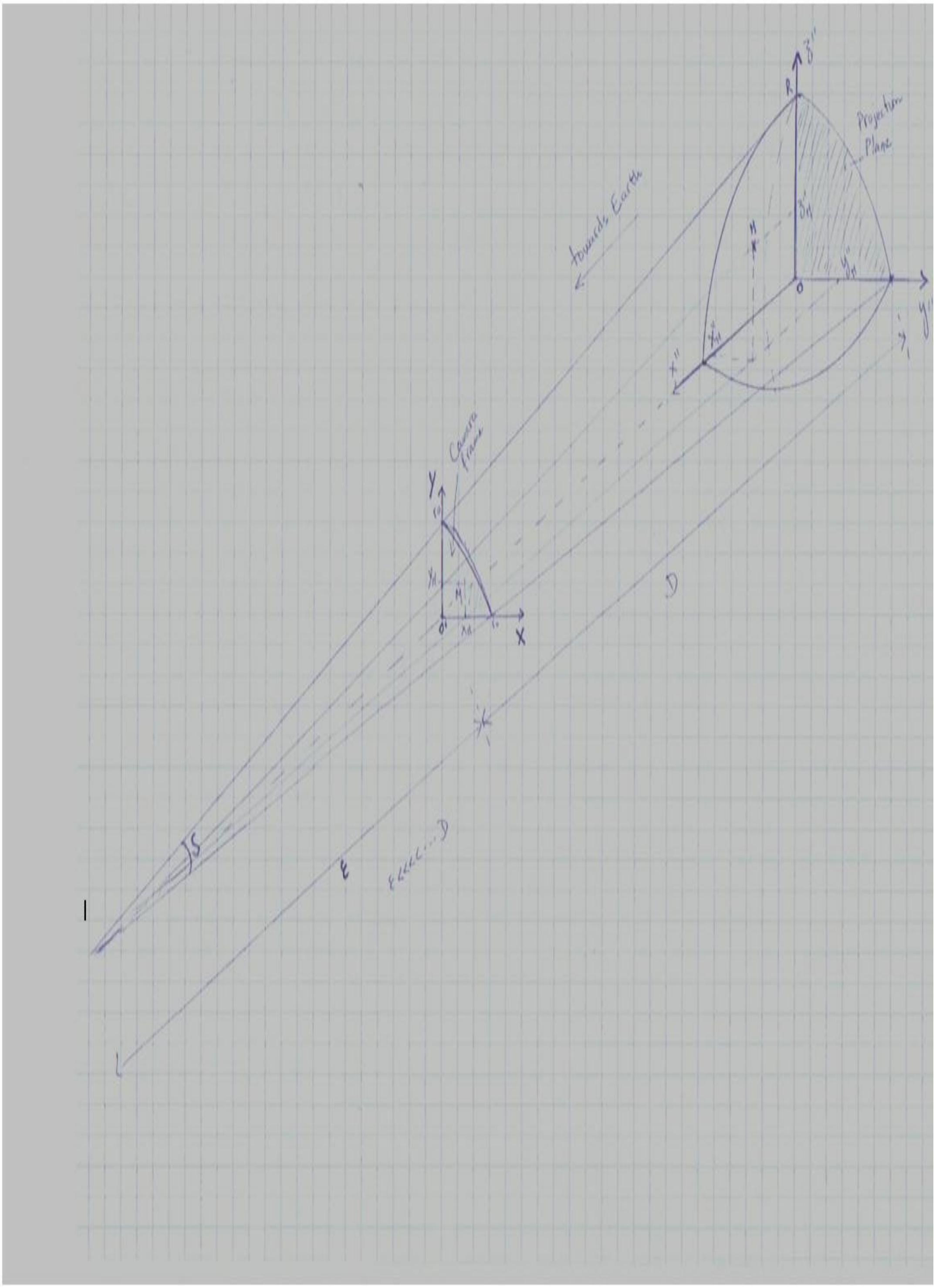

Figure A.1: Simplified drawing of the camera projection of solar coordinates.

In addition, the triangle $(oz"_m I)$ gives

$$\frac{z"R}{D-Rx"}=\frac{Y-Yc}{\epsilon}. \tag{A.5}$$

From these equation one gets

$$\frac{Y-Yc}{r_0}=\frac{z"}{1-Sx"}, \tag{A.6}$$

where $S=R/D$ is the apparent semi-diameter.
By writing the same relation from the triangle $(oy"_m I)$, one gets

$$\frac{X-Xc}{r_0}=\frac{y"}{1-Sx"}. \tag{A.7}$$

Finally, equations 5.1 and 5.2 are obtained by replacing the expressions of x", y" and z" (equations A.1 – A.3) in the equations A.6 and A.7.

Appendix B

The hflows_synoptic package

The 'hflows_synoptic' package is a set of IDL routines used to create synoptic maps of horizontal velocity flows and their residuals from the daily velocity flows generated by the ring diagram analysis of GONG data using the GONG ring diagram pipeline. Examples of synoptic flow and residual flow maps are shown in figures 7.1 and 7.2 for Carrington rotation 1997 at two different depths.
In addition, the package calculates three other fluid dynamics descriptors; the divergence and the vorticity of the horizontal velocity and the vertical velocity. A readme file of the hflows_synoptic package is given at the end of this appendix and the source code is available for download on the HELAS website[1].
The divergence and vorticity of the horizontal velocity are given as follows:

$$div(v_h) = \frac{\delta v_x}{\delta x} + \frac{\delta v_y}{\delta y} \tag{B.1}$$

$$vort(v_h) = \frac{\delta v_y}{\delta x} - \frac{\delta v_x}{\delta y} \tag{B.2}$$

The vertical velocity (v_z) is derived from the continuity equation knowing the horizontal velocity divergence and the density ρ (Komm *et al.*, 2004) such as

$$\frac{\delta \rho}{\delta t} + \frac{1}{\rho}(\frac{\delta \rho}{\delta x}v_x + \frac{\delta \rho}{\delta y}v_y + \frac{\delta \rho}{\delta z}v_z) + (\frac{\delta v_z}{\delta z} + div(v_h)) = 0 \tag{B.3}$$

---

[1] http://www.mps.mpg.de/projects/seismo/software/SYNOPTIC_FLOW_MAPS

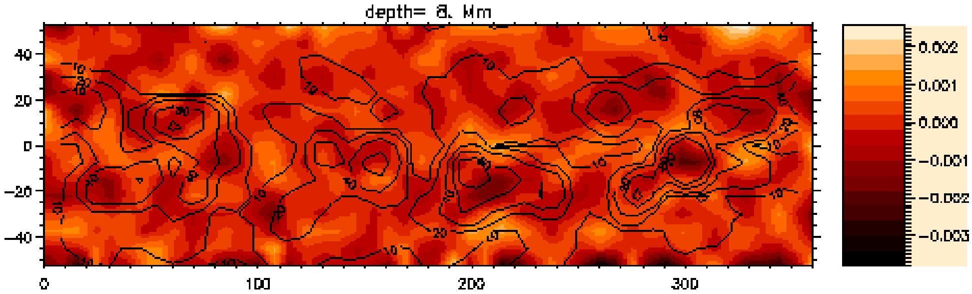

Figure B.1: Synoptic map of Carrington rotation 1993 at 8 Mm of a difference between vertical velocities, obtained from two different profiles of density (Model S - CS3).

The second and third terms in the LHS are the density fluctuation in the (x,y)-plane which is approximately averaged out because of the big spatial extension of the patch. Also, because of the considered length of the time serie one can neglect the first term in the LHS. The solution to the resulting simplified differential equation gives the vertical velocity at each depth. The depth range only consists of a limited discrete set of depths provided by the inversion of the flows.

$$v_z(r_d) = \frac{1}{\rho(r_d)} \int_{r_d}^{R} \rho div(v_h) dz + v_z(R) \frac{\rho(R)}{\rho(r_d)} \tag{B.4}$$

In figures B.2 and B.3, the three quantities are displayed in synoptic maps as a function of latitude and Carrington longitude for Carrington rotations 1993 and 1997 at depth 7.1 Mm. Contours in the maps correspond to the unsigned magnetic field derived from MDI magnetic synoptic maps[1] of same Carrington rotations, rebinned in standard ring diagram patches for the dense-pack mosaic. These figures are optional outputs of the package. The package also allows to use several density profiles to measure the vertical velocity. Figure B.1 shows the difference between vertical velocities derived from two different density profiles corresponding to model S and model CS3 (see figure 4.1). The maximum difference is given at the locations of strong downflows that coincide with the location

---

[1] http://soi.stanford.edu/magnetic/index6.html

of strong magnetic field.

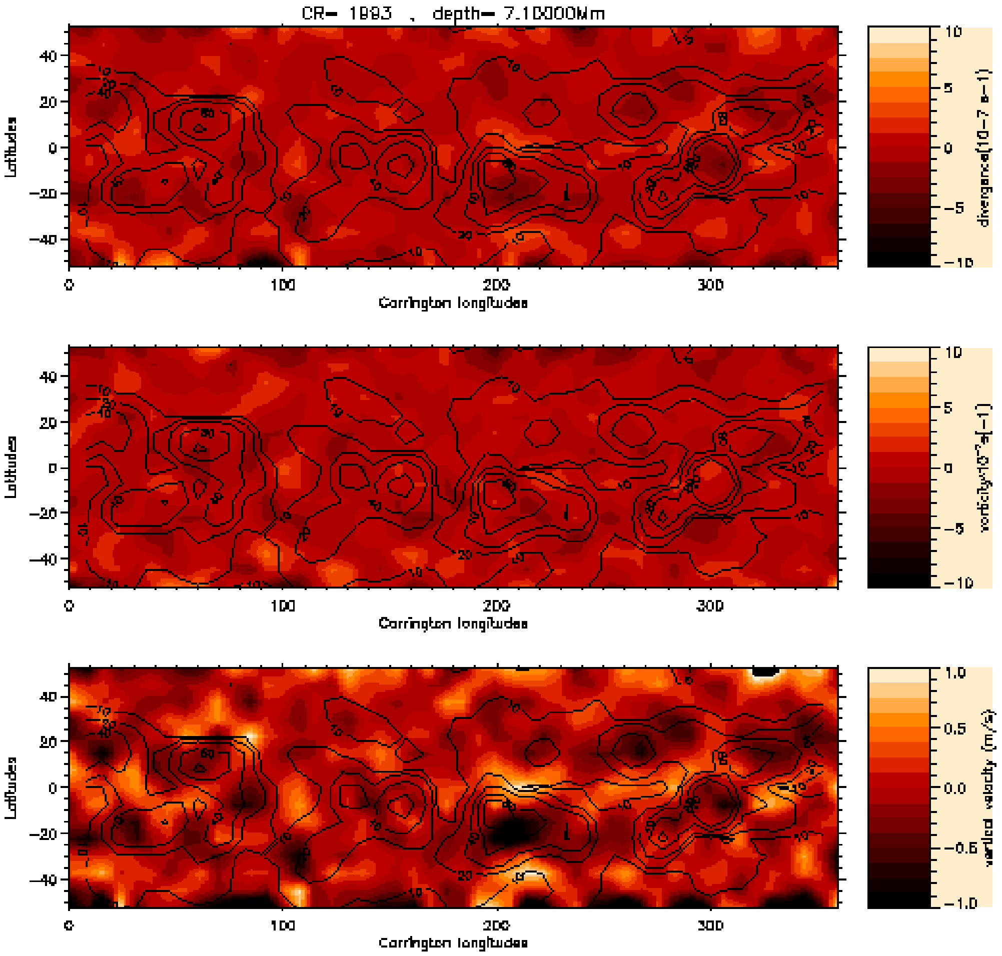

Figure B.2: Synoptic maps of the horizontal velocity divergence (upper) and vorticity (middle) and the vertical velocity (bottom) of Carrington rotation 1993 taken at depth 7.1 Mm. Maps are overplotted by contours of unsigned magnetic field rebinned in standard patches of the dense-pack mosaic.

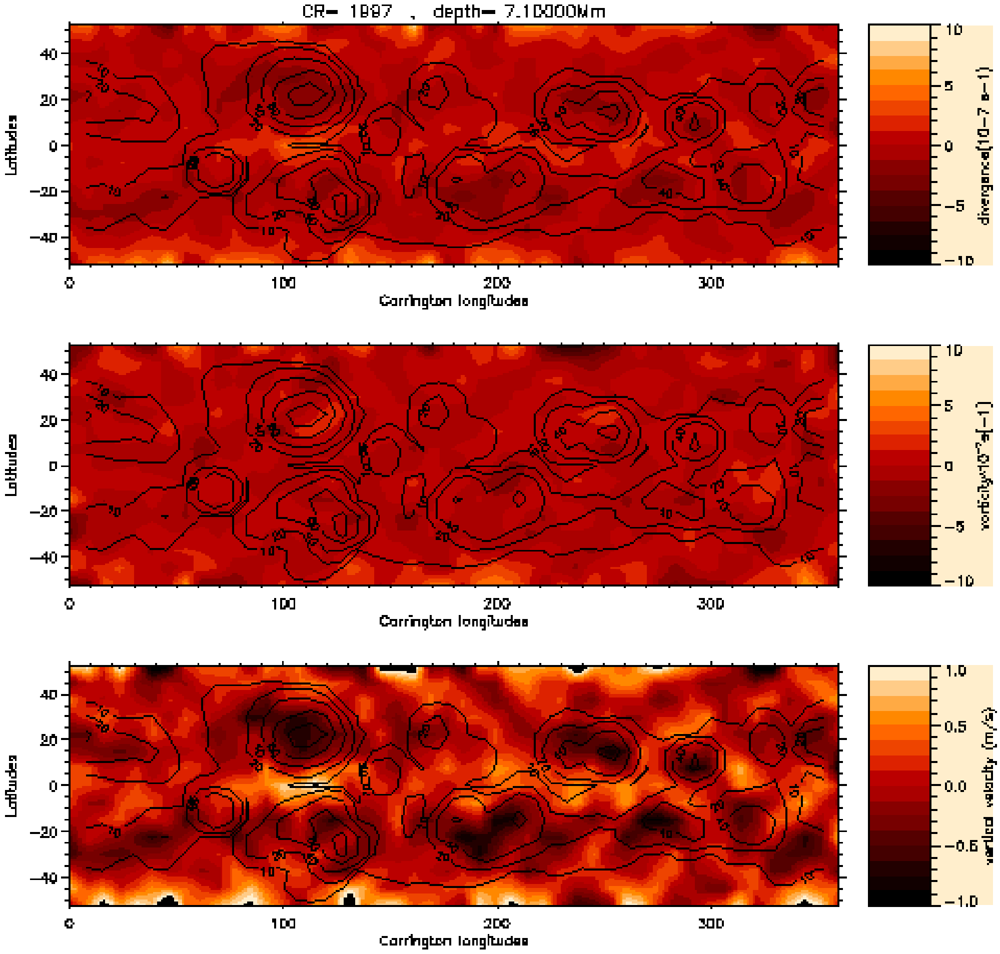

Figure B.3: Same as figure B.2 but for Carrington rotation 1997

README FILE

Package name: HFLOWS_SYNOPTIC

Author: AMEL ZAATRI

2009.07.27.

Purpose: The 'hflows_synoptic' package is a set of IDL routines used to create synoptic maps of horizontal velocity flows and their residuals from the daily velocity flows generated by the ring diagram analysis of GONG data using the RINGPIPELINE.

The data: The data to be used are daily directories containing the inversion velocity files as generated by the ringpipeline. Currently there is data stored in the directory 'data/' for CR 2062. To get other data, download it from the GONG website http://gong2.nso.edu/archive/patch.pl?menutype=h.

Installation and usage

- create a working directory (exp. in your home directory)

  ```
  mkdir /home/hflows_synoptic/
  ```

- Go to this directory and copy the file hflows_synoptic.tar.gz inside

  ```
  cd /home/hflows_synoptic/
  cp /downl_syn/hflows_synoptic.tar.gz .
  ```

  where /downl_syn/ is the directory where the file has been downloaded

- untar and unzip the hflows_synoptic.tar.gz using

  ```
  gunzip hflows_synoptic.tar.gz
  tar -xvf hflows_synoptic.tar
  ```

  This will generate:

  lib/ : directory containing all the idl routines needed to execute the main program.
  data/ : directory containing some data that are needed for running the program with more options.
  exples/: directory containing synoptic flow maps and synoptic flow residuals as well as other fluid descriptors for Carrington rotation 2062. The used magnetic synoptic map is given in data/
  get_varsynoptic.pro: routine used to create the save file of the paramaters used to lunch the main program.
  plot_synoptic.pro: Main program used to plot the synoptic maps.

  At this stage you need to open an IDL session to execute the program

  ```
  idl
  ```

- add the path of lib/ directory to your IDL path (and don't forget the TEXtoIDL package too!):

  ```
  IDL> !path='/home/hflows_synoptic/lib/:' + !Path
  IDL> !path='/home/texttoidl/:' + !Path
  ```

- generate the data file (file_synoptic) See point II below.

- execute the main program.

  The following example will generate the synoptic flow map and the synoptic residual flow map for CR=1993 (high activity period) as well as the fluid descriptors (divergence,vorticity,vertical velocity) at depth 8Mm. A MDI magnetic synoptic map is tacken as a background for the maps. This allows to see how the flows behave in regions with different activity levels. Notably, residual synoptic flow maps are generated to focus on flows around acitve regions. The fluid descriptor maps are overlapped by countours of unsigned binned magnetic flux (see below).

```
IDL> plot_synoptic,1993,file_synoptic,dpthMm=[8.],
$ magneto='data/synop_Ml_0.1993.fits',
typemag='MDI',mode='ps',1
```

Another exemple is given for the Carringon rotation 2062 (low activity period) with a GONG magnetic synoptic map.

```
IDL> plot_synoptic,2062,file_synoptic,dpthMm=[8.],$
magneto='data/mrmds071112t0000c2062_000.fits.gz',
typemag='GONG',mode='ps',1
```

Inputs of the plot_synoptic program

```
plot_synoptic, CRN, file_synoptic,
dpthMm=dpthMm,
magneto=magneto,typemag=typemag,mode=mode,
fluid_descriptors,lamd
```

- CRN: Carrington rotation number for which the synoptic map is generated

  IMPORTANT: In order to construct a synoptic map you need to have some days from the previous CR of the chosen Carrington rotation and some from the next CR. Precisely, you need the following days to construct a synoptic map for the Carrington rotation CRN:
  1- 3 GONG days of the Carrington rotation CRN-1
  2- The Whole GONG days of the Carrington rotation CRN (24)
  3- 4 GONG days of the Carrington rotation CRN+1

- file_synoptic: IDL save file of variables used to generate a synoptic map.

  ** Ist Case: If the arborescence of directories as it is given in the GONG website is conserved (month_dir/day_dir) then use the following IDL command to generate the save file:

```
idl> get_varsynoptic,dir,dir_ve,file
```

dir: directory where the monthly directories are
dir_ve: the directory where the velocity files are located
(default 've/INVERSIONS/')

** 2nd Case: If the arborescence is different:

1- Create your daily directory list (ndays=number of daily directories) [dir_days]

NB: The daily directory name is used to get the date of the corresponding day. Therefore, it has to contain the date of the corresponding day in the format string/year/month/day/t/hour/min or string/year/month/day. 'string' can be of any length (the whole path can be used as well).

To be sure that you re generating the correct dates from the directory name try:

```
idl> dirday2date,your_dirname,date
idl> print,date ;
date=[year,month,day,hour,minute,second]
```

2- use the routine find_L0.pro to generate the Carrington longitude of the central meridian (L0). L0 is an array of ndays elements -L0 of each day- (add dir_ve to the daily dir name)

- use the routine get_cr.pro to get the Carrington rotation number array (cr) of ndays elements -cr of each day-

3- Get Carrington rotation numbers. It is not needed in the program but helps to choose the Carrington rotation number of the synoptic map to be built.

```
IDL> cru=unique(cr) & print,cru
```

4-save the obtained varaibles

```
ID>save,dir_days,dir_ve,L0,cr,cru,file=file
```

NB: Please keep the names of the variables as given here, because this notation is used in the main program.

- dpthMm: range of depths in Mm

  If dpthMm is not given, the program will use the range depth [4.,8.,12.].
  NB: in order to get trusty measurements of the velocity flows, it is better to stay within the limits: 2.Mm¡ dpthMm ¡15.Mm

- magneto: This paramater has to be set to a filename corresponding to a GONG synoptic magnetic map (fits file) of the used Carrington rotation if it is available. This map will be used as a background in the synoptic flow maps and as contours overplotting the fluid descriptor 2D representation.

- typemageto: This parametr is set to the type of the magnetic synoptic map

  - typemag='MDI'
  The MDI magnetic synoptic maps are available for download from: http://soi.stanford.edu/magnetic/index6.html. Enter the Carrigton rotation number (CRN) and get the file synop_Ml_0.?.fits (where ?=CRN)

  - typemag='GONG'
  The GONG magnetic synoptic maps are available for download from: http://gong2.nso.edu/archive/patch.pl?menutype=f

  If magneto is not given the synoptic flow maps will have a blank background.

- mode: This keyword is set to either output ps files or display a movie.

  - mode='ps' : synoptic maps are generated into ps files for the given depths [dpthMm]

  - mode='movie': a movie of synoptic flows and their residuals is shown from 2Mm to 15Mm.

- fluid_descriptors: If this parameter is set to 1 the program will generate an addtionnal ps file for each given depth with a 2D representation of the following parameters:
  - Divergence of the flow.
  - Vorticity of the flow.
  - Vertical velocity.
  If the magnetic map is given These plots will be overlapped by contours of unsigned binned magnetic flux contours for some chosen values (depending on the activity). ['binned' means averaged B over a ring tile (15deg/15deg)]

  For details concerning each of these fluid descriptors see the paper by Komm et. al (2004).

- lamd: regularization parameter
  The horizontal velocity flows as given in the GONG website by now have been measured using the RLS method for 10 values of the smoothness parameter. 1¡lamd¡5. Actually this range of ld gives almost same velocity results. In order to see a difference, one has to use a bigger value of lamd. However, it is usually fixed to lamd=5. which is the default value set in the program.

Note concerning the storage of the measured synoptic velocity data
The calculation of the synoptic velocities is time consuming. In order to avoid doing the calculation each time one wants to get synoptic maps for different depths or parameters, the program creates a save file in the data/ directory after the first calculation of the velocities. The file gets the name 'syn_v_CR?.save' (?=CRN). Then, each time the program is lunched, it checks first for the availability of the save file of the given CRN in the data/ directory, if it exists, the variables will be restored from it and the calculation is avoided if it doesn t exist the program does the calculation and stores another save file for the given Carrington rotation number. The save file would also allow the user to do its own explorations.

In the given exemples, the program will not do any proper calculations from the given file_synoptic, but will simply restore the data from saved files as these have been given in the data/ directory. These files are provided in order to get a quick look of the results that are generated. The user could also create its own save files for the same CRN and compare with the given ones (don t forget to change the name of the given files, say by adding an extention .org , otherwise they will be overwritten).

PS: In case of any difficulty using this package or of any detected bug, please send an email to amel@kis.uni-freiburg.de.

References

Abdelatif, T. E., Lites, B. W., and Thomas, J. H. (1986). The interaction of solar p-modes with a sunspot. i - observations. *ApJ*, **311**, 1015–1024. 48

Altrock, R., Howe, R., and Ulrich, R. (2008). Solar Torsional Oscillations and Their Relationship to Coronal Activity. In R. Howe, R. W. Komm, K. S. Balasubramaniam, & G. J. D. Petrie , editor, *Subsurface and Atmospheric Influences on Solar Activity*, volume 383 of *A.S.P. C.S.* 154

Anderson, E. R., Duvall, T. L., and Jefferies, S. M. (1990). Modeling of solar oscillation power spectra. *ApJ*, **364**, 699. 79, 95

Antia, H. M. and Basu, S. (1994a). Measuring the helium abundance in the solar envelope: the role of the equation of state. *ApJ*, **426**, 801–811. 46

Antia, H. M. and Basu, S. (1994b). Nonasymptotic helioseismic inversion for solar structure. *A&A suppl. ser.*, **107**, 421–444. 46

Antia, H. M. and Basu, S. (2007). Local helioseismology using ring diagram analysis. *Astro. Nach.*, **328**, 257. 79

Appourchaux, T., Belkacem, K., Broomhall, A. M., Chaplin, W. J., Gough, D. O., Houdek, G., Provost, J., Baudin, F., and Boumier, e. a. (2009). The quest for the solar g modes. *ArXiv e-prints*. Accepted for publication in Astr. - Sol. and Stel. Astrophy. 28

Asplund, M., Grevesse, N., and Sauval, A. J. (2005). The Solar Chemical Composition. In T. G. Barnes III & F. N. Bash, editor, *Cosmic Abundances as Records of Stellar Evolution and Nucleosynthesis*, volume 336, pages 25–+. 54

Asplund, M., Grevesse, N., Sauval, A. J., and Scott, P. (2009). The chemical composition of the sun. *Ann. Rev. A& A*, **47**, 481–522. 55

Basu, S. (2007). Modelling the solar interior. In S. S. Hasan & D. Banerjee, editor, *Kodai School on Solar Physics*, volume 919 of *AIPCS*, pages 1–23. 33

Basu, S. and Antia, H. M. (1997). Seismic measurement of the depth of the solar convection zone. *MNRAS*, **287, Issue 1**, 189–198. 46

Basu, S. and Antia, H. M. (1999). Large-scale flows in the solar interior: Effect of asymmetry in peak profiles. *ApJ.*, **525**, 517–523. 95

Basu, S. and Antia, H. M. (2000). Solar cycle variations of large-scale flows in the sun. *Sol. Phys.*, **192, Issue 1/2**, 469–480. 22

Basu, S. and Antia, H. M. (2001). Seismic investigation of changes in the rotation rate in the solar interior. In A. Wilson, editor, *the SOHO 10/GONG 2000 Workshop: Helio- and asteroseismology at the dawn of the millennium*, pages 179 – 182. ESA Publications Division. 20

Basu, S., Chaplin, W. J., Elsworth, Y., New, R., and Serenelli, A. M. (2009). Fresh insights on the structure of the solar core. *ApJ*, **699, Issue 2**, 1403–1417. 44, 54

Beck, J. G. (1999). A comparison of differential rotation measurements. *Solar Physics*, **191**, 47–70. 15

Beckers, J. M. (2007). Effects of Foreshortening on Shallow Sub-surface Flows Observed with Local Helioseismology. *Sol. Phy.*, **240**, 3–7. 146

Birch, A. C. (2008). Current issues in helioseismology. *Journal of Physics: Conference Series*, **118, Issue 1**. Proceedings of the Second HELAS International Conference. 48

Bogart, R. S. and et al. (1995). Plane-wave analysis of solar acoustic-gravity waves: a (slightly) new approach. In J. Hoeksema, V. Domingo, B. Fleck, and B. Battrick, editors, *Helioseismology. ESA SP, Proceedings of the 4th Soho Workshop,*, page 147. ESA. 90

Bogart, R. S., Discher de Sá, L. A., González Hernández, I., Patrón Recio, J., Haber, D. A., Toomre, J., Hill, F., Rhodes, Jr., E. J., Xue, Y., and the SOI Ring Diagrams Team (1997). Plane-wave analysis of 501 data. In J. Provost & F.-X. Schmider, editor, *Sounding Solar and Stellar Interiors*, volume 181. 79

Brandenburg, A. (2005). The case for a distributed solar dynamo shaped by near-surface shear. *ApJ*, **625**, 539. 15

Braun, D. C., Duvall, T. L., and J., B. (1988). The absorption of high-degree p-mode oscillations in and around sunspots. *ApJ*, **335**, 1015–1025. 48

Brown, T. M. (1996). Techniques for observing solar oscillations. In T. Roca-Cortés and F. Sánchez, editors, *VI Canary Islands Winter School of Astorphysics: The structure of the Sun*, pages 1–45. Cambridge University Press. 43

Brun, S. A. and Toomre, J. (2002). Turbulent Convection under the Influence of Rotation: Sustaining a Strong Differential Rotation. *ApJ*, **570**, 865–885. 19

Bumba, V. and Klvana, M. (1994). Concerning the solar rotation rates estimated using tracers. *Solar Physics*, **153**, 437–440. 16

Canuto, V. M. and Mazitelli, I. (1991). Stellar turbulent convection - A new model and applications. *ApJ*, **370**, 295–311. 67

Carrington, R. C. (1858). On the distribution of solar spots in latitude. *MNRAS*, **19**, 1. 10

Chakraborty, S., Choudhuri, A. R., and Chatterjee, P. (2009). Why does the sun's torsional oscillation begin before the sunspot cycle? *Physical Review Letters*, **102, issue 4**. 22

Chaplin, W. J., Elsworth, Y., Howe, R., Isaak, G. R., McLeod, C. P., Miller, B. A., van der Raay, H., Wheeler, S. J., and New, R. (1996). Bison performance. *Sol. Phys.*, **168**, 1–18. 44

Charbonneau, P. (2005). Dynamo models of the solar cycle. *Living Rev. Solar Phys.*, **2**. [Online Article]: cited [04.09.2009] http://www.livingreviews.org/lrsp-2005-2. 11

Charbonneau, P. (2009). Stellar magnetic fields: From the sun to compact objects. part i: Solar and stellar dynamos. *39th Saas-Fe Advanced Course. In press*. 11

Choudhuri, A. R., Schlüssler, M., and Dikpati, M. (1995). The solar dynamo with meridional circulation. *A&A*, **303**, 29. 13

Christensen-Dalsgaard, J. (2002). Helioseismology. *Reviews of Modern Physics*, **74, Issue 4**, 1073–1129. 46

Christensen-Dalsgaard, J. (2003). *Lecture notes on Stellar Oscillations*. Aarhus Universitet. 5th edition. 28, 38, 40

Christensen-Dalsgaard, J. (2008). ADIPLSthe Aarhus adiabatic oscillation package. *APSS*, **316, 1-4**, 113. 66

Christensen-Dalsgaard, J., Schou, J., and Thompson, M. J. (1990). A comparison of methods for inverting helioseismic data. *MNRAS*, **242**, 353. 99

Christensen-Dalsgaard, J., Proffitt, C., and Thompson, M. (1993). Effets of diffusion on solar models and their oscillation frequencies. *ApJ*, **403**. 32

Christensen-Dalsgaard, J., Dappen, W., Ajukov, S. V., Anderson, E. R., M., A. H., Basu, S., and et al. (1996). The Current State of Solar Modeling. *Science*, **272**, 1286. 65, 66, 69

Corbard, T. (1998). *Inversion des mesures héliosismiques: La rotation interne du soleil.* Ph.D. thesis, Université de Nice- Sophia Antiplis. 18

Corbard, T. (2003). Ring diagram analysis with gong++ data (first draft). http://www.obs-nice.fr/corbard/ring_doc.ps. 88

Corbard, T. and Thompson, M. J. (2002). The subsurface radial gradient of solar angular velocity from mdi f-mode observations. *Sol. Phy.*, **205**(2), 211–229. 15, 20, 184, 185, 193

Corbard, T., Toner, C., Hill, F., Hanna, K. D., Haber, D. A., Hindman, B. W., and Bogart, R. S. (2003). Ring-diagram analysis with gong++. In H. Sawaya-Lacoste, editor, *SOHO 12 / GONG+ 2002. Local and global helioseismology: the present and future*, page 255. ESA P. D. 79, 114

Corbard, T., Reiter, J., and Thompson, M. J. (2008). Inferring the sub-surface rotational gradients using f-modes and ridge fitting analysis. Private communication. 20

Deubner, F. L. (1975). Observations of low wavenumber nonradial eigenmodes of the sun. *A& A*, **44, 2**, 371–375. 78

Deubner, F. L., Ulrich, R. K., and Rhodes, E. J. (1979). Solar p-mode oscillations as a tracer of radial differential rotation. *A& A*, **72**, 177–185. 78

Dikpati, M. and Gilman, P. A. (2009). Flux transport solar dynamos. In M. Thompson and A. B. et al., editors, *The origin and Dynamics of Solar Magnetism*, pages 67–75. SSS of ISSI. 14, 15

Dikpati, M., Corbard, T., Thompson, M. J., and Gilman, P. (2002). Flux transport solar dynamos with near-surface radial shear. *ApJ*, **575**(1), 41. 15

Duvall, T. L. (1998). Recent results and theoretical advances in local helioseismology. In *Structure and Dynamics of the Interior of the Sun and Sun-like Stars SOHO 6/GONG 98 Workshop*, page 581. 20, 48

Duvall, T. L. and Harvey, J. W. (1984). Rotational frequency splitting of solar oscillations. *Nature*, **310**, 19–22. 18

Duvall, T. L., Dziembowski, W. A., Goode, P. R., Gough, D. O., Harvey, J. W., and Leibacher, J. W. (1984). Internal rotation of the sun. *Nature*, **310**, 22–25. 18

Forestini, M. (1999). *Principes fondamentaux de structure stellaire*. Gordon and Breach Science Publishers. 33

Foukal, P. (1976). Spectoscopic evidence for a higher rotation rate of magnetized plasma at the solar photosphere. *ApJ*, **203**, 145–148. 16

Gabriel, A. H., Grec, G., Charra, J., Robillot, J. M., Cortés, T. R., Turck-Chièze, S., Bocchia, R., and et al. (1995). Global oscillations at low frequency from the soho mission (golf). *Sol. Phys.*, **162**, 61–99. 44

García, R. A., Turck-Chièze, S., Jiménez-Reyes, S. J., Sebastian, J., Ballot, J., Pallé, P. L., Eff-Darwich, A., Mathur, S., and Provost, J. (2007). Tracking solar gravity modes: The dynamics of the solar core. *Science*, **316,issue 5831**, 1591. 38

García, R. A., Jiménez, A., Mathur, S., Ballot, J., Eff-Darwich, A., Jiménez-Reyes, S. J., Pallé, P. L., Provost, J., and Turck-Chièze, S. (2008). Update on g-mode research. *Astro. Nachricht.*, **329, Issue 5**, 476. 38

Giles, P. M. (1999). *Time-distance measurements of large-scale flows in the solar convection zone*. Ph.D. thesis, Stanford University. 24

Gilman, P. A. and Miller, J. (1986). Nonlinear convection of a compressible fluid in a rotating spherical shell. *ApJ.S.S.*, **61**, 585–608. 19

Gizon, L. and Birch, A. C. (2005). Local helioseismology. *Living Rev. Solar Phys.*, **2, 6**. [Online Article]: cited [22.09.2009],http://www.livingreviews.org/lrsp-2005-6. 48

González-Hernández, I. (2003). GONG problems. Private communication. 142

González-Hernández, I. (2008). Subsurface flows from ring diagram analysis. *Journal of Physics: Conference Series*, **118, Issue 1**. Proceedings of the Second HELAS International Conference. 79

González Hernández, I., Patron, J., Bogart, R. S., and the SOI Ring Diagrams (1998). Meridional Flows From Ring Diagram Analysis. In S. Korzennik, editor, *Structure and Dynamics of the Interior of the Sun and Sun-like Stars*, volume 418. 79

González-Hernández, I., Patrón, Bogart, R. S., and the SOI ring diagram team (1999). Meridional flows from ring diagram analysis. *ApJ*, **510**, 153–156. 24

González-Hernández, I., Komm, R., Hill, F., Howe, R., Corbard, T., and Haber, D. A. (2006). Meridional circulation variability from large-aperture ring-diagram analysis of global oscillation network group and michelson doppler imager data. *ApJ.*, **638**, 576–583. 24, 84, 96

González Hernández, I., Kholikov, S., Hill, F., Howe, R., and Komm, R. (2008). Subsurface Meridional Circulation in the Active Belts. *Sol. Phys.*, **252**, 235–245. 145

Gough, D. (1985). Inverting helioseismic data. *sol. Phys.*, **100**, 65–99. 79

Grec, G. (2009). Private communication. 58

Haber, D., Hindman, B., Toomre, J., Bogart, R., Thompson, M., and Hill, F. (2000). Solar shear flows deduced from helioseismic dense-pack samplings of ring diagrams. *Sol. Phys.*, **192**, 335–350. 95

Haber, D. A., Hindman, B. W., Toomre, J., Bogart, R. S., Larsen, R. M., and Hill, F. (2002). Evolving submerged meridional circulation cells within the upper convection zone revealed by ring-diagram analysis. *ApJ*, **570, issue 2**, 855–864. 24, 107

Hale (1908). On the probable existence of a magnetic field in sun-spots. *ApJ*, **28**, 315–343. 10

Hanasoge, S. M. (2008). *Theoretical studies of wave interactions in the sun*. Ph.D. thesis, Stanford university. 47

Hanasoge, S. M., Larsen, R. M., Duvall, T. L., DeRosa, M. L., Hurlburt, N. E., Schou, J., Roth, M., Christensen-Dalsgaard, J., and S. K. Lele, S. K. (2006). Computational acoustics in spherical geometry: Steps toward validating helioseismology. *ApJ*, **648, Issue 2**, 1268–1275. 47

Harvey, J. W., Hill, F., Hubbard, R., Kennedy, J. R., Leibacher, J. W., Pintar, J. A., Gilman, P. A., Noyes, R. W., and et al. (1996). The global oscillation network group (gong) project. *Science*, **272**, 1284. 43

Hathaway, D. H. (1996). Doppler measurements of the sun's meridional flow. *ApJ*, **460**, 1027. 23

Hathaway, D. H., Nandy, D., Wilson, R. M., and Reichmann, E. J. (2003). Evidence that a deep meridional flow sets the sunspot cycle period. *ApJ*, **589**, 665–670. 23

Hill, F. (1988). Rings and trumpets - three-dimensional power spectra of solar oscillations. *ApJ*, **333**, 996. 48, 78

Hill, F. (1995). Local helioseismology via ring diagrams and trumpet surfaces. In R. K. Ulrich, E. J. Rhodes, and W. Dappen, editors, *GONG '94: Helio- and Astero-Seismology from the Earth and Space*, page 484. ASPCS. 79

Hill, F. (2008). Helioseismology and the solar cycle: Past, present and future. *Journal of Astrophy. and Astro.*, **29**, 75–84. 18

Hill, F., Toomre, J., and November, L. J. (1983). Variability in the power spectrum of solar five-minute oscillations. *Sol. Phys.*, **82**, 411–425. 78

Hill, F., Deubner, F.-L., and Isaak, G. (1991). Oscillation observations. In A. N. Cox, W. C. Livingston, and M. S. Matthews, editors, *Solar interior and atmosphere*, pages 329–400. 40

Hindman, B. W., Haber, D. A., and Toomre, J. (2006). Helioseismically determined near-surface flows underlying a quiescent filament. *ApJ*, **653**, 725–732. 79

Howard, R. and Labonte, B. J. (1980). The sun is observed to be a torsional oscillator with a period of 11 years. *ApJ Lett.*, **239**, 33–36. 21

Howe, R. (2009). Solar interior rotation and its variation. *Living Rev. Solar Phys.*, **6, 1.** [Online Article]: cited [27.08.2009], http://www.livingreviews.org/lrsp-2009-1. 15, 21

Howe, R., Christensen-Dalsgaard, J., Hill, F., and et al., R. K. (2000). Deeply penetrating banded zonal flows in the solar convection zone. *ApJ*, **533, issue 2**, 163–166. 22

Howe, R., Komm, R. W., Hill, F., Haber, D. A., and Hindman, B. W. (2004). Activity-related changes in local solar acoustic mode parameters from mdi and gong. *ApJ*, **608**, 562–579. 96

Howe, R., Christensen-Dalsgaard, J., Hill, F., Komm, R., Schou, J., and Thompson, M. J. (2009). A note on the torsional oscillation at solar minimum. *ApJ Lett.*, **701, issue 2**, 87–90. 22

Komm, R. and Howard, H. (1993). Meridional flow of small photospheric magnetic features. *Sol. Phys.*, **147, issue 2**, 207–223. 23

Komm, R., Corbard, T., Durney, B. R., Hernández, I. G., Hill, F., Howe, R., and Toner, C. (2004). Solar subsurface fluid dynamics descriptors derived from global oscillation network group and michelson doppler imager data. *ApJ*, **605, Issue 1**, 554–567. 21, 137, 215

Komm, R., Morita, S., Howe, R., and Hill, F. (2008). Emerging Active Regions Studied with Ring-Diagram Analysis. *Ap.J*, **672**, 1254–1265. 137

Komm, R., Howe, R., and Hill, F. (2009). Emerging and Decaying Magnetic Flux and Subsurface Flows. *Sol. Phys.*, **258**, 13–30. 137

Komm, R., Howe, R., Hill, F., and Hernández, I. G. (2009). Subsurface zonal flows. *Sol. Phys.*, **254, issue 1**, 1–15. 22

Kosovichev, A. G., Schou, J., Scherrer, P. H., and et al., R. S. B. (1997). Structure and rotation of the solar interior: Initial results from the mdi medium-l program. *Sol. Phy.*, **170**, 43–61. Issue 1. 20

Krieger, L., Roth, M., and von der Lühe, O. (2007). Estimating the solar meridional circulation by normal mode decomposition. *Astro. Nach.*, **328, issue 3**, 252. 24

Leibacher, J. and Stein, R. F. (1970). A new description of the solar five-minute oscillation. *Astroph. Letters*, **7**, 191. 28

Leighton, R. B., Noyes, R. W., and Simon, G. W. (1962). Velocity fields in the solar atmosphere. i. preliminary report. *ApJ*, **135**, 474. 28

Maunder (1904). Note on the distribution of sun-spots in heliographic latitudes,1874-1902. *MNRAS*, **64**, 747–761. 10

Morel, P. (1997). CESAM: A code for stellar evolution calculations. *A&A Suppl. Series*, **124**, 597. 66

Nandy, D. (2009). Outstanding issues in solar dynamo theory. In S. S. Hasan and R. J. Rutten, editors, *Magnetic Coupling between the Interior and the Atmosphere of the Sun*. ASSP, Springer-Verlag. 11

Parker, E. N. (1955). Hydromagnetic dynamo models. *ApJ*, **122**, 293. 13

Patrón, J. (1994). *Tridimensional distribution of horizontal velocity flows under the solar surface*. Ph.D. thesis, Universidad de La Laguna. 78

Patrón, J., Hill, F., Rhodes, E. J., Korzennik, S. G., and Cacciani, A. (1995). Velocity fields within the solar convection zone: Evidence from oscillation ring diagram analysis of mount wilson dopplergrams. *ApJ*, **455**, 746. 78

Patrón, J., Hernández, I. G., Chou, D. Y., and Team, T. T. (1998). Time evolution of horizontal subsurface flows in the sun. *ApJ*, **506**, 450–455. 79

Pijpers, F. P. (2006). *Methods in helio- and asteroseismology*. Imperial college press. 28

Provost, J. (1997). Theoretical solar models. In J. Provost and F. X. Schmider, editors, *Sounding solar and stellar interiors*, pages 121–136. 33

Provost, J. (2008). Nosc: Nice oscillations code. *ApSS*, **316, 1-4**, 135. 56, 66

Reiter, J. (2007). Frequencies of solar oscillations for global and local helioseismology. *Astron. Nachrichten*, **328**, 245. 20

Rhodes, E. J., Cacciani, A., and et al., S. K. (1990). Depth and latitude dependence of the solar internal angular velocity. *Sol. Phy.*, **351**, 687. 19

Roth, M. and Stix, M. (2008). Meridional circulation and global solar oscillations. *Sol. Phys.*, **251, issue 1-2**, 77–89. 24

roth, M., Doerr, H. P., Zaatri, A., and Thompson, M. J. (2009). . In preparation, to be submitted to Sol. Phys. 80

Scherrer, P. H., Bogart, R. S., Bush, R. I., Hoeksema, J. T., G, A. G. K. A., Schou, J., and et al. (1995). The solar oscillations investigation - michelson doppler imager. *Sol. Phys.*, **162**, 129–188. 43

Schou, J. and Bogart, R. S. (1998). Flow and horizontal displacements from ring diagrams. *ApJ.*, **504**, 131. 95

Schou, J., Antia, H. M., and et al., S. B. (1998). Helioseismic studies of differential rotation in the solar envelope by the solar oscillations investigation using the michelson doppler imager. *ApJ*, **505**, 390–417. issue 1. 18, 20

Schwabe, H. (1838). Schwabe's observations of sunspot variations. *RASC*, **17**, 409–412. published in 1931. 10

Serenelli, A., Basu, B., Ferguson, J. W., and Asplund, M. (2009). New solar composition: The problem with solar models revisited. submitted to ApJ. 55

Snodgrass, H. B. (1984). Separation of large-scale photospheric doppler patterns. *Sol. Phys.*, **94**, 13–31. 17, 87, 94

Spiegel, E. A. and Zahn, J. P. (1992). The solar tachocline. *A&A*, **265,1**, 106–114. 19

Stix, M. (2002). *The Sun - An Introduction*. Springer-Verlag, 2nd edition. 11

Thompson, M. J. (1990). A new inversion of solar rotational splitting data. *Sol. Phy.*, **125**, 1. 194

Thompson, M. J. (1998). Inversion Methods. In F.-L. Deubner, J. Christensen-Dalsgaard, & D. Kurtz, editor, *New Eyes to See Inside the Sun and Stars*, volume 185 of *IAU Symposium*, pages 125–134. 99

Thompson, M. J., Toomre, J., Anderson, E. R., Antia, H. M., Berthomieu, G., Burtonclay, D., Chitre, S. M., Christensen-Dalsgaard, J., Corbard, T., De Rosa, M., Genovese, C. R., Gough, D. O., Haber, D. A., Harvey, J. W., Hill, F., Howe, R., Korzennik, S. G., Kosovichev, A. G., Leibacher, J. W., Pijpers, F. P., Provost, J., Rhodes, Jr., E. J., Schou, J., Sekii, T., Stark, P. B., and Wilson, P. R. (1996). Differential rotation and dynamics of the solar interior. *Science*, **272**, 1300–1305. Issue 5266. 17, 19

Thompson, M. J., Christensen-Dalsgaard, J., Miesch, M. S., and Toomre, J. (2003). The internal rotation of the sun. *Annu. Rev. Astron. Astrophys*, **41**, 599. 16, 19

Ulrich, R. K. (1970). The five-minute oscillations on the solar surface. *ApJ*, **162**, 993. 28, 78

Ulrich, R. K. and Boyden, J. E. (2006). Carrington Coordinates and Solar Maps. *Sol. Phys.*, **235**, 17–29. 208

Unno, W., Osaki, Y., Ando, H., and Shibahashi, H. (1989). *Nonradial Oscillations of Stars*. University of Tokyo Press. 28

Vorontsov, S. V., Christensen-Dalsgaard, J., Schou, J., Strakhov, V. N., and Thompson, M. J. (2002). Helioseismic measurement of solar torsional oscillations. *Science*, **296, Issue 5565**, 101–103. 22

Wang, W. and Liu, X. W. (2008). Are oxygen and neon enriched in pne and is the current solar ne/o abundance ratio underestimated? *MNRAS lett.*, **389, Issue 1**, 33–37. 55

Weiss, N. O. and Thompson, M. J. (2009). The solar dynamo. In M. Thompson and A. B. et al., editors, *The origin and Dynamics of Solar Magnetism*, pages 53–66. SSS of ISSI. 11

Wolf, M. (1852). On the periodic return of the solar spots. *MNRSA*, **13**, 29. 10

Yang, Q., Snyder, J. P., and Tobler, W. R. (2000). *Map Projection Transformation: Principles and Applications*. Taylor & Francis. 114

Zhao, J. and Kosovichev, S. G. (2004). Torsional oscillation, meridional flows, and vorticity inferred in the upper convection zone of the sun by time-distance helioseismology. *ApJ*, **603, issue 2**, 776–784. 22